CHEMICAL REVIEWS

Review

Cite This: Chem. Rev. 2019, 119, 3193−3295

pubs.acs.org/CR

Synthetic Approaches for Halide Perovskite Thin Films

Wiley A. Dunlap-Shohl,[†] Yuanyuan Zhou,[‡] Nitin P. Padture,*[,‡] and David B. Mitzi*[,†,§]

[†]Department of Mechanical Engineering and Materials Science, Duke University, Durham, North Carolina 27708, United States

[‡]School of Engineering, Brown University, Providence, Rhode Island 02912, United States

[§]Department of Chemistry, Duke University, Durham, North Carolina 27708, United States

ABSTRACT: Halide perovskites are an intriguing class of materials that have recently attracted considerable attention for use as the active layer in thin film optoelectronic devices, including thin-film transistors, light-emitting devices, and solar cells. The "soft" nature of these materials, as characterized by their low formation energy and Young's modulus, and high thermal expansion coefficients, not only enables thin films to be fabricated via low-temperature deposition methods but also presents rich opportunities for manipulating film formation. This comprehensive review explores how the unique chemistry of these materials can be exploited to tailor film growth processes and highlights the connections between processing methods and the resulting film characteristics. The discussion focuses principally on methylammonium lead iodide ($CH_3NH_3PbI_3$ or $MAPbI_3$), which serves as a useful and well-studied model system for examining the unique attributes of halide perovskites, but various other important members of this family are also considered. The resulting film properties are discussed in the context of the characteristics necessary for achieving high-performance optoelectronic devices and accurate measurement of physical properties.

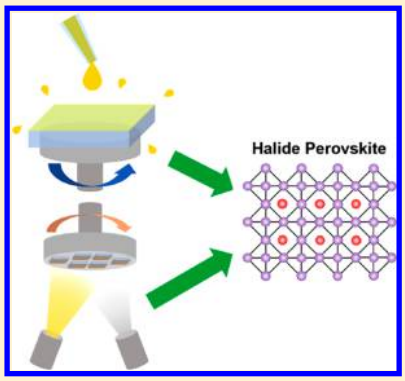

CONTENTS

1. Introduction 3194
2. Fundamentals of Halide Perovskite Crystal, Device, and Film Structures 3195
 2.1. Crystal Structure 3195
 2.2. Common Perovskite Thin Film Device Structures 3197
 2.3. Perovskite Thin Film Characteristics 3198
  2.3.1. Thin Film Chemical and Phase Compositions 3199
  2.3.2. Thin Film Morphologies and Microstructures 3200
3. Perovskite Growth Mechanisms 3203
 3.1. Simultaneous Growth from Precursors ("One-Step") 3203
  3.1.1. Theory of Classical Nucleation and Growth 3203
  3.1.2. Growth from Solutions 3207
  3.1.3. Growth from Vapor Phase 3209
 3.2. Sequential Growth from Precursors ("Two-Step") 3210
  3.2.1. Kinetics of Reactions 3210
  3.2.2. Growth from Solutions 3210
  3.2.3. Growth from Solid Phase 3211
  3.2.4. Growth from Vapor Phase 3211
  3.2.5. Intermediate-Aided Diffusion 3212
 3.3. Crystallization within Confined Spaces 3212
 3.4. Grain Growth and Microstructural Evolution 3213
 3.5. Influence of External Fields 3215
4. Deposition Methods 3216
 4.1. "One-Step" Deposition Approaches 3217
  4.1.1. Basic Spin-Coating 3217
  4.1.2. "Solvent Engineering"/Antisolvent Washing 3219
  4.1.3. Gas-Quenching 3221
  4.1.4. Anti-Solvent/Solvent Extraction 3221
  4.1.5. Drop-Casting 3222
  4.1.6. Dual-Source and Single-Source Evaporation 3223
  4.1.7. Pulsed Laser Deposition (PLD) 3223
  4.1.8. Resonant-Infrared Matrix-Assisted Pulsed Laser Evaporation (RIR-MAPLE) 3225
  4.1.9. Capillary Thin Film Growth 3225
  4.1.10. Melt-Processing 3226
 4.2. "Two-Step" Deposition Approaches 3226
  4.2.1. In Situ Dipping 3227
  4.2.2. Interdiffusion of Stacked Precursor Layers 3228
  4.2.3. Vapor-Assisted Solution Processing 3229
  4.2.4. Sequential Vapor Deposition 3229
  4.2.5. Electro/Chemical Bath Deposition 3231
 4.3. Scalable Processing Methods 3231
  4.3.1. Doctor-Blading 3231
  4.3.2. Slot-Die Coating 3232
  4.3.3. Meniscus-Assisted Solution Printing 3233
  4.3.4. Soft-Cover Coating 3233

Special Issue: Perovskites

Received: May 19, 2018
Published: November 2, 2018

DOI: 10.1021/acs.chemrev.8b00318
Chem. Rev. 2019, 119, 3193−3295

4.3.5. Spray-Coating 3233
4.3.6. Inkjet Printing 3233
4.3.7. Outlook for Commercialization 3234
5. Post-Deposition Treatments 3234
5.1. Annealing 3234
5.1.1. Alternatives to Conductive Annealing 3235
5.1.2. Solvent Annealing 3236
5.1.3. Vacuum-Assisted Annealing/Drying 3237
5.1.4. MAX (X = I or Cl) Annealing 3238
5.2. Organic-Gas Dosing 3239
5.2.1. Methylamine Defect-Healing 3239
5.2.2. Pyridine-Mediated Recrystallization 3240
5.2.3. Formamidine-Induced Perovskite Conversion 3241
5.2.4. Large-Molecular Amine Gas-Induced Passivation 3241
5.3. Ion-Exchange Induced Perovskite Interconversion 3242
5.4. Mechanical Compression 3243
6. Effects of Precursor Composition and Additives 3243
6.1. Effects of Stoichiometry on Film Formation 3244
6.1.1. BX_2-Rich Precursors 3244
6.1.2. AX-Rich Precursors 3244
6.1.3. Halide/Non-Halide "Spectator" Precursors 3247
6.2. Substitutional Modifications in 3D Perovskites 3251
6.2.1. A-Site Substitution 3251
6.2.2. B-Site Substitution 3256
6.2.3. X-Site Substitution 3260
6.3. Other Additives for 3D Perovskites 3264
6.3.1. Water and Aqueous Acids 3264
6.3.2. Organic Molecules 3265
6.3.3. Quantum Dots 3266
6.4. Low-Dimensional Perovskites 3266
6.4.1. Low-Dimensional Hybrid Perovskites/Large Organic Cation Incorporation 3266
6.4.2. Low-Dimensional All-Inorganic Perovskites 3268
7. Substrate-Perovskite Interactions 3270
7.1. Impact of Substrate on Film Nucleation and Growth 3270
7.1.1. Effects of Substrate Geometry 3270
7.1.2. Effects of Surface Chemistry 3271
7.1.3. Epitaxy 3272
7.2. Interdiffusion between Perovskite and the Substrate 3274
7.3. Interfacial Chemical Reactions 3274
7.4. Impact of Substrate on Film Electrical Properties 3275
8. Conclusions 3275
Author Information 3276
Corresponding Authors 3276
ORCID 3276
Notes 3276
Biographies 3276
Acknowledgments 3277
References 3277

1. INTRODUCTION

Halide perovskites have rapidly emerged as a topic of vigorous research activity, as an unprecedented class of semiconductors with a broad range of optoelectronic applications.[1] These materials possess not only outstanding material properties, including in many cases direct and tunable bandgaps,[2−7] high electron/hole mobilities,[8−10] strong light-absorption coefficients,[11] and high defect tolerance coupled with low nonradiative recombination rates (as established by long photogenerated carrier lifetimes and diffusion lengths),[12−14] but also are extremely easy to fabricate, even being compatible with room-temperature deposition processes.[15,16] This unique combination of attributes enables the prospect of high-performance thin film optoelectronic devices manufactured by solution processing or other low-cost fabrication methods and has stimulated intense interest in the emerging field of "organic-inorganic electronics."[17] While early device research focused on thin film transistors[18−20] and light-emitting diodes (LEDs),[21−23] halide perovskites have achieved their most recent success in photovoltaics (PV), with perovskite solar cells (PSCs) displaying rapid evolution of power conversion efficiency (PCE) relative to other thin film technologies over the past decade.[24−29] Halide perovskites are also receiving renewed interest for use in efficient LEDs,[7,30−34] as well as high-performance photodetectors (visible/infrared,[35,36] X-ray,[37,38] and gamma-ray[39]), lasers,[40,41] nonlinear optics,[42−44] and spintronics.[45] Furthermore, halide perovskites are a useful platform for the examination of diverse novel chemical/physical phenomena, such as lower-dimensional magnetism,[46] dielectric confinement/room-temperature exciton features,[47−50] Rashba-Dresselhaus and other spin-related effects,[51−56] and a combination of "soft" chemical/mechanical character (i.e., low formation energy and stability dictated by a delicate thermodynamic balance, low mechanical stiffness, and large thermal expansion coefficients) with attributes of more traditional inorganic semiconductors.[1,57−61]

Despite the high intrinsic quality of the halide perovskites for optical and electronic application, the properties and performance of halide perovskite thin films are dictated to a large degree by the way they are processed. For both device application and scientific study, these films must be carefully fabricated to meet the specific needs of a given device type and architecture, as well as to ensure the quality and accuracy of measurements of microstructure-sensitive physical properties such as carrier mobility. The aim of this review, therefore, is to serve as a guide to the many routes that have been developed for the deposition of high-quality halide perovskite thin films, primarily over the past decade, and to highlight the ways in which the "soft" nature of these materials presents both unique challenges and opportunities in their fabrication. Given that most recent research has focused on Pb- and Sn-based perovskites for PV applications, the review will be centered around the processing of these systems, especially methylammonium lead iodide ($CH_3NH_3PbI_3$ or $MAPbI_3$), which exemplifies the advantages and obstacles encountered when working with this family of materials. However, we expect that the principles and approaches discussed will apply to the broader family of halide perovskites, as well as to related classes of "soft" crystalline materials.

This review is intended to be comprehensive and to provide a thorough description of the major classes of processing routes for halide perovskite thin films. However, we have endeavored to make the paper as accessible to those seeking only the essential information regarding a certain type of deposition process, as to those wishing to gain a holistic understanding of the field. In that spirit, a brief description of

DOI: 10.1021/acs.chemrev.8b00318
Chem. Rev. 2019, 119, 3193−3295

each of the following sections is given below to help guide the reader to the portions of the review that are most relevant to their needs. Section 2 introduces the basic aspects of perovskite crystal structure, device architectures, and microstructure, and how they pertain to processing considerations. Section 3 provides a theoretical basis underlying the relevant processes of film formation, although comprehensive understanding of halide perovskite thin film growth is still in its early stages. This section proceeds from an overview of classical theories of nucleation and growth before delving into more system-specific considerations (i.e., simultaneous vs sequential deposition of precursors, solution vs vapor-based film growth). Sections 2 and 3 are intended to provide a conceptual and scientific foundation for the material in later sections, avoiding emphasis on specific techniques. Section 4, by contrast, is focused on exploring those techniques, employing the concepts introduced in the preceding sections to examine how the processing methods that have so far been used in perovskite optoelectronics can be applied to achieve thin films of suitable microstructures/morphologies for high-performance devices or material property measurement. In section 5, effects of postdeposition treatments such as solvent annealing or exposure to vacuum are explored, again employing concepts introduced in sections 2 and 3. Effects of the perovskite precursor composition are considered in section 6, including cation and halide substitution, as well as more subtle changes such as alloying/doping, changes in stoichiometry, and the use of additives to modify thin film growth. Section 6 also draws from the material in sections 2 and 3, but it is intended to highlight important chemistry-induced deviations from the behavior of the prototypical $MAPbI_3$ system. Section 7 covers a slightly different aspect of chemistry, namely, the influence of the substrate on thin film growth and properties. Finally, section 8 provides a summary and some perspectives for future research in the area of halide perovskite thin film deposition.

2. FUNDAMENTALS OF HALIDE PEROVSKITE CRYSTAL, DEVICE, AND FILM STRUCTURES

Before immersion in the details of halide perovskite film deposition, a consideration of basic perovskite crystal chemistry, as well as typical targeted film and device structures, provides an important bearing on what makes certain film characteristics beneficial or undesirable in a given context. Accordingly, this section first provides a brief introduction to the essential features of halide perovskites and thereafter discusses more detailed aspects of film composition, microstructure, and defects, and their implications for film quality and device functionality.

2.1. Crystal Structure

Although there are many structural variants within the perovskite family (examined in more detail in previous reviews[62−64]), they all share the same motif, derived from the crystal lattice of the original perovskite, the mineral $CaTiO_3$. In this structure, which may be more generally expressed using the chemical formula ABX_3, corner-sharing BX_6 octahedra form an extended three-dimensional (3D) network, with A cations residing in the cuboctahedral spaces formed within the B−X framework (Figure 1). The structure is stabilized by the electrostatic interaction between the A-site cations and the anionic B−X framework, and it may also involve hydrogen bonding between organic A cations and the halogen anions, although the latter interactions are complicated at processing-relevant temperatures by dynamic disorder[65,66] and are irrelevant for all-inorganic compositions. In order to form this structure, several requirements must be met. In most cases, A and B are cations and X is an anion; the valences of A and B must therefore sum to three times that of X in order to maintain charge balance (i.e., for halide perovskites, the A and B cations are predominantly monovalent and divalent, respectively). Furthermore, the structure can only accommodate certain combinations of ions due to restrictions on their relative sizes. These restrictions are most often expressed in terms of the Goldschmidt tolerance factor, t, given in terms of the ionic radii r_A, r_B, and r_X:[67]

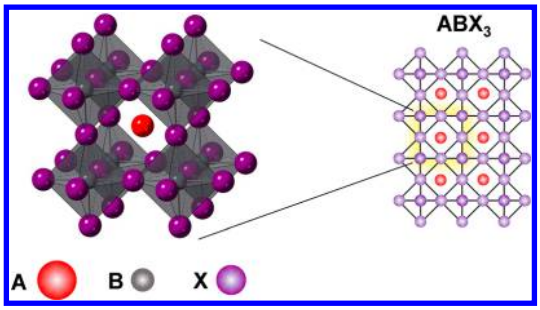

Figure 1. Crystal structure of the 3D perovskites: X anions (violet spheres) are located at the vertices of the octahedra and B cations (gray spheres) at their centers, while the A cations (red sphere) reside in the interstitial spaces between the BX_6 octahedra.

$$t = \frac{r_A + r_X}{\sqrt{2}(r_B + r_X)} \quad (1)$$

Empirically, the 3D perovskite structure is favored for values of t between 0.8 and 1.[63] Also, of importance is the octahedral factor,

$$\mu = r_B/r_X \quad (2)$$

which assesses whether the B atoms will prefer an octahedral coordination of X atoms (as opposed to favoring larger or smaller coordination numbers); this condition is satisfied for values of μ between 0.4 and 0.9.[68] While these are useful guidelines, these metrics derive from simplified models based on hard-sphere packing, which do not capture the full subtleties of interatomic interaction and may be based on uncertain data for ionic radii (especially for nonspherical molecular cations). Nevertheless, these factors can provide useful intuition for rationalizing the stability of certain perovskite-derived structures. Most perovskites of current interest for PVs (i.e., $APbI_3$, where A is $CH_3NH_3^+$/MA^+/methylammonium, $HC(NH_2)_2^+$/FA^+/formamidinium, or Cs^+), as well as some used in LEDs (e.g., $MAPbBr_3$ or $CsPbBr_3$), adopt either the ideal or a slightly distorted 3D perovskite structure (although this structure may not be the most thermodynamically stable one at room temperature, as discussed further in section 6.2). On the basis of the above tolerance factors and assuming the largest metal halide framework (B = Pb and X = I), we can deduce a limit on the size of the A cation, at approximately 2.6 Å for the 3D perovskite framework, which corresponds to no more than 2−3 C−C or C−N bond lengths (i.e., the 3D framework imposes quite stringent constraints on the selection of organic cations that can participate within the perovskite structure and associated thin films).

DOI: 10.1021/acs.chemrev.8b00318
Chem. Rev. 2019, 119, 3193−3295

While the choice of organic cation is relatively limited for 3D perovskites, two-dimensional (2D) analogs are also possible and offer vast additional flexibility. Such structures consist of alternating sheets of the corner-sharing metal halide octahedra interspersed with monolayers or bilayers of the A cations (Figure 2). Although their lateral extent is still confined by the size of the 2D metal halide lattice, organic A site cations can be arbitrarily long, enabling the placement of large, high-aspect ratio cations such as those based on aliphatic or aromatic groups. Furthermore, the geometry of the 2D octahedral arrangement implies (typically) a BX_4^{2-} inorganic repeat unit (as opposed to a BX_3^- unit in the 3D structure); therefore, the negative charge associated with the extra anion must be balanced by an additional positive charge. For the most commonly encountered layered lead halide perovskites such as those based on phenethylammonium [$C_6H_5(CH_2)_2NH_3^+$ or PEA^+] or butylammonium [$C_4H_9NH_3^+$ or BA^+] lead iodide, a bilayer of monovalent cations forms between two adjacent lead halide sheets, creating a van der Waals gap between them (Figure 2A); such compositions thus have A_2BX_4 stoichiometry. Alternatively, each pair of cations in the above scheme may be replaced by a single divalent cation with tethering groups at either end to connect to adjacent halide sheets (Figure 2B), leading to ABX_4 stoichiometry. One challenge posed by the anisotropy of the layered hybrid perovskites relates to the fact that charge carriers can travel easily in the plane of the inorganic sheets but generally cannot easily cross from one layer to another, as the less conductive organic component (as well as the van der Waals gap, if present) impedes transport. During thin film deposition of 2D systems, a key aspect for many device/measurement applications therefore relates to control over which crystallographic orientations are preferred relative to the substrate.

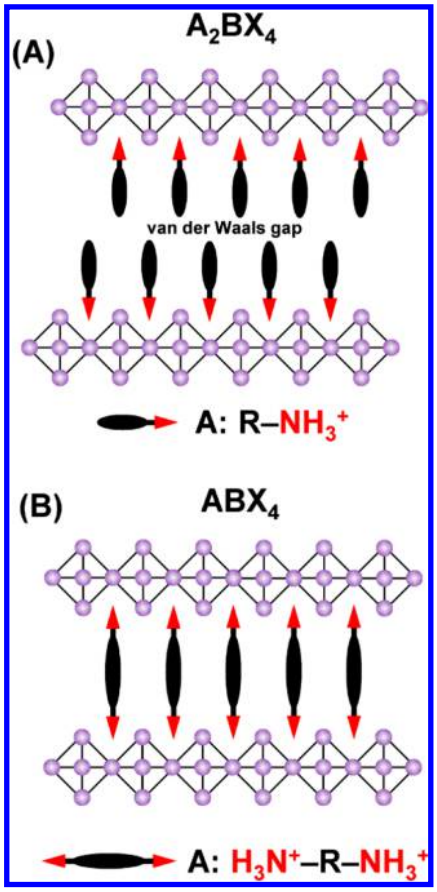

Figure 2. Possible crystal structures of the 2D perovskites. (A) In the A_2BX_4 structure, two monovalent organic cations are bonded to the inorganic sheet per BX_4 repeat unit, forming a bilayer of these cations between the inorganic sheets, with van der Waals interaction between the organic layers. (B) In the ABX_4 structure, each organic cation contains two positively charged tethering groups at either end, enabling each cation to bond to two adjacent inorganic sheets.

The properties of the layered perovskites may be tuned not only by changing the chemistry of the large organic cation or the inorganic sheets but also by blending mixtures of large (A′) and small (A) cations, such that the structures consist of variable thickness layers of the 3D perovskite terminated by the large organic cations. Such quasi-2D structures are often referred to as Ruddlesden−Popper (monovalent A′) or Dion−Jacobson (divalent A′) phases.[69] Ruddlesden−Popper phases are the most widely studied and adopt the generalized chemical formula $A'_2A_{n-1}B_nX_{3n+1}$, where each 3D perovskite layer is n octahedral (metal halide) layers thick (Figure 3).

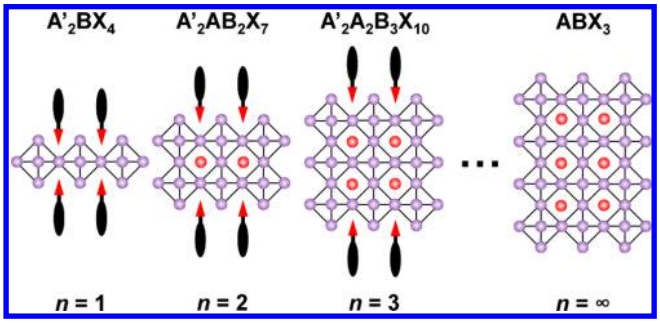

Figure 3. Ruddlesden−Popper series. Starting from the 2D perovskite (n = 1), as successive octahedral sheets are added to the inorganic layer (increasing n), the crystal structure and physical properties of the material approach those of the 3D perovskite ($n = \infty$).

Varying the large/small organic cation blend allows a smooth variation of physical properties from the 2D (n = 1) to the 3D ($n = \infty$) perovskites, providing a useful method to tune film optoelectronic character (e.g., band gap). A notable feature of using larger-n (typically $n > 3$) Ruddlesden−Popper perovskites relates to the reduced tendency for the metal halide layers to lie flat on the substrate during film deposition with increasing n, allowing for enhanced electrical connectivity across the film thickness (strategies for depositing such films are explored in section 6.4.1).[70,71] The relatively small energy barrier separating the formation of Ruddlesden−Popper family members with adjacent n values makes it difficult to form single-phase thin films (especially for large n). This effect is evinced by the fact that attempts to synthesize films using a target stoichiometry (a particular n value) often produce mixtures of the desired phase and Ruddlesden−Popper perovskites with larger and smaller n, which also leads to more complicated optoelectronic character of such films.[31,72] Nevertheless, the variable bandgap and improved material stability conferred by the large organic cation have enabled Ruddlesden−Popper perovskites to serve as active layers both for efficient LEDs[7,31] as well as PSCs that display substantially enhanced stability relative to those based on the 3D perovskites.[73]

Although recent research has been most focused on perovskites with the crystal structures described above, many

DOI: 10.1021/acs.chemrev.8b00318
Chem. Rev. 2019, 119, 3193−3295

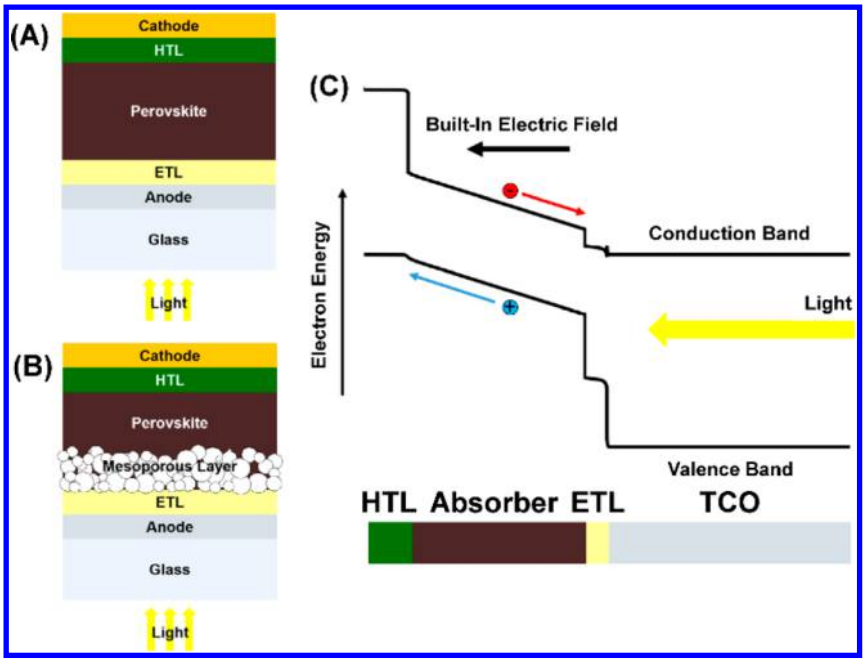

Figure 4. Common PSC architectures: (A) planar PSC, (B) mesoporous PSC, and (C) band diagram of a PSC. Not drawn to scale.

other structural possibilities exist within the perovskite family. Recently, the divalent ethylenediammonium ($H_3NC_2H_4NH_3^{2+}$ or en^{2+}) cation has been shown to incorporate into $MASnI_3$[74] and $FASnI_3$[75] perovskites without destabilizing the 3D network, apparently as a result of formation of Sn and I vacancies that are necessary to maintain charge balance. Two-dimensional structures also afford considerable structural diversity; while the layered structures shown in Figures 2 and 3 can be conceptually derived by slicing the 3D perovskite framework along the (100) direction and stacking these sections up in alternation with layers of organic cations, other cuts from the 3D inorganic framework [e.g., along (110) or (111) directions] can also be stabilized through the appropriate selection of organic cation or stoichiometry.[64] Here, periodic arrangements of cation vacancies may also accommodate ions of different valence than found in the prototypical structure, enabling, for example, the replacement of Pb^{2+} by less toxic Bi^{3+} or Sb^{3+}.[63] It is also possible for the inorganic layer to be corrugated into complicated structures in which the connectivity of the BX_6 octahedra is arranged in motifs such as zigzags or staircases as opposed to planar sheets. Detailed discussion of these and other structures can be found elsewhere.[62−64]

2.2. Common Perovskite Thin Film Device Structures

Although this review does not focus on the processing of entire perovskite devices, it is still important to consider basic information about device design in order to fully appreciate the complexity of halide perovskite film deposition (e.g., the perovskite must be deposited on top of at least one of the preceding device layers). Therefore, interaction of the perovskite with these underlying layers can be critical to film structural evolution. Often, it is taken for granted that the substrate is a flat, inert surface; however, there are many cases in which this assumption is not valid, and the substrate chemistry can play a significant role in film formation and device operation (as discussed in more detail in section 7). Device performance can also be a useful metric for understanding film quality, although it also couples with other device features that may be completely irrelevant to the perovskite film. Nevertheless, high quality of the perovskite thin film is a necessary (though by no means sufficient) condition for outstanding device performance, and thus the latter can be used as a proxy for the former if other components of the device are suitably controlled. Below are discussed some basic concepts relating to the construction of perovskite solar cells, LEDs, and photodetectors, which may have bearing on film deposition, and, therefore, discussion in later sections of this review.

Perovskite solar cells (PSCs) are generally constructed in a p-i-n or n-i-p architecture, wherein the nominally intrinsic perovskite absorber is sandwiched between a p-type hole transport layer (HTL) and an n-type electron transport layer (ETL), as shown in Figure 4A (possibly also including a mesoporous scaffold that may be either semiconducting or insulating, as shown in Figure 4B). In general, it may not be the case that the perovskite is strictly intrinsic (*i*), with the position of the Fermi level strongly depending on fabrication conditions[76−79] as well as the substrate.[80−82] However, the perovskite layer is generally less heavily doped compared to the adjacent materials, and therefore, it may have relatively little impact on the built-in electric field across the device,[83,84] although this may not always be the case.[85] The anode and the cathode contact the ETL and the HTL, respectively, and are either metals or transparent conducting oxides (TCOs). Although, subject to some inconsistency in the literature, here we adopt the convention that the anode and cathode are the terminals through which the electrons and holes are extracted, respectively (Figure 4C), as this nomenclature best represents current flow through the device under normal power-generating conditions.

Considerations of perovskite film grain size and crystallographic orientation are particularly important for PSCs. It is generally desirable to have grains that are large enough to extend across the full thickness of the active layer to mitigate the possibility of trap states or carrier blocking at grain boundaries. It is also beneficial to arrange favorable crystallo-

DOI: 10.1021/acs.chemrev.8b00318
Chem. Rev. 2019, 119, 3193−3295

graphic orientations for carrier transport perpendicular to the substrate, so that carriers can be extracted efficiently (particularly for 2D and quasi-2D perovskite films, for which the metal halide layers should ideally orient perpendicular to the substrate). Other important figures-of-merit characterizing films intended for solar absorber use are carrier lifetime and diffusion length, which specify the average length of time or distance, respectively, a photogenerated carrier can be expected to persist within or travel through the film before recombining with another carrier and losing its energy as light (radiative recombination, an unavoidable and even sometimes desirable process, as in the case of LEDs) or heat [nonradiative or Shockley-Read-Hall (SRH) recombination, due to defects within the crystal lattice that generate states deep within the band gap that can trap photogenerated carriers]. Long carrier lifetimes and/or diffusion lengths are generally taken as evidence of a low trap state density and SRH recombination rate (as radiative recombination is generally dictated by intrinsic rather than defect-related material properties) and thus indicative of high film quality. Carrier lifetime is most often measured by techniques such as time-resolved photoluminescence (TRPL) spectroscopy, which serve as more convenient and less ambiguous means of assessing material quality than building and testing a device.

The choice of whether a planar or a mesoporous device architecture is employed has important bearing on film formation and properties. The planar architecture is typical of most commercial (not perovskite) solar cell architectures, in which the device comprises nominally flat layers stacked atop one another. The mesoporous architecture represents a key characteristic of dye-sensitized solar cells,[86] from which PSCs were originally derived. For this device architecture, the perovskite active layer is partially or totally infiltrated within the pores of a layer composed of partially sintered oxide nanoparticles (scaffold). Attaining the advantages of mesoporous substrates (i.e., intimate contact between the perovskite and the scaffold) requires that perovskite infiltration into the pores be at least mostly complete. Thus, mesoporous substrates tend to be more amenable to solution rather than vapor-based perovskite film deposition. Additional considerations regarding mesoporous substrates include mechanical anchoring[61] and possible shifts in perovskite properties as a result of confined crystallization (as discussed in sections 3 and 7),[87,88] as well as the benefits of disrupting the planarity of the substrate surface, which may allow films with more random crystallographic texture to be obtained (which may or may not be desirable, depending on the context).

Solar cell performance is typically characterized by the short-circuit current density (J_{SC}), the open-circuit voltage (V_{OC}), and the fill factor (FF), which are then used to calculate the PCE (η) based on the irradiance I incident upon the cell:

$$\eta = \frac{J_{SC} V_{OC} \mathrm{FF}}{I} \tag{3}$$

By itself, PCE is not especially useful for revealing the physical origins of device/film performance, but high PCE is compelling evidence of a high-quality active layer, and it is more frequently reported than more absorber-specific metrics such as photogenerated carrier lifetime measurements. The J_{SC} can be used to decouple optical and electrical losses, though these may originate in other device layers (as in the case of parasitic absorption, wherein layers lying in front of the absorber prevent some light from reaching it and generating collectable electron−hole pairs). The V_{OC} is particularly sensitive to SRH recombination, though not the location within the device where it originates, and it can also be affected by band alignment with the adjacent layers. The FF can also be affected by recombination and/or by electrical losses such as high series resistance or low shunt resistance that may or may not be associated with the absorber (e.g., pinholes lower the shunt resistance, while high-resistance secondary phases or low carrier density increase series resistance). Taken together, these metrics can provide additional insight into film quality in a suitably designed experiment.

Other types of devices tend to use similar or even simpler structures. For example, perovskite LEDs rely on essentially the same architecture as PSCs, with minor changes, as the ETL and HTL must be designed for carrier injection as opposed to extraction. This distinction can be slight, as high-performance PSCs may also be operated as reasonably efficient LEDs;[26,89] however, a well-designed LED is optimized for efficient operation in the forward diode current regime rather than in reverse. Optimal LED design may also be better served by materials with different band positions than those typically used in the equivalent PSCs. Different device types may also entail different demands on the nature of the active layer (and the associated film deposition of these layers). While similar considerations of crystallographic orientation apply to both LEDs and solar cells, the LED emitter may be improved by small rather than large grains, which can confine carriers and boost radiative recombination.[30,32]

Perovskite photodetectors, being identical to PSCs except for operating under reverse rather than forward bias, have been reported using inverted[36] (i.e., p-i-n) and conventional[90,91] (i.e., n-i-p) PSC architectures with only minor or no modification to the deposition techniques, although small alterations to the device structure may be necessary in order to optimize reverse-bias performance. For example, while shunt path formation is detrimental to solar cells and photodetectors alike, solar cells can tolerate much higher shunt conductance without suffering severe losses in performance than can photodetectors. This requirement arises because the dark current at reverse bias is equivalent to the detector noise, which may be increased substantially by even very small leakage paths or defect populations.[36] Thus, additives may be introduced to improve crystallinity or reduce defect concentration in the perovskite film,[36] or additional device layers may be needed to seal pinholes and prevent undesired contact between nonadjacent layers to reduce the dark current.[91] Otherwise, film deposition methods should be controlled especially stringently to ensure absolutely conformal coverage of the substrate by the perovskite active layer. A key metric specifying the performance of a photodetector is the detectivity D, defined in terms of the device active area A, frequency bandwidth f, and noise-equivalent power (NEP):

$$D = \frac{\sqrt{Af}}{\mathrm{NEP}} \tag{4}$$

A high detectivity implies a high signal-to-noise ratio and, due to its high sensitivity to leakage currents, is an unambiguous sign of a conformal thin film with good defect characteristics.[36]

2.3. Perovskite Thin Film Characteristics

Besides device architecture (or equivalently, the substrate/film configuration for property measurement), further discussion of film deposition relies on an understanding of metrics used to

DOI: 10.1021/acs.chemrev.8b00318
Chem. Rev. 2019, 119, 3193−3295

evaluate film quality. Below are detailed some characteristics that have significant bearing on device performance or property measurement.

2.3.1. Thin Film Chemical and Phase Compositions. As discussed in section 2.1, there are numerous perovskite chemistries, which in turn determine the associated film structure and properties. Unintentional variations in chemistry can lead to detrimental effects on film quality. Dopants and impurities, while not necessarily affecting the overall structure, can nevertheless exert significant influence over perovskite characteristics. For example, minor deviations from the ideal stoichiometry can induce point defects such as vacancies, interstitials, or antisite defects that may dope the perovskite,[76−79] introduce charge carrier traps,[92] or contribute to hysteresis in current density−voltage characteristics (or $J-V$ curves).[93] Hysteresis is frequently witnessed in perovskite devices as a difference in the $J-V$ curves depending on voltage sweep rate and direction[94] and is frequently attributed to interfacial defects[95−97] and/or ion migration.[93,98,99] The strength of the former effect indicates that hysteresis may largely be influenced by factors that are not necessarily related to the bulk properties of the perovskite films themselves, but the persistent influence of the latter indicates that film quality is still a relevant concern if hysteresis is to be entirely eliminated from the device. More significant deviations from ideal stoichiometry can also introduce secondary phases, which may be beneficial, benign, or undesirable depending on their amount and distribution within the thin film. On the other hand, a compelling advantage of the halide perovskite family is the wide range of band gaps accessible through compositional tuning,[3−7,100,101] enabling optoelectronic devices to be optimized for emission or detection from the near-infrared (IR) to the ultraviolet (UV) and for narrow- and wide-band gap solar cells to be fabricated for use in tandem PVs. In these cases, it is crucial that the composition be precisely and reliably controlled to obtain the targeted band gap.

It is frequently assumed that the initial target perovskite composition in the precursor feedstock is maintained in the final processed films, and very often no further effort to quantify composition is described. However, unexpected compositional changes may occur during the various processing steps. MA halides are particularly volatile, and it is therefore often desirable to expose the films to an environment rich in these species during any heat treatment steps in order to compensate for their evolution from the film (e.g., transforming a Pb-halide film to perovskite through annealing in saturated MA-halide vapor, as discussed in section 4.2.3, or subjecting already deposited perovskite films to this treatment, as discussed in section 5.1.4). In addition, certain additives may form secondary phases within the films that can be difficult to detect, but they may alter the composition of the absorber slightly by preferentially binding to selected chemical perovskite components (e.g., KI, which is discussed in further detail in section 6.2.1.3). Thus, a need exists to ensure the chemical compositions of the final perovskite films and to use techniques that compensate for elemental losses.

The reactivity of halide perovskites can be an especially important consideration in the context of film formation (as well as long-term thin film degradation). The stability of $MAPbI_3$ with respect to decomposition into its component binary halides rests on a thermodynamic "knife-edge," with the formation enthalpy favoring decomposition[102] but the overall Gibbs free energy (barely) favoring the perovskite due to a stabilizing entropic contribution.[103,104] This precarious position is an important factor underlying halide perovskite film formation and underscores the ease with which such films may be either assembled or decomposed. Interactions between solvents and the organic cation, such as prospective conversion of methylammonium to dimethylammonium by interaction with the common solvent *N*,*N*-dimethylformamide (DMF), can also lead to unexpected compositional changes of the thin film and possible deterioration of its optoelectronic properties.[105,106] Redox chemistry of Pb can be troublesome regardless of whether the perovskite is organic−inorganic or fully inorganic. Zhao et al.[107] have observed that $MAPbI_3$, $CsPbI_3$, and $CsPbBr_3$ react spontaneously with metals such as Al, Cr, Ag, and Yb, even in the absence of moisture, light, and oxygen, leading to oxidation of the foreign metal and reduction of Pb^{2+} to Pb^0, degrading the films without participation or loss of the organic (or other inorganic) cation or the halide anion. Thus, it should be emphasized that no aspect of the chemistry of the systems employed in the fabrication of halide perovskite films can be taken for granted, as unseen or subtle effects can potentially have a large impact on the composition and properties of the final film.

Phase purity in perovskite films is also important. Nonperovskite secondary phases can be inclusions (dispersed over various length scales) and/or reside at grain boundaries/interfaces. For the prototypical $MAPbI_3$ perovskite, the most commonly encountered secondary phase is PbI_2, which can result from incomplete transformation of the precursors or decomposition of the film, and it is usually readily visible in X-ray diffraction (XRD) patterns or scanning electron microscopy (SEM) images. In the proper amounts, PbI_2 is frequently invoked as a beneficial inclusion that can passivate interfaces and/or grain boundaries (as discussed further in section 6.1.1).[108,109] In fact, PbI_2 is itself a PV material that may be able to contribute to the photogenerated carrier population in $MAPbI_3$ thin films,[110] possibly partially mitigating disadvantages resulting from its presence. Nevertheless, excessive amounts of PbI_2 can impede carrier transport, and its presence should be carefully controlled to ensure optimal film quality.

Other perovskite systems, notably $FAPbI_3$[111,112] and $CsPbI_3$,[113,114] are thermodynamically unstable at room temperature relative to nonperovskite phases that have the same chemical composition but different crystal structure and inferior optoelectronic properties (strategies to obtain phase-pure perovskite films of these compositions are discussed in section 6.2.1). At best, inclusions of nonperovskite phases might reduce performance by acting as "dead spots" in the thin film, but they may also serve as seed crystals for transformation of the perovskite to the nonperovskite phase. While these issues can be circumvented by blending with other perovskite compositions [e.g., $FA_{1-x}Cs_xPbI_3$,[115] $FA_{1-x}MA_xPb(I_{1-x}Br_x)_3$,[116] $CsPb(I_{1-x}Br_x)_3$[117]], increasing the chemical complexity of these systems also increases the combinatorial availability of other secondary phases that may have potentially detrimental effects on film quality. Alternatively, such blended compositions can potentially phase segregate into perovskites with different compositions and properties, as in the case of systems based on mixtures of I^- and Br^- (as discussed in more detail in section 6.2.3.1)[118] or in the case of higher-*n* Ruddlesden−Popper layered perovskite films (as noted in section 2.1 and discussed in more detail in section 6.4.1).[31] It is, therefore, important to ensure that secondary phases are at least controlled, if not entirely eliminated, to ensure that the

DOI: 10.1021/acs.chemrev.8b00318
Chem. Rev. 2019, 119, 3193−3295

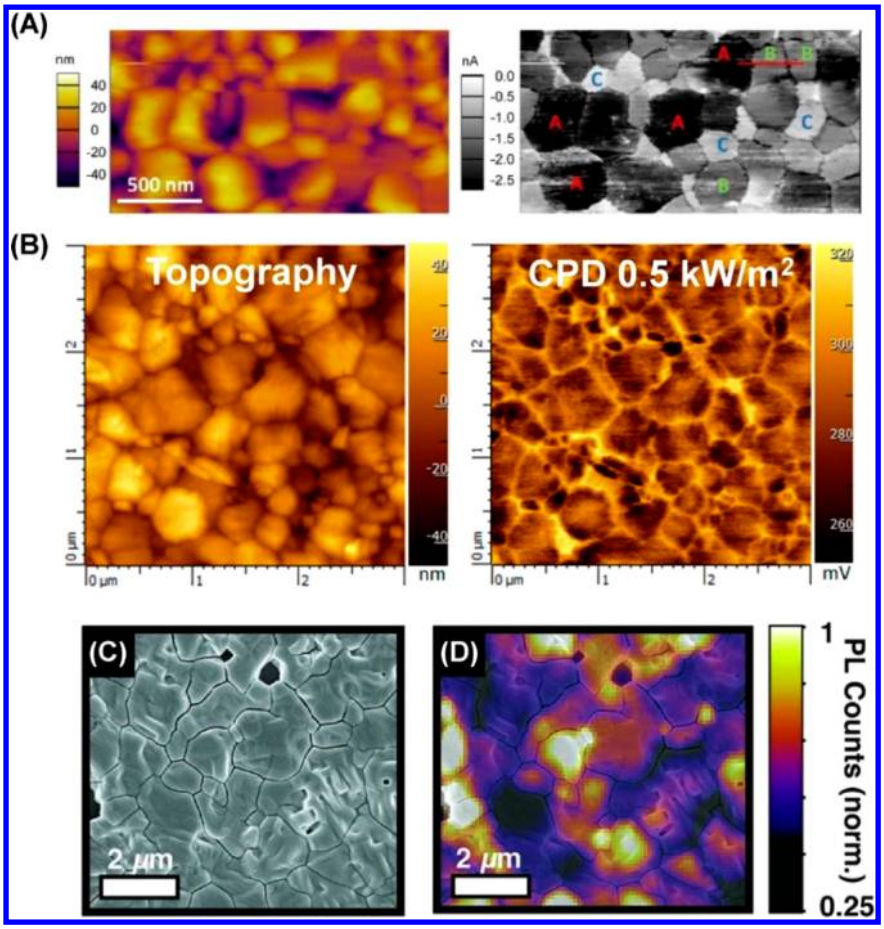

Figure 5. Effects of grain boundaries on electronic properties. (A) Topographical (colored) and photoconductive (grayscale) AFM maps of a $MAPbI_3$ film surface, displaying heterogeneity in current collection between different grains, as well as at grain boundaries. Reprinted with permission from ref 127. Copyright 2018 AIP Publishing. (B) Topographical AFM and KPFM maps of contact potential difference (CPD) on $MAPbI_3$ films, displaying electrical response of the grain boundaries under illumination. Adapted from ref 135. Copyright 2015 American Chemical Society. (C) SEM and (D) composite SEM/fluorescence microscopy images of a $MAPbI_{3-x}Cl_x$ thin film, displaying heterogeneous luminescence of the interior grain surfaces as well as reduced luminescence at grain boundaries. Reprinted with permission from ref 136. Copyright 2015 AAAS.

perovskite film is free of "dead spots," obstacles to carrier transport, local property variations and "carrier sinks," or other discontinuities that might adversely affect device performance or accurate property measurement (note that, in some cases, carefully staged progressions of phase mixtures may be tailored to potentially boost device performance).[31]

2.3.2. Thin Film Morphologies and Microstructures. *2.3.2.1. Basic Morphological Aspects.* One crucial aspect of perovskite film morphology/microstructure relates to whether it fully covers the substrate, with minimal pinholes, bare spots, or surface roughness. For devices, this condition allows for (i) maximizing device active area, (ii) eliminating shunt paths through which leakage current might flow, and (iii) enabling conformal deposition of overlying device layers. Generally, such well-covered films can be obtained by emphasizing dense and uniform nucleation of the perovskite grains and avoiding rapid consumption of the available precursors that leads to the formation of large but poorly connected crystallites (as discussed in more detail in sections 3 and 4).

It is also generally considered desirable for most perovskite active layers to have large grains in order to facilitate carrier motion, which might be blocked by grain boundaries.[119] In the context of high-performance PSCs and photodetectors, it is important for the grains to extend across the full film thickness, as horizontal grain boundaries may impede carrier transport and extraction, while vertical grain boundaries are less likely to adversely impact these processes. Postdeposition treatments, generally with the goal of increasing grain size, are discussed in more detail in section 5. Large grain size is not a universal requirement, however. As mentioned earlier, LED active layers generally benefit from fine grain structure, since small grain size can help to spatially confine electron−hole pairs and enhance radiative recombination.[30,32] There is even some debate as to whether large grains are necessary for efficient PV conversion, as previous computational modeling has shown that defects at grain boundaries in $MAPbI_3$ are relatively benign,[14] and indeed high-performance PSCs with very large FF have been demonstrated despite the absorbers having small grains.[120,121] It is, however, worth noting that grain boundaries can possess undesirable characteristics that are independent of their intrinsic electronic properties. Grain boundaries may serve as "highways" for the detrimental transport of ions and environmental species (oxygen, moisture),[93,122,123] and mechanical integrity can be reduced in perovskite films that have small grain size.[124,125] Thus, a high grain boundary density can be associated with reduced thin film stability in addition to compromised performance. Regardless of whether the grains are large or small, however, it is generally essential for all device active layers to have a highly compact and dense

DOI: 10.1021/acs.chemrev.8b00318
Chem. Rev. 2019, 119, 3193−3295

microstructure consisting of close-packed grains free of pinholes or other voids.

2.3.2.2. Crystallographic Orientation. While average grain size is the most commonly used metric in specifying microstructural defects in perovskites, a polycrystalline thin film has rich characteristics, such as grain size distribution, grain shape, and crystallographic orientation/texture, all of which have varying degrees of effect on the film properties. In the context of the 3D perovskites, there is evidence that favoring certain grain crystallographic orientations may be at least as important for PV as grain size.[126] Photoconductive atomic force microscopy (AFM) indicates that certain types of grains allow much more efficient photocurrent collection than others (Figure 5A)[127,128] and that the "highest-performing" grains may make up a relatively small fraction of the entire film.[128] Different grain facets have also shown different levels of effectiveness in their PV parameters, as measured by photoconductive AFM, leading to subgranular variation in local carrier collection.[129] In $MAPbI_3$ films, a preferred (110) grain orientation (for the room-temperature tetragonal phase, hereafter denoted "tet(110)") is often associated with enhanced PV performance[130] and may be induced by the presence of Cl (as discussed in more detail in section 6.1.3).[131,132] While some have proposed that Cl mediates bonding of the perovskite to TiO_2 (a commonly used ETL in PSCs),[133,134] preferred tet(110) orientation in the presence of Cl has been observed on other substrates and may indicate that the tet(110) facets are intrinsically the most stable and that Cl simply aids their growth.[132]

In general, for devices based on 3D perovskite thin films, it is unclear to what extent performance and film properties are controlled by qualities that are intrinsic to the orientation of the grains as opposed to how those orientations interact with other device layers. The effect of crystallographic orientation is much more evident in layered perovskites (e.g., 2D or Ruddlesden−Popper) thin films, however. As noted in section 2.1, the pronounced anisotropy of the crystal structure results in anisotropy of the carrier mobility, wherein transport is easy along the planes of corner-sharing metal halide octahedra but not across them. It is thus imperative to ensure that the orientations of layered perovskite films relative to the substrate are optimized according to the requirements of the specific application (i.e., parallel for transistors, where in-plane transport is needed, and perpendicular for solar cells and LEDs, where cross-plane transport is most important). Film deposition strategies aimed at controlling layer orientation are discussed in detail in section 6.4.

2.3.2.3. Grain Boundaries. The grain boundaries themselves are also a source of rich complexity. There is no general agreement on the overall impact of grain boundaries, perhaps because their nature is highly sensitive to the preparation and chemistry of the perovskite film. Some researchers have suggested, based on Kelvin probe force microscopy (KPFM) and conductive AFM results, that grain boundaries in $MAPbI_3$ can play a role in determining the potential distribution within the film and separating and collecting photogenerated electron−hole pairs, thus reducing the likelihood of recombination (Figure 5B).[127,135] It has also been observed, based on reduction of luminescence at grain boundaries relative to the grain interior, that grain boundaries may be sources of harmful trap states that should be avoided (Figure 5, panels C and D).[136] Others contend that although the luminescence may be reduced there, SRH recombination lifetimes at grain boundaries can be on par with or even exceed those observed at the film surfaces or in the grain interiors.[137] Ciesielski et al.[119] have observed that such enhancement of the luminescence at grain boundaries may originate from carrier blocking, causing carriers to pile up near them, where the local enhancement in carrier density enhances the radiative recombination rate. This observation implies not only a benign defect nature of the grain boundaries (presumably a beneficial effect) but that carriers might be prevented from crossing them (presumably detrimental). Such reports, however, frequently overlook the complexities of grain boundary characteristics, with different types of boundaries possibly giving rise to very different carrier transport or recombination dynamics. A notable exception is a study by Jiang and Zhang,[127] who have deduced from photoconductive AFM measurements that boundaries between grains of similar photocurrent-generating capacity often display enhanced PV performance relative to the grain interiors, while the PV behavior of boundaries separating dissimilar grains is intermediate between that of the adjacent grain interiors (Figure 5A). They propose that differences in the photocurrent obtained from different classes of grains may pertain to crystallographic orientation, with XRD and electron backscatter diffraction (EBSD) measurements suggesting that these classes of grains may be associated with tet(310), tet(110), and tet(202) orientations, though no effort was made to connect specific orientations with levels of PV performance.[127] This study also points to a key challenge posed by the soft nature of perovskites with respect to the determination of crystallographic orientation of individual grains and other fine-level microstructural features in halide perovskites. That is, techniques that are ordinarily used to examine crystal structure on the atomic scale that rely on electron diffraction [e.g., EBSD in an SEM or selected-area electron diffraction (SAED) in transmission electron microscopy (TEM)] can also easily damage the sample, inhibiting high-resolution diffraction patterns from being obtained. There is, therefore, a need for the development of techniques that can provide the same information via gentler probing methods, which could benefit research into halide perovskites as well as other classes of soft crystalline materials.

It should also be noted that a universal disadvantage of grain boundaries is that they facilitate the ingress of atmospheric or other adventitious species that can degrade the perovskite (as well as egress of decomposition products, efficient removal of which may accelerate degradation). Emphasis on large grain size can therefore avoid such problems in addition to possible detrimental effects on film electronic properties. For example, using a MACl/methylamine gas-assisted deposition (such techniques are further explored in section 5.2), Ji et al.[138] obtained $MAPbI_3$ films with considerably larger apparent grain size than reference films prepared without the above additives. (Note that estimation of grain size from SEM or AFM images can be misleading as discussed further in section 3.4; thus, we will employ the more conservative term "apparent grain size" throughout the text when these techniques are used.) The large-grain films, as well as PSCs fabricated using them, displayed considerably higher resistance to degradation than the small-grain films, illustrating the benefits of large grain size. Degradation induced by the presence of grain boundaries can also be avoided by packing them with a moisture-repelling material. For example, Zong et al.[139] recently used a hydrophilic−hydrophobic−hydrophilic triblock polymer, Plur-

DOI: 10.1021/acs.chemrev.8b00318
Chem. Rev. 2019, 119, 3193−3295

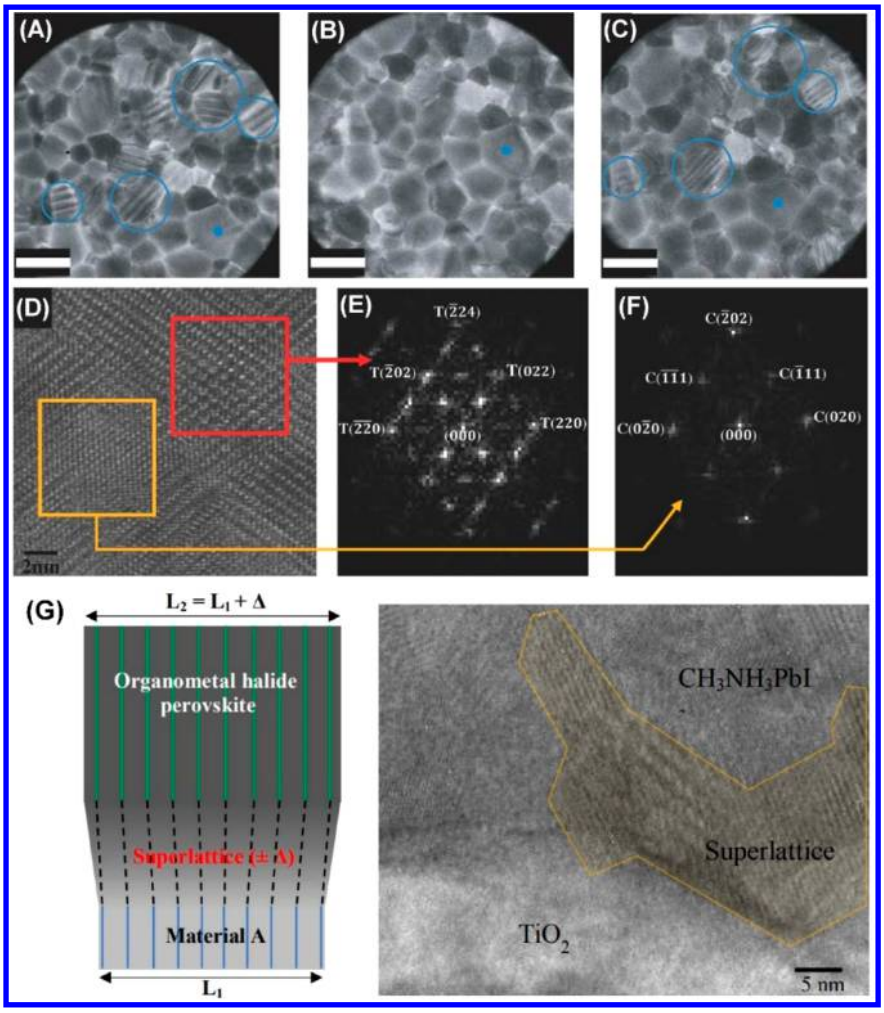

Figure 6. (A) Bright-field TEM images of $MAPbI_3$ thin films, with some grains displaying striped contrast (circled regions) characteristic of twin domains at room temperature; (B) the same film after in situ heating to 70 °C (above the tetragonal-to-cubic phase transition), in which the contrast has been erased; (C) the same film after cooling back to room temperature, in which the twin domains have reappeared. In (A−C), the same grain is identified with a blue dot and the scale bar is 500 nm. Reprinted from ref 141 under CC BY 4.0 (license information available at https://creativecommons.org/licenses/by/4.0/). (D) HRTEM image of coexistence of tetragonal and cubic regions within a single grain in a $MAPbI_3$ thin film, with phase contrast qualitatively evident by differences in the lattice fringes as well as in SAED patterns corresponding to (E) tetragonal and (F) cubic lattices; (G) schematic and HRTEM image of the interface between $MAPbI_3$ and TiO_2, indicating tetragonal-cubic superlattice formation near the border between these materials that may help to accommodate strain through lattice matching. Reprinted with permission from ref 142. Copyright 2018 Wiley-VCH.

onic P-123, to protect grain boundaries in $MAPbI_3$ thin films. The hydrophilic poly(ethylene oxide) ends of the polymer tether to adjacent perovskite grains, while the hydrophobic poly(propylene oxide) in the center of the polymer resists attack by moisture. The P-123-protected perovskite was considerably more stable than pristine $MAPbI_3$ under exposure to moisture (70% relative humidity), heat (100 °C), and AM1.5G illumination, demonstrating the importance of protecting the grain boundaries.

2.3.2.4. Intragranular Defects. Beyond grain boundaries, other crystal defects should also be considered, such as domain boundaries, stacking faults, dislocations, and twin planes. As with grain boundaries, the implications of many such defects in halide perovskites remain poorly understood. Even basic descriptions of such defects are seldom encountered in the literature, perhaps because the soft nature of the perovskites implies that detailed inspection of these features entails significant risk of destroying them, as noted above. Kutes et al.[128] provided some evidence for a connection between possible dislocations or other intragrain linear or planar defects and local electrical properties, but fundamental understanding of these relationships is not available. Hermes et al.[140] observed the formation of striated domains in piezoresponse force microscopy (PFM) maps of $MAPbI_3$ films and proposed that this material is ferroelastic, forming periodic twin domains to compensate for strain induced by the cubic-to-tetragonal phase transition that occurs when the perovskite is cooled after annealing. Rothmann et al.[141] observed similar subgranular features using low-dose TEM images (Figure 6A), which could unambiguously be assigned to twin domains formed along (112) mirror planes. The domains could be erased and regenerated by respectively raising or lowering the sample temperature through the tetragonal-to-cubic phase transition at 57 °C (Figure 6B,C), suggesting that twinning does indeed arise as a consequence of strain associated with that transition. Kim et al.[142] have also observed from high-resolution TEM (HRTEM) images and SAED patterns, in addition to twin structures, that although the tetragonal rather than the cubic

DOI: 10.1021/acs.chemrev.8b00318
Chem. Rev. 2019, 119, 3193−3295

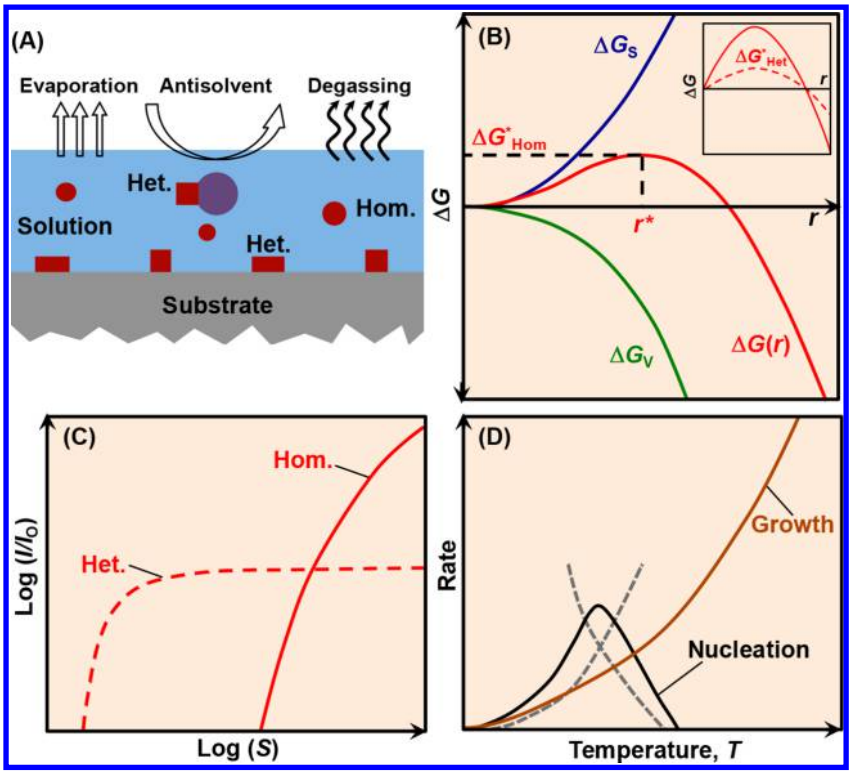

Figure 7. Schematic illustrations of classical: (A) homogeneous and heterogeneous nucleation during supersaturation of a thin film of a solution; (B) free energy change (ΔG), sum of surface (ΔG_S), and volume (ΔG_V) free energy changes, as a function of nucleus radius (r) for homogeneous nucleation (inset: heterogeneous nucleation); (C) normalized nucleation rate (I/I_0) as a function of supersaturation ratio (S) for homogeneous and heterogeneous nucleation; and (D) nucleation and growth rates as a function of temperature (dashed lines represent the two competing effects, number of stable nuclei and frequency of "monomer" attachment, that govern the nucleation rate). Adapted from ref 143. Copyright 2015 American Chemical Society.

phase of $MAPbI_3$ is stable at room temperature, both phases can coexist in $MAPbI_3$ thin films prepared by a variety of different methods (Figure 6, panels D−F). Moreover, these phases can organize themselves into regular superlattices of alternating cubic and tetragonal domains. Observations of these structures near the interface with substrate materials (e.g., TiO_2) indicate that such superlattices may form spontaneously to accommodate interfacial strain, possibly improving the quality of adhesion to the substrate (Figure 6G).[142] The implications of intragranular defects on perovskite thin film properties are opaque in general, however, and further study is needed to clarify this aspect of microstructure.

While there is much that remains obscure regarding the nature of many of the halide perovskite defects, the forgiving nature of these materials has permitted device performance benchmarks to rapidly advance despite this lack of knowledge. Much of the recent research regarding perovskite film microstructure has focused on more elementary considerations such as obtaining conformal coverage or stabilizing a desired perovskite phase. However, it is expected that continued improvements in film quality and device performance may be contingent on understanding and controlling the subtler aspects of the perovskite film defect structure (as noted in this section), as well as on gaining a deeper knowledge of the underlying film growth mechanisms, as detailed in the next section.

3. PEROVSKITE GROWTH MECHANISMS

The synthesis/processing of halide perovskite films can be broadly classified into two types of methods, "one-step" and "two-step," the specific mechanics of which are described in detail in section 4. Here we refer to the processes occurring in the one-step and two-step methods as "simultaneous" and "sequential" growth from precursors, respectively, and they form the basis of the structure of this section on perovskite growth mechanisms. Simultaneous growth generally occurs in myriad techniques involving evolution of crystalline perovskite thin films from solution or vapor precursors that contain a nominally uniform mixture of all chemical ingredients. Sequential processes occur in all the other techniques that entail the spatially and/or temporally distinct introduction/reaction of precursors (solid, liquid, and vapor), which ultimately react to form crystalline perovskite films.

The growth of the final crystalline perovskite film involves a series of generally poorly understood and complex processes, which depend on several processing variables and the specific system under consideration. Therefore, general theories that describe these complex processes do not exist. However, classical theories can be invoked to describe the most basic of the processes. These descriptions can serve as a foundation to build upon as further complexities are added with the expansion of our understanding of perovskite growth mechanisms. The ultimate goal is to have deterministic control over the growth processes for the reliable deposition of perovskite films with consistent high quality and desired structure/properties (as discussed, for example, in section 2.3).

3.1. Simultaneous Growth from Precursors ("One-Step")

3.1.1. Theory of Classical Nucleation and Growth. *3.1.1.1. Nucleation.* Nucleation is the most important initial

DOI: 10.1021/acs.chemrev.8b00318
Chem. Rev. 2019, 119, 3193−3295

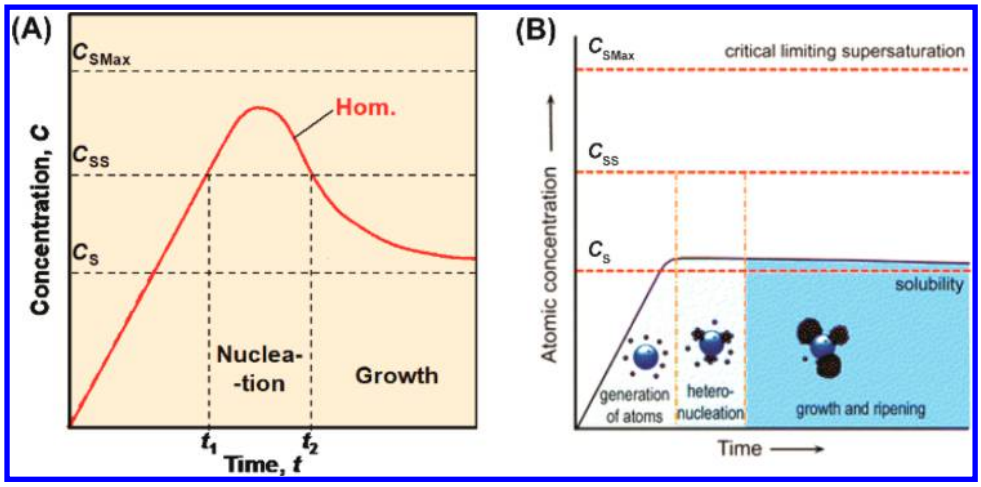

Figure 8. LaMer diagram for (A) homogeneous and (B) heterogeneous formation of particles from solution. Here, C_S is the equilibrium solubility limit, C_{SS} is the supersaturation limit at which nuclei begin to form, coincident with time t_1, while t_2 is the time at which the concentration falls below C_{SS} as a result of depletion of "nutrients," curtailing further nucleation. C_{sMax} is the critical limiting supersaturation (i.e., the concentration at which the nucleation rate approaches infinity).[157] (A) Adapted from ref 157. Copyright 1950 American Chemical Society. (B) Republished with permission from ref 158. Copyright 2013 Royal Society of Chemistry.

phenomenon in thin film formation, dictating the nature of the subsequent growth processes and, ultimately, the characteristics of the final product. As such, it is very important to understand nucleation behavior so that it can be controlled and programmed. In reality, there can be significant temporal overlap between the occurrence of the nucleation and growth processes, but they are treated separately here for the sake of convenience. In the case of one-step deposition methods, typically a precursor solution containing all the components of the perovskite is deposited on a substrate as a film, or the precursors are simultaneously evaporated and collect on a substrate. Various methods are used to accomplish this process, which are described in detail in section 4. Here, consider a generic precursor-solution film deposited onto a substrate (Figure 7A).[143] Removal of any of the solvent will cause the concentration of the precursor solution in the film to increase, driving it toward (or beyond) saturation. There are several ways the solvent can be removed, but evaporation due to isothermal heating is perhaps the most commonly used method.[143−146] Note that an increase in temperature can also affect the solubility, which can increase or decrease depending on the specific system. Certain perovskite systems, such as $MAPbI_3$ in γ-butyrolactone (GBL) or $MAPbBr_3$ in DMF, exhibit inverse solubility, wherein solubility decreases with an increase in temperature.[147] The solvent can also be removed by other methods, such as by using an antisolvent (or orthogonal solvent) or jet of compressed gas to extract the precursor solvent at or near room-temperature (such techniques are discussed in sections 4.1.2−4.1.4).[143,148−150]

In classical nucleation, the saturation of the precursor typically results in the appearance of molecules of the nucleating phase (also referred to as "monomers" and can be atoms, ions, molecules, or formula-units),[151] which can cluster together into single-crystal nuclei. These nuclei will appear at the substrate/precursor-solution interface and/or within the precursor solution (Figure 7A), referred to as heterogeneous and homogeneous nucleation, respectively. Heterogeneous nucleation can also occur at the interface between preexisting colloidal particles (if present) and the precursor solution (or at the top surface of the precursor solution; however, this case is not considered here as it is expected to be less common, although Chen et al.[152] have recently suggested that top-surface nucleation may be key to understanding crystallization behavior of Ruddlesden−Popper phases). In the case of homogeneous nucleation, the total free-energy change ΔG as a function of nucleus (spherical) radius, r, is given by[153]

$$\Delta G(r) = -V\Delta G_V + A\gamma_{CL} \tag{5}$$

where V is the volume of the nucleus, A is its area, ΔG_V is the volume free energy change, and γ_{CL} is the energy associated with the interface between the liquid (L) and the crystalline (C) nucleus. Specifically,[153]

$$\Delta G(r) = \left(-\frac{4\pi r^3}{3V_M}\right)RT\ln(S) + 4\pi r^2\gamma_{CL} \tag{6}$$

where V_M is the molar volume of the nucleus, R is the gas constant, T is absolute temperature, and $S = C/C_S$ is the saturation ratio, where C is the solute concentration in the precursor solution and C_S is the equilibrium solubility limit. The free energy change ΔG is the sum of the free energy change (positive) associated with the creation of a unit area of new nucleus/precursor−solution interface and the free energy change (negative) associated with the conversion of a unit volume of precursor solution to crystalline nucleus. Eq 6 is plotted schematically in Figure 7B, where the maximum (ΔG^*_{Hom}) in ΔG occurs at the critical nucleus radius (r^*); nuclei with radii $r < r^*$ dissolve back into the precursor solution, while nuclei with radii $r > r^*$ are thermodynamically stable and they will grow.[143] At constant temperature, $r^* \propto 1/\ln(S)$.[143] Nucleation is considered heterogeneous when nuclei form on foreign surfaces (e.g., substrate or colloidal particles), where the energy barrier, ΔG^*_{Het}, is reduced significantly through effective reduction of the interface energy, $\gamma \times f(\theta)$, where $0 < f(\theta) < 1$ (Figure 7B, inset).[154] The parameter $f(\theta)$ is given by[143,154]

$$f(\theta) = \frac{1}{4}(2 + \cos\theta)(1 - \cos\theta)^2 \tag{7}$$

where θ is the contact angle in the Young equation:[143,155]

DOI: 10.1021/acs.chemrev.8b00318
Chem. Rev. 2019, 119, 3193−3295

$$\cos\theta = \frac{\gamma_{SL} - \gamma_{SC}}{\gamma_{CL}} \quad (8)$$

with γ_{SL} and γ_{SC} being the surface energies associated with the substrate (S)−liquid (L) and the substrate (S)−crystalline (C) nucleus interfaces, respectively. In contrast to homogeneous nucleation, heterogeneous nucleation sites are limited by the available areas of the substrate and the colloidal particles within the precursor solution (or, as discussed above, the overlying liquid−gas interface).[143]

The rate of nucleation (in units of # m^{-3} s^{-1}) is given by classical nucleation theory:[143,153,154]

$$I \propto \exp\left(\frac{-Q_D}{RT}\right)\exp\left(\frac{-\Delta G^*}{RT}\right) \quad (9)$$

where $I = I_{Hom}$ for $\Delta G^* = \Delta G^*_{Hom}$ ($f(\theta) = 1$) and $I = I_{Het}$ for $\Delta G^* = \Delta G^*_{Het}$ ($0 < f(\theta) < 1$), and Q_D is the activation energy for the transport of "monomers" to the nucleus/solution interface. Figure 7C (at constant T) plots eq 9, showing the ease of nucleation at low supersaturation (S) and the importance of homogeneous nucleation at high S.[143,156] In the case of heterogeneous nucleation, the normalized nucleation rate is high at lower S because the energy barrier is lower, but it plateaus at high S because of the limitation on the available nucleation sites.[143] Typically both types of nucleation phenomena likely take place in perovskite film formation, with heterogeneous nucleation dominating at low S and homogeneous nucleation dominating at high S.[143]

At constant S, the first exponential term in eq 9 increases with increasing temperature, while the second exponential term decreases, as illustrated schematically in Figure 7D.[143,156] The net result is that the overall nucleation rate goes through a maximum as a function of temperature.[143] At low temperatures, despite the high thermodynamic driving force for nucleation, diffusion is slow and limits the overall nucleation rate.[143] In contrast, at high temperatures, the driving force for nucleation is low but diffusion is rapid. Thus, the maximum nucleation rate occurs at an intermediate temperature, as illustrated schematically in Figure 7D.[143]

It is also important for the size distribution of the nuclei to be narrow to ensure uniformity of the final thin film microstructures. Here, we invoke the LaMer diagram (Figure 8), which is often used to qualitatively describe the kinetics of classical homogeneous nucleation in the context of precipitation of monodispersed crystalline nanoparticles from a solution.[157] In this description, nucleation is considered as a reaction, with solvated "monomers" in solution as the reactant and solid-state crystalline nuclei as the product. This diagram plots the "monomer" concentration in solution as a function of reaction time. The concentration (C) increases linearly with time during saturation until a supersaturation limit (C_{SS}) is reached, resulting in homogeneous nucleation ($r > r^*$). The depletion of "monomers" due to nucleus formation results in a decrease in C, causing it to fall below C_{SS} and suppressing further nucleation. To achieve a high density of uniform-sized nuclei, the time interval (t_2−t_1) should be as short as possible to ensure a single, rapid "burst" of nucleation, typically achieved through rapid saturation.[159] The right-hand portion of the diagram pertains to growth of the nuclei, which is discussed in section 3.1.1.2. While the LaMer diagram is strictly intended to describe homogeneous nucleation, this concept can be applied to heterogeneous nucleation, with heterogeneous nucleation occurring at $C \ll C_{SS}$ (Figure 8),[158] provided $r > r^*$. In the case of thin film nucleation, secondary heterogeneous nucleation on colloidal particles is also possible, where these nuclei can settle on the substrate and get incorporated into the thin film during the subsequent growth process. There is also a well-known "nucleation-free" growth mechanism called spinodal decomposition, where rapid, spontaneous (no energy barrier) unmixing of two distinct thermodynamically stable phases can occur under certain conditions.[160,161] Spinodal decomposition occurs in some metal alloys, ceramics, and glasses,[160,161] but it may not be important in the solution-processing of perovskite thin films.[143]

For the controlled growth of uniform, full-coverage solid-state films from solution precursors, it is generally necessary to have heterogeneous nuclei on the substrate, rather than heterogeneous nucleation on colloidal particles or homogeneous nucleation, which can result in incomplete film coverage.[143,162−164] Also, considering that the amount of perovskite "nutrients" in the precursor film is finite, it is desirable to have a high density of the heterogeneous nuclei on the substrate to result in uniform, full-coverage thin films. However, the resulting films are likely to be fine-grained, requiring further grain-growth treatments (discussed in sections 3.4 and 5). Otherwise, a low nuclei density will result in the growth (laterally and vertically, as discussed in the following section) of the limited number of nuclei into islands that may never coalesce as the "nutrients" in the precursor film are exhausted. Such discontinuous morphologies are generally disadvantageous in the context of thin film (opto)electronic devices, as adjacent layers may contact each other through the bare spots, causing unwanted leakage currents. Figure 9 (panels A and B) illustrates the low and high nuclei-density situations, respectively, in one-step growth of $MAPbI_3$ perovskite thin films. Since the subsequent microstructural evolution of these perovskite films, and the performance of the resulting PSC (or other devices), depends on nucleation, it is important to be able to control this process deterministically.[143] Thus, basic scientific understanding of perovskite nucleation is necessary because the ease and simplicity of one-step methods are attractive in the context of commercial manufacturing of PSCs and other devices (as discussed further in section 4).[143]

While this classical theory can capture the nucleation phenomenon in the simplest of systems, such as nucleation of water droplets from vapor,[166] the nucleation of crystalline perovskite from a precursor solution is much more complicated, the realm of so-called "non-classical" nucleation (Figure 10).[151] This behavior arises because there are multiple ions in perovskite,[167] and the polar aprotic solvents used are much more complex,[168] resulting in a variety of interactions within the precursor solution during saturation. Furthermore, various additives are often incorporated into the precursor solution to obtain full-coverage perovskite thin films.[169] Thus, precursor saturation generally results in the formation of intermediate entities other than perovskite crystalline nuclei, such as clusters of intermediate solid phase (adducts, complexes) that can be amorphous or crystalline, comprising both perovskite and solvent ingredients (discussed in more detail in section 3.1.2.1, as well as sections 4.1.1−4.1.4 and 4.2, and section 6.1).[168] There is debate whether these clusters can be treated as prenuclei, which transform into crystalline perovskite nuclei.[168] There is also evidence for the formation

DOI: 10.1021/acs.chemrev.8b00318
Chem. Rev. 2019, 119, 3193−3295

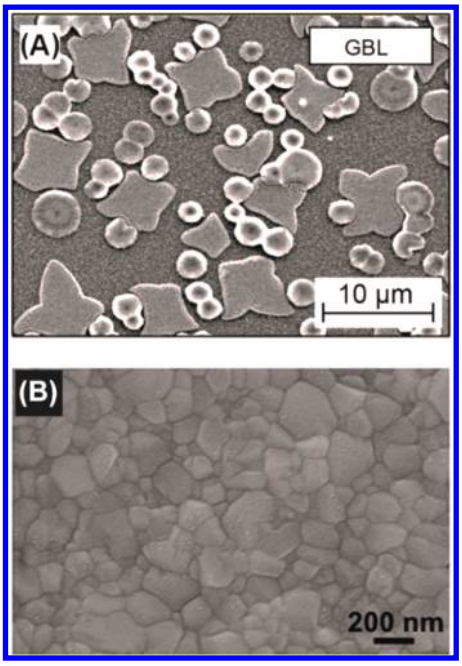

Figure 9. SEM micrographs (top surface) of $MAPbI_3$ thin films processed with (A) low nucleation density (from GBL solvent) (Reprinted with permission from ref 165. Copyright 2013 Macmillan Publishers Ltd.: Nature) and (B) high nucleation density conditions (Republished with permission ref 150. Copyright Royal Society of Chemistry). In (A), the star- and circle-shaped features are $MAPbI_3$, while the darker background is the fluorine-doped tin oxide (FTO) substrate; in (B), the $MAPbI_3$ film completely covers the substrate.

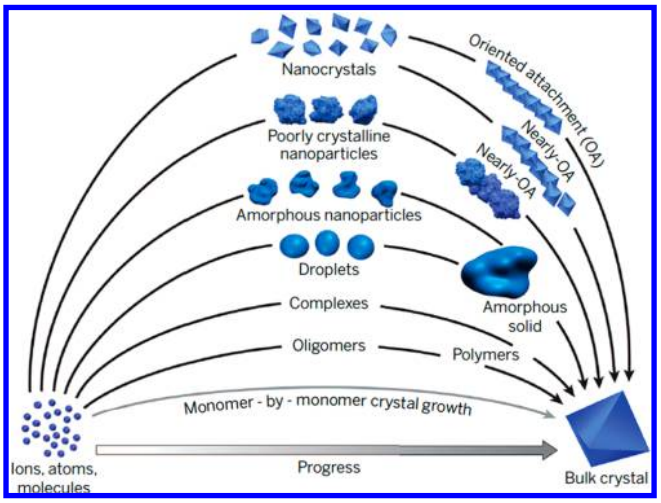

Figure 10. Pathways to nucleation/crystallization by classical "monomer" and nonclassical particle (multi-ion complexes to fully formed nanocrystals) attachment. Reprinted with permission from ref 151. Copyright 2015 AAAS.

of solid intermediate-phase films (amorphous and/or crystalline) rather than isolated clusters in some cases.[27,148,170] The perovskite crystalline nuclei then form on or within the intermediate-phase films. It is also possible that several different precursor phases may nucleate simultaneously, forming a heterogeneous film composed of distinct solid phases that blend together only afterward when annealed.[171] Once again, all these mechanisms are highly dependent on the specific system and conditions, precluding any generalizations and warranting further study.

3.1.1.2. Growth. Stable nuclei will grow in order to reduce the overall free energy as long as the solute concentration is above the solubility limit (C_s). Note that new stable nuclei will continue to nucleate as the existing nuclei are growing. There are three major classical mechanisms by which nuclei growth can occur:[172] (i) island growth (Volmer–Weber; Figure 11A),

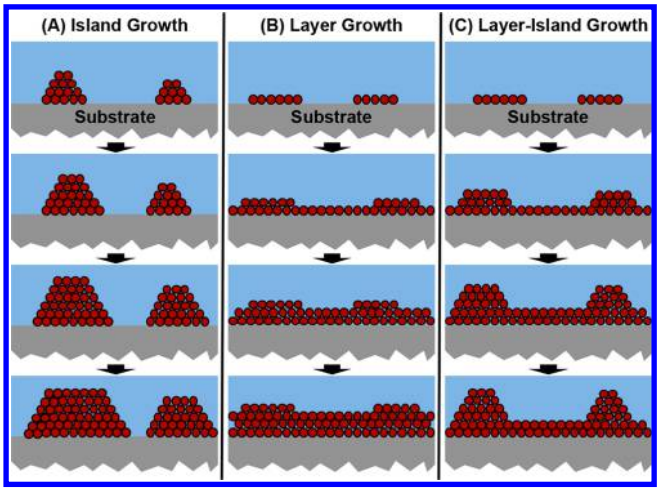

Figure 11. Schematic illustration of the three major growth mechanisms: (A) island growth (Volmer–Weber), (B) layer growth (Frank-van der Merwe), and (C) layer-island growth (Stranski-Krastanov).

(ii) layer growth (Frank-van der Merwe; Figure 11B), and (iii) layer-island growth (Stranski-Krastanov; Figure 11C). In the island growth mechanism, the nuclei grow both vertically and laterally via attachment of "monomers." In this case, bonding between the "monomers" of the growing phase is much stronger than that between the "monomers" and the substrate surface. Eventually, the islands coalesce to form a dense polycrystalline thin film provided there are sufficient "nutrients" in the precursor film. Layer growth typically occurs in epitaxial systems, where bonding between the "monomers" and the substrate is much stronger. Layer-island growth can also occur in epitaxial systems but in cases where the bonding between the monomers and the substrate may not be as strong. The island growth mechanism (Volmer–Weber) is most likely to be pertinent to perovskite thin films, as it generally does not require or involve epitaxy (exceptions are discussed in section 7.1.3).[173]

The rate-limiting step in the island growth process can be[172] (i) diffusion of the "monomers" toward the nucleus or (ii) attachment of new material to the surface of the crystalline nucleus by interface reaction. In the case of diffusion-controlled growth, the rate is given by[159]

$$\frac{dr}{dt} = \frac{2DV_M(C_\infty - C)}{r} \tag{10}$$

where C is the solute concentration at the nuclei surface, C_∞ is the solute concentration far from the nuclei ($C_\infty > C_S$), and D is the diffusivity for the solute diffusing through the solution, given by[159]

$$D = D_O \exp\left(\frac{-Q_D}{RT}\right) \tag{11}$$

where D_O is a temperature-independent pre-exponential term and Q_D is from eq 9. For "simultaneous" approaches of

DOI: 10.1021/acs.chemrev.8b00318
Chem. Rev. 2019, 119, 3193−3295

perovskite solution processing, it is unlikely that the growth is limited by diffusion, considering the ready availability of the "monomers" at the solution/crystal interface. Instead, it is most likely to be controlled by the rate of interface-reaction attachment. There are two types of interface-reaction controlled growth mechanisms:[159] (i) mononuclear and (ii) polynuclear. In the former, island growth occurs by "monomer" layer-by-layer deposition on the crystal, resulting in faceted grains at the surface.[159] In the latter, island growth occurs by the deposition of multiple "monomer" layers, resulting in rounded grains.[159] Both types of grain morphologies are observed in perovskite thin films, indicating that the operative mechanism depends on the specific process and system. Mononuclear growth rate depends on the area of the nucleus/grain:[159]

$$\frac{dr}{dt} = K_1 r^2 \tag{12}$$

whereas polynuclear growth rate is independent of the nucleus/grain size:[159]

$$\frac{dr}{dt} = K_2 \tag{13}$$

with K_1 and K_2 being rate constants. Once again, the growing islands will eventually coalesce to result in dense, polycrystalline thin films provided there are sufficient "nutrients" in the precursor solution film.

The overall growth kinetics in terms of amount (fraction) of solid formed, y, can also be modeled using the Johnson–Mehl–Avrami–Kolmogorov (JMAK) equation:

$$y = 1 - \exp\left[\frac{\pi}{3} I \left(\frac{dr}{dt}\right)^3 t^4\right] \tag{14}$$

where the expression for I is given by eq 9. The JMAK equation can be rewritten as

$$y = 1 - \exp(K_3 t^n) \tag{15}$$

where K_3 is a temperature-dependent rate constant and n is the exponent, and it can be used for practical analysis by fitting sigmoidal y–t data and extracting K and n values. The solid fraction y is very difficult to measure directly; therefore, easily accessible proxies are often used, such as peak intensity in X-ray diffraction[174] or scattering[175] patterns, or the strength of readily distinguishable spectroscopic absorbance features.[176] Unfortunately, the deduction of growth mechanisms from such empirical fitting is open to question.

During the growth of nuclei, Ostwald ripening can also occur, where smaller crystals can dissolve back in the solution by virtue of their small radius of curvature, saturating the solution locally. Simultaneously, the "monomers" from this saturated solution will deposit on larger crystals, making them grow at the expense of the smaller crystals. This phenomenon is discussed in more detail in section 3.4.

3.1.2. Growth from Solutions. The myriad solution-processing one-step methods used for depositing perovskite thin films that are described in detail in section 4 have been highly successful, although they are largely empirical in nature and rely heavily on chemical intuition. Much of the research has focused on obtaining target thin films that embody the desirable attributes that are necessary for achieving performance, stability, and scalability of the resulting devices (see section 2.3), including perovskite composition and phase purity, full substrate coverage, lack of pinholes, smooth film surface, perfect interface with the substrate, large grain size, and tailored grain boundaries. In order to accomplish high film quality, researchers have several variables at their disposal, including solvents, additives, treatments (e.g., antisolvent, as discussed in sections 4.1.2 and 4.1.4), processing conditions (e.g., temperature, time, atmosphere, as discussed in sections 5 and 6.3.1), and external fields (e.g., electrical, magnetic, light, as discussed in section 3.5).

Regarding the solvent, Table 1 lists typical polar aprotic solvents used for the solution processing of perovskites, along with their enthalpy of solvation (Pb^{2+}) and Mayer Bond Order (MBO). The latter is a good measure of the effectiveness of the solvent in solubilizing Pb-containing perovskites, where the effectiveness is inversely proportional to the MBO value.[168] Generally, the solvents dissolve the inorganic PbI_2 salt, where a strong coordination bond forms between the O-donor ligands in the solvent and the Pb atoms.[177] The organic halide precursor (MAI) dissolves more readily in the solvent, and it can coordinate to the Pb atoms. But, for example, GBL appears to be different because it dissolves PbI_2 only in the presence of MAI in the solution. Regardless, these precursor solutions are not necessarily considered to be "true" solutions, as they can contain clusters or colloidal particles.[162] Various additives are also introduced to the precursor solutions for achieving the desired perovskite thin films and are discussed in detail in section 6. Considering the staggering number of variables and the acute system-specificity, the growth mechanisms cannot be generalized. However, two broad classes of mechanisms that appear to be fundamentally different can be defined based on whether intermediate solid phases (i) do not form or (ii) do form, during precursor solution supersaturation. These are discussed using select examples from the literature. Figures 7A and 12 illustrate schematically the possible nucleation mechanisms for the two classes, respectively.

Table 1. Commonly Used Aprotic Solvents [Dimethyl Sulfoxide (DMSO), Dimethylformamide (DMF), *n*-Methyl Pyrrolidone (NMP), γ-Butyrolactone (GBL), Acetonitrile (ACN)] in the Solution-Processing of Perovskite Thin Films and Their Enthalpy of Solvation (Pb^{2+}) along with Calculated Mayer Bond Order (MBO)[168]

solvent	$\Delta H_{solv:Pb}{}^{2+}$ (kcal mol^{-1})	MBO
DMSO	−412	1.50
DMF	−403	1.88
NMP	−401	1.90
GBL	−384	1.99
ACN	−374	3.03

When no intermediate solid phase(s) form, the situation is close to the classical nucleation/growth described above in section 3.1.1, where the perovskite crystallites nucleate directly from the precursor solution and grow, consuming all of the "nutrients" from the precursor solution. Unfortunately, it is quite difficult to ascertain unequivocally if such intermediate phases are absent or present, especially if they are amorphous in nature. Nevertheless, the formation of such phases can be suppressed by using ionic-liquid solvents or solvents with high MBO. For example, Moore et al. used methylammonium formate (MAF) ionic liquid to form a solution of $MAPbI_3$ precursors, where only phase-pure $MAPbI_3$ has been shown to crystallize upon heating, with no formation of intermediate

DOI: 10.1021/acs.chemrev.8b00318
Chem. Rev. 2019, 119, 3193−3295

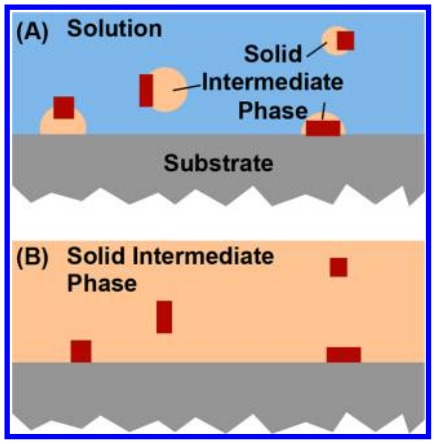

Figure 12. Schematic illustration of perovskite nucleation on intermediate phase: (A) within solution and (B) thin film.

phases (at least crystalline ones).[178] The resulting dense $MAPbI_3$ perovskite thin films have full coverage, most likely due to a high density of heterogeneous $MAPbI_3$ nuclei.[178] More recently, Foley et al. have used an additive, tetrahydrothiophene oxide (THTO), in the $MAPbI_3$ precursor (in GBL solvent) to increase the bond unsaturation, thereby suppressing the formation of an intermediate phase.[179] Very slow nucleation is reported in that study. However, in both of the above studies the nucleation kinetics were not quantified, and no attempt was made to apply classical nucleation theory. Furthermore, the presence of amorphous intermediate solid phases in these cases cannot be discounted because only XRD is used to follow the evolution of crystalline $MAPbI_3$. In another study, it was shown that solid $HPbI_3$ or $MAPbI_3$, when exposed to methylamine gas (CH_3NH_2) at room temperature, turns into a clear liquid solution ($MAPbI_3{\cdot}xCH_3NH_2$) that spreads, which can now serve as the precursor thin film (see section 5.2 for details). Here saturation occurs as a result of degassing (by lowering the CH_3NH_2 partial pressure) at room temperature, which leads to very rapid nucleation of $MAPbI_3$ grains and their growth, without the formation of a solid intermediate phase.[60,180,181]

3.1.2.1. Role of Precursor-Solvent Intermediates. As mentioned earlier, in most of the popular solution-processing methods for perovskite thin film formation using aprotic solvents (Table 1), a solid intermediate-phase (clusters and/or continuous films) forms. One can envision two scenarios: perovskite nucleation could occur within the solid intermediate-phase (i) while the latter is still forming (clusters) in the liquid precursor solution film or (ii) after the latter has formed into a solid thin film. These are depicted schematically in Figure 12 (panels A and B, respectively). The case in Figure 12A is rather difficult to access, but there is evidence of clusters (colloidal particles) in the precursor solutions and thin films,[162−164,182] on which $MAPbI_3$ may nucleate and then grow. Alternatively, external species such as quantum dots may be deliberately added in order to control the density and distribution of nucleation sites (discussed further in section 6.3.3).[183,184] The second case (Figure 12B) has also been observed experimentally and is generally relevant to many of the most popular single-step solution processing recipes, such as spin-coating (discussed further in section 4.1.1) and "solvent engineering" (discussed further in section 4.1.2), particularly those involving the common solvents DMF and DMSO, which coordinate strongly to Pb.

It is worthwhile to discuss briefly some of the characteristics of the most commonly encountered intermediates (e.g., the quasi-binary adducts $PbI_2{\cdot}DMF$ and $PbI_2{\cdot}n$DMSO and the quasi-ternary complexes $MAI{\cdot}PbI_2{\cdot}DMF$ and pMAI·$m$$PbI_2$·$n$DMSO, the precise stoichiometry of which will be explored below), as they can have a subtle but powerful influence on the morphology and quality of solution-processed films. Moreover, misunderstanding of the crystal structure of these intermediates has been widely propagated through the recent literature, leading to substantial confusion. Even in some of the pioneering works on high-performance solar cells enabled by (or in spite of) intermediate formation,[16,27,148,162] these intermediates are often depicted as having a structure derived from intercalation of solvent or solvent and MAI molecules within the van der Waals gaps in the layered structure of PbI_2, the two-dimensional nature of which is otherwise preserved.[16,27,148,162] This misconception has persisted despite several early single-crystal X-ray diffraction studies on PbI_2·DMF,[185] $PbI_2{\cdot}2DMSO$,[186] and $MAI{\cdot}PbI_2{\cdot}DMF$[187] demonstrating that, while the local bonding of the inorganic Pb−I framework does resemble the edge-sharing octahedral network of PbI_2, it is arranged in one-dimensional (1D) ribbons or chains rather than 2D sheets. This underlying 1D structure also more easily explains the rod- or fiberlike structure that is typically witnessed for these intermediates. More recent studies by Guo et al.[188] and Rong et al.[189] likewise indicate that PbI_2·DMSO (distinct from the $PbI_2{\cdot}2DMSO$ compound above) and $(MA)_2Pb_3I_8{\cdot}2DMSO$ possess similar 1D structural motifs to the above PbI_2-solvent adducts and identify distinct phases in XRD patterns that are suggested to be MAI−PbI_2−DMSO complexes with alternative stoichiometry ($3MAPbI_3{\cdot}2DMSO$, $3MAPbI_3{\cdot}DMSO$) but whose crystal structures were not resolved. $(MA)_2Pb_3I_8{\cdot}2DMSO$ appears to be the most favorable phase of the quasi-ternary DMSO-containing intermediates, as crystals of this phase are obtained by cooling an equimolar solution of MAI and PbI_2 in GBL:DMSO (7:3 by volume) or drop-casting the solution and slowly evaporating the solvent, despite its relative deficiency in MAI.[188,189]

Study of these structures is valuable beyond the intuition they provide regarding the morphology of colloidal species or intermediate films, and it reveals both interesting similarities and differences resulting from variation of the solvent. The complexes composed exclusively of PbI_2 and solvent molecules (i.e., $PbI_2{\cdot}DMF$, $PbI_2{\cdot}DMSO$, $PbI_2{\cdot}2DMSO$) feature Pb−O bonds within the quasi-octahedral coordination structure surrounding the Pb atoms and are, thus, properly termed Lewis adducts, while in the MAI-PbI_2-solvent complexes, Pb coordinates only to I, forming true edge-sharing PbI_6 octahedra.[185−188] The full network of the complex is stabilized by hydrogen bonds connecting I atoms to H atoms in the methyl and ammonium groups on DMSO and MA^+, respectively, as well as connecting the O atoms in DMSO with the H atoms in the ammonium groups on MA^+ (rather than to Pb, as would be the case for a true Lewis adduct with the solvent). Despite these similarities, the complexes based on DMF exhibit some intriguing differences relative to those from DMSO. Per the observations of Guo et al.,[188] there appear to be many more possible stoichiometries of crystalline precursor phases incorporating DMSO than DMF. Moreover, the $MAPbI_3{\cdot}DMF$ intermediate is unstable at room temperature in the absence of a high chemical potential of ambient DMF, whereas $(MA)_2Pb_3I_8{\cdot}2DMSO$ is stable until heated above room temperature. Furthermore, the MAI:PbI_2 ratio in

DOI: 10.1021/acs.chemrev.8b00318
Chem. Rev. 2019, 119, 3193−3295

$MAPbI_3$·DMF evidently matches that of the final perovskite, allowing it to form simply through release of the solvent, while conversion of $(MA)_2Pb_3I_8$·2DMSO requires uptake of additional MAI in order to produce the perovskite, by way of the two other distinct crystalline MAI·PbI_2·*n*DMSO phases identified by Guo et al.[188] This difference may be especially consequential for deposition of perovskites for several reasons. First, the volume difference relative to $MAPbI_3$ is smaller for $(MA)_2Pb_3I_8$·2DMSO than for $MAPbI_3$·DMF, which may imply less strain in the film during conversion to $MAPbI_3$. Second, the diffusive component of the interaction between MAI and $(MA)_2Pb_3I_8$·2DMSO presumably allows perovskite crystallization to proceed more slowly and gently than it would through simple loss of the solvent, which may promote higher crystallinity and reduced defect populations. Third, persistence of solvent in the precursor film may provide a "solvent annealing" effect, wherein grain growth is aided by the presence of solvent vapor that softens the film as it evaporates during the thermal annealing step (the "solvent annealing" technique is discussed further in section 5.1.2).

Overall, many of the most successful single-step strategies for fabricating the absorber in high-efficiency PSCs involves the formation of a DMSO-containing intermediate. For example, Jeon et al.[148] have shown the formation of a dense, crystalline MAI-PbI_2-DMSO intermediate-phase film progressing from the liquid precursor film (MAI+PbI_2 in DMSO/GBL solvent mixture), triggered by the dripping of a toluene antisolvent onto the precursor film. It has been suggested that the GBL evaporates during spin-coating and that the antisolvent treatment removes excess DMSO, resulting in the intermediate-phase formation. Ahn et al.[170] have also employed a DMSO-containing intermediate to fabricate $MAPbI_3$ films using DMF as the primary solvent and diethyl ether as the antisolvent, and the resulting film appears to be amorphous.[170] The solid intermediate-phase thin films are then heat-treated (at 100−150 °C) to drive out the DMSO in a controlled way, thereby converting them to perovskite films. If properly controlled, the formation of the solid intermediate-phase film can lead to high quality final perovskite thin films that are smooth, pinhole-free, and that provide full coverage of the substrate. The ease, reliability, and compositional versatility of these methods have made them highly popular in the PSC field (see sections 4.1.2−4.1.4 for further discussion). In contrast, simple heating of the precursor film without the antisolvent treatment often results in uncontrolled evaporation of the solvent, resulting in poor quality thin films (*vide infra*). Note that several different types of additives can also be used to affect various aspects of the formation of perovskite thin films and are discussed in section 6.

The homogeneous nucleation of the perovskite crystalline phase within the solid intermediate-phase film (Figure 12B) during heat treatment has not been studied in any detail, but it is likely to be similar to what is described in section 3.1.1. However, there is an additional strain term due to the solid-state nature of the phase transformation. Thus, eq 5 becomes[161]

$$\Delta G(r) = -V(\Delta G_V - \Delta G_S) + A\gamma \quad (16)$$

where ΔG_S is the free energy change associated with the sustained strain and γ is the energy associated with the perovskite/intermediate-phase interface. In the case of heterogeneous nucleation, an additional term is included, associated with the gain in the free energy (ΔG_D) due the elimination of the defects where nucleation occurs:[161]

$$\Delta G(r) = -V(\Delta G_V - \Delta G_S) + A\gamma + \Delta G_D \quad (17)$$

Upon further heat treatment, these perovskite nuclei grow, consuming the intermediate-phase matrix, in a solid-state phase transformation associated with the thermally activated diffusion and elimination of DMSO or other extraneous components of the intermediate from the structure. Once again, simultaneous growth will occur, as described in section 3.4.

While the formation of intermediate phases can often be beneficial if properly controlled, they can also impede the fabrication of high-quality, compact films. As noted above, in perovskite "solutions," precursors are often not thoroughly dissolved but rather form colloidal particles by complexing with the solvent. Yan et al.[162] have shown that colloids formed in solutions of PbI_2 or MAI-deficient to equimolar mixtures of MAI and PbI_2 in DMF tend to form large rodlike colloids (which presumably inherit their morphology from the 1D crystal structure of the PbI_2·DMF and $MAPbI_3$·DMF intermediates described above), while in MAI-rich solutions the colloids are smaller and have reduced aspect ratio. The morphology of the resulting films can, therefore, be directly influenced by the colloidal character of the solution, with rodlike colloids leading to a dendritic microstructure punctuated by large voids when the solution evaporates naturally (as in the case of single-step spin-coating, discussed further in section 4.1.1), whereas more isotropic colloids lead to more conformal coverage of the substrate. The dendritic microstructure is observed regardless of whether the solution is aged or freshly filtered,[190] signifying that nucleation and growth of the colloids can occur quite rapidly, within the time scale of the spin-coating process. However, the "memory" that the final perovskite films possess of the colloidal character of the precursor solution can be a useful attribute if one is able to tailor the solution appropriately, as discussed in greater detail in section 6. For example, Han et al.[15] demonstrated that a thiocyanate additive can dramatically increase the size of the colloids in the precursor solution, which in turn arrange themselves on the substrate and are converted to perovskite whose apparent grain size scales with the colloid size. Using a similar strategy, Li et al.[191] found that a synergistic effect between DMSO and MACl additives significantly increases the colloidal size in solution, leading to a large enhancement of the apparent grain size compared to the case in which DMSO was used alone. The above examples highlight that a strong understanding of the "hidden" interactions between the precursors, solvent, and additives can provide both useful clues to avoiding adverse morphological effects as well as provide leverage over mechanisms that may be exploited to enhance film quality. Unfortunately, such interactions are necessarily specific to the particular combination of these ingredients, and detailed understanding may not yet exist for many relevant systems of interest.

3.1.3. Growth from Vapor Phase. There are several vapor-based perovskite thin film deposition methods (described in detail in sections 4.1.6−4.1.8, 4.2.3, and 4.2.4). The one-step vapor-based deposition method is typically based on dual-source (solid metal and organic halides) coevaporation in vacuum, where the mixture of the vapors condense on the substrate (typically held at room temperature).[192,193] Dual-source coevaporation offers more deposition control compared

DOI: 10.1021/acs.chemrev.8b00318
Chem. Rev. 2019, 119, 3193−3295

to single-source evaporation.[194] While significant progress has been made in the technology of vapor-deposition of high quality perovskite thin films, the fundamental understanding of the growth mechanisms is lagging.[195] The nature of the evaporated precursors govern the perovskite deposition, but the substrate has also been shown to play an important role. Using UV photoelectron spectroscopy (UPS), Olthof et al.[196] have shown that that first few nanometers of the deposit are not the perovskite phase and that complex and substrate-dependent chemical reactions are likely to occur during the early stages of film deposition. In the case of organic substrates, that thickness is ∼3 nm, and in the case of metal-oxide substrates, it is 10−30 nm. Zhou et al.[197] and Xu et al.[198] have reported the formation of MAI-rich and PbI_2-rich buffer layers on ZnO and ITO substrates, respectively. Patel et al.[96] have likewise indicated for $MAPbI_3$ films deposited by coevaporation (see section 4.1.6) onto inorganic versus organic substrates that, in the former case, amorphous $MAPbI_3$ regions are present near the interface (as revealed by diffuseness of the SAED patterns in HRTEM measurements), while in the latter, crystalline $MAPbI_3$ extends to the interface. The final apparent grain size of the perovskite thin films has also been found to depend on the substrate (Figure 13).[196] The formation of an amorphous perovskite layer suggests that conventional mechanisms of heterogeneous nucleation of crystalline perovskite on the substrate and its growth by attachment at crystalline surface defects, such as ledges or screw dislocations, may not be at play. Thus, the fundamental understanding of the perovskite deposition mechanisms in vapor-based methods awaits further basic studies.

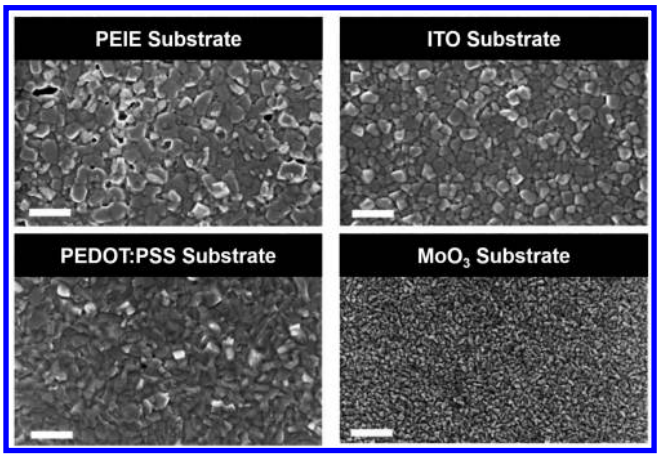

Figure 13. Top-surface SEM micrographs of $MAPbI_3$ thin films processed using the dual-source coevaporation method on different substrates. The scale bar in all images is 500 nm. Reproduced with slight format modification from ref 196 under CC BY 4.0 (license information available at https://creativecommons.org/licenses/by/4.0/).

3.2. Sequential Growth from Precursors ("Two-Step")

Sequential growth from precursors occurs in perovskite thin films deposited using two-step methods and entails deliberate reaction between different precursor species (solid, liquid, and vapor). The main advantage of the different two-step methods, which are described in detail in section 4.2, is the moderation of the reaction between the organic and the inorganic parts of the precursor, which typically occur very rapidly during execution of one-step methods. Just as in the case of simultaneous growth, sequential growth of the final crystalline perovskite film also involves a series of poorly understood complex processes that depend on several variables and the specific system under consideration. As such, general theories that describe these complex processes do not yet exist.

3.2.1. Kinetics of Reactions. In the case of $MAPbI_3$, the first step is typically the deposition of a solid PbI_2 thin film on the substrate, followed by reacting this film with MAI in either solution, solid, or vapor form in the second step. The initial PbI_2 films play an important role in determining the growth mechanisms and are discussed in greater detail in section 3.2.2. The three most popular two-step methods are[143] (i) solid−liquid,[165,199] (ii) solid−solid,[200] and (iii) vapor−solid.[201] There are also several other variations of these three methods. The simple reaction pertaining to the solid−liquid method in the context of $MAPbI_3$ thin film deposition is[143]

$$PbI_2(s) + MAI(soln) \rightarrow MAPbI_3(s) \quad (18)$$

Similarly, the reactions pertaining to solid−solid and vapor−solid methods are, respectively:[143]

$$PbI_2(s) + MAI(s) \rightarrow MAPbI_3(s) \quad (19)$$

$$PbI_2(s) + MAI(g) \rightarrow MAPbI_3(s) \quad (20)$$

While the detailed mechanisms of the formation of $MAPbI_3$ in the two-step methods are complex, as a first approximation it can be assumed that the generic reaction (Figure 14A),

$$AX + BX_2 \rightarrow ABX_3 \quad (21)$$

will be limited by the diffusion of the reactants through the layer of the ABX_3 product (Figure 14B). The general kinetics of the reaction can then be written as follows:

$$x^2 = K_4 t \quad (22)$$

where x is the thickness of the $MAPbI_3$ layer formed at time t and K_4 is a rate constant given by $K_4 = K_{O4} \exp(-Q_R/RT)$, with Q_R being the activation energy for the diffusion process controlling the reaction. The overall kinetics can also be described by the JMAK equation (eq 14 or 15) with y being the amount (fraction) of the ABX_3 formed. These analyses can be applied to $MAPbI_3$ and other halide perovskites. However, as noted previously, they only provide practical guidance, as they are empirical and highly system-specific and, therefore, do not provide mechanistic understanding/insights.

3.2.2. Growth from Solutions. In the first method for preparing $MAPbI_3$ thin films, a solid PbI_2 film is first deposited onto a substrate (flat-planar or mesoporous oxide) followed by dipping in a MAI solution (typically in anhydrous 2-propanol solvent), as discussed in more detail in section 4.2.1.[165,199] The nature of the initial PbI_2 thin film plays a key role in determining the growth mechanisms and the quality of the final film. This is primarily because there is a 2-fold molar volume expansion associated with Reaction 18,[112,202,203] where MAI intercalates into the layered PbI_2 structure. However, there have been limited studies on understanding the detailed growth mechanisms. Schlipf et al.[202] used grazing-angle X-ray scattering to investigate the inner film morphology during the evolution of $MAPbI_3$ for a dense predeposited PbI_2 film (Reaction 18). It was found that the lateral confinement by the dense PbI_2 retards Reaction 18 and forces the grains to grow in the vertical direction.[202] The strain due to the lateral constraint can retard the conversion to perovskite and also lead to cracking/peeling and high roughness.[143,202] Also, the pro-

DOI: 10.1021/acs.chemrev.8b00318
Chem. Rev. 2019, 119, 3193−3295

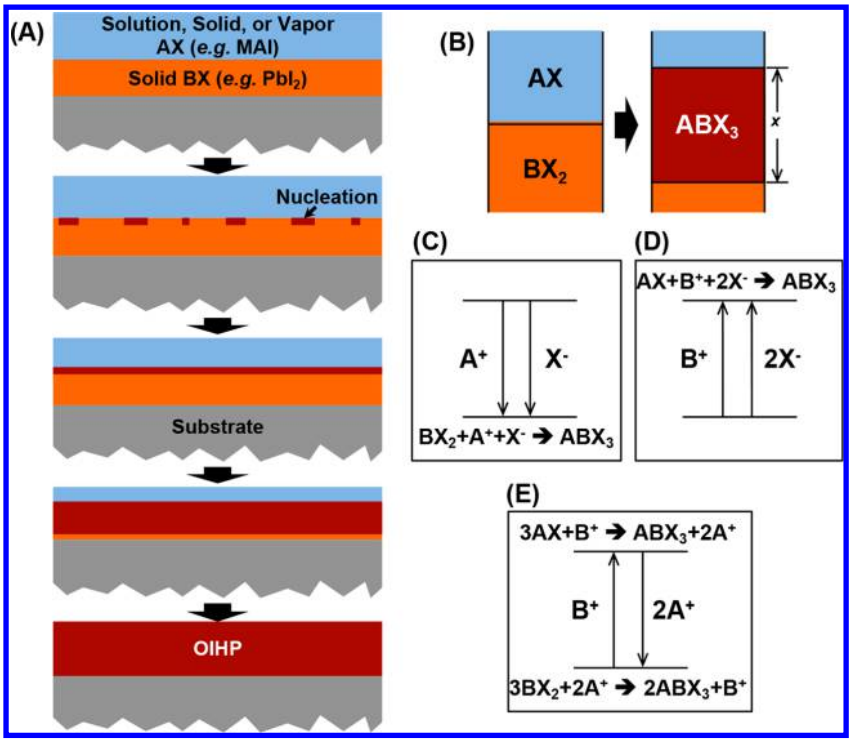

Figure 14. Schematic illustrations of (A) possible stages in the two-step methods, (B) two-step reaction, and (C–E) the possible reaction pathways. Adapted from ref 143. Copyright 2015 American Chemical Society.

longed dipping needed to complete the reaction can result in the degradation of the as-formed $MAPbI_3$ in contact with the 2-propanol solvent. To that end, for example, amorphous initial PbI_2 films[204] and porous PbI_2 films[205−207] have been used to promote the reaction and to accommodate the volume expansion. Examples of other approaches that have been found to be effective include tailoring of PbI_2 porosity and crystallinity,[208] prealloying the PbI_2 films (e.g., $PbI_2{\cdot}x$MAI,[209] $PbI_2{\cdot}x$FAI[210]), the use of density-matched intermediate films (e.g., $PbI_2{\cdot}x$DMSO) for topotactic conversion,[27,211] and performing multiple MAI infiltration cycles.[203]

In a recent study, Ummadisingu and Grätzel have used a combination of XRD, SEM, SEM-photoluminescence (PL), SEM-cathodoluminescence (CL), and confocal laser scanning fluorescence microscopy (CLSFM) to elucidate the sequential growth mechanisms for $MAPbI_3$ thin films.[176] They have shown that the first stage in this process is the heterogeneous nucleation and growth of the new PbI_2 from the poor-crystallinity, porous initial PbI_2 thin film.[176] Relatively large PbI_2 crystals (∼500 nm) form on top of the existing PbI_2 film within 2 s of dipping. They grow as faceted PbI_2 crystals, while consuming the surrounding PbI_2 thin film, into larger islands. Subsequently, the reaction with MAI appears to start at the edges and grain boundaries of the newly grown PbI_2 crystals, resulting in a part of the crystals being converted into $MAPbI_3$ through the intercalation of the MAI into the layered PbI_2 structure. Eventually, most of the PbI_2 is consumed by the formation of $MAPbI_3$ grains. The grains then grow, resulting in densely packed thin films of $MAPbI_3$. In the case of mesoporous oxide substrates, some residual PbI_2 remains, presumably within the pores.[176] While this study provides new insights into the sequential growth of $MAPbI_3$ films, it is not clear if they apply universally to other conditions and systems.

3.2.3. Growth from Solid Phase. In the second method, instead of MAI-solution dipping, Xiao et al.[200] spin-coated a MAI thin film on top of a dense, pinhole-free PbI_2 film, creating a stack of solid PbI_2 and MAI layers on a substrate. The subsequent heat treatment (at 100 °C) enables the solid-state Reaction 19 between the two layers, resulting in the formation of a $MAPbI_3$ thin film. The details of the growth mechanisms are not clear, but they are closest to what is described in Figure 14A and eq 22. It has been suggested that the MAI solution starts reacting with the PbI_2 layer during spin-coating, and that during the interdiffusion heat treatment the formation of solid, fine-grained $MAPbI_3$ is complete within seconds.[200] Thus, the nature of nucleation of $MAPbI_3$ crystals during this fast process, and how the two stacked layers of solid PbI_2 and MAI convert to a single solid layer of $MAPbI_3$, is an important subject for future research. The generic Reaction 21 resulting in the formation of dense ABX_3 can be controlled by diffusion of both A^+ and X^- (Figure 14C), both B^{2+} and $2X^-$ (Figure 14D), or counter-diffusion of $2A^+$ and B^{2+} (Figure 14E).[143,160] The slowest diffusing species will control the overall diffusion in order to avoid charge imbalance.[143] Thus, the diffusion process will determine at which interface and how quickly the new ABX_3 forms.[143]

3.2.4. Growth from Vapor Phase. In the third method, Chen et al.[201] reacted atmospheric-pressure MAI vapor at 150 °C with a somewhat porous solution-deposited PbI_2 film, resulting in dense, polycrystalline $MAPbI_3$ thin films after 2 h. Results from interrupted experiments show evidence of what appear to be $MAPbI_3$ nucleation-centers (∼10 nm) that are at least initially on the surface of the PbI_2 layer.[201] Hu et al.[212] used nanoporous vapor-deposited initial PbI_2 thin films and showed that its reaction (Reaction 20) with MAI vapor is diffusion limited, and it progresses from the top of the film to the bottom. More recently, Hsiao et al.[213] and Li et al.[214] have

DOI: 10.1021/acs.chemrev.8b00318
Chem. Rev. 2019, 119, 3193−3295

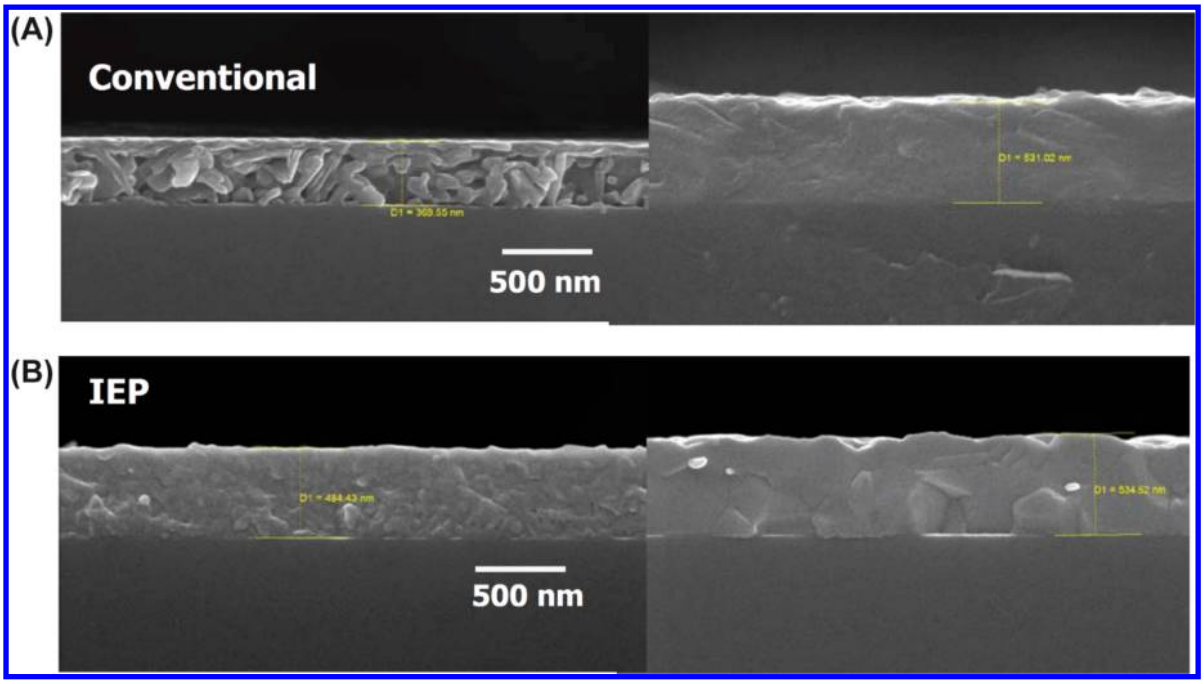

Figure 15. Cross-sectional SEM images of (A) PbI_2-to-$FAPbI_3$ ("conventional" process) and (B) PbI_2·DMSO-to-$FAPbI_3$ conversion ("intramolecular exchange process"/"IEP"). Note the small thickness change in (B) compared with (A). Reprinted with permission from ref 27. Copyright 2015 AAAS.

used partial-vacuum vapor methods to gain better control over the process. Unfortunately, the growth mechanisms in this method are still poorly understood. In some other studies, instead of MAI vapor, atmospheric-pressure MA^0 (CH_3NH_2) gas has been used at room temperature, and the processes that occur are akin to the two-step sequential methods for the preparation of $MAPbI_3$ thin films.[60] Here, PbI_2,[215] $HPbI_3$,[181] or NH_4PbI_3[216] initial thin films are used, and the reactions and the growth mechanisms are described in more detail in section 5.2.

3.2.5. Intermediate-Aided Diffusion. As alluded to in section 3.1.2.1, reaction of solvent molecules with the Lewis acid PbI_2 can form crystalline adducts with a general chemical formula of PbI_2·xSLV, where SLV represents a common perovskite solvent such as DMF,[185] DMSO,[27,211] or NMP.[217] Such PbI_2·xSLV adduct films can be used as the initial thin films in the two-step methods. Here, upon reaction (reaction 23) of PbI_2·xSLV with MAI,[211] FAI,[27,217] or mixed MAI/FAI solutions,[27] a facile conversion reaction occurs, resulting in the formation of $MAPbI_3$, $FAPbI_3$, or $(MA,FA)PbI_3$, and the release of SLV molecules:

$$PbI_2{\cdot}x\mathrm{SLV(s)} + \mathrm{MAI(soln)\ or\ FAI(soln)} \rightarrow MAPbI_3\mathrm{(s)\ or\ }FAPbI_3\mathrm{(s)} + x\mathrm{SLV(g)} \quad (23)$$

This process was first introduced as "intramolecular exchange" by Yang et al.[27] (see Figure 15A). Here, the SLV molecules within the adduct can be easily replaced by MAI or FAI because MAI or FAI exhibit much higher affinity (ionic bonds) toward PbI_2 compared with the solvent (Lewis acid−base interaction). In this context, the predeposited PbI_2·xSLV layers that are highly uniform and dense can be directly converted to $MAPbI_3$ or $FAPbI_3$ perovskites after this process. Figure 15B shows cross-sectional SEM images of an initial PbI_2·xDMSO and the converted $FAPbI_3$ thin film via intramolecular exchange, where only a small increase in the film thickness is observed, indicative of the small volume expansion after Reaction 23. In comparison, in the conventional two-step formation process using an initial PbI_2 thin film, a significant increase in the film thickness is observed in Figure 15A. The x value in PbI_2·xSLV can also have an important effect on the density and morphology of the PbI_2·xSLV film, which consequently affects the final film morphology.[211] As mentioned earlier, besides PbI_2·xSLV, other adducts such as PbI_2·xMAI[209] and PbI_2·xFAI[210] are also used as the precursor phase for facile formation of high-quality perovskite thin films, where the same intermediate-aided diffusion mechanism applies.

3.3. Crystallization within Confined Spaces

Mesoporous PSCs, where the perovskite forms within mesopores (5−20 nm) of oxide scaffolds, are popular due to some advantages they offer over planar PSCs, such as reduced hysteresis in the J−V response due to matched extraction of electrons/holes[218] and better adhesion due to mechanical interlocking.[125] In this case, much of the previous nucleation and growth discussion that focused on the simpler case of planar perovskite films needs to be modified to consider the 3D constraint placed by the scaffold. Although this problem is significantly more complex, constrained-crystallization theories developed in the fields of geology and cements[219−223] could be adopted and built upon, at least in the simpler case of simultaneous (one-step) growth of mesoporous perovskite thin films. Consider a perovskite nucleus of critical size (r^*) in a tubular mesoporous pore (radius r_p), most likely nucleated heterogeneously due to the abundance of nucleation sites available within mesoporous oxide scaffolds (Figure 16A). As the crystal grows (Figure 16B), the right and left hemispherical ends will be in equilibrium with the supersaturated solution, attaining a curvature of $\kappa_E = 4/(2r_p - \delta)$, where δ is the thickness of the solution channel and the cylindrical part of the

DOI: 10.1021/acs.chemrev.8b00318
Chem. Rev. 2019, 119, 3193−3295

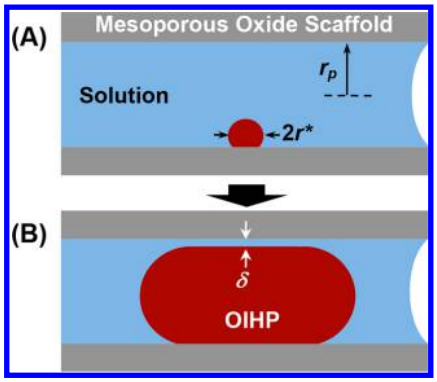

Figure 16. Schematic illustration of organic−inorganic halide perovskite (OIHP) growth from solution, within the confines of a pore within a mesoporous oxide.

crystal has a curvature $\kappa_S = 2/(2r_p - \delta)$.[220] The following relation must be satisfied at equilibrium:[220]

$$\frac{2\gamma_{LC}}{r_p - \frac{1}{2}\delta} = \frac{\left(\frac{RT}{V_m}\right)}{\ln\left(\frac{K_E}{K_M}\right)} \tag{24}$$

where K_E and K_M are the solubility products for the curved (with curvature κ_E) and macroscopic crystal, respectively; γ_{LC} and V_M are the solution-crystal surface tension and molar volume, introduced in eqs 5 and 6, respectively. The growth of this crystal will exert pressure, p, due to the 3D constraint, which is absent in the planar thin film case, and it is given by[220]

$$p = \gamma_{CL}(\kappa_E - \kappa_S) = \frac{\left(\frac{RT}{V_m}\right)}{\ln\left(\frac{K_E}{K_S}\right)} \tag{25}$$

where K_S is the solubility product in the liquid channel. Similar calculations can be performed for other geometries, such as a spherical pore fed by tubular channels.[220] If the mesoporous scaffold has adequate strength, the back pressure from the pore walls can force the perovskite crystal to grow in the axial direction as saturation, S, increases. Also, the overall 3D constrained shrinkage of the perovskite crystals from the solution will result in net tensile strain in the perovskite. This is consistent with ∼1% tensile strain estimated from XRD analysis of $MAPbI_3$ crystallized within a mesoporous TiO_2 scaffold.[87] However, there are other effects that are not considered, which could be important. For example, the area of the interface between perovskite and oxide (e.g., TiO_2) is significantly greater than that in the case of planar perovskite thin films, which could play an important role in the energetics of the stability of the perovskite phases. In this context, it is known that the undesirable "yellow" δ-$FAPbI_3$ nonperovskite phase within mesoporous TiO_2 scaffolds does not transform to the desirable "black" α-$FAPbI_3$ perovskite polymorph upon simple heating, whereas it transforms readily in the planar form.[224,225] The reasons for this phenomenon, which precludes the use of the simple one-step process for making $FAPbI_3$-based mesoporous PSCs, are not known, but it is highly likely that interface-energetics and strain could be responsible for this behavior. In the case of two-step processing of perovskites within mesoporous oxide scaffolds, the situation is much more complicated, and relevant theories/analyses are not available to build upon.

PSCs with some of the highest PCEs reported so far contain a mesoporous layer;[28] however, without deep understanding of crystallization of mesoporous perovskites, the further development of these PSCs will remain largely empirical, with the attendant limitations on the nonincremental progress that can be made. Detailed studies to address these shortcomings face formidable challenges, most of which are related to the small length scales (nanometers) and fast time scales (seconds) at which the relevant phenomenon occur, and the difficulties with in situ and ex situ characterization at those scales. This also presents an unprecedented opportunity for new theoretical and experimental research in this uncharted area. Also, any new low-dose characterization techniques developed for studying perovskites in general could be brought to bear on this more complicated problem.

3.4. Grain Growth and Microstructural Evolution

Generally, large grains are desirable in polycrystalline semiconductors used for solar cells, photodetectors, and transistors because defects such as grain boundaries degrade the device performance,[226] although, as noted in section 2.3.2.3, calculations indicate that one of the advantages of the hybrid perovskites is the relatively benign nature of the grain boundaries.[14] Large grains reduce the density of grain boundaries, at which charge recombination can occur due to elevated charge-trap densities.[14,122,136,143] Grain boundaries can also affect other properties such as conductivity, dielectric constant, and carrier mobility.[143] Furthermore, as mentioned in section 2.3.2.3, polycrystalline perovskites can be viewed as having a 3D grain boundary network, where the grain boundaries can serve as "highways" for ion-migration[93] and moisture ingress,[123] resulting in the faster degradation of perovskite thin films. While it is clear that grain boundaries within the thickness of the perovskite films (in-plane) could be detrimental, the direct benefit of having grain size much larger than the film thickness (equivalently, only vertical grain boundaries) has not been demonstrated.[143] As alluded to in section 2.3.2.3, large grains are not always necessary or even desirable for certain device designs, particularly LEDs.[30,32] Nevertheless, as the PCEs of PSCs approach the theoretical maximum, eliminating even relatively benign defects such as grain boundaries will become increasingly important.

There is a thermodynamic driving force for grains in a dense, polycrystalline perovskite film to coarsen, but this process is kinetically limited. Note that the term "coarsening" is used to imply an increase in the average grain size of an already-formed microstructure, as distinct from more general nuclei growth, which may also occur by consumption of a precursor phase or phases. It is also important to define a "grain" since there is some confusion in the perovskite and PSC literature, as similar features are sometimes referred to as "domain," "aggregate," or "morphological feature." By definition, a grain is the smallest microstructural unit that is a true single crystal and is bounded on all sides by grain boundaries, interfaces, or surfaces. In other words, all locations within the grain have the same crystallographic orientation or its variant (e.g., twin) with respect to each other. Grain size is the most important microstructural quantity reported in the literature for polycrystalline perovskite thin films, and it is generally measured using image analyses of SEM or AFM images, which contain grain boundary grooves. It is implicitly assumed that the grain boundary grooves represent the intersection of every grain boundary with that surface.[143] As noted in section 2.3.2.3, this assumption may not

DOI: 10.1021/acs.chemrev.8b00318
Chem. Rev. 2019, 119, 3193−3295

be valid, because the pathway by which the grooves form during processing depends on how the grains grow and coalesce. In this context, grain size of polycrystalline metals, ceramics, or inorganic semiconductors is measured using grooves that are produced deliberately by thermal or chemical etching.[143] Grain boundary grooves occur as a result of preferential evaporation and/or chemical attack of grain boundaries, which are more disordered compared to the grain interior, ensuring the delineation of each and every grain boundary. Since halide perovskite thin films are not amenable to chemical or thermal etching, there may be grain boundaries in the as-formed perovskite films that do not form grooves during processing. Also, grain surfaces in as-deposited perovskite thin films can have wrinkles, which can be mistaken for grain boundary grooves.[143] Figure 17 shows an example of

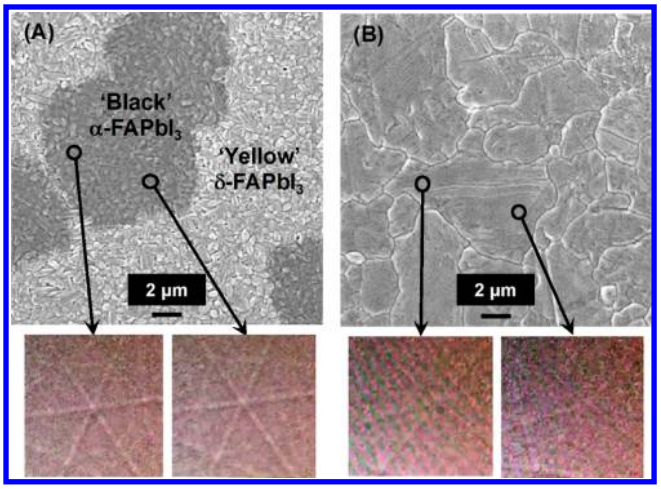

Figure 17. Top-surface SEM micrographs and corresponding EBSD patterns in $FAPbI_3$ thin films. (A) Composite film of large (~5 μm) "black" α-$FAPbI_3$ perovskite grains embedded within a fine-grained (~500 nm) "yellow" δ-$FAPbI_3$ nonperovskite matrix. (B) Fully converted α-$FAPbI_3$ perovskite thin film. Identical EBSD patterns from different areas within the grains, regardless of their surface morphologies, further attesting that they have the same crystallographic orientation. Adapted with permission from ref 227. Copyright 2018 American Chemical Society.

this feature in $FAPbI_3$ perovskite films.[227] In other words, the use of as-formed features in SEM images to measure the grain size may result in an overestimation of this quantity, and, thus, it is referred to as the "apparent grain size" throughout this review.

The two most important classical grain-coarsening mechanisms are solid-state grain growth and matrix-phase (solid or liquid)-mediated Ostwald ripening relevant to halide perovskite thin films. It is a common misconception that all grain coarsening is Ostwald ripening. Note that Ostwald ripening is a subset of general coarsening and specifically refers to coarsening in the presence of a continuous second phase, typically a liquid. The differences in the curvatures of small and large grains provide the thermodynamic driving force for both mechanisms. Topology of individual grains is a particularly important consideration in solid-state grain growth. Figure 18A is a 2D schematic illustration of a polycrystalline material containing grains of different sizes and coordination numbers (sides).[160] Here, grains with less than six sides have concave grain boundaries (dihedral angle $\phi < 120°$) and will shrink at the expense of the growth of neighboring grains with more

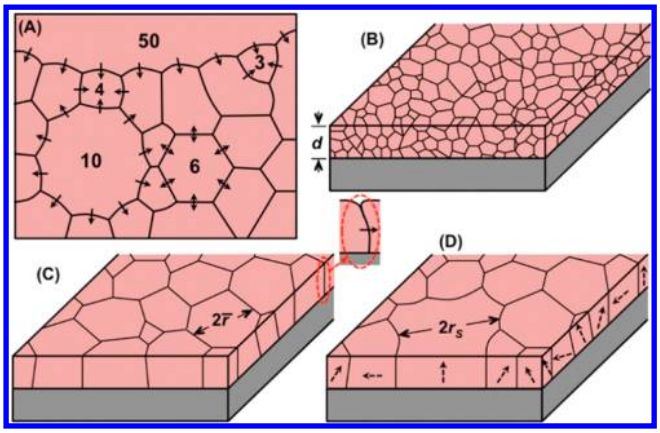

Figure 18. Schematic illustrations of (A) 2D microstructure showing motion of grain boundaries (number of sides to a grain is indicated in a few representative cases),[160] (B) fine-grained thin film, (C) coarse-grained "stagnated" thin film (inset: cross section showing grain-boundary groove imposing drag on a grain boundary moving to the right), and (D) secondary grain growth (dashed arrows indicate the same crystallographic orientation).[228] (A) reprinted with permission from ref 160. Copyright 1976 Wiley; (B−D) modified with permission from ref 228. Copyright 1990 Annual Reviews.

than six sides ($\phi > 120°$), whereas grains with exactly six sides (dihedral angle $\phi = 120°$) are stable. Here, "monomer" species in smaller grains will diffuse across the solid-state grain boundary between those two grains to the larger grain, which results in the motion of the grain boundary in the opposite direction. This makes the convex curvature even sharper and more species migrate to the larger grain, until the smaller grain disappears at the expense of the growth of the larger grain. Grain coarsening rate is then given by the Turnbull relation:[160]

$$r_t^n - r_o^n = K_S t \tag{26}$$

where r_0 and r_t are grain radii at time zero and at t, respectively, exponent $n = 2$, and K_S is the rate constant given by $K_S = K_{OS} \exp(-Q_B/RT)$, with Q_B being the activation energy for grain-boundary motion, which is related to the solid-state diffusion of the relevant species. Unlike bulk 3D materials, the coarsening occurs slowly in thin films and typically stagnates when the average grain size ($2\bar{r}$) approaches the film thickness (d), at which point all grain boundaries intersect the top surface and the bottom interface with the substrate (Figure 18, panels B and C).[143,228] Assuming isotropic grain boundary energy, this coarsening "stagnation" arises from drag forces exerted by the surface and the interface on the moving grain boundaries.[228] In particular, significant drag is expected to be exerted by grain boundary grooves at the surface (see Figure 18, panels A and C, inset).[228] Figure 9B presents an example of a SEM image of the top surface of a typical $MAPbI_3$ thin film (~300 nm thickness) with an average grain size of ~300 nm showing extensive grooving. Subsequently, secondary coarsening (also called exaggerated or abnormal grain growth) occurs in anisotropic thin films. For this situation, a few favorably oriented grains, whose low-energy crystallographic planes constitute the thin film surface and the interface with the substrate, grow rapidly, resulting in large-grained, textured thin films (Figure 18D).[143,228] The system tends to maximize the area of those surfaces and interfaces through the growth of the favorably oriented grains at the expense of the less favorably oriented grains.[143] The coarsening rate of those favorably oriented grains (for radius $r_S \gg \bar{r}$) is given by[228]

DOI: 10.1021/acs.chemrev.8b00318
Chem. Rev. 2019, 119, 3193−3295

$$\frac{dr_S}{dt} \approx M\left[\frac{(\gamma^*_{CV} + \gamma^*_{SC}) - (\gamma_{CV} + \gamma_{SC}) + \gamma_{GB}}{d}\right] \quad (27)$$

where M is the grain boundary mobility; γ^*_{CV} and γ^*_{SC} are the average surface and interface energies, respectively, of all the normal grains; γ_{CV} and γ_{SC} are the surface and interface energies, respectively, of the favorably oriented grains; and γ_{GB} is the grain boundary energy. Eq 27 implies that by minimizing the energy (γ_{SC}) of the interface between the favorably oriented grains and the substrate through judicious choice of substrates for better adhesion, one can achieve rapid secondary grain-growth.[143] The Dupré work of adhesion between the film and the substrate, W_{SC}, is given by[229]

$$W_{SC} = \gamma_{SV} + \gamma_{CV} - \gamma_{SC} \quad (28)$$

where γ_{SV} is the surface energy of the substrate (one may not have independent control over the energy terms other than γ_{SC} in eqs 27 and 28 for a given perovskite). This analysis suggests that grain sizes that are significantly larger than the film thickness (d) can be obtained, but it is invariably associated with strong crystallographic texture in the thin film, which can be either a desirable or undesirable attribute,[143] as noted in section 2.3.2.2.

In the case of Ostwald ripening, a matrix phase (e.g., liquid) is required to be present between the grains. Here, the smaller grains with higher chemical potential, by virtue of their curvature, dissolve in the matrix phase preferentially over larger grains.[230] In the process, the matrix becomes locally supersaturated in "monomers," which deposit on larger grains with lower chemical potential, resulting in the net coarsening of the grains.[143] Thus, the slower of the two steps, diffusion of the "monomers" through the matrix phase (diffusion-controlled) and their attachment on the larger grains (interface-reaction controlled) controls the overall Ostwald ripening process. The Ostwald ripening kinetics are also described by eq 26, where the exponent $n = 2$ for interface-reaction-controlled and $n = 3$ for diffusion-controlled processes.[230] Ostwald ripening can also occur via evaporation−condensation (vapor phase), which is also driven by curvature differences, and is likewise described by eq 26.[231]

The poor thermal stability of perovskites limits the processing windows (temperature, time) for both one-step and two-step methods. Thus, the grain size of the as-deposited perovskite thin films is typically small (few hundred nanometers), requiring postdeposition grain growth/coarsening (strategies for increasing grain size are discussed in more detail in section 5). For example, panels A and C of Figure 19 show top-view and cross-section images of a $MAPbI_3$ thin film, respectively, with an average apparent grain size of ∼280 nm and apparent grain boundary density of ∼8900 nm μm^{-2}. With the use of a MACl-additive-assisted approach, the grains could be coarsened to ∼3 μm with apparent grain boundary density of only ∼400 nm μm^{-2} (Figures 19, panels B and D).[138] Another example is shown in Figure 19E (cross-sectional TEM micrograph of a whole PSC), where $MAPbI_3$ grains appear to span the thickness of the film using an excess-MAI-assisted approach. Figure 19 (panels F and G) shows a high-resolution TEM micrograph and selected-area electron diffraction pattern, respectively, from the marked area within a grain, showing high crystallinity and confirming the single-crystal nature of the grain.[232]

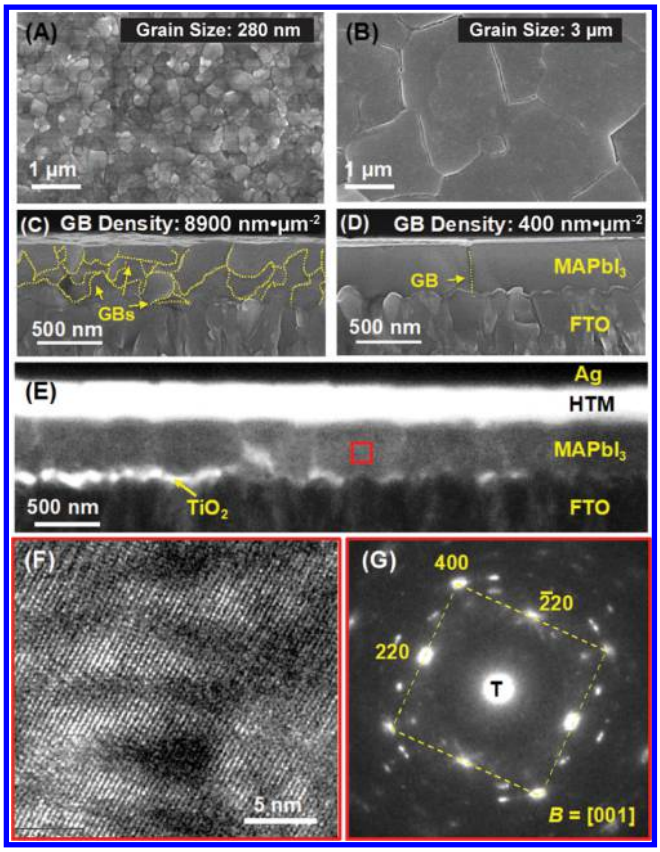

Figure 19. Top-view and cross-sectional SEM micrographs of $MAPbI_3$ thin films: (A and C) fine-grained film prepared from a $MAPbI_3{\cdot}CH_3NH_2$ precursor with a high-density apparent grain boundary network and (B and D) coarse-grained film prepared from a $MAPbI_3{\cdot}MACl{\cdot}CH_3NH_2$ precursor with a low-density apparent grain boundary network. Adapted from ref 138. Copyright 2017 American Chemical Society. (E) Cross-sectional TEM image of PSC with $MAPbI_3{\cdot}MACl{\cdot}CH_3NH_2$-derived perovskite thin film and (F) high-resolution TEM image and (G) SAED pattern from the red square marked in (E). Reproduced with permission from ref 232. Copyright 2015 Wiley-VCH.

3.5. Influence of External Fields

Electric or magnetic fields can influence the crystallization behavior of many conventional materials such as Si,[233] $CaCO_3$,[234] and polymers.[235] In the case of $MAPbI_3$, the crystal structure may respond to the electric or magnetic fields more actively due to its "soft" nature.[93] Since hybrid perovskites generally contain polar organic cations that can respond to electric fields, crystals are, therefore, likely to be ferroelectric[236] (although this effect might be complicated by dynamic disorder and/or transition to a centrosymmetric cubic phase[237] at temperatures relevant for processing). Thus, imposing a DC or AC electric field might possibly tune the nucleation rates and preferred growth orientation, resulting in perovskite thin films with unique characteristics such as tailored texture and grain size/morphology, similar to those effects reported in other materials.[238−242] However, there have been very limited studies in this area in the context of simultaneous (one-step) growth. Zhang et al.[243] have claimed that the optimized external electric field (2.5 V μm^{-1}) can facilitate the one-step crystallization of $MAPbI_3$ films and improve their crystallinity. The devices produced from these films also exhibit a stronger built-in electric field, which is

DOI: 10.1021/acs.chemrev.8b00318
Chem. Rev. 2019, 119, 3193−3295

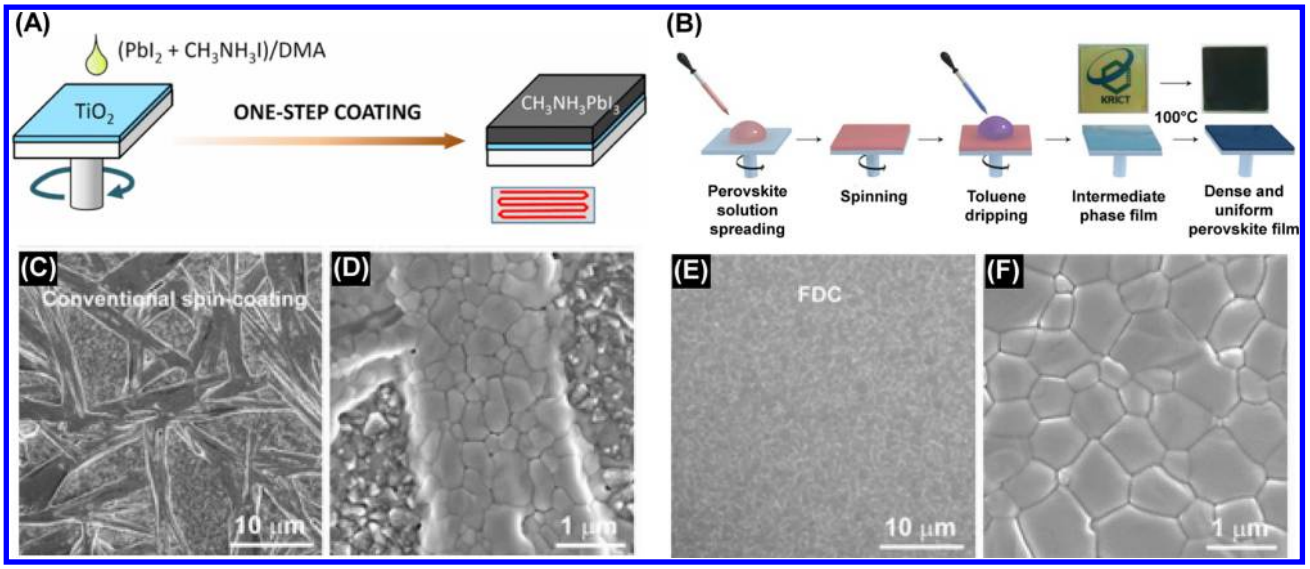

Figure 20. "One-step" spin-coating process (A), where a perovskite precursor solution is deposited onto the substrate, which is then rotated rapidly to distribute and dry the precursor film, and thereafter annealed to complete the formation of the perovskite thin film. Reproduced from ref 249 under CC BY 3.0 (license information available at https://creativecommons.org/licenses/by/3.0/). The solvent engineering technique (B), which is similar to one-step spin-coating except that an antisolvent is dripped onto the film while it spins, causing rapid intermediate-phase formation (or direct crystallization of the perovskite). Adapted with permission from ref 148. Copyright 2014 Macmillan Publishers Ltd. Typical morphology of a $MAPbI_3$ thin film prepared by (C and D) one-step spin-coating and (E and F) solvent engineering. Reprinted with permission from ref 149. Copyright 2014 Wiley-VCH.

beneficial for the charge separation/transport in PSC devices. This effect could be attributed to a tailored ion polarization by the electric field.

Application of a magnetic field has also been claimed to influence the nucleation and crystal growth of $MAPbI_3$ perovskite thin films. Wang et al.[244] have observed that, by imposing an optimized magnetic field of 80 mT, the resultant $MAPbI_3$ films appear to have larger crystalline grains and exhibit improved optoelectronic properties. It has been suggested that the Lorentz force on the ions due to the magnetic field tends to order them, resulting in a more ordered intermediate phase. However, how this better-ordered intermediate phase affects nucleation and growth is not known. Williams et al.[245] have also shown that when Fe is partially substituted for Pb in $MAPbI_3$, application of a magnetic field increases apparent grain size and improves film coverage. However, introduction of Fe reduces optoelectronic quality of the films (as observed by others)[246] and appears to increase the propensity of twinning, demonstrating that competing effects may also be brought about by the presence of an additive in conjunction with the application of some external field. The exact role of electric and magnetic fields on crystallization remains to be explored and confirmed, and research in this direction may lead to new avenues for controlling the microstructures (e.g., texture, grain size) in halide perovskite films.

A limited study on the effect of light (1-sun illumination) during one-step antisolvent processing of perovskite thin films of complex compositions has been shown to have a detrimental effect on the quality of the films.[247] In contrast, in the two-step (sequential) method, illumination may result in superior quality perovskite films.[247] As mentioned in section 3.2.2, the formation of $MAPbI_3$ during the sequential process may be preceded by the heterogeneous nucleation and crystallization of new PbI_2 on top of the initial PbI_2 thin film. Under increasingly intense illumination (up to 1 sun), the size of the PbI_2 nuclei has been found to decrease while the nuclei density increases.[247] It has been proposed that the surface traps in PbI_2 are populated by photogenerated carriers, most probably holes, thereby increasing the surface charge. In order to compensate for this excess positive charge, I^- ions from the MAI solution are expected to migrate to the PbI_2/solution interface, thereby decreasing the value of γ_{CL} in eqs 6 and 8. The net result is a decrease in the ΔG^*_{Het} and r^*, which promotes rapid nucleation of small crystals (generally desirable for a uniform film free from pin holes). The authors also considered the effects of heating due to the light and found that heating has the opposite effect, promoting the growth of the crystals rather than nucleation of new ones, leading to larger but more dispersed crystallites.[247]

4. DEPOSITION METHODS

A key advantage offered by the halide perovskites that makes them unique among high-performance semiconductors is their processability, as evinced by the many facile and low-temperature routes by which they may be formed. As mentioned in section 3, the halide-perovskite thin film deposition methods are broadly classified as one-step, where all the precursors are deposited simultaneously onto the substrate or two-step, where each precursor is deposited separately or sequentially onto the substrate. Note that there is some ambiguity in the literature regarding these designations. For example, the popular solvent engineering method (section 4.1.2), where an antisolvent is dripped onto the precursor film during spin-coating, is sometimes described as a two-step procedure, with the application of the precursor solution and antisolvent counted as two separate steps. In that context, annealing of the precursors may also be considered as a separate fabrication step (though it is seldom referred to as such in the halide perovskite literature), in which case almost all perovskite fabrication recipes are multistep procedures. However, the growth mechanisms described in section 3 are

DOI: 10.1021/acs.chemrev.8b00318
Chem. Rev. 2019, 119, 3193−3295

best classified according to the chosen scheme of whether the precursors (generally metal halides and/or organic cation salts) are deposited simultaneously (one-step) or sequentially (two-step). In this section, we provide a more detailed description of some of the major one-step and two-step methods, with focus on the technique and the methodology. We conclude with a discussion of techniques compatible with deposition of perovskites on large-area substrates, a topic that spans both deposition classifications described above.

4.1. "One-Step" Deposition Approaches

4.1.1. Basic Spin-Coating. Arguably the simplest method of preparing perovskite films is one-step spin-coating, which was used in the first successful report of PSCs by Kojima et al. in 2009.[248] As mentioned in section 3, in this process, a solution is prepared, consisting of the precursors MAI and PbI_2 (other precursors may be substituted, for example, FAI for MAI and SnI_2 for PbI_2) dissolved in a polar solvent such as DMF, DMSO, GBL, NMP, or mixtures of such solvents. This solution is then dropped onto a spinning substrate held in place by a clamp or vacuum chuck (Figure 20A). As the substrate spins (at hundreds to thousands of revolutions per minute), liquid is removed from its surface, at first primarily by centrifugal force flinging excess solution off the substrate and afterward by evaporation of the remaining solvent. As the solvent evaporates, the concentration of the perovskite precursors increases until it reaches the solubility limit (supersaturation), at which point crystallization of the perovskite begins (see discussion in section 3.1).

Depending on the details of the recipe, the film that forms may consist of either the targeted perovskite composition or an intermediate phase. In most cases, the as-formed film is transferred to a hot plate or other heat source for a relatively low-temperature anneal (typically 100−150 °C) for a duration ranging from a few minutes to a few hours. The annealing step has several purposes: (i) remove any remaining solvent to cause supersaturation, (ii) assist in the nucleation and growth of the perovskite, and (iii) coarsen the grains. Many different variations on this theme exist. For example, precursors may be nonstoichiometric, include spectator species, or contain other additives that promote grain growth or otherwise alter the film microstructure (as discussed in section 6). Alternatively, the different precursors may be deposited sequentially by spin-coating or spin-coating followed by a different deposition method (as discussed in section 4.2). In this section, we will concern ourselves specifically with one-step spin-coating from a stoichiometric solution of MAI and PbI_2, since this is the most basic method for the most widely used perovskite, $MAPbI_3$.

Despite its straightforwardness, the method described above tends to yield very rough films with poor coverage on the substrate.[165] When the most popular solvent, DMF, is used, a dendritic morphology of rodlike perovskite crystallites is obtained for planar substrates (Figure 20, panels C and D).[149,165,190,250,251] In addition to poor coverage (see also Figure 9A), one-step spin-coating can also lead to incomplete pore filling when employing a mesoporous substrate.[249] Unsurprisingly, the corresponding PSC devices tend to perform poorly due to the formation of shunt paths across the film, and high-performance solution-processed perovskite devices are more often produced by more complicated but effective methods relying on solvent engineering[148] or two-step deposition.[165] This morphology may be explained by noting that removal of the solvent proceeds relatively slowly (compounded by the fact that many of the solvents capable of dissolving PbI_2 in useful amounts, such as DMF and DMSO, have high boiling points/low vapor pressures), with supersaturation of the precursor solution being limited by the evaporation rate of the solvent during the spin procedure and possibly also the annealing step. As discussed in section 3.1.1, slow evaporation of the solvent may allow significant growth of existing nuclei to proceed concurrently with nucleation of new precursors, scavenging "nutrients" in the solution that might otherwise be available to generate a higher density of nuclei. Preferably, film growth proceeds through a high density of nuclei with a narrow size distribution in order to ensure that the resulting film entirely covers the substrate.

The shape and chemistry of the nuclei can also have a substantial impact on film morphology, as they may consist not of the perovskite but rather of solid perovskite-solvent intermediates, as discussed in section 3.1.2.1. For example, reports focusing on spin-coating of stoichiometric mixtures of MAI and PbI_2 from DMF solutions have proposed that the intermediate phase obtained after spin-coating (but before annealing) is composed of a MAI-PbI_2-DMF complex,[190,252] macroscopic crystals of which adopt a rod/needle-like habit presumably inherited from their 1D crystal structure (as discussed in section 3.1.2.1).[253] This explanation is further supported by noting that the rodlike structures themselves appear to be composed of smaller grains (Figure 20, panels C and D),[149] which signifies that the perovskite is obtained through transformation of a solid intermediate phase whose original morphology is preserved even after the excess solvent is removed from the film. The high aspect ratio of these intermediate phases can further exacerbate the problems associated with slow nucleation and rapid growth, as they do not pack tightly but rather scatter loosely across the substrate, leaving large voids in between. It is also worthwhile to consider the possibility that the complexes nucleate and grow as colloids in solution prior to deposition, and they are then deposited onto the substrate. Kerner et al.[190] note that, despite the growth of colloids up to micron scale as the solution ages, the dendritic morphology is obtained regardless of whether the precursor solution is freshly filtered, suggesting that nucleation and growth of the intermediate can occur rapidly, within the time required to perform the spin-coating step.

The challenges associated with the formation of large, poorly connected intermediates may be mitigated by removing the solvent quickly in order to favor rapid and uniform nucleation before the noncontinuous dendrites have a chance to grow to appreciable size. Per the discussion of the LaMer diagram in section 3.1.1.1, uniformity of the nuclei can be assured by stimulating a rapid "burst" of nucleation in as short a span of time as possible. This approach forms the basis for solvent engineering and related methods, which involve removal of the solvent by drenching the precursors with an antisolvent while the substrate is still spinning, thereby rapidly increasing the supersaturation ratio S;[148,149] such processes are described in greater detail in the following section. An alternative means of removing the solvent from the film quickly is to expose it to vacuum immediately after the spin. Several reports have indicated that, as the vacuum drying pressure is reduced, the film becomes more compact and conformal.[250,254,255] This process has been used to produce large-area PSCs with PCE over 20%, and the films produced using this process also exhibit considerably slower monomolecular PL decay rates

DOI: 10.1021/acs.chemrev.8b00318
Chem. Rev. 2019, 119, 3193−3295

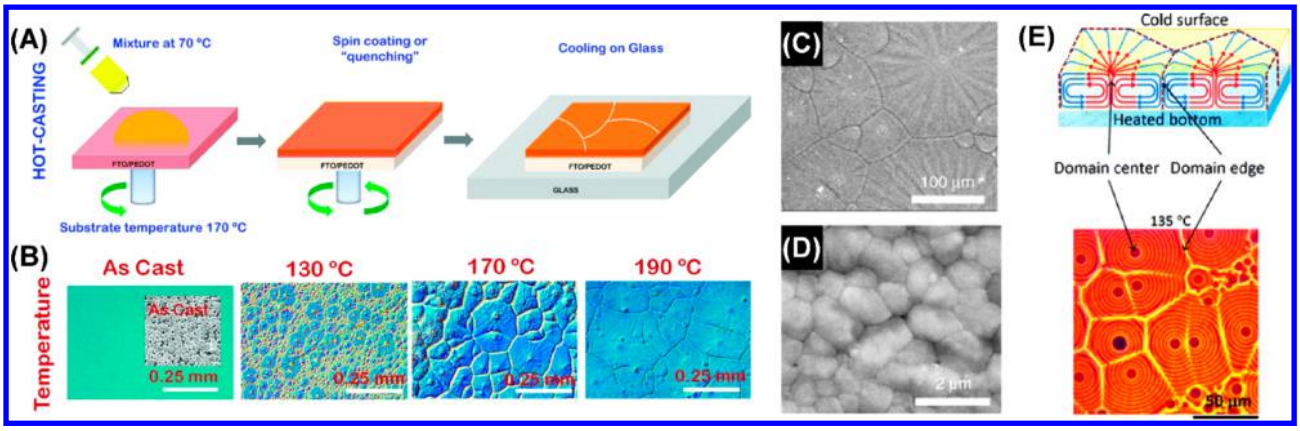

Figure 21. (A) Schematic of the hot-casting process: (B) optical microscope images of hot-cast perovskite films processed by spin-coating at different temperatures. Reprinted with permission from ref 258. Copyright 2015 AAAS. (C) Low- and (D) high-magnification SEM images of $MAPbI_3$ films prepared by doctor-blading on heated substrates with methylammonium chloride and methylammonium hypophosphite additives, clearly showing that the large, 100 μm-sized domains in (C) are themselves apparently composed of much smaller grains of size on the order of 1 μm. Reproduced with slight format modification from ref 264 under CC BY 4.0 (license information available at https://creativecommons.org/licenses/by/4.0/). (E) Schematic of the Rayleigh-Bénard convection cells and optical microscope image of hot-cast perovskite processed by doctor-blading. Republished with permission from ref 263. Copyright 2015 Royal Society of Chemistry.

than those produced by conventional one-step processing, indicating a reduction in the trap density of these films that complements the improved morphology.[255]

Another way to circumvent the growth of large, high-aspect ratio intermediates is to alter the solution chemistry, as by replacing DMF with the much less polar 2-methoxyethanol (2ME).[256] PbI_2 dissolves only sparingly in 2ME by itself but relatively well if codissolved with MAI, indicating that coordination with the solvent is limited relative to that with MAI. Correspondingly, the coverage of films processed from 2ME is superior to that of those from DMF, although far from perfect. Rather than consisting of dendrites comprised of smaller grains, the microstructure of the 2ME films appears to consist of roughly spherical aggregates that are themselves comprised of smaller grains. This feature may indicate that colloids forming in the 2ME solution simply prefer a more isotropic shape than those that form in DMF, and it reflects the dominance of the MAI-mediated coordination as opposed to a direct Pb-solvent bond. Alternatively, the lower boiling point of 2ME in conjunction with the lower solubility of the precursors in this solvent may assist in more rapidly reaching supersaturation during deposition, thereby increasing the nucleation density.

Another example of how modifying the solvent can be effective in improving the perovskite microstructure is the use of a saturated mixture of methylamine (CH_3NH_2 or MA^0) in acetonitrile (ACN).[257] Unlike 2ME, ACN is incapable of appreciably dissolving PbI_2 even in the presence of MAI; however, the bubbling of MA^0 gas into the solvent allows PbI_2 to go into solution. Most likely, the enhanced solubility is connected with the ability of $MAPbI_3$ to form a liquid "melt" of $MAPbI_3{\cdot}xCH_3NH_2$,[180] which is evidently miscible with ACN. Spin-casting from this solution yields films with a compact microstructure, uniform coverage, and grains with reasonably large apparent size closely resembling those prepared by solvent engineering (and even smoother than those obtained using a conventional solvent engineering method). In this case, the perovskite appears to crystallize directly during spin-coating, as the XRD pattern of an unannealed film contains peaks only belonging to $MAPbI_3$ (although the formation of an amorphous intermediate cannot be discounted). An additional benefit of changing the solvent is that the films deposited from MA/ACN have a carrier lifetime (as measured by TRPL) over 20 times as long as a film prepared from DMF, indicating that this process is associated with fewer defects as well as improved microstructure. The champion PSC fabricated using this method reached PCE over 18%, attesting to the high quality of the films.[257]

The perovskite crystallization dynamics may also be affected by temperature. Although most spin-coating approaches take place at room temperature, heating the substrate before solution deposition can drastically change the film morphology. Nie et al.[258] detailed a "hot-casting" approach (Figure 21A) in which the substrate is heated to 180 °C immediately prior to spin-casting of a 1:1 PbI_2:MACl solution in DMF (the solution itself is also maintained at 70 °C) and thereafter being subjected to an anneal at 100 °C. This process yields an unusual morphology, in which large, leaflike structures nearly a millimeter across cover the substrate (Figure 21B). As noted in section 3.1.1, classical theory suggests that suppression of the thermodynamic driving force for nucleation as well as enhanced diffusivity will strongly favor growth over nucleation at higher temperatures. Meanwhile, the hot substrate can also cause dewetting of the precursor solution on the substrate due to the high interfacial energy.[259,260] In other words, the contact angle (θ) in eq 7 will be altered due to the hot substrate. These dynamics might plausibly lead to the observed microstructure, wherein sparsely distributed nuclei grow rapidly to extreme size. Nevertheless, finer structure is in fact evident within the large domains (Figure 21, panels C and D), as confirmed by several other groups.[261,262] It is most probable that they are composed of "sub-grains" with much smaller size than the apparent domain size. This discrepancy may be explained by noting that the "hot-casting" approach does not take place under conditions remotely approximating thermal equilibrium. Although the substrate is hot, it is presumably placed on a room-temperature vacuum chuck and then covered with solution that is nominally more than 100 °C cooler. Therefore, the thermal gradient, causing fluid convection as shown in Figure 21E, may dominate the crystallization dynamics as much as or more than the nominal temperature. These results may be better interpreted by the explanation of Deng et al.,[263]

DOI: 10.1021/acs.chemrev.8b00318
Chem. Rev. 2019, 119, 3193−3295

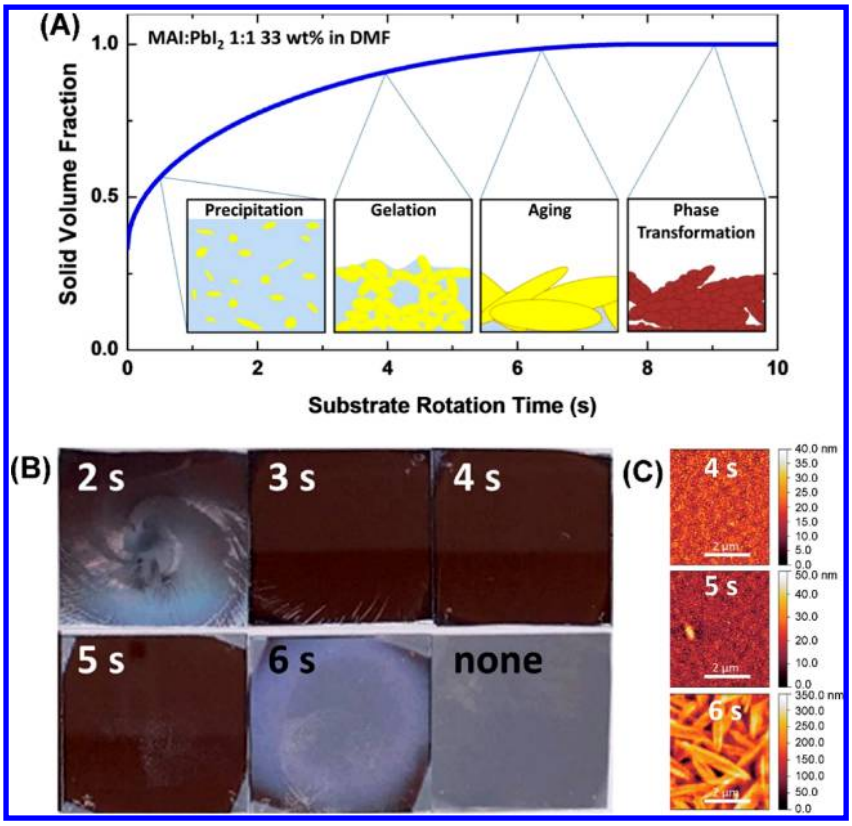

Figure 22. (A) Schematic of perovskite-solvent nucleation and growth during the spin-coating of $MAPbI_3$ from DMF solution; (B) photographs demonstrating the effects of solvent wash timing in the solvent engineering process: washing too early is characterized by macroscopic nonuniformity (spirals or streaks), while washing too late yields matte films similar in appearance to the unwashed film; (C) AFM images reveal that films washed near the gelation point (~4 s) have a compact microstructure, while those washed too late have a rodlike microstructure resembling that of films prepared by simple spin-coating. Republished with permission from ref 190. Copyright 2016 Royal Society of Chemistry.

who observe similar morphology in doctor-bladed (see section 4.3.1) perovskite films on hot substrates. They attribute these patterns to Rayleigh-Bénard convection behavior driven by the temperature difference between the substrate and ambient air, with the edges of the "leaves" corresponding to the boundaries of adjacent convection cells (Figure 21E).[263] Nevertheless, hot-casting is clearly a successful approach toward attaining uniform film coverage via a one-step spin-coating process, and the champion PCE of 18% is clear evidence of their quality.[258]

As a final note, an alternative means of modulating crystallization kinetics without changing the solvent is to change the stoichiometry and/or chemistry of the precursors. Doing so can have a significant impact on whether and which intermediate phases form, and it provides a means of influencing the nucleation behavior of the perovskite. These methods are covered more extensively in section 6, as well as other additives that have been used to alter the microstructure or other film properties.

4.1.2. "Solvent Engineering"/Antisolvent Washing. A slight modification to the simple spin-coating procedure that has been used extensively in recent literature and proven highly effective for the fabrication of high-efficiency PSCs, including the current published record as of this writing,[265] is frequently termed solvent engineering, in reference to the first paper to report this technique.[148] In this procedure, most typically a stoichiometric solution of the perovskite precursors is prepared and spin-coated as above. While the substrate is spinning, a nonpolar antisolvent (e.g., toluene, chlorobenzene, or diethyl ether) is dripped onto the substrate (Figure 20B). The basic principle of this approach is that application of the antisolvent accelerates supersaturation of the precursor solution by two mechanisms: (i) driving out the solvent much faster than it would evaporate by itself (increasing the precursor-solution concentration C in eq 6) and (ii) reducing the intrinsic precursor solubility in the remaining solution upon mixing of antisolvent into it (reducing the equilibrium concentration C_s in eq 6). This drives a rapid "burst" of nucleation, and thus, the high nucleation density so obtained yields a flat and uniform perovskite film with a compact, pinhole-free microstructure (Figure 20, panels E and F). The initial report of this method detailed what were at the time record-setting performance PSCs,[24,148] and "solvent-engineering" has remained at the forefront of perovskite research ever since, yielding many devices with PCE of over 20%.[25,26,29,89,266] It is also a highly versatile technique, adaptable to many different perovskite systems and many different device architectures. The consistency of film morphology across different substrates may be rationalized in the context of eq 6, wherein application of the antisolvent sharply depresses the solubility of the precursors, thereby increasing the saturation ratio and therefore reducing the critical radius r^* for nucleation. The rapid formation of densely packed nuclei accounts for the characteristic morphology comprised of densely packed grains. Increasing the saturation ratio also boosts the magnitude of the volumetric contribution to the free energy change in eq 6, reducing the influence of the surficial term and thus reducing the relative importance of the substrate in controlling the formation of the film.

DOI: 10.1021/acs.chemrev.8b00318
Chem. Rev. 2019, 119, 3193−3295

While solvent engineering is a reliable and portable process, some finesse is required to wash the substrate at the correct time. The ordinary one-step spin-coating method may be thought of as a sol−gel process wherein the precursor film transitions from a colloidal solution of perovskite-solvent intermediates (the sol) to a network of the colloids that still incorporates the solvent (the gel) but is more mechanically rigid and well-bonded to the substrate (as shown schematically in Figure 22A).[190] The existing nuclei then grow by consuming the available nutrients in the remaining precursor solutions and transform to the perovskite through evolution of the solvent. It is critical to wash the substrate with the antisolvent as close as possible to the gelation point, as doing so allows the antisolvent to easily permeate and remove solvent from the film through the channels in the gel, while the elastic nature of the precursors in the gel state resists ablation by the antisolvent jet. If the antisolvent is applied too early, the gel will not have completely formed and the film will show signs of damage, ranging from extreme nonuniformity to smaller scratches or spirals (Figure 22B). On the other hand, if the antisolvent is applied too late, film formation will proceed as if the substrate had not been washed at all, yielding films that are effectively identical to those produced by the simple spin-coating process described in the previous section (Figure 22C).[190]

The ideal washing time/gelation point will generally be unpredictable, varying not only according to the solvent, concentration, and spin-speed, but also with more subtle variables characteristic of the ambient environment (e.g., temperature, presence of other solvent vapors in the deposition chamber). Fortunately, a simple rule can guide the device-maker, as the different stages of the sol−gel process are readily visible. In particular, an abrupt transition of the film from transparent to hazy can be observed while it spins. The gelation point occurs roughly 1−2 s before this transition, so the antisolvent should be applied at this point. Kerner et al.[190] report good reproducibility of this protocol across films fabricated at different laboratories using different tools.

As with the basic spin-coating process, the choice of the perovskite precursor solvent can be important in solvent engineering processes. In the original paper that introduced the technique as applied to PSCs, Jeon et al.[148] indicated that formation of a MAI-PbI_2-DMSO intermediate (the XRD pattern of which indicates that it is likely $(MA)_2Pb_3I_8\cdot 2DMSO$[188]) was a critical factor in attaining high-quality films. Ahn et al.[170] observed that, while films prepared from precursor solutions using only DMF as the solvent often had pinholes, addition of DMSO to the solution yielded more uniform films. The authors of this study also found that the latter films consisted of a DMSO-containing intermediate phase immediately after spin-coating, but that this phase could be converted to $MAPbI_3$ by a brief postanneal. Although Jeon et al.[148] also observed similar formation of intermediate phases, their solvent/antisolvent combination (DMSO:GBL/toluene) was completely miscible; consequently, the DMSO content of the as-spun film could be highly dependent on how the antisolvent was applied.[148] By contrast, Ahn et al.[170] used diethyl ether, miscible with DMF but not DMSO, as the washing solvent, proposing that the exact stoichiometry of MAI:PbI_2:DMSO present in solution should be largely preserved in the as-deposited film. In this manner, they obtained an average PCE above 18% among 41 cells, with a champion cell of 19.7%, at the time a high value for PSCs prepared using a one-step fabrication procedure.

Whether present in exact stoichiometry or not, the formation of the organic iodide-PbI_2-DMSO intermediate of some type appears to be central to attaining PCE above 20% via solvent engineering, as many reports of such cells demonstrate.[25,26,29,89,265−267] Bai et al.[268] studied the effects of different DMF/DMSO ratios used in the $MAPbI_3$ solvent engineering precursor solution and determined that it was desirable to tune this ratio, such that a film containing only $(MA)_2Pb_3I_8\cdot 2DMSO$ as the crystalline phase was formed immediately after spin-coating. Among DMSO:PbI_2 concentration ratios of 0, 1, 4.2, 10, and 14.1/pure DMSO solvent (at a fixed molarity of 1 M, with the remainder of the solvent made up by DMF), DMSO:PbI_2 = 4.2 and 10 led to a pure $(MA)_2Pb_3I_8\cdot 2DMSO$ precursor film, while the others contained some amount of $MAPbI_3$. (Why $MAPbI_3$ appears in the film prepared from the pure DMSO solvent is not entirely clear but may stem from an interaction between MAI and DMF that prevents the former from reacting with $(MA)_2Pb_3I_8\cdot 2DMSO$.) These ratios also led to the strongest tet(110) peaks in the XRD pattern of the final perovskite film, as well as the largest apparent grains in a compact network. Cross-sectional SEM observations of the final perovskite films showed a high density of pinholes and voids in the film processed without DMSO, especially at the interface, while those processed with DMSO were much more compact. On the basis of these observations, Bai et al.[268] suggest that, in the absence of DMSO, application of the antisolvent causes crystallization of the perovskite to propagate from the top surface of the film rather than from the substrate, leading to poor contact at the bottom surface. Formation of the $(MA)_2Pb_3I_8\cdot 2DMSO$ intermediate, on the other hand, presumably allows the perovskite to begin crystallizing from the bottom surface when the precursor film is heated from below (i.e., during the annealing step rather than the antisolvent application step), desorbing DMSO in a slower and gentler manner that improves the crystallinity of the final perovskite. Alternatively, as noted in section 3.1.2.1, strain caused by the volume contraction from $MAPbI_3\cdot DMF$ to $MAPbI_3$ may lead to interfacial delamination, while the similar densities of $(MA)_2Pb_3I_8\cdot 2DMSO$ and $MAPbI_3$ may result in less strain as the film forms. Bai et al.[268] further posit that a phase-pure intermediate is desirable because the bottom-up crystallization of the perovskite should lead to large, columnar grains with few horizontal grain boundaries. If $MAPbI_3$ is already embedded within the precursor film, these inclusions will grow in all directions and interfere with the perovskite crystallizing upward from the intermediate, presumably leading to a denser network of grain boundaries. The concentrations using DMSO:PbI_2 ratios that yielded optimal morphology (i.e., 4.2 and 10) also yielded the highest PCE when the films were integrated into PSCs. An additional benefit of large DMSO component in the solvent is broadening of the antisolvent dropping window during which acceptable films may be produced, which is attributed to the enhanced stability of the $(MA)_2Pb_3I_8\cdot 2DMSO$ intermediate in the presence of a large amount of DMSO.[189,268,269] Furthermore, decomposition of $(MA)_2Pb_3I_8\cdot 2DMSO$ has been suggested to improve the mobility of grain boundary motion through the local dissolution of $MAPbI_3$ in the evolved DMSO vapor (effectively solvent annealing the perovskite, as discussed further in section 5.1.2).[270] Thus, the formation of an intermediate phase during the solvent engineering process appears to be quite important for the formation of a compact film with large grain size and

DOI: 10.1021/acs.chemrev.8b00318
Chem. Rev. 2019, 119, 3193−3295

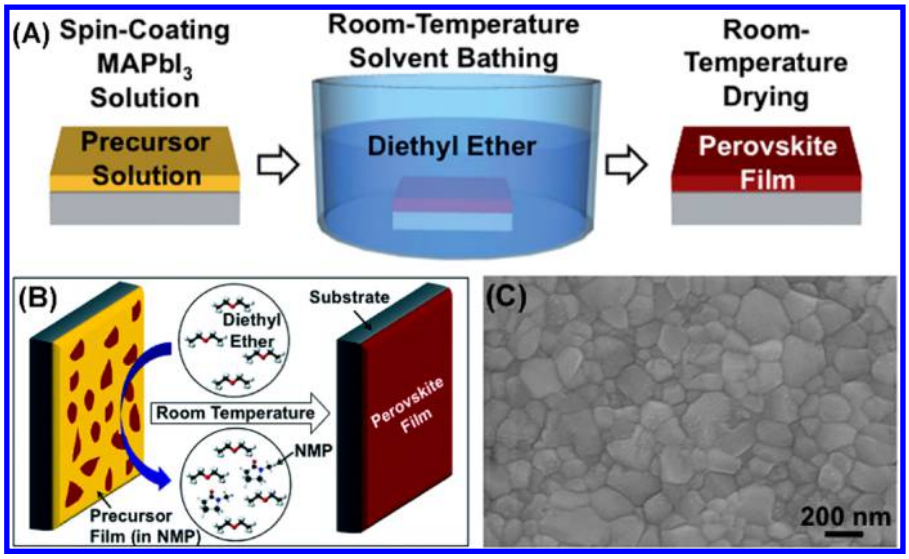

Figure 23. Antisolvent/solvent extraction process: (A) the precursor solution is coated onto the substrate by a deposition approach such as spin-coating or doctor-blading, which is then immersed in an antisolvent bath containing, for example, diethyl ether, which extracts the perovskite solvent from the film; (B) the remaining solvent in the film diffuses into the antisolvent bath, inducing crystallization of the perovskite; (C) typical morphology of a $MAPbI_3$ perovskite thin film deposited by antisolvent/solvent extraction exhibits compact grain structure. Republished with permission from ref 150. Copyright 2015 Royal Society of Chemistry.

good interfacial bonding to the substrate, which is crucial for the operation of optoelectronic devices.

The chemistry of the antisolvent is also important to the deposition process. In their early study, Xiao et al.[149] investigated 12 different solvents, finding that short-chain alcohols (methanol, ethanol, and ethylene glycol) yielded only PbI_2 films due to the high solubility of MAI; tetrahydrofuran and nitriles (benzo- and aceto-) yielded nearly transparent films of unclear composition; isopropanol and chloroform yielded good grain structure but macroscopic nonuniformity in the center of the substrate; but aromatics (xylene, toluene, chlorobenzene) yielded both uniform coverage and good grain structure. Bu et al.[271] used nontoxic, nonpolar ethyl acetate to fabricate cells with PCE up to 19.4%, with perovskite layers adopting the characteristic close-packed grain structure. Paek et al.[267] studied the effect of using several nonpolar antisolvents in the deposition of mixed-composition $(FAPbI_3)_{0.85}(MAPbBr_3)_{0.15}$ and found that it is better if the washing antisolvent is both miscible with the perovskite solvent and has high boiling point. Somewhat contrary to the findings of Ahn et al.,[170] Paek et al.[267] found that solvents such as diethyl ether and *p*-xylene, which are not miscible with DMSO, led to lower-performing PSCs than those that are, such as chlorobenzene, toluene, or trifluorotoluene (TFT). The lower performance of the devices fabricated from films washed with the former solvents may be explained in part by the reduced absorbance and increased roughness of these films. Additionally, the use of highly volatile solvents, such as ether, may lead to macroscopic nonuniformity that can hurt performance. The best-performing devices in this study were produced using TFT (best PCE > 20%), although even the ether-washed devices were able to yield reasonably good performance levels (best PCE > 17%).[267] Overall, solvent engineering is a highly reliable process for producing high-quality films, but as with all deposition methods, it requires careful refinement of processing parameters in order to yield high performance.

As a final note, the temperature of the antisolvent can also be a useful variable for obtaining further control over the process. Liu et al.[272] have demonstrated that while the traditional solvent engineering process developed for Pb-based perovskites does not yield perfect coverage in the case of $FA_{0.75}MA_{0.25}SnI_3$, increasing the temperature of the antisolvent to 65 °C or above allows a conformal morphology to be recovered. This effect was attributed to improved miscibility of the chlorobenzene antisolvent with the DMSO solvent; however, DMSO is already miscible with chlorobenzene at room temperature. Therefore, this explanation may not fully account for the improved coverage. As discussed previously (eq 9 and Figure 7D), the maximum nucleation rate may occur at that temperature,[143,153,154] providing a possible alternative explanation. However, further work will be needed to distinguish which of these effects is more important.

4.1.3. Gas-Quenching. Closely related to solvent engineering is the gas-quenching technique, in which the antisolvent is replaced with a blast of inert gas such as Ar or N_2.[273] The gas serves essentially the same purpose as the antisolvent, promoting rapid supersaturation of the solution and leading to film morphologies that are essentially identical to those produced by solvent engineering. Note that supersaturation in this case is stimulated solely by rapidly increasing the concentration through accelerated evaporation of the solvent rather than simultaneously reducing the solubility limit as in solvent engineering. While not nearly as widespread as solvent engineering, the PCE of devices produced by gas quenching appear to be compatible with similar performance levels, with reasonably large-area (0.5 cm^2) devices reaching 20%.[274] Gas-quenching also appears to be portable to other perovskite compositions, having been successfully applied to both MA- and FA-based perovskite systems.[273,274] By removing the need for the antisolvent, gas-quenching reduces the dependence of the fabrication process on toxic or otherwise hazardous solvents (such as chlorobenzene, toluene, or diethyl ether), a compelling advantage in terms of both material costs and safety concerns.

4.1.4. Anti-Solvent/Solvent Extraction. A similar approach to solvent engineering applies the antisolvent not

DOI: 10.1021/acs.chemrev.8b00318
Chem. Rev. 2019, 119, 3193−3295

during spin-casting (or film deposition), but afterward, through immersion in a bath of the antisolvent (Figure 23, panels A and B).[150] The same principle as in solvent engineering/gas-quenching is at work here (i.e., exchange of the solvent for an antisolvent drives up the saturation ratio in the precursor solution), leading to rapid and uniform nucleation of the perovskite grains. This antisolvent, which must again be miscible with the solvent but not dissolve the perovskite, extracts the solvent from the preperovskite film within seconds to a couple of minutes, leaving a perovskite film of similar microstructure to those produced by solvent engineering (Figure 23C). This method, first reported by Zhou et al.[150] using NMP and diethyl ether as solvent and antisolvent, respectively, offers some advantages over solvent engineering, as it (i) avoids the difficulty of precisely timing and uniformly applying the antisolvent (which can reduce reproducibility), (ii) reduces the chance of film damage by the high-speed interaction of the solvent jet with the rapidly spinning film, (iii) can be carried out at room temperature, and (iv) is compatible with roll-to-roll manufacturing processes, as the perovskite precursors need not be deposited by nonscalable methods such as spin-coating. The initial report yielded respectable PSC performance, with the PCE of the devices prepared by antisolvent/solvent extraction rising above 15%.[150] The kinetics of antisolvent/solvent extraction can also be controllable (e.g., by introduction of stirring in the antisolvent bath), thereby accelerating the extraction of the excess solvent in the film and thus the perovskite nucleation.[275] Use of this technique contributes to the formation of smoother perovskite films, and it is especially useful for depositing perovskites that exhibit intrinsically rapid growth behavior, such as Br-rich perovskites.[275]

Antisolvent/solvent extraction, though less widely used than solvent engineering, appears to be similarly versatile in its ready application to other perovskite systems. Eperon et al.[276] prepared low band gap $FA_{0.75}Cs_{0.25}Pb_{0.5}Sn_{0.5}I_3$ films through immersion in an antisolvent bath, which could be integrated as an absorber into single-junction PV cells reaching almost 15% PCE or used as the bottom cell in a 2-terminal (4-terminal) tandem cell reaching 17% (>20%) (the top cell is prepared by solvent engineering). Some care must be taken, however, when considering other perovskite compositions besides $MAPbI_3$, as the transport properties of different ions can change the crystallization dynamics, leading to substantial changes in morphology. For example, the higher diffusivity of Br^- relative to I^- results in pinholes in mixed-halide perovskite films.[275] Per eq 10, the growth rate of a nucleus (assuming diffusion-limited island growth) is proportional to the diffusivity of the species involved.[159] As grain growth becomes more favorable relative to nucleation, the grains become larger but also more disconnected.[275] This problem may be surmounted, however, by increasing the rate at which the solvent is removed from the precursor film into the antisolvent bath, which can be simply accomplished by stirring the bath. Agitation of the bath adds a convective component to the mass transfer of the NMP solvent out of the film, improving the favorability of nucleation and density of crystallites, recovering the desirable morphology of the pure iodide perovskites prepared by antisolvent/solvent extraction.[275]

A key advantage of antisolvent/solvent extraction is that it allows the benefits of solvent engineering to be extended to scalable deposition techniques. Adaptation of this technique does require design of a solvent that allows the film to stay wet long enough to be transferred from a film production line to the antisolvent bath. Nevertheless, this challenge is surmountable: the most successful single-junction cell prepared using antisolvent/solvent extraction was prepared initially by doctor-blading (see section 4.3.1) rather than spin-coating from a compound NMP-DMF solvent, whose high boiling point allows high tolerance for time delay between blade-coating and immersion into the ether bath.[277] The antisolvent/solvent extraction process, when complemented with an MACl additive to the perovskite solution, yields large, well-connected grains (which appear to be well over 1 μm) and a best PSC efficiency of over 19%.[277] Overall, the antisolvent/solvent extraction process appears to be quite promising for application of the mechanisms at work in the highly successful solvent engineering process to large-area devices.

4.1.5. Drop-Casting. A very simple method of solution-processing perovskites, albeit one that does not generally produce well-formed thin films per se, is to simply deposit the precursor solution onto a substrate and let the solvent evaporate naturally or under the influence of a mild anneal. This method has been successfully applied to an all-mesoporous architecture in which the entire device consists of a mesoporous scaffold on an FTO/glass substrate composed of an ETL (usually mesoporous TiO_2), a porous graphitic carbon electrode, and a nonconductive layer (usually ZrO_2) separating the ETL from the electrode.[278−280] A mesoporous HTL (such as NiO_x) may also be inserted, and some of the highest performing PSCs of this variety (reaching nearly 15% PCE) include this layer.[281] The mesoporous layers are fabricated first (including the top carbon electrode), and deposition of the perovskite by drop-casting completes the device. As is the case for other architectures, perovskite deposition may be separated into one-step or two-step deposition approaches, the latter of which will be discussed in section 4.2. The drop-casting method is enabled here mainly because the crystallization of perovskite is fully constrained within the thick, multiple mesoporous layers, unlike the typical planar thin film device structure. While these cells possess only modest PCE, they enjoy the remarkable distinction of high stability in the ambient (no drop in PCE while exposed to 1-sun illumination in ambient air for >1000 h), perhaps because the thick (∼10 μm) carbon electrode offers a high degree of resistance to moisture. The authors of the first study propose that the addition of small amounts of 5-ammoniumvaleric acid (5-AVA) cations is important for improving pore filling and interface bonding, under the hypothesis that the carboxyl group anchors to the metal oxide scaffold, while the ammonium group bonds to the perovskite.[278] In other words, the 5-AVA ions effectively reduce the surface energy γ_{SC} of the perovskite−TiO_2 interface (per eq 28), increasing the strength of the film−substrate bonding. A later report suggested that an additive of guanidinium chloride ($NH_2C(=NH)NH_2{\cdot}HCl$) could serve a similar function while also suppressing SRH recombination, boosting performance of the HTL-free mesoporous cells to >14%.[279] Somewhat surprisingly, the best-performing cells of this type are fabricated using a moisture-assisted process, wherein an additive to the perovskite precursor, NH_4Cl, is claimed to form an intermediate phase within the pores of the scaffold. This intermediate phase is then converted into perovskite under exposure to moist air, evidently by deprotonation of the ammonium ion to yield volatile ammonia and hydrogen chloride gases that evolve from the scaffold.[280] The resulting

DOI: 10.1021/acs.chemrev.8b00318
Chem. Rev. 2019, 119, 3193−3295

PSCs have a champion PCE of 15.6% and high (though only up to a certain point) air-stability. The best-performing cells are exposed initially to relative humidity of 45% to complete the removal of NH_4Cl then kept thereafter at 35% RH.[280] Cells exposed to relative humidity at 55% or above degrade noticeably over the course of a few days (after initial improvement), demonstrating the limits of this architecture's ability to preserve the integrity of the absorber.[280]

4.1.6. Dual-Source and Single-Source Evaporation. One of the earliest reports of efficient PSCs detailed perovskite films produced not by solution-processing but rather by vapor deposition (still, however, a one-step deposition), wherein the perovskite precursors are thermally evaporated or sublimed in a vacuum chamber and collect on a substrate mounted at the top of the chamber (Figure 24A). Liu et al.[193] demonstrated that coevaporation of MAI and $PbCl_2$ sources could lead to highly uniform films (though with small apparent grain size, on the order of few hundred nanometers) (Figure 24B) and that PSCs fabricated using these films could reach a champion PCE of 15.4%. Subsequent reports using essentially the same process (in some cases PbI_2 is used as the inorganic source as well) have yielded similar film morphology.[282−284]

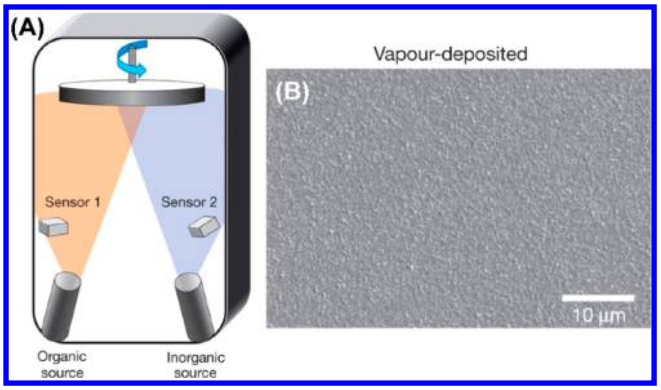

Figure 24. (A) Coevaporation process: substrates are fixed to a rotating platen at the top of a vacuum chamber, facing downward; the component halides AX and BX_2 are heated from boats or crucibles at the base of the chamber, vaporizing and traveling to the substrate, where they react to form the desired perovskite phase. (B) SEM image of perovskite deposited by coevaporation, showing a compact and uniform microstructure with small apparent grain size. Reprinted with permission from ref 193. Copyright 2013 Macmillan Publishers Ltd.

An advantage to vapor-based deposition that complements the relative ease of preparing uniform perovskite films is that they are not as sensitive to the presence of substrate defects (such as pinholes or dust particles) that interfere with the flow of the solution nor to the problems presented by nonuniform evaporation of the solvent. Indeed, the removal of the need for toxic solvents is another compelling argument for preferring vapor-deposition methods. The limitations of vapor-phase processing are also clear. As noted in section 3.1.3, there is a lack of understanding regarding the basic mechanisms of crystallization from the vapor phase. However, the origin of compact but small grains in the coevaporated films is easily rationalized, since coevaporation of the precursors should lead to a high and uniform density of nucleation sites on the substrate, leading to the compact grain structure. Since the perovskite synthesis reaction is extremely favorable, nucleation should proceed faster than growth of the grains, leading to the small grain size. Vapor-deposition presents another challenge, as it is particularly difficult to control the evaporation rate of MAI since conventional quartz crystal thickness monitors do not provide reliable readings for this volatile material.[285] MAI evaporation is therefore often handled using open-loop control, in which a certain source temperature is set for the duration of the deposition.[283,284] Despite these challenges, PSCs prepared by coevaporation are approaching parity with their solution-processed analogs, with several reports of PCE exceeding 20%.[284,286]

An early example of vapor-phase deposition involved layered perovskite structures deposited by a simplified variant of coevaporation (termed single-source thermal ablation or SSTA), wherein the precursors are deposited on a tantalum sheet, which functions similarly to a boat in conventional thermal evaporation.[287] Rather than being evaporated at controlled deposition rates, however, the precursors are rapidly vaporized by passing a large current (80−90 A) through the sheet over a matter of seconds. The rapidity of SSTA is key to its success, as the precursors can vaporize and reassemble on the substrate without substantial decomposition if heated sufficiently quickly. Film thickness for SSTA is controlled by the amount of the precursor material initially deposited on the tantalum sheet and/or by controlling the source-to-sample distance during the deposition. This process has been used to successfully fabricate photoluminescent films of $(BA)_2SnI_4$, $(PEA)_2PbI_4$, and $(PEA)_2PbBr_4$, the latter of which are also electroluminescent at liquid nitrogen temperature.[287] SSTA is also suitable for producing Ruddlesden−Popper perovskites such as $(BA)_2MASn_2I_7$,[287] as well as incorporating particularly large organic cations (which present problems for solution processing due to their affinity for nonpolar rather than polar solvents) into the perovskite structure.[23,288,289] In particular, room-temperature electroluminescence could be obtained from a SSTA-deposited film of a quaterthiophene-derived perovskite, $(H_3NC_2H_4{-}C_{16}H_8S_4{-}C_2H_4NH_3)PbCl_4$, concretely demonstrating the advantages of this process for the formation of these complex hybrid structures.[23] SSTA has also been applied to the deposition of $MAPbI_3$, yielding homogeneous films with compact grain structure, similar to that obtained by coevaporation.[290] The performance of PSCs made using the resulting films, however, did not display an advantage over coevaporation, reaching a level of ∼12%.[290] Overall, the most compelling benefit of SSTA is the ability to integrate organic compounds of great complexity into the perovskite structure and to do so by way of a relatively simple and quick process.

4.1.7. Pulsed Laser Deposition (PLD). Another deposition technique that can address the challenge of accurately controlling the deposition rate of the organic component is PLD. PLD resembles SSTA and thermal evaporation in that the precursors are rapidly projected from a source onto a substrate in vacuum, but the energy required to vaporize them is provided by a UV laser striking the material rather than a more conventional heat source (Figure 25A). The use of the UV laser, however, introduces a complication in that the ablated particles are considerably more energetic than those that are thermally evaporated and can sputter material (particularly volatile organics such as MAI) from the surface of the substrate. As a result, the use of a stoichiometric target of MAI and PbI_2 leads to films that essentially only consist of PbI_2.[291] This problem can be mitigated by changing the substrate orientation [i.e., substrates may be mounted either

DOI: 10.1021/acs.chemrev.8b00318
Chem. Rev. 2019, 119, 3193−3295

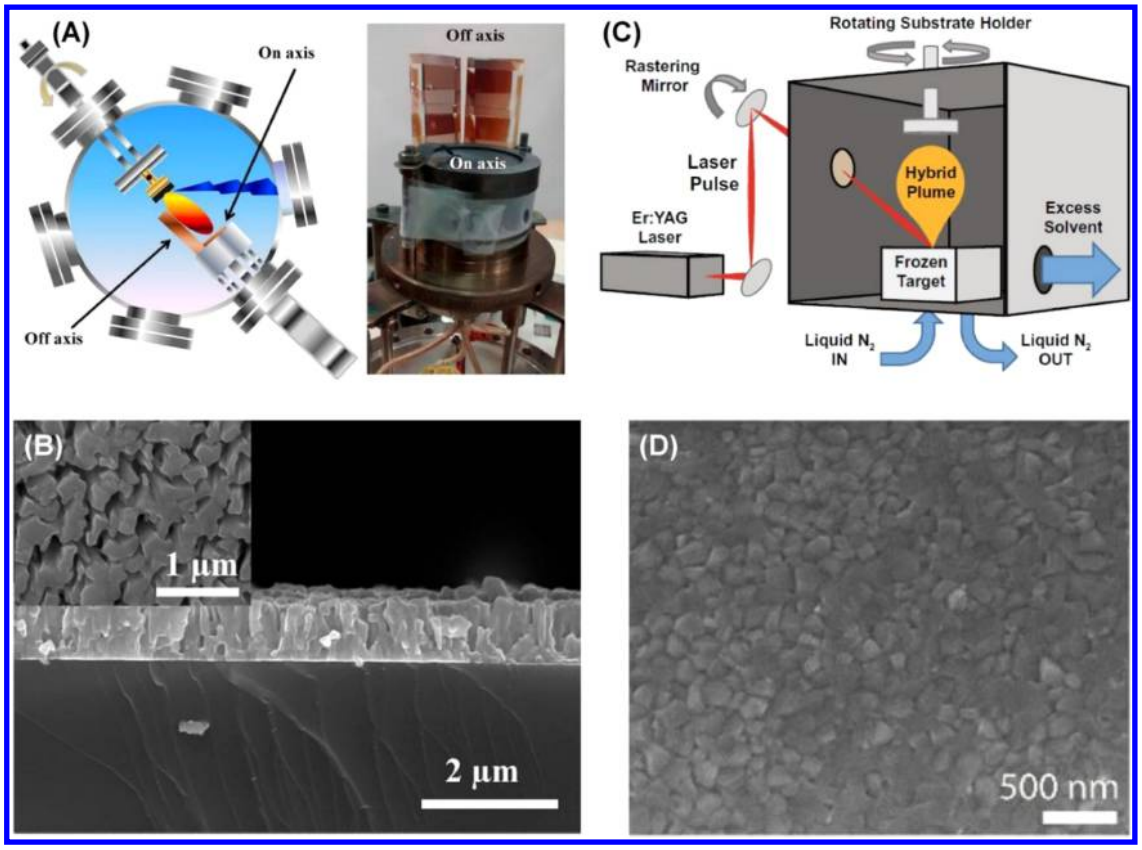

Figure 25. Laser ablation techniques for thin film deposition. (A) In the pulsed-laser deposition process, a laser is directed at a solid target composed of the precursor materials, generating a plume of ablated material that collects on the substrates, reassembling to form films of the desired composition. Samples may be mounted on- or off-axis, affecting the plume-substrate interaction. (B) Microstructure of a $MAPbI_3$ film deposited by off-axis PLD, showing the pillared microstructure and void pattern in cross-sectional and top-down (inset) SEM images. Adapted from ref 291. Copyright 2015 American Chemical Society. (C) In the resonant infrared matrix-assisted pulsed laser evaporation (RIR-MAPLE) technique, the solid target is replaced with a cryogenically frozen solution of the precursor, and the laser energy is selected for resonance with the chemical bonds of the solvent, avoiding damage to the precursors. Reprinted with permission from ref 292. Copyright 2018 Springer Nature. (D) Microstructure of a $MAPbI_3$ film deposited by RIR-MAPLE, demonstrating similar compact, apparently small-grained morphology similar to that yielded by thermal coevaporation. Adapted from ref 293. Copyright 2018 American Chemical Society.

on-axis (facing the target) or off-axis (perpendicular to the target)] (Figure 25A). The off-axis configuration lessens the effects of high-energy particles impacting the film as it grows, allowing phase-pure $MAPbI_3$ films to be grown at a MAI:PbI_2 stoichiometry in the target of only 4:1 (generally, a more MAI-rich stoichiometry would be needed for PLD).[291] The morphology of these films is somewhat unique, with SEM images indicating a pillared structure, although it is not clear whether the pillars are single grains or are themselves composed of smaller crystallites (Figure 25B). There also appear to be pillar-shaped voids in the films, which are visible both in cross-section and top-view images. Interestingly, the addition of Cl^- to the target yields a similar morphology as seen from top-view images; however, in cross-section the films present a bilayer structure (i.e., a region near the substrate composed of apparently very small, tightly packed grains, and a region above that possessing a similar pillared structure to the pure iodide perovskite, but with the pillars inclined about 30° from vertical). Even more intriguing is that addition of F^- instead of Cl^- appears to recover the morphology of the pure iodide. Unfortunately, no explanation is offered for the chemistry-induced changes in morphology. The presence of voids combined with the small grain size calculated from the XRD patterns (<100 nm) suggest that these films are not ideal for integration into devices, and indeed PSCs prepared using the mixed-halide (I^-/Cl^-) target exhibited relatively low PCE, ~7%.[291] The authors also investigated the on-axis configuration, finding that a much larger ratio of 18:1 MAI:PbI_2 could compensate for the loss of the organic component, but that heating of the substrate at 90 °C during the deposition was needed to obtain a stoichiometric film. A subsequent study of on-axis deposited films found that a softening atmosphere of Ar/H_2 (90/10 mixture) could help avoid loss of the organic component, and that pure $MAPbI_3$ films could be deposited from a target composed of a 12:1 ratio of MAI:$PbCl_2$.[294] The morphology of these films is much closer to those produced by thermal evaporation (apparently small, compact grains with few voids or pinholes).[294] Perhaps as a result of the improved morphology, the performance of the best PSC generated by this process reached almost 11%, though this device also possessed significant hysteresis, and the stabilized PCE was not reported.[294] The overall similarity of the film morphology prepared by PLD and by thermal coevaporation is not surprising in view of the similarity of the deposition conditions (simultaneous deposition of the perovskite precursors on the substrate leading to fast nucleation but slower growth). The discrepancy among performance levels may instead be due to the higher energy of the particles bombarding the substrate, which may not only sputter off the lighter organics but also

DOI: 10.1021/acs.chemrev.8b00318
Chem. Rev. 2019, 119, 3193−3295

possibly lead to detrimental point defects that act as recombination sites.

4.1.8. Resonant-Infrared Matrix-Assisted Pulsed Laser Evaporation (RIR-MAPLE). The problems of energetic particle bombardment in PLD can be solved by a subtler configuration of the target-laser interaction, which forms the basis for the resonant-infrared matrix-assisted pulsed laser evaporation (RIR-MAPLE) technique[295] (Figure 25C). If the target is composed of a solution of the precursors rather than a pellet of the precursors themselves and the laser energy is resonant with one of the bonds in the solvent (generally necessitating an IR wavelength) then ablation of the target solution should proceed in a much gentler manner. The solvent, rather than the precursors, accepts the majority of the energy and vaporizes, carrying the precursors to the substrate on the solvent plume. This method offers a greater degree of control over the composition of the film compared to PLD, since the stoichiometry of the precursors in the target solution should be transferred to the substrate, even for relatively volatile components like MAI. Indeed, Barraza et al.[292] demonstrated that phase-pure $MAPbI_3$ films (as determined by XRD) could be deposited using stoichiometric targets, while MAI-rich targets yielded $MAPbI_3$ films with impurity XRD peaks that could be assigned to $(MA)_4PbI_6{\cdot}2H_2O$, indicating the transfer of excess MAI (the water in the hydrate most likely originates from exposure of the films to the ambient air humidity during the XRD measurement). The morphology of these films is akin to that produced by both PLD and thermal coevaporation, consisting of apparently small but densely packed grains (Figure 25D). This microstructure may again be rationalized by noting that, assuming that the precursors transit to the substrate in a uniform beam, nucleation of perovskite crystallites on the substrate should occur uniformly and densely, leading to tightly packed small grains. While the microstructure of the RIR-MAPLE films is similar to that of spin-cast films prepared by solvent engineering on microscopic scales, at larger scales (on the order of tens of micrometers), the RIR-MAPLE films are significantly rougher, comprised of a network of craterlike features.[293] This topography might indicate impact by solvent or solution droplets, as a result of either incomplete vaporization by the laser or else by coalescence of the solvent while in transit from the target to the substrate.

One complication of RIR-MAPLE is that, while the target solvent should be pumped away by the dynamic vacuum, it can also co-deposit on the substrate along with the precursors. This problem is exacerbated by the challenge of finding a suitable solvent for the process. An Er:YAG laser, for example, emits at a wavelength of 2.94 μm (or energy of ∼0.42 eV), which is resonant with hydroxyl bonds, a convenient choice for water-based solutions. For perovskites, however, water is an undesirable solvent, and there are few OH-containing solvents that can dissolve lead halide salts. Barraza et al.[292] circumvented this challenge using a mixture of a good lead halide solvent (DMSO) with a polar polyalcohol OH donor (ethylene glycol or glycerol). The low vapor pressures of these solvents leads to their incorporation into the films; however, they can be driven off through postannealing.[292] While the presence of DMSO is most likely benign, the effects of residual polyalcohol are less clear. Time-of-flight secondary ion mass spectrometry (TOF-SIMS) measurements of $MAPbI_3$ films grown by RIR-MAPLE have also indicated elevated levels of Na, Ca, and Cl relative to those prepared by spin-coating.[293] Despite the higher impurity levels compared to spin-coating, $MAPbI_3$ films prepared by RIR-MAPLE have comparable optoelectronic properties to spin-cast perovskite and do not suffer from especially high trap densities, as evidenced by a PL lifetime of ∼70 ns and PCE of 12% attained in the first and so far only report of $MAPbI_3$ PSCs with absorber deposited by RIR-MAPLE.[293] This deposition method as applied to halide perovskites is still relatively untested, and it is likely that further investigation into target preparation and composition may lead to finer control of film morphology and purity.

4.1.9. Capillary Thin Film Growth. An inventive method for the fabrication of self-encapsulating, industrially compatible PSCs involves fabricating two half-cells (i.e., anode/ETL on one substrate, cathode/HTL on another), stacking them in a sandwich configuration, infiltrating a solution of the perovskite precursors between them, and driving out the solvent under a combination of light mechanical pressure (by clamping the substrates together), heat, and vacuum (by placing the structure in a vacuum oven at 100 °C for 12 h).[296,297] While PSCs produced by this method yielded PCE no better than ∼13%, the paucity of such reports leave room for the possibility that further optimization of the processing or device architectures might lead to further improvements. Unfortunately, the nature of the self-encapsulating process also complicates key film characterization techniques such as SEM and XRD, so accurate processing-morphology relationships may be more difficult to obtain. Nevertheless, since the crystallization of perovskites occurs in a relatively confined environment, it is envisioned that the grain growth of perovskites will be suppressed, leading to microstructures with relatively fine grains, a hypothesis that awaits experimental validation.

Along similar lines, Chen et al.[298] have reported a method that can allow the growth of perovskite thin films with large apparent lateral grain size. In this method, two flat substrates are clamped together and immersed in a heated perovskite precursor solution, causing the solution to flow upward into the gap between the substrates (which can be tuned by varying the clamping force). Chen et al.[298] suggest that, due to the elevation of the substrates above the heated solution, the solution cools as it rises. They also suggest that the resulting reduction in the equilibrium solubility limit C_S causes the precursors to precipitate onto the substrate (or existing nuclei), while convection driven by the thermal gradient replenishes the precursors necessary for continued growth from the bulk solution below. While plausible, this explanation does involve a potential complication. Although it is generally the case for many solvent−solute combinations that C_S does indeed increase as temperature rises, certain perovskite-solvent combinations (including the ones used in the above study, such as $MAPbI_3$ in GBL or $MAPbBr_3$ in DMF) exhibit behavior wherein C_S decreases with temperature (as noted in section 3.1.1), a fact that has been exploited to rapidly grow large single crystals.[147] Thus, other mechanisms may explain the supersaturation process in this system (e.g., supersaturation may arise as the solvent escapes through the gap between the substrates, as exposure to vacuum is also noted as an important solvent-removal step). Regardless of the mechanism, it is clear that $MAPbX_3$ films of high quality and apparent single-crystalline nature can be prepared using this method.[298] Chen et al.[299] have also explored this process and find that the character of the substrate can have an important impact on the speed of precursor diffusion and hence the growth speed of the

DOI: 10.1021/acs.chemrev.8b00318
Chem. Rev. 2019, 119, 3193−3295

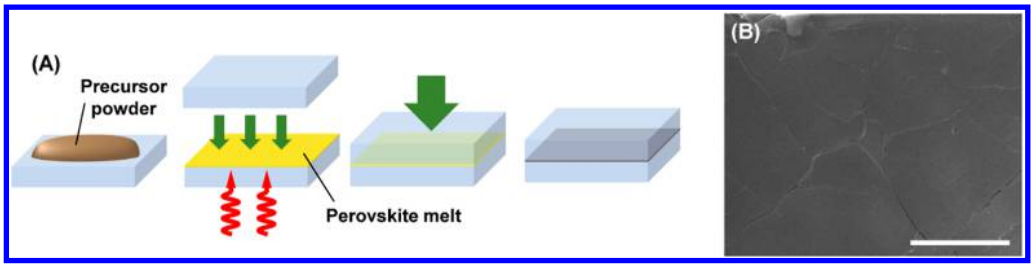

Figure 26. (A) Melt-processing technique: perovskite or unreacted precursor powder is placed on a substrate; the substrate is heated to melt the powder and is capped by a superstrate; the sandwich structure is cooled, with possible application of pressure; the melt resolidifies upon cooling, leaving a perovskite film that fuses the sub- and superstrates. (B) Microstructure of (β-Me-PEA)$_2$PbI$_4$ thin film deposited by melt-processing (scale bar: 50 μm), showing grains that appear to be extremely large yet remain compact. Reproduced from ref 300. Copyright 2017 American Chemical Society.

crystals. Since the available reservoir of precursors within the capillary is severely limited by the constrained volume, it is necessary to maintain a high concentration near the crystal as it grows, or local depletion of the precursors may cause the perovskite crystals to nucleate in many places instead of one, yielding a polycrystalline film. To avoid this problem, the authors used hydrophobic poly(bis(4-phenyl)(2,4,6-trimethylphenyl))amine (PTAA)-coated ITO substrates on which the solution does not easily wet. Thus, drag on the precursor species caused by interaction with the substrate can be avoided, and solution uptake speed within the PTAA-bounded capillary is increased more than a hundred-fold relative to a glass-bounded (i.e., wetting) capillary. In this study, crystallization was achieved by placing the substrates on a hot plate at 100−120 °C after infiltration of the MAPbI$_3$/GBL solution, causing supersaturation by the inverse solubility mechanism described above. High-quality nominally single-crystal thin films could also be obtained in this manner, demonstrating high hole and electron mobilities and carrier diffusion lengths well over 10 μm, as well as high PV performance.[299]

4.1.10. Melt-Processing. While not yet demonstrated for 3D perovskites, a melt processing film deposition approach has been successful for 2D systems, wherein the perovskite precursors are melted into the liquid state and laminated onto a substrate by pressing with a heated or unheated superstrate such as polyimide or glass (Figure 26A). Here, the melt can be considered as a precursor solution with 100 wt % concentration, and therefore, the pinholes or voids, which frequently occur during conventional solution crystallization due to the depletion of the precursor ions during Volmer−Weber growth of a polycrystalline perovskite film (see section 3.1.1.2), will be avoided. Mitzi et al.[20,301] first demonstrated that tuning of the organic cation [modified versions of the PEA$^+$ or naphthylethylammonium ($C_{10}H_7C_2H_4NH_3^+$ = NEA$^+$) cations] in layered Sn-based systems could cause the melting transitions to occur at temperatures below those associated with appreciable decomposition. Of the compounds studied, substitutions of functional groups (e.g., halogen atoms or methyl groups) at positions close to the organic cation ammonium tethering group were found to be most effective at reducing the melting temperature, possibly due to steric effects on bonding in the inorganic framework.[20] Remarkably, the melting temperature could be tuned by ∼100 °C by the substitution of different PEA-derived organic cations within the SnI$_4^{2-}$-based layered perovskites. Melt-processed (PEA)$_2$SnI$_4$ films were integrated into transistors, which displayed superior field-effect mobilities to those prepared using spin-cast active layers, presumably as a result of the larger apparent grain size (on the order of 1−10 μm) provided by the melt-processed films.[20] This improvement in apparent grain size can be considered a consequence of the reduced competition between decomposition and grain growth at higher temperatures, allowing an increase in the grain coarsening rate constant K_S (eq 26) without breaking down the perovskite. Melt-processing carries an additional advantage in that the lamination process is self-encapsulating, since the top superstrate acts as a moisture and oxygen barrier that protects the sensitive perovskite layer from the environment. More recently, Li et al.[300] have demonstrated that, although melting of 2D layered (PEA)$_2$PbI$_4$-based perovskites occurs at higher temperature than the corresponding Sn-based systems, tuning of functional groups on the PEA cation can reduce the melting temperature enough to avoid significant decomposition during the processing, yielding apparently large, compact, flat grains extending over several tens of microns (Figure 26B). An early report on Ge-based hybrid perovskites also points to the fact that Ge-based systems melt at a lower temperature than either the Pb-based or Sn-based analogs, possibly pointing the way to further exploration of these compounds.[302] While there are as yet few reports using this process, it shows great potential, both for its simplicity (e.g., absence of solvents) and the inherent protection that the lamination process affords. A significant drawback, however, is that its utility currently seems to be limited to the layered systems, as conventional 3D perovskites (at least those based on Sn and Pb halide frameworks) appear to decompose at temperatures lower than the prospective melting point and, are, therefore, not compatible with this approach.

4.2. "Two-Step" Deposition Approaches

Though the low solubility of lead halides is troublesome in the sense that it limits the number of suitable solvents for typical one-step solution-processing methods, the constrained solubility can be an advantage in that it allows for the development of a wider range of two-step deposition approaches, without fear that the second step will dissolve the underlying lead halide layer. From a manufacturing perspective, two-step methods may be less desirable relative to one-step methods due to their added complexity. However, they also offer finer control over the deposition. Two-step deposition methods have enjoyed widespread success in all stages of the development of PSCs and have been employed in the fabrication of some of the highest-efficiency PSCs yet reported.[28] The combinatorial possibilities afforded by two-step deposition processes are too numerous to list. However, all of these methods rely on essentially the same steps: first, a

DOI: 10.1021/acs.chemrev.8b00318
Chem. Rev. 2019, 119, 3193−3295

metal precursor (usually a Pb-based salt, for example, a Pb halide, but occasionally Pb oxides/chalcogenides, or an organic−inorganic adduct of the Pb halide with a solvent) is deposited on the substrate; then, the substrate is exposed to a vapor, liquid, or solid of the organic salt to drive the reaction (involving substantial diffusion) that produces the perovskite (as noted in section 3.2.1), possibly followed by a postanneal to drive off any excess organic salt and better crystallize the material. This section explores how the details of the different two-step methods impact the associated perovskite film morphologies/structures, coupled with associated device impacts.

4.2.1. In Situ Dipping. The two-step method predates the advent of PSC technology by over a decade. In 1998, Liang et al.[199] reported a method for fabricating $MAPbI_3$ films (as well as a variety of 2D Pb- and Sn-based perovskites) in which films of the metal iodides were first formed either by spin-coating from a saturated methanol solution or by thermal evaporation. These films were then dipped into a solution of the organic ammonium iodide (isopropanol and MAI for $MAPbI_3$, isopropanol/toluene and butylammonium or phenethylammonium iodide for the most common 2D perovskites), during which in situ formation of the perovskite occurs. While the 2D Pb-halide perovskites formed completely within minutes, 3D $MAPbI_3$ films produced by this method required several hours for complete reaction, most likely because 3D systems lack the van der Waals gap of the 2D structures that facilitates cation/anion diffusion.[199] Reaction in the organic-cation-containing solution leads to substantial apparent grain growth for the 2D systems, although this also potentially leads to increased surface roughness.[199] Besides the kinetics of transformation, a main challenge associated with the conversion of planar PbI_2 films to perovskite is the transformation of a dense layered structure to a less dense 3D structure (in the case of $MAPbI_3$ formation), as noted in section 3.2.2. Lateral pinning of the grains forces the perovskite to grow vertically, inducing strain that can break them into smaller crystallites.[202]

Using a mesoporous rather than a planar architecture can accelerate the Pb halide-to-perovskite conversion significantly. The two-step dip method was applied by Burschka et al.[165] in 2013 to form $MAPbI_3$ PSCs in which the perovskite completely infiltrates within the mesoporous TiO_2 scaffold. The scaffold appears to significantly aid the reaction between PbI_2 and MAI, as a 20 second dip in the MAI solution produced a PSC with 15% PCE, at the time a significant milestone for not only PSCs but also organic, dye-sensitized, and solution-processed solar cells.[165] The enhanced kinetics of this process may be related to the nanoscaled size of the PbI_2 grains, which are grown within a confined mesoporous TiO_2 environment. Per the observations of Ummadisingu and Grätzel,[176] transformation of the PbI_2 crystallites proceeds from edges and grain boundaries. Thus, the higher surface area-to-volume ratio of the nanosized grains should allow the reaction to complete more rapidly than for the larger, denser PbI_2 crystallites in a planar film. The reaction may also be aided by the high density of perovskite grain boundaries and perovskite/TiO_2 interfaces within the mesoporous layer, given the tendency of grain boundaries to act as "highways" for the ingress of external species, as noted in section 3.4. In the context of eq 22, use of the mesoporous as opposed to a planar PbI_2 layer increases the effective diffusivity (rate constant K_4), reducing the conversion time needed to achieve a given film thickness. It is notable, however, that some PbI_2 within the mesoporous layer remains inaccessible to conversion. This phenomenon may arise where the local porosity of the scaffold is particularly low. In such a case, the PbI_2 precursor solution might more easily penetrate into these regions than MAI, as the former moves through the scaffold in the liquid state while the latter transports in the solid state, in which diffusion proceeds much more slowly. Ummadisingu and Grätzel[176] note also that excessively long conversion time promotes Ostwald ripening of the perovskite grains, which leads to larger crystallites but compromises surface coverage. Obtaining optimal transformation of the PbI_2 film can present a substantial challenge, as the best achievable grain structure produced by this method may still contain some unreacted precursor. Note, however, that remnant PbI_2 may be beneficial if properly distributed, as discussed in section 6.1.1.

While use of the mesoporous architecture can speed up the transformation of the initial Pb halide layer, the formation of a $MAPbI_3$ crust or capping layer on the film surface can impede further reaction.[303] This problem may be avoided by dispensing with the capping layer altogether. The in situ dipping method may also be used to produce all-mesoporous cells similar to those discussed in section 4.1.5, wherein a PbI_2 solution is drop-cast into the scaffold, followed by the immersion of the substrate into a MAI/isopropanol solution as above.[281,304] These methods offer similar device performance (∼15%) to both the partially mesoporous cells of Burschka et al.[165] Because of the extended times required for full conversion to perovskite while immersed in the MAI solution (for 3D structures), such methods are less suitable for either mesoporous devices using a capping layer above the perovskite-infiltrated scaffold or for planar PSCs.

An alternative to relying on a mesoporous oxide is to introduce porosity into the planar lead halide film. Not only do the pores more freely admit the organic salt, but they also allow the volume expansion of the film without buildup of strain, as noted in section 3.2.2. Such layers may be fabricated in a variety of ways. Liu et al.[205] found that, by keeping spin-cast PbI_2 films wet for several minutes after spin-coating with the remnant DMF solvent, Ostwald ripening of the PbI_2 crystallites could lead to large crystals with more void space between the grains. Growth of the grains could be terminated by annealing the films to drive off the solvent. Liu et al.[205] determined that the porosity of the PbI_2 films (estimated from SEM images) could increase 5-fold, from 3.1 to 15.8%, over the course of a 7 min aging step. The use of the porous PbI_2 layer over the dense one significantly advances the transformation to perovskite, with increasing porosity leading to reduced PbI_2 residue and enhanced light absorption of the final perovskite film, as well as enhanced PCE of PSCs prepared using the above films (although diminishing returns were obtained for aging longer than 7 min).[205] Alternatively, the inclusion of additives such as 4-*tert*-butylpyridine, which are relatively stable at room temperature but easily driven off by a mild anneal, can be incorporated into the PbI_2 precursor solution.[206] After the anneal, these additives leave behind void spaces that lead to a porous layer. As in the previous report, perovskite films prepared from the porous PbI_2 films transform much more rapidly and completely than those prepared from compact PbI_2 layers, as determined by XRD and UV−vis measurements.[206] Besides the porosity, the mass transport of organic ammonium iodides into PbI_2 crystallites is also affected by the crystallinity. In a study by Zhou et al.,[305] PbI_2 films with controlled crystallinity and porosity are

DOI: 10.1021/acs.chemrev.8b00318
Chem. Rev. 2019, 119, 3193−3295

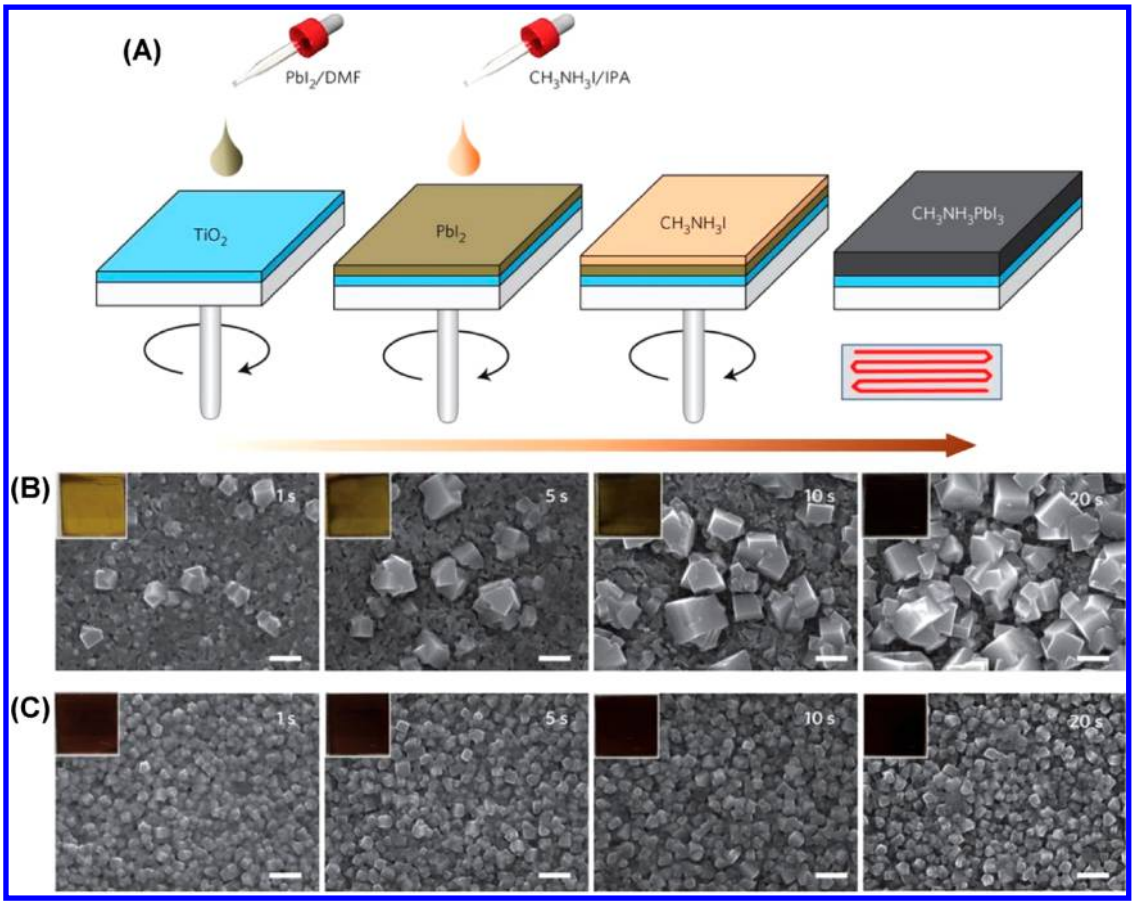

Figure 27. (A) "Two-step" spin-coating process, shown schematically for the deposition of $MAPbI_3$. (B and C) Dependence of $MAPbI_3$ prepared by the two-step spin-coating process on loading time (i.e., the length of time the solution is left on the substrate prior to starting the spin cycles) and concentration of the MAI precursor solution, shown in SEM images; insets: photographs of films used for SEM. Lower MAI concentration (panel B, 0.038 M) enables the formation of large cubelike grains whose density can be increased for longer loading times; higher concentration (panel C, 0.063 M) leads to denser, smaller grains whose distribution is less sensitive to loading time. Reprinted with permission from ref 306. Copyright 2014 Macmillan Publishers Ltd.

prepared, and low-crystallinity, porous PbI_2 allows the most facile formation of phase-pure perovskite.

4.2.2. Interdiffusion of Stacked Precursor Layers. Although increasing the temperature of the in situ dipping process might improve the rate of transformation of PbI_2 to perovskite (per the Arrhenius dependence of the diffusion rate constant K_4 introduced in eq 22), adverse competing processes such as redissolution of the perovskite might complicate the process. This problem can be avoided by introducing the organic halide in the solid rather than the solution phase, so that reaction temperatures may be increased without solvent-aided decomposition. As a result, the perovskite grown from the solid-state precursor reaction will show more controlled morphology, mimicking the overall morphology of the predeposited PbI_2 film. In this regard, Xiao et al.[200] introduced an alternative two-step process, wherein PbI_2 and MAI layers are sequentially spin-cast onto an ITO/poly(3,4-ethylenedioxythiophene):poly(styrenesulfonate) (PEDOT:PSS) substrate then annealed for an hour or more to interdiffuse and react the precursors. This method led to a uniform and compact microstructure, though still apparently possessing smaller grains and performance comparable to the dipping-processed mesoporous cells reported by Burschka et al.,[165] with the added benefit of low hysteresis and high FF (in some cases exceeding 80%).[200]

Note that the rapidity of the reaction between the perovskite precursors entails that the dynamics of the dip-coating process remain relevant to the two-step spin-coating process. The time window or "loading time" between deposition of the organic salt solution on the PbI_2-coated substrate and starting the spin recipe essentially duplicates the conditions of dip-coating. The parameters in this step can therefore be important variables that control the final film morphology. Im et al.[306] investigated the effects of the concentration and loading time of the MAI solution, finding that longer loading times at lower MAI concentrations produced a capping layer of perovskite cuboids in the final film (Figure 27). The geometry of these cuboids is important for the performance of the resulting PSCs. Larger cuboids are associated with lower MAI concentration (0.038 M), presumably resulting from a lower density of seed crystals and result in both enhanced light absorption near the band edge and higher EQE at red and infrared wavelengths in PSCs prepared using these films. These improvements come at some slight cost to V_{OC}, possibly due to the increased roughness of the large cuboids, which may lead to shunt paths through the top layers. Conversely, a higher MAI concentration (0.063 M) results in much smaller but more tightly packed cuboids with inferior light absorption and corresponding reductions in device performance parameters, particularly J_{SC} and *FF*. The best device in this study, with PCE of 17%, was produced using

DOI: 10.1021/acs.chemrev.8b00318
Chem. Rev. 2019, 119, 3193−3295

the lower MAI concentration, despite the slight loss in V_{OC} relative to the intermediate concentration.[306]

Like the in situ dipping method, the two-step spin-coating method can be hampered by the challenges of diffusing the organic salt into a dense, compact PbI_2 film and managing its resulting expansion. Likewise, these challenges can be overcome by similar techniques that reduce the average or effective density of the precursor film. Further improvements to the two-step process were realized in the report of Yang et al.,[27] through the introduction of an "intramolecular exchange" process, wherein a Lewis adduct PbI_2·DMSO solid film is deposited as the first step instead of PbI_2, followed by spin-coating of a solution of the organic ammonium halides MAX (for the highest-performing cell, a mixture of FAI and MABr) and thereafter annealing. MAX thus displaces the solvent molecules in the adduct, forming the perovskite (as explored in section 3.2.5).[27] The resultant films show improved apparent grain size but maintain the compact grain structure relative to those produced by the more conventional two-step method, in which the initial film consists of PbI_2 rather than the PbI_2-DMSO complex. The resulting PSCs showed exceptional performance, leading to the first certified PCE of a PSC above 20%.[27]

4.2.3. Vapor-Assisted Solution Processing. As noted in section 3.2, the organic ammonium halide precursor may be introduced by liquid-, solid-, or vapor-based methods. In all of these methods, the perovskite most probably nucleates on the surface of the solid precursor film and then propagates inward. An early report made use of a vapor-assisted solution process (VASP), in which PbI_2 films deposited by spin-coating were subjected to MAI vapor by sprinkling MAI powder around the films in a capped Petri dish and heating the container at 150 °C (Figure 28A).[201] The VASP method creates a solid−vapor reaction interface between precursors, resulting in fewer heterogeneous nucleation sites that eventually grow into large apparent perovskite grains while retaining the original smooth PbI_2 film morphology (Figure 28B). This process leads to films with compact grains spanning the full film thickness, and what was at the time the highest PCE for a planar PSC, 12.1%. A notable drawback, however, is that VASP is a sluggish process, requiring 4 h for complete reaction between the PbI_2 underlayer and MAI.[201] Li et al.[308] conducted the same process at low pressure (∼0.3 Torr), allowing the conversion of PbI_2 (and $PbCl_2$) to take place at lower temperatures and shorter times (120 °C for 2 h) and yielding devices with higher PCE ∼16%, despite the final films appearing to have smaller grains than those in the initial report. Successive reports have yielded similar film morphologies and performance levels for a variety of perovskite compositions, including those with mixed halides and mixed organic cations.[307,309]

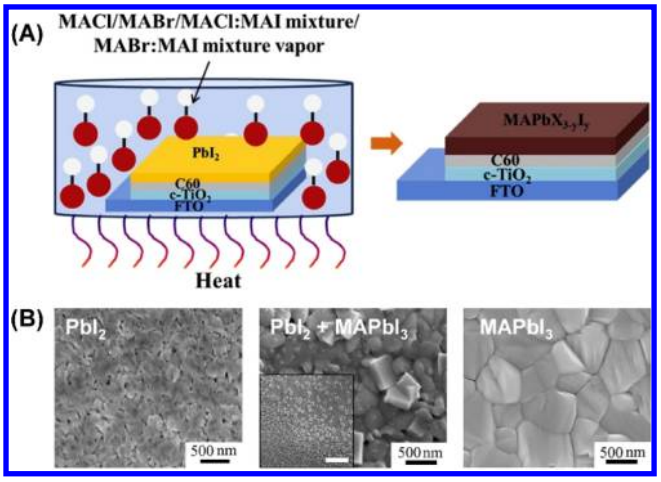

Figure 28. Vapor-assisted solution processing (VASP) of $MAPbI_3$ perovskite. (A) Schematic of the VASP process. Reprinted with permission from ref 307. Copyright 2017 Elsevier. Morphology of the transformed thin film at different stages of the VASP process (inset: wider view with 3 μm scale bar). (B) Adapted from ref 201. Copyright 2014 American Chemical Society.

More traditional vapor-based methods have also been employed to deposit the organic component. In 2014, Leyden et al.[310] demonstrated the use of a tubular reactor, where N_2 gas at 100 Pa carried MAI vapor from the hot zone (at 185 °C) onto thermally evaporated $PbCl_2$ films in a colder zone at a nominal temperature of 130 °C (actual temperature 160−170 °C), where it reacts to form perovskite with smooth, compact morphology. The authors observed that substrate temperature represents a particularly important processing parameter—i.e., extending above 170 °C leads to conversion of $PbCl_2$ films to PbI_2 with little retention of organic material, while falling below 145 °C leads to films that are unstable in air, rapidly turning transparent. This latter effect is plausibly due to accumulation of excess MAI on the films, which is hygroscopic and may promote the formation of MAI-rich hydrates when exposed to moisture in air. The best-performing cell in this report reached almost 12% PCE, although it also exhibited considerable hysteresis.[310] Subsequent work has explored other compositions, such as $FAPbI_3$[311,312] and $MAPbBr_3$,[313] the latter having been processed into LEDs with luminance above 500 cd/m^2. Yin et al.[314] have demonstrated that low pressures and inert carrier gases are not necessary for the production of high-PCE PSCs, using a simple reactor consisting of a glass tube connected to a heat gun with programmable temperature and flow rate. In this method, heated air from the gun sweeps across MAI powder, carrying it to a PbI_2 film further down the tube. The PSCs prepared using this method reached 18.9% PCE.

4.2.4. Sequential Vapor Deposition. Although single- and dual-source coevaporation are gaining ground as viable methods for the production of high-quality perovskite films, organic ammonium halides have proven difficult to control when treated as a normal evaporation point source,[285] making it challenging to match to the lead halide deposition rate (as noted in section 4.1.6). Nevertheless, an early report[285] of sequential evaporation using brute-force evaporation of the MAI onto heated $PbCl_2$-coated substrates (held at 65, 75, or 85 °C) at a constant source temperature of 85 °C, aided by a postanneal in vacuum to drive off excess MAI, was able to reach parity in performance with contemporary coevaporated cells,[193] along with comparable morphology. In this study, 75 °C was found to be the optimal substrate temperature, as lower temperature led to incomplete conversion of the underlying $PbCl_2$ layer, while higher temperature led to poor crystallinity.[285] In a later report,[213] the organic ammonium halide was treated as a static vapor in the chamber rather than a point source, and deposition conditions were controlled by heating the entire chamber to 75 °C and varying the pressure via a gate valve connecting the chamber to the vacuum pump (Figure 29A). Different pressures yielded considerably different films (Figure 29, panels B−E): at 10^{-5} Torr, the initial lead halide film did not completely react, and at 10^{-4} Torr, perovskite

DOI: 10.1021/acs.chemrev.8b00318
Chem. Rev. 2019, 119, 3193−3295

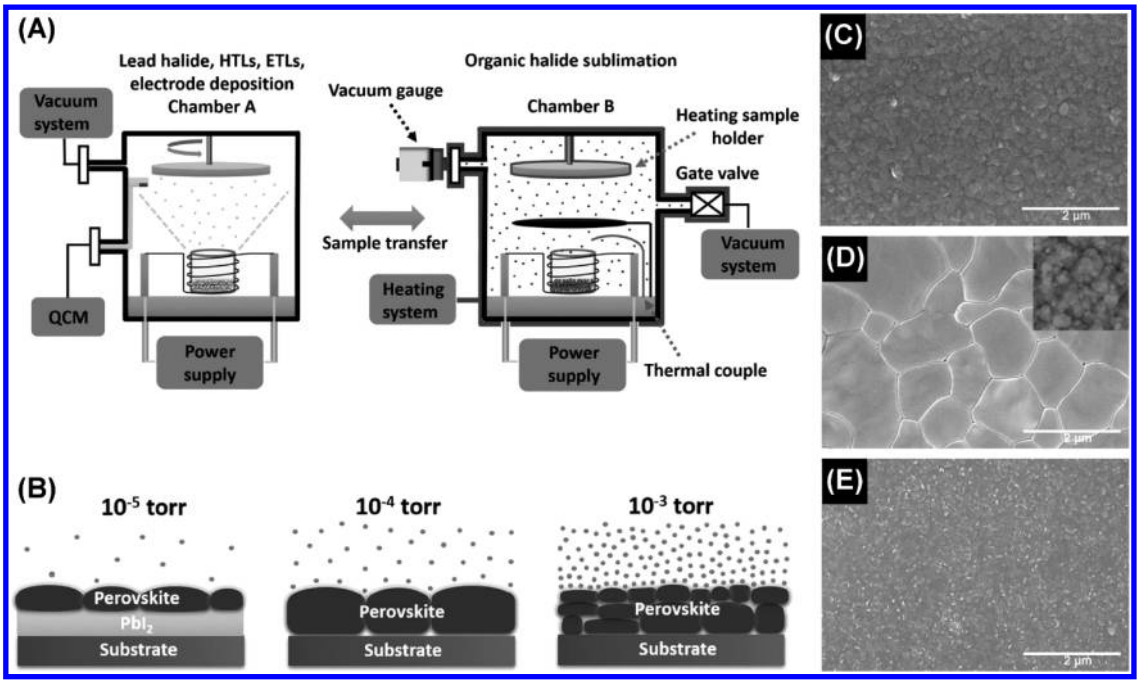

Figure 29. (A) Schematic illustration of $MAPbI_3$ deposition by sequential thermal evaporation; (B) schematic illustration and top-view SEM images (C−E) of the effect of MAI pressure on apparent grain size during the second step: (C) at 10^{-5} Torr, PbI_2 does not fully react; (D) at 10^{-4} Torr, substantial grain growth occurs; and (E) at 10^{-3} Torr, excessively high flux of MAI leads to small grains, possibly as a result of rapid nucleation. Reprinted with permission from ref 213. Copyright 2016 Wiley-VCH.

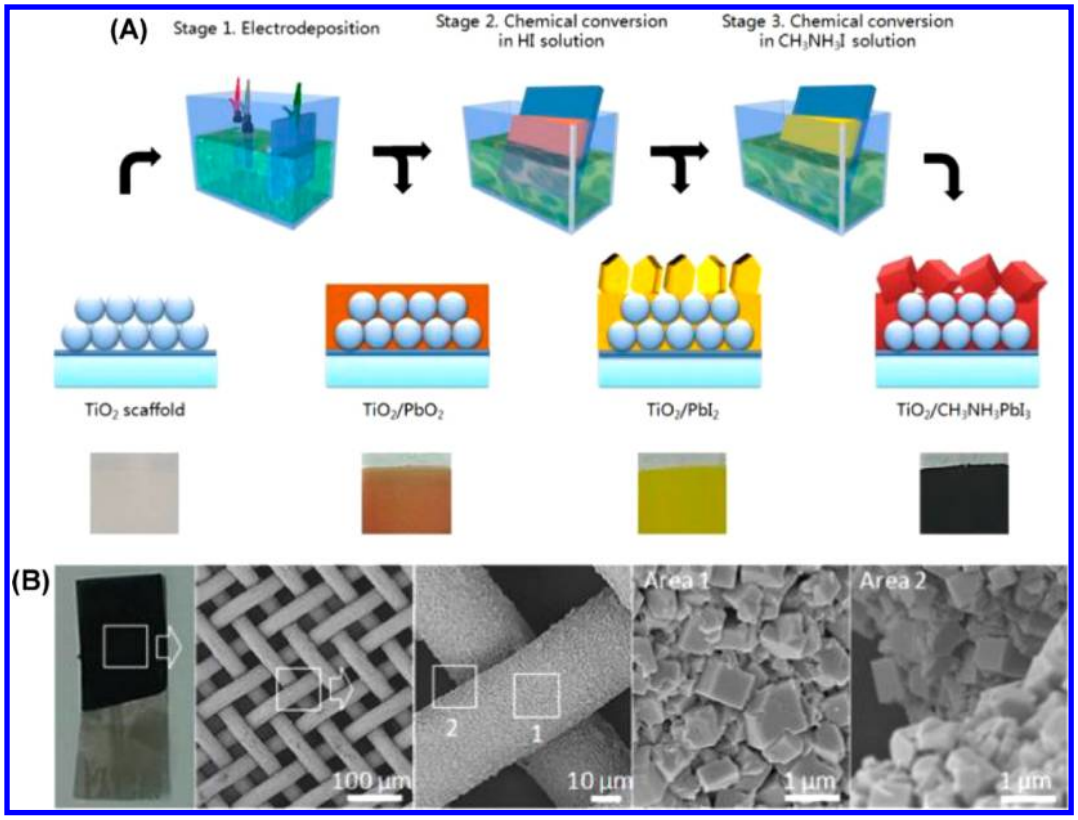

Figure 30. (A) (Electro)chemical bath deposition process: a B-metal-containing precursor BY_n is deposited electrochemically or chemically onto the substrate; optionally, the B-metal precursor is converted into the metal halide BX_2; and finally, the B-metal precursor is immersed in a solution of AX, which diffuses into and reacts with the film, forming the perovskite. (B) Perovskite films fabricated on stainless steel mesh by electro/chemical bath deposition of the precursors display conformal coating of the substrate and cuboidal grains. Reprinted with permission from ref 316. Copyright 2015 Elsevier.

DOI: 10.1021/acs.chemrev.8b00318
Chem. Rev. 2019, 119, 3193−3295

grains whose apparent lateral size far exceeded their thickness were obtained; at 10^{-3} Torr, the perovskite grains appeared to be much smaller, perhaps indicating that the high flux of MAI caused too rapid nucleation of the perovskite grains.[213]

While rapid nucleation is generally preferred for solution deposition methods because it ensures uniform film coverage on the substrate, favoring growth over nucleation may be more helpful for sequential vapor deposition, because the initial lead halide film (solid matrix for the nucleation of perovskite) is already compact and uniform. Therefore, it may become more important to focus on grain growth strategies, since the films will most probably conserve their morphology as they convert from the pure lead halide to perovskite (although a highly compact PbI_2 film may lead to undesirable strain as it transforms to perovskite, as discussed in section 3.2.2). Unsurprisingly, devices using the apparently large-grained films prepared at 10^{-4} Torr outperformed those prepared at 10^{-3} Torr and achieved a stabilized PCE of 17.5%.[213] Subsequent tailoring of the absorber/ETL interface enabled improvement of the stabilized PCE of such devices to 18.7%, a value among the highest for PSCs using an absorber prepared solely by evaporation, with the additional distinction of virtually negligible hysteresis.[315] This process, however, does possess the characteristic drawback of two-step methods in that the deposition of the absorber is a slow process, taking place over a couple hours.

4.2.5. Electro/Chemical Bath Deposition. There are a few reports concerning deposition of perovskite by the versatile and scalable methods of chemical or electrochemical bath deposition. Chen et al.[316] first fabricated PbO_2 films on mesoporous TiO_2 scaffolds by electrodeposition, then converted the film to PbI_2 by immersion in a solution of HI in ethanol, and finally to $MAPbI_3$ by immersion of the PbI_2 films in MAI/isopropanol solution (Figure 30A). An intriguing aspect of this work is that the PbI_2 intermediate film does not appear to favor the crystallographic orientation with the (00*l*) planes lying parallel to the substrate, and SEM images confirm that the flakelike crystallites stand on end rather than lying flat, an unusual behavior for this layered material. The authors explain this phenomenon by positing that growth of the PbI_2 crystallites is most favorable along the basal plane rather than perpendicular to it, as well as in directions unconstrained by neighboring crystallites, resulting in fastest growth perpendicular to the substrate. Larger PbI_2 crystals are produced by more dilute hydriodic acid solutions; the size of the PbI_2 grains appears to translate to those of the final $MAPbI_3$ grains. The $MAPbI_3$ films themselves appear to form a jumbled network of cuboids that appear to be far too rough for conventional film devices, yet the authors are able to achieve a surprisingly high PCE > 10%, forsaking an HTL and directly applying a thick carbon electrode to the $MAPbI_3$ film.[316] A further benefit of this approach is that conformal films can be obtained on substrates of arbitrary complexity. Chen et al.[316] illustrate this feature by depositing perovskite on stainless steel mesh (Figure 30B) using the same process, obtaining good coverage and similar perovskite film morphology compared to those deposited on flat substrates.

Koza et al.[317] were able to achieve $MAPbI_3$ films with a similar but more ordered microstructure via a related process, in which the electrodeposited PbO_2 layer was converted directly to $MAPbI_3$ by immersion in a solution of MAI in isopropanol, an intriguing result that emphasizes the reactive nature of MAI. It should, however, be noted that the PbO_2 layer does not fully convert, as evidenced in both XRD patterns as well as SEM images. The authors studied the effects of temperature on this conversion process and found that as the temperature of the MAI solution increased so did the favorability of the tet(110) orientation of the perovskite planes relative to the tet(001) orientation. In either case, the perovskite films prepared by electrodeposition possessed much lower trap densities and higher PL intensities compared to films prepared by spin-coating of a PbI_2 solution, followed by immersion in a MAI solution, suggesting a higher material quality.[317] The Pb precursor may also be deposited by chemical bath deposition and converted thereafter to the perovskite by chemical vapor deposition of MAI, as Luo et al.[318] demonstrated using PbS as the starting film, yielding a final film morphology similar to that produced by other CVD methods. Overall, these methods show promise for the deposition of perovskite films on large and/or irregular surfaces, but they have not yet attracted widespread attention.

4.3. Scalable Processing Methods

While the techniques described above are quick, effective, and relatively reproducible methods of producing PSCs in the laboratory, many are mainly spin-coating-based methods, explored for the purpose of demonstrating solution/vapor/solid chemistries for perovskite deposition and for targeting record-setting small-area PSCs. They are generally unsuitable for direct adoption in large-scale manufacturing (e.g., due to issues of large substrate handling/throughput, film uniformity, and materials usage). As attention has turned from improving the PCE of laboratory PSCs toward upsizing PSC designs to commercial scale, more reports have emerged detailing methods for perovskite deposition that are compatible with high-throughput manufacturing. Many of these methods (notably, doctor blading and inkjet deposition) derive from printing technology. While these methods are ultimately more likely to be adopted for commercial production of PSCs and modules, less attention has been focused on them relative to spin-coating, and the overall state of the art in PCE of the resulting devices is lower. This deficit also attests to the increasing difficulty in producing defect-free films for larger cell size. Nevertheless, recent advances in processes compatible with large-area deposition have demonstrated that achieving reasonable PCE for commercial-scale devices is a realistic goal, limited more by process engineering challenges than by fundamental scientific obstacles.[319] Among the methods considered in this section are doctor-blading, slot-die casting, and spray-coating/inkjet printing.

4.3.1. Doctor-Blading. Doctor-blading, or blade-coating, is a deposition method relying on a similar principle to that of spin-coating (i.e., by forming a thin layer of solution from which the solvent evaporates uniformly, the precursors reach the saturation point and precipitate in an even manner as the film dries). Unlike spin-coating, however, the excess solution is removed by sweeping a blade across the substrate at a precisely fixed height rather than by spinning rapidly. This method is, therefore, ideally suited to roll-to-roll manufacturing, as the solution can first be deposited on a moving substrate and then swept under a stationary blade. Early attempts at doctor-blading led to films/devices that suffered from discontinuous morphology, similar to that observed for spin-cast films from analogous Cl-containing precursor solutions (further discussed in section 6.1.3). The blade-coated cells performed better compared to spin-cast cells deposited from the same solution

DOI: 10.1021/acs.chemrev.8b00318
Chem. Rev. 2019, 119, 3193−3295

(except for the concentration) when fabricated in ambient atmosphere.[320,321] These cells are still susceptible to degradation in the ambient environment, however, and improve in performance as the humidity during fabrication is reduced, presumably as a result of improved coverage and continuity of the films. The authors attributed the difference between the spin-cast and doctor-bladed cells to the larger and more densely packed domains in the latter, which would therefore more effectively resist penetration of moisture and oxygen.

A more recent report employs doctor blading of a stoichiometric solution of $MAPbI_3$ in DMF over a heated substrate (at 100−160 °C) (similar to the hot-casting approach pioneered by Nie et al.[258] for the spin-cast perovskites discussed in section 4.1.1) to produce highly iridescent and colorful perovskite films.[263] While the PCE of these cells (∼12%) underperforms state-of-the-art spin-cast cells, this process provides some useful insight into the effect of the heated substrate on the perovskite film growth. The microstructure of the perovskite film produced by this method is composed of features on several different scales: first, an arrangement of domains ∼10−50 μm in scale, which superficially resemble grains but are distinguishable from true grains by their substructure; within these domains, an arrangement of equally spaced concentric rings, forming a circular Bragg grating, and within the rings themselves, nanocrystalline grains apparently ∼500 nm in size (the larger-scale domains and rings are visible in Figure 21E). Each feature is attributed to a distinct process. The small grains are produced by the familiar process of nucleation and growth, assumed to occur homogeneously within the solution as the blade sweeps across the substrate. The large domains arise from Rayleigh-Bénard convection induced by the high temperature gradient between the hot substrate and the ambient surface of the solution, generating convection cells whose junctions form the boundaries between the domains in the final film. Finally, the rings are formed by a variation of the "coffee-ring" effect,[322] wherein the solution is presumed to dry from the edge of each convection cell inward. As the solution retracts, deposited material accumulates at the edge of each solution droplet, where the solution is pinned until the surface tension generated in the drying droplet is sufficient to break the edge free and reestablish the equilibrium contact angle. This process repeats until the solvent is consumed, accounting for the concentricity and periodic spacing of the rings. These rings also explain the iridescence of the films, since they act as a reflection grating. Though this feature may not be particularly useful for PV or LEDs, it is a useful example of a solution-processed photonic microstructure, which may find application in other technologies (e.g., in distributed feedback lasers), wherein the use of a circular Bragg grating can symmetrize the output beam but can be expensive to fabricate due to the lithographic techniques involved.[323] Here, the prospective lasing material and the grating are one and the same and may be fabricated quickly, in a single step.

Improvements in doctor-blading of the perovskite have been driven by careful control over the evaporation of the solvent. Yang et al.[277] applied a combination of doctor-blading with antisolvent/solvent extraction and investigated the impact of the solvent on the optimal time span between the blade-coating and antisolvent immersion steps. By analogy to solvent engineering, a small processing window exists in which the wet film must be exposed to the antisolvent in order to obtain good absorber morphology. Solvents with lower vapor pressure, such as a mixture of DMF and NMP, can extend this window substantially (on the order of minutes, compared to seconds for the pure DMF solvent) and thus enable greater resilience against process variation. Addition of excess MACl to the precursor aids apparent grain growth and film uniformity, ultimately leading to small-area (0.12 cm^2) device PCE of above 19%, large-area (1.2 cm^2) device PCE of over 17%, and 4-cell module (total area 12.6 cm^2) PCE of over 13%.[277] Further improvements were reported by Deng et al.,[324] who observed that, although high-quality $MAPbI_3$ films could be obtained by blade-coating using slow coating speeds where film crystallization is governed by solvent evaporation at the meniscus formed between the blade and substrate, at practical coating speeds (20 mm/s or more), film formation falls within the Landau-Levich regime, in which the film emerges from underneath the blade still wet and solution dynamics within the wet film become important. As perovskite islands crystallize, the surrounding solution is attracted to them, resulting in depletion of solute in the regions between the first-forming islands and consequently a discontinuous morphology and highly uneven thickness of the final film. The driving force for the flow toward the islands is speculated to be a locally enhanced evaporation rate near the perovskite islands. To counter this effect, Deng et al.[324] added various surfactants (at ∼20 ppm) to the precursor solution, which build up a surface tension gradient as a result of the solution flow inward to the perovskite islands. As the evaporative flows concentrate the surfactant near the perovskite islands, the local surface tension is reduced, driving a Marangoni flow outward that opposes the original motion of the solution, the net result of which is to suppress the net solution flow and the consequent film discontinuity and thickness variation. The most effective surfactant, L-α-phosphatidylcholine, could also improve contact to hydrophobic substrates such as the HTL PTAA. With the use of this technique, small-area (7.5 mm^2) PSCs with PCE over 20% and large-area modules (33.0, 57.6 cm^2) with ∼15% PCE were attained, using a reasonable blading speed of 50 mm/s.

4.3.2. Slot-Die Coating. Slot-die coating (also referred to as slot-casting or slit-casting) is quite similar to doctor-blading but differs in the respect that the precursor solution is dispensed onto the substrate at a precise rate by a die that serves as a print head,[325] rather than being controlled by the position of a blade held above the substrate (though the dispenser may be employed for this purpose). The evaporation rate of the solvent and the crystallization rate of the solutes are thus controlled by the solution flow rate as well as substrate condition and ambient environment (particularly heating, but also whether the ambient atmosphere is stagnant or flowing). If properly tuned, this process is perfect from a material efficiency standpoint, since there is no need to remove excess solution.[325,326] Like spin-casting, slot-die coating of perovskites can proceed in either one or two steps. Schmidt et al.[327] compared the one- and two-step processes for flexible cells, in which all layers were slot-die coated, finding that the one-step process yields devices with higher PCE, although both are relatively mediocre in this respect (4.9 and 2.6% for one- and two-step, respectively). The low performance is most likely at least in part attributable to the high film roughness and apparently small grains, as seen in AFM images. Cotella et al.[328] also found that one-step slot-die coating leads to very rough and discontinuous films when coated onto room-

DOI: 10.1021/acs.chemrev.8b00318
Chem. Rev. 2019, 119, 3193−3295

temperature substrates, but that roughness and coverage could be improved considerably by increasing the substrate temperature to 65 °C, presumably due to increasing the solvent evaporation rate and inducing more rapid nucleation. Morphology could be further improved by subjecting the just-deposited solution to an "air-knife," more rapidly driving off the solvent than natural evaporation and presumably leading to a higher nucleation density by accelerating supersaturation (much as in the gas-quenching process discussed in section 4.1.3). With the use of this process, small-area (0.0625 cm^2) device PCE > 9% was attained.[328]

4.3.3. Meniscus-Assisted Solution Printing. A modified doctor-blading process, referred to by the authors as meniscus-assisted solution printing (MASP), combines elements of both conventional blade-coating and slot-die coating. As in slot-die coating, the perovskite solution is dispensed as a print head sweeps across the substrate. Fine control of the geometry of the die/print head as well as the relative motion between it and the substrate determine the shape of the meniscus that forms between them.[329] At this meniscus, evaporation of the solvent generates a convective flow of solution that transports solute to the contact line between the substrate, solution, and air, where it precipitates to form the perovskite grains. If the substrate speed is too slow, the crystallization front will connect the upper and lower plates. If it is too fast, the perovskite grains will form as by conventional doctor-blading, in this case yielding nonuniform grain structure unsuitable for devices. Proper substrate speed, however, yields a close-packed microstructure and is compatible with $FA_{0.85}MA_{0.15}PbI_{2.55}Br_{0.45}$ PSCs reaching nearly 20%, among the highest to date for perovskite cells via scalable processing methods.[329] A significant drawback, however, is that, for the processing parameters reported (DMSO solvent, 60 °C substrate temperature), the optimal substrate speed is 12 μm/s, which is too slow to be practical for integration in a high-throughput production line.[329] Nevertheless, optimization of the processing parameters, perhaps by adjustment of temperature and/or changing to a lower-boiling-point solvent (such as 2ME[256] or MA/ACN,[257] as discussed in section 4.1.1), might allow for more useful processing speeds. Alternatively, the use of surfactants, as noted in section 4.3.1, can help to avoid the necessity of operating within the evaporation-controlled regime of film formation, allowing faster coating in the Landau-Levich regime.

4.3.4. Soft-Cover Coating. A technique very similar to MASP is "soft-cover deposition" in which a film is deposited by first dropping a solution onto a heated substrate then covering the solution with a flexible sheet (such as polyimide) to spread the solution across the entire substrate.[330] The top sheet is then peeled back in a controlled manner to expose the solution. Thermally driven evaporation of the solvent drives rapid crystallization of the perovskite film, which possesses larger apparent grain size and longer-lived PL than comparable spin-cast films, while maintaining a compact microstructure. Large-area PSCs (1 cm^2) produced via this technique have reached a PCE of >17%, not as high as MASP, but with the benefit of orders of magnitude more rapid processing speed (i.e., the top cover may be exposed at a rate of 5−500 mm/s).[330]

4.3.5. Spray-Coating. Spray-coating, like slot-die coating, offers the promise of coating large-area substrates with minimal wasted material, as well as the potential for precise patterning of perovskite films. For this approach, a perovskite ink or precursor solution is ejected through a nozzle, aerosolizing it. The resulting droplets travel to the substrate, where the solvent evaporates, depositing the perovskite precursors, which may then be annealed to generate the final film. Ideally, droplets are made as small as possible in order to avoid film roughness. For example, piezoelectric transducers may be used to vibrate the nozzle at ultrasonic frequency to generate an ultrafine mist.[331] One of the first reports of PSCs fabricated by ultrasonic spray coating from a DMF solution investigated the effects of substrate temperature, finding that while films coated onto room-temperature substrates had poor surface coverage owing to the formation of flower- or starburst-like structures, increasing the temperature led to much more conformal coverage.[331] While spray-coating can be challenging due to the many variables that must be simultaneously controlled during the process (i.e., substrate temperature, solvent boiling point, droplet size distribution, solution flux), the tunability of this process can also be advantageous. Heo et al.[332] demonstrated that, by properly balancing the evaporation rate of a DMF/GBL solvent on the substrate with replenishment by the spray, the optimal film morphology of compact and connected grains could be obtained. In this process, the incoming solvent partially dissolves and refluxes the already deposited grains, presumably promoting their growth through Ostwald ripening. Commensurate with the improved morphology, the PSCs prepared by this method reach 18% PCE, the highest currently reported for spray-cast cells.

4.3.6. Inkjet Printing. A deposition process closely related to spray-coating is inkjet printing, wherein the solution is ejected through a nozzle as described above, but the resulting jet may be steered carefully (in some cases, drop by drop) in order to achieve precise patterns.[333] There are thus far fewer reports concerning inkjet printing of halide perovskites, but similar considerations appear to apply as in spray-coating (as well as in other deposition methods). Li et al.[334] obtained discontinuous films with large disclike features several tens of micrometers in diameter when printing a 1:1 solution of MAI:PbI_2 in GBL onto mesoporous TiO_2 substrates; however, simultaneously reducing the PbI_2 content relative to MAI and introducing MACl was found to lead to more uniform film coverage. Mathies et al.[335] found that annealing the wet films obtained from printing a solution of $MAPbI_3$ in 7:3 GBL:DMSO (by volume) led to the formation of a discontinuous needlelike morphology, but that exposure to vacuum immediately after deposition could lead to a dense and conformal microstructure. Mathies et al.[335] also investigated effects of droplet spacing and multiple passes of the print head over the substrate, finding that the latter could boost apparent grain size (most likely by Ostwald ripening/refluxing of the grains as noted in the previous section), but that the droplet spacing did not appear to significantly alter the morphology. Liang et al.[336] also found, using a similar solution (but in this case, 4:6 DMSO:GBL by volume), that vacuum exposure was effective at yielding a conformal film and avoiding the formation of a dendritic microstructure. Additionally, apparent grain size could be tuned by modulating the substrate surface properties. While bare TiO_2 led to small grains, increasing the contact angle by evaporating thin layers of C_{60} allowed a substantial boost in the apparent grain size, presumably due to a reduction of the nucleation density as a result of the reduced wettability. However, excessively thick layers of C_{60} led again to smaller grains, through a not well-understood process. Optimizing the C_{60} thickness led to PCE of over 17%,[336] a

DOI: 10.1021/acs.chemrev.8b00318
Chem. Rev. 2019, 119, 3193−3295

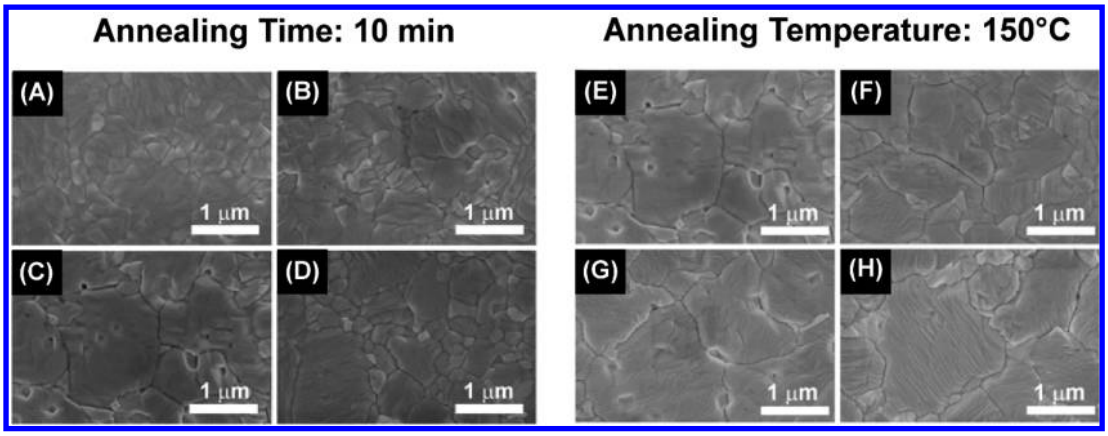

Figure 31. Effect of annealing on the microstructure of $MAPbI_3$ films: (A−D) annealed for 10 min at (A) 110 °C, (B) 130 °C, (C) 150 °C, and (D) 170 °C; (E−H) are annealed at 150 °C for (E) 10, (F) 15, (G) 20, and (H) 25 min. Republished with permission from ref 340. Copyright 2016 Royal Society of Chemistry.

value close to the best spray-coated cell mentioned in the previous section.

4.3.7. Outlook for Commercialization. Although the efficiency of large-area photovoltaic devices and modules still considerably lags that of laboratory-scale devices, recent improvements may provide a path to commercialization. As in the case of small-area devices, most attention thus far has focused on solution-deposition approaches, with much less attention focused on vapor-based deposition. In terms of demonstrated efficiency of modules with high geometric fill factor as well as overall efficiency of large-area devices in general, doctor-blading and related techniques are most advanced, although spray-coating and inkjet printing also appear to be promising.[319] These deposition techniques are all well-suited to established large-scale manufacturing processes and easily adaptable to flexible substrates. It has been noted that vapor-based deposition techniques may also offer attractive options for commercialization, owing to an industrial heritage of established similar technologies such as organic LEDs, reduced dependence on toxic solvents, and the ease of fabricating perovskite top cells on textured silicon bottom cells in multijunction device architectures.[195] However, despite recent advances, vapor-based deposition techniques for large-area PSCs have lagged solution-based techniques considerably in terms of efficiency. While this deficit is likely reflecting the vast difference between the extent of research focus on solution- versus vapor-deposition methods, there are some inherent differences that may continue to hinder the latter. Vapor deposition techniques tend to require more time and capital expense than solution deposition techniques[319,337] and also suffer from difficulty in controlling relative evaporation rates of the precursors. The most efficient and stable PSCs tend to involve two or more cations on the "A" site in the perovskite absorber,[25,26,265,338] in principle requiring fine control over several sources if such compositions are to be prepared by vapor deposition methods. Gil-Escrig et al.[339] have deposited triple-cation $Cs_{0.5}FA_{0.4}MA_{0.1}Pb(I_{0.83}Br_{0.17})_3$ absorbers, obtaining 16% PCE, demonstrating that such pathways may not be completely out of reach. However, the advanced state of efficient, high-throughput solution processes makes them the most likely candidates for commercialization of PSCs or other perovskite devices in the immediate future.

5. POST-DEPOSITION TREATMENTS

As introduced in sections 3 and 4, a key step in many perovskite thin film fabrication methods is a postdeposition treatment that drives the reaction between precursors, removes solvents or additives, and/or improves film morphology. Most frequently, such post-treatments are accomplished by annealing the film at moderate temperatures (hybrid perovskites can generally tolerate no more than 150−160 °C, while the inorganic analogs may be annealed to ∼300 °C) on a hot plate. This feature illustrates a key disadvantage of the soft and unstable nature of the halide perovskites, as common semiconductor processing techniques are unavailable or at least severely constrained by the possibility of decomposition. However, other chemical or physical treatments, many that make use of the facile reactivity of the perovskite, may also be applied that can modify the annealing process, or obviate it entirely. While in section 4 we considered overall film deposition approaches, in this section we explore in more detail the strategies that have been developed for annealing perovskite films or precursor films, as well as other important techniques and processes associated with further treatment and refinement of already-deposited perovskite thin films.

5.1. Annealing

Almost all reports of halide perovskite film fabrication involve an annealing step. For some deposition methods, heat treatments can occur concurrently with the deposition (e.g., vacuum deposition or doctor-blading onto a heated substrate). Postdeposition annealing is particularly important in the context of solution deposition, wherein film formation may be retarded by remnant solvent or other volatile species, necessitating their removal. On the other hand, deposition methods that yield more pure perovskite films may still benefit from a postdeposition anneal by allowing grain coarsening to occur. As discussed in section 3.4, grain growth is driven by an input of thermal energy over an extended period of time, but it is constrained by the onset of perovskite film decomposition. This effect is illustrated in a study by Zhu et al.[340] in which the grains in solvent-engineered perovskite films are coarsened by post-treating with spin-cast MAI and then annealing at various temperatures and durations (similar techniques are explored in section 5.1.4). Figure 31 (panels A−D) depicts the morphological effects of 10 min annealing at 110, 130, 150, and 170 °C after the MAI treatment. Below 170 °C, the

DOI: 10.1021/acs.chemrev.8b00318
Chem. Rev. 2019, 119, 3193−3295

average apparent grain size increases monotonically with temperature, demonstrating the effects of the grain growth process. At 170 °C, the apparent grain size lies between that of the 110 and 130 °C annealed films. At this temperature, grain growth may be compromised by concurrent thermal decomposition of the film. Equivalently, annealing the film at the same temperature but over different time spans yields similar results (Figure 31, panels E−H), with longer durations at 150 °C affording more time for coarsening to proceed and consequently for increased apparent grain size.

5.1.1. Alternatives to Conductive Annealing. Despite its wide use in the perovskite literature, the annealing step is seldom emphasized as a process worthy of description beyond noting its temperature and duration; often, the heat source will not even be specified. While in most cases it can be assumed that a hot plate is used for this purpose, potentially important information is obscured by the terseness of these descriptions. Like spin-coating, hot plate-annealing represents an attractive choice for the perovskite film maker due to its operational simplicity, enabled by inexpensive and ubiquitous laboratory equipment. However, this simplicity masks a complex conductive heat-transfer process dependent on a number of factors, including the hot-plate material (e.g., ceramic vs metal), film substrate (especially its thickness), and any intervening layers between the substrate and perovskite film (e.g., ETL or HTL in PSCs), as well as the nature of the interfaces between each of these components. Also, potentially relevant are concerns of uniformity, resulting from the distribution of heating elements in the plate and migration of "hot spots" as the equipment ages. Moreover, perovskite films are rarely fabricated in a stagnant atmosphere but rather in a circulating glovebox or fume hood with rapidly flowing air, adding a significant convective component to the heat-transfer pathway. The complexity of these heat-transfer modes implies that, while straightforward to accomplish in the laboratory, hot plate-annealing is far removed from the physical ideal of placing the film in equilibrium with a uniform thermal reservoir. Hot plate-annealing is, thus, also similar to spin-coating in the respect that it is largely unsuited for application to large-scale industrial processing due to irreproducibility, as well as difficulties associated with achieving conductive heat transfer from the plate to a moving substrate, as in roll-to-roll manufacturing. It is, therefore, important to consider other annealing mechanisms that may be more easily applied to industrial processes and that rely on other modes of heat transfer.

Zhou et al.[341] directly compared the effects of conductive annealing on a hot plate to those of convective annealing in an oven for $MAPbI_{3-x}Cl_x$ films prepared by one-step spin-coating. Both sets of films were annealed in air at relative humidity ranging from 10 to 90%. The oven-annealed films displayed more uniform coverage and smaller pinholes than the hot plate annealed films at humidity below 50%, but the advantage of oven annealing at 50% RH and above is less clear. Nevertheless, PSCs prepared using the oven-annealed films outperformed those annealed on the hot-plate at all humidity levels, demonstrating that the superior uniformity offered by oven annealing may translate to improved film quality and consistency.[341]

Both conductive and convective thermal annealing processes are not considered practical for large-scale solution production of halide perovskite thin films, especially for roll-to-roll manufacturing processes. In the cases where annealing is performed using ovens or hot plates it takes 5 min to 1 h to remove the solvent fully from perovskite precursor films and complete the crystallization process. Assuming a roll-to-roll process is conducted at the speed of 1 m s^{-1} then a furnace 600 m long will be needed for an annealing duration of 10 min, which is not practical for commercial manufacturing.[344] Furthermore, the thermal annealing steps are expected to add to the energy payback time of PSCs.[345] Therefore, it is necessary to develop alternative methods to replace thermal annealing for efficient/low-cost PSC production.

Radiative or optical annealing methods offer some promise for resolving this issue. Troughton et al.[346] have reported the use of near-infrared radiation (NIR) from a halogen lamp for annealing $MAPbI_3$ precursor solution films (precursor ratio: $MAI:PbCl_2$ = 3:1), which enables rapid formation of the $MAPbI_3$ perovskite thin film within 2.5 s. For comparison, to prepare a phase-pure $MAPbI_3$ film based on the same precursor composition using conventional thermal annealing, a 30 min heat treatment at 100 °C is needed. As shown in Figure 32A, when the film is optically (NIR) annealed, the heating of the sample is attributed not only to energy absorption in the film layer itself but also to the energy absorption in the transparent-conductive-oxide-coated substrate.[347] Thus, NIR annealing works much more efficiently than conventional thermal annealing at promoting ultrafast crystallization of halide perovskite films. Troughton et al.[346] have further fabricated PSCs based on NIR-annealed $MAPbI_3$ perovskite films, achieving a PCE similar to that of PSCs based on thermally annealed $MAPbI_3$ films.

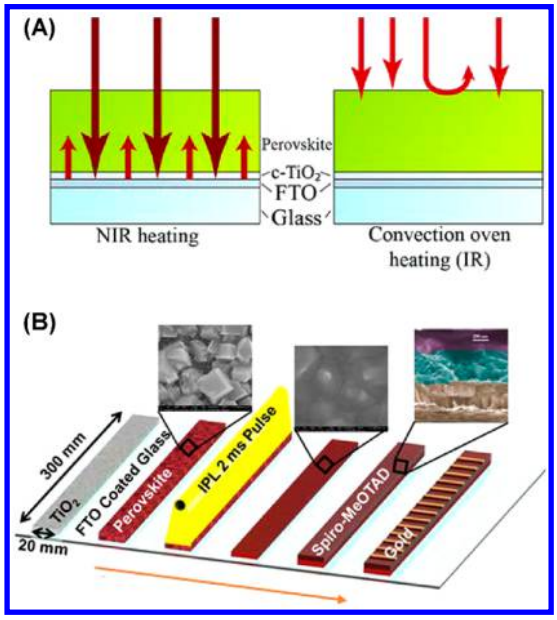

Figure 32. (A) Schematic representation of the heating mechanism of NIR optical annealing of perovskite precursor films compared with that of convective thermal annealing. Adapted with permission from ref 346. Copyright 2016 Royal Society of Chemistry. (B) Schematic representation of the process using pulsed-light to sinter the as-deposited perovskite for fabricating PSCs. Adapted from ref 343. Copyright 2016 The American Chemical Society.

In a later report, Troughton et al.[342] employed a new process of photonic flash-sintering based on xenon flash-bulb emission, which converts freshly spin-coated perovskite precursor thin films (precursor ratio: $MAI:PbCl_2$ = 3:1) to

DOI: 10.1021/acs.chemrev.8b00318
Chem. Rev. 2019, 119, 3193−3295

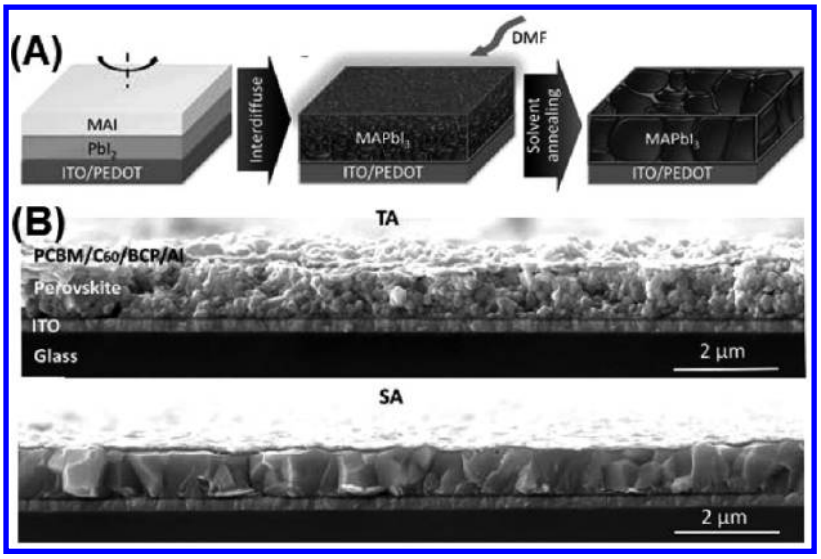

Figure 33. (A) Schematic representation of the solvent annealing method for growing large-grain perovskite thin films. (B) Cross-sectional SEM images showing the larger apparent grain size in the $MAPbI_3$ thin film using solvent annealing (lower) compared with the film using conventional thermal annealing (upper). Reprinted with permission from ref 353. Copyright 2014 Wiley-VCH.

fully crystallized $MAPbI_3$ thin films within a short time period of as little as 1 ms. Most recently, Sanchez et al.[348] have used flash infrared-annealing (FIRA) to process large-area $MAPbI_3$ thin films on glass and plastic substrates without the use of antisolvents, where irradiation durations are as short as 2 s. Lavery et al.[343] have also applied optical annealing to the processing of $MAPbI_3$ perovskite films, using an intense pulsed light source (2000 J of energy in a 2 ms pulse of light generated by an xenon lamp) as the energy source. Here, as shown in Figure 32B, the $MAPbI_3$ thin film was made using a typical two-step dipping method with average apparent grain size of ~200 nm. After the optical sintering step, the average apparent grain size of the $MAPbI_3$ perovskite film increases to ~1 μm, without sacrificing film coverage on the substrate.[343] PSCs made with the incorporation of the optical sintering step show improved PCE, attributed to the reduced apparent grain boundary density as a result of the grain coarsening in the $MAPbI_3$ film.[343]

Pulsed-laser irradiation can also be a tunable source for performing optical annealing. Amendola et al.[349] have found that, by performing pulsed-laser irradiation in a liquid environment, $MAPbI_3$ perovskite nanoparticles can be obtained easily, which confirms the effectiveness of the laser-induced perovskite crystallization. Jeon et al.[350] have presented the crystallization of hybrid perovskite thin films using scanning near-infrared laser irradiation (λ = 1064 nm). By varying the laser irradiation conditions, the morphology and microstructure of $MAPbI_3$ thin films can be widely tuned while maintaining excellent local film uniformity. Hooper et al.[347] showed that photothermal heating of the underlying transparent-conducting substrate is responsible for the generation of thermal energy. As with any scanning irradiation method, the heating is local, leading to lateral thermal gradients. It remains to be seen what effect these gradients have on the uniformity of the films over large areas.

All the above-mentioned studies have focused only on the synthesis of MA-based thin films. While optical/radiative annealing has demonstrated great promise in these reports, there is still a lack of control over the actual temperature conditions employed, making it difficult to gain fundamental insights into the perovskite crystallization processes induced by optical annealing. To improve process control, Pool et al.[344] designed an optical annealing chamber with halogen lamps as the heating source. With the use of this chamber, the temperature can be controlled precisely and relatively easily. The detailed crystallization process of perovskites upon optical annealing is revealed by ex situ or in situ materials characterization. A similar mechanistic study has also been reported by Dou et al.[351] By fully understanding the crystallization kinetics of hybrid perovskites, it has been shown that thin films with optimal microstructures, and thus PSCs with superior PCE, can be achieved. Importantly, Pool et al.[344] have also demonstrated that this method can be amenable to preparing high-quality $FAPbI_3$ thin films, which are technically more challenging to make than $MAPbI_3$ (as discussed further in section 6.2.1.1).

Radiation outside the visible or near-visible portion of the spectrum can also be employed in a similar manner to the above reports. For example, Cao et al.[352] have adopted microwave irradiation to treat the $MAPbI_3$ precursor film at a fixed output power. It has been shown that the microwaves can remove the solvent quickly, inducing rapid crystallization of $MAPbI_3$ thin films with a relatively large apparent grain size of ~400 nm.

5.1.2. Solvent Annealing. Solvent annealing, or more accurately solvent vapor annealing, was previously applied to increase polymer chain mobility in polymer thin films, and it is widely recognized in the field of organic PVs.[354] Originally, in this method, the polymer film is exposed to a solvent atmosphere at room-temperature, causing the polymer to swell. This method has also been found to be very useful for enhancing perovskite film crystallinity and quality and for achieving higher-performance PSCs. Xiao et al.[353] reported the use of solvent annealing for treating $MAPbI_3$ thin films, performed according to the procedure shown in Figure 33A, where a substrate capped with sequentially deposited layers of MAI and PbI_2 is placed on a hot plate, and the solvent vapor is introduced by placing a drop of the solvent on the hot plate. The whole system is covered by a Petri dish to contain the solvent-vapor atmosphere. As shown in the SEM images in

DOI: 10.1021/acs.chemrev.8b00318
Chem. Rev. 2019, 119, 3193−3295

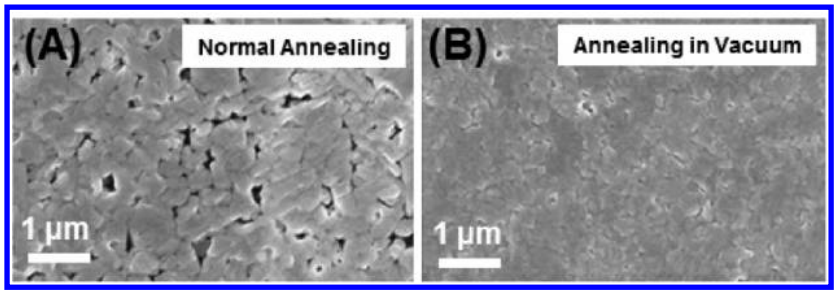

Figure 34. Top-view SEM images showing the morphology of a $MAPbI_3$ film (derived from a precursor composition of $PbCl_2$ and MAI, molar ratio: 1:3) processed with (A) conventional thermal annealing and (B) vacuum-assisted annealing. Adapted from ref 358. Copyright 2015 American Chemical Society.

Figure 33B, the $MAPbI_3$ films annealed in a DMF solvent vapor show significantly higher apparent grain size and crystallinity, compared to films made using normal thermal annealing at the same temperature without the DMF vapor present. As a result, the carrier-diffusion lengths of $MAPbI_3$ thin films are increased to more than 1 μm. While the mechanisms underlying solvent annealing-induced grain growth have not been discussed in detail in this study, it is assumed that the DMF solvent vapor can "soften" the thin film structure (presumably by forming liquid or liquidlike phases at the film surface and at grain boundaries) and allow facile migration of grain boundaries.[353] With consideration of the possible formation of a continuous liquid phase during solvent-vapor annealing, it is likely that the grain growth occurs by the Ostwald ripening process, as described in section 3.4.

Following the report by Xiao et al.,[353] solvent annealing methods using different types of solvent vapors have been tried for preparing large-grain $MAPbI_3$ films. Liu et al.[355] systematically investigated the effect of solvent-vapor type (DMF, GBL, and DMSO) on the grain growth of $MAPbI_3$ thin films, as these are the most commonly used polar aprotic solvents for perovskite precursor solution preparation. The average apparent grain size in the resultant $MAPbI_3$ films is roughly the same for GBL and DMF but much larger for DMSO. This ordering may reflect the trend for the vapor pressure of these solvents at room temperature (GBL: 1.5 Torr; DMF: 2.7 Torr; and DMSO: 0.42 Torr), with the less volatile DMSO presumably able to more readily infiltrate the film and remain in the condensed state while confined. Although DMF is more volatile than GBL, it has a lower Mayer bond order and, thus, its higher propensity to coordinate to Pb balances its increased vapor pressure, perhaps explaining the similarity of the DMF- and GBL-annealed film microstructures. The DMSO solvent, which exhibits the lowest vapor pressure and the strongest coordination power, is expected to have the most obvious interaction with the $MAPbI_3$ perovskite films, and thus results in the largest apparent grain size. On the basis of this correspondence, it is speculated that during the solvent-annealing treatment, the vapor of the polar solvents attacks the films preferably on surfaces and grain boundaries and mediates the grain growth. Besides the commonly used solvents that exhibit high solubility for $MAPbI_3$, alcohol-based solvents (e.g., methanol, ethanol, isopropanol)[356] and mixed solvent systems[357] are also used for improving the solvent annealing approach. Optimizing the solvents for solvent annealing is important for achieving the best films for PSCs and related optoelectronic devices, due to a generally expected trade-off in the microstructural features (e.g., coverage, grain size, surface roughness, grain boundary grooving, pinholes, film−substrate interfaces) in the final films.

Solvent annealing has also been applied to the preparation of large-grain $FAPbI_3$ perovskite thin films. Interestingly, a mechanism that differs from the case of $MAPbI_3$ films is proposed to be responsible for the grain growth. Yadavalli et al.[227] studied the evolution of $FAPbI_3$ films by monitoring the phase and microstructure development of a spin-coated nonperovskite $FAPbI_3$ precursor film upon DMSO solvent vapor annealing. Annealing such a film in the solvent vapor allows the nucleation and grain growth of perovskite $FAPbI_3$ within the nonperovskite $FAPbI_3$ matrix, which finally forms a phase-pure $FAPbI_3$ perovskite thin film with exceptionally large grain size (~5 μm). The presence of DMSO vapor significantly lowers the activation energy barrier for the nonperovskite-to-perovskite $FAPbI_3$ phase transformation. The effect of solvent vapor type on the solvent annealing of $FAPbI_3$ films has not been widely studied, however, making it an interesting research topic for the future.

5.1.3. Vacuum-Assisted Annealing/Drying. Vacuum can be controlled as an additional processing parameter during perovskite precursor thin film annealing, impacting the chemical-conversion kinetics of the reagents. In particular, vacuum may be useful when the excess components in the perovskite precursors are not easily removed through conventional ambient-pressure thermal annealing. Xie et al.[358] have demonstrated the use of vacuum-assisted annealing for synthesizing $MAPbI_3$ films from a precursor mixture of 3:1 MAI:$PbCl_2$. In this combination, $MAPbI_3$ is formed by the reaction $3MAI + PbCl_2 \rightarrow MAPbI_3 + 2MACl$, where the byproduct MACl sublimes at 195 °C. Without the application of vacuum during annealing, MACl cannot be rapidly eliminated from the film, resulting in moderate MACl aggregation. These aggregates induce the formation of small pores in the film after the MACl is fully sublimed during further annealing. Application of vacuum during annealing accelerates the sublimation of MACl, driving the formation reaction of $MAPbI_3$ forward and facilitates crystallization. The temperature during vacuum-assisted annealing also impacts perovskite crystallization. By controlling the vacuum level and annealing temperature, Xie et al.[358] achieved balanced MACl formation and sublimation. The resultant $MAPbI_3$ thin films not only inherit the merits of strong texture and crystallinity from the mixed-precursor (i.e., MAI and $PbCl_2$) approach but also have full coverage on the substrates (Figure 34) and a root-mean-square (RMS) roughness of as low as 9 nm. In this context, the $MAPbI_3$ thin films formed via the vacuum-assisted annealing method may exhibit significantly enhanced optoelectronic properties for PSC operation. It has also been found

DOI: 10.1021/acs.chemrev.8b00318
Chem. Rev. 2019, 119, 3193−3295

that the vacuum may help to completely eliminate the MACl in the $MAPbI_3$ perovskite film, thereby improving the operational stability of devices prepared using such films. Han et al.[15] have demonstrated the use of vacuum-based treatment for removal of both additives as well as solvent. As discussed in more detail in section 6.2.3.2, relatively large additions of MASCN (e.g., 40 mol % excess relative to $MAPbI_3$) appear to enable growth of large grains of $MAPbI_3$, with no postdeposition heat treatment necessary. In this case, the vacuum-treatment removes both the solvent and the excess MASCN (possibly as MA^0 and HSCN gases) from the sample.

Vacuum can also be directly used in the absence of heating to dry the precursor film and crystallize the perovskite when a stoichiometric precursor ratio is used, as noted in section 4.1.1. Gao et al.[359] applied vacuum pumping on a freshly spin-coated precursor thin film derived from a 1:1 MAI:PbI_2 precursor solution in DMF. The vacuum pumping allows for rapid removal of DMF solvent from the precursor films, inducing rapid nucleation of $MAPbI_3$ and resulting in the formation of exceptionally smooth $MAPbI_3$ thin films.[359] In a similar study reported by Li et al.,[255] DMSO was used instead of DMF as the solvent for the deposition of perovskite of nominal "$FA_{0.81}MA_{0.15}PbI_{2.51}Br_{0.45}$" composition, reflecting the stoichiometry of the precursor solution rather than the final film. In this case, after drying the precursor film under vacuum, a uniform solid film [referred to as a Lewis acid−base adduct, probably incorrectly, as discussed in section 3.1.2.1, and perhaps consisting of an FA- and Br-containing analog of $(MA)_2Pb_3I_8{\cdot}2DMSO$] distinct from the expected perovskite phase, is first crystallized. The stronger coordination power of DMSO compared to DMF may be responsible for the observed difference. The perovskite-adduct is then transformed to perovskite during a subsequent thermal annealing step, while the smooth film morphology is retained during the conversion process. By using the vacuum-assisted drying method, Li et al.[255] demonstrated 1 cm^2 PSCs with a certified PCE of 19.6%, which was a record for cells of that size at the time. Li et al.[255] have also shown that this method is versatile for preparing perovskite films over a wide range of other compositions.

5.1.4. MAX (X = I or Cl) Annealing. MAX (X = I or Cl) annealing is a unique processing method developed exclusively for making perovskite thin films, especially $MAPbI_3$. The main purpose of MAX annealing is to create a MA^+-ion-rich environment that facilitates the formation and grain growth of $MAPbI_3$ films. It also raises the ambient chemical potential of volatile MAX, preventing associated film decomposition due to its evolution from the film during annealing. While similar to the two-step spin-coating and VASP processes discussed in sections 4.2.2 and 4.2.3, MAX annealing can also be applied to already formed perovskite films deposited by other processes, as its effects on grain growth and prevention of decomposition are generally applicable. Note also that, for processing $MAPbI_3$ thin films, when MABr annealing is applied, an ion-exchange reaction can occur that leads to the formation of $MAPbI_{3-x}Br_x$ films instead of $MAPbI_3$.[270,360] By contrast, annealing in MACl does not induce significant ion exchange in $MAPbI_3$ films, since Cl does not easily incorporate into the $MAPbI_3$ lattice, as is explained in more detail in section 6.1.3.

The MAX-annealing processing setup is similar to that used in solvent annealing (section 5.1.2) and also to VASP (section 4.2.3). As shown in Figure 35A, the annealing of $MAPbI_3$ perovskite thin films is performed in a closed vessel where

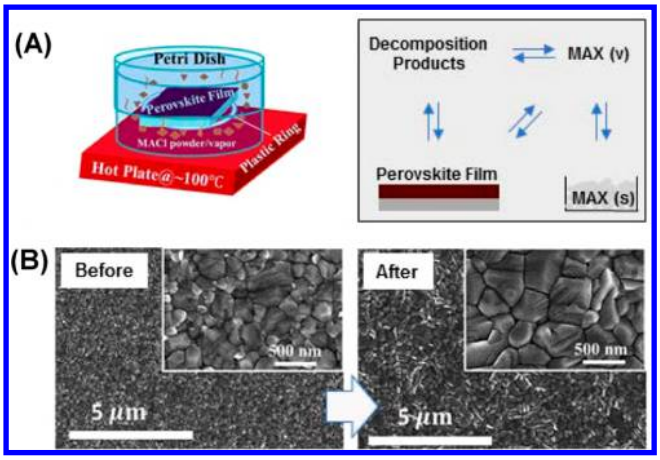

Figure 35. (A) Schematic illustration of the setup for performing MAX (X = Cl or I) annealing and the proposed chemical equilibrium during the MAX annealing process of $MAPbI_3$ films. Adapted from ref 363. Copyright 2015 American Chemical Society. Also adapted with permission from ref 362. Copyright 2017 Royal Society of Chemistry. (B) Top-view SEM images showing the morphology of the $MAPbI_3$ thin film before and after MACl annealing. Adapted with permission from ref 362. Copyright 2017 Royal Society of Chemistry.

MACl (or MAI) powder is also present. When MACl is used, the low sublimation temperature of 195 °C and enthalpy of sublimation (78 kJ mol^{-1}) allows the generation of sufficient MACl partial pressure at a moderate annealing temperature of ∼100 °C.[361,362] The SEM images in Figure 35B show that the $MAPbI_3$ perovskite films processed with the MACl-annealing have increased apparent grain size and reduced apparent grain-boundary density. It is likely that the excess MACl vapor compensates the partial loss of the MA^+ ions during the annealing process, which reduces the formation of typical defects in the thin films such as grain boundaries. In a very similar approach, Tosun et al.[363] have observed that postannealing of $MAPbI_3$ films in a MAI-vapor atmosphere also results in a significant increase in apparent grain size and carrier lifetime. The effect of MAX annealing is consistent with the observed grain growth phenomenon that occurs when excess MAX phases are incorporated in the solution processing of $MAPbI_3$ thin films.[232,277]

MAX-annealing can also be conducted in the solid phase. Here, MAX is simply solution-deposited on the top of the as-fabricated $MAPbI_3$ films as a thin capping layer (very similar to the two-step spin-coating process described in section 4.2.2), followed by thermal annealing. Using solid-MACl annealing, Chen et al.[131] have shown that a thin textured intermediate top-layer forms immediately after the deposition of MACl on top of a regular polycrystalline $MAPbI_3$ film. Upon subsequent thermal annealing, the characteristic texture propagates through the entire $MAPbI_3$ film, resulting in a new $MAPbI_3$ film with a strong orientation favoring tet(110) planes. In addition to texture development, solid-MAX annealing can also induce abnormal grain growth behavior, as reported by Dong et al.[132] After multicycle coating of MAI/MACl blends and annealing, some of the $MAPbI_3$ grains in the thin film exhibit exceptionally large apparent size, up to ∼3 μm. The texture propagation and abnormal grain growth behavior appear to be related to both MA^+ and Cl^- ions; although the exact mechanisms are still unclear, they may relate to the preferential orientation of perovskite films grown from Cl-containing precursors, as discussed further in section 6.1.3. MAX-

DOI: 10.1021/acs.chemrev.8b00318
Chem. Rev. 2019, 119, 3193−3295

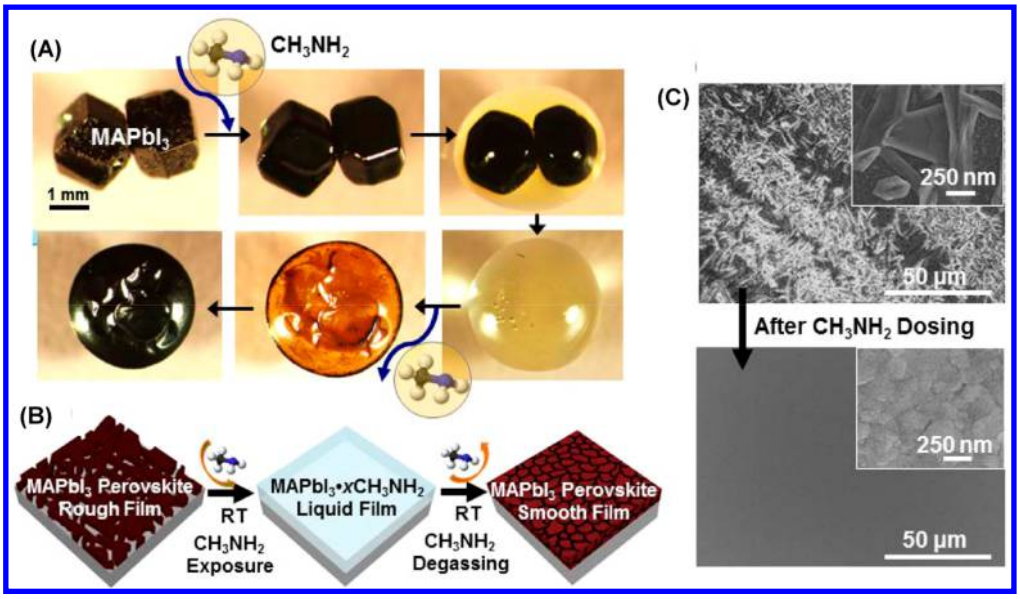

Figure 36. (A) In situ optical microscopic observation of the interaction of $MAPbI_3$ perovskite with CH_3NH_2 gas (a model experiment). (B) Schematic representation of the process of smoothing $MAPbI_3$ perovskite thin films using the CH_3NH_2 gas dosing method. (C) Top-view SEM images comparing the $MAPbI_3$ perovskite film morphology before (top) and after (bottom) the CH_3NH_2 gas dosing. Reprinted with permission from ref 180. Copyright 2015 Wiley-VCH.

annealing has also recently been applied to allow so-called "vertical recrystallization" of $FAPbI_3$ thin films. Following this approach, Xie et al.[364] have coated a solid layer of MACl on top of the solution-formed δ-$FAPbI_3$ nonperovskite thin film and then annealed the stacked layers. The phase transformation from nonperovskite to perovskite occurs gradually during annealing, resulting in a compact and highly textured $FAPbI_3$ film. $FAPbI_3$ thin films fabricated using this solid-MACl annealing method show much longer carrier lifetimes and enhanced PSC performance, attributed to the unique microstructure developed during solid-MACl-annealing.

5.2. Organic-Gas Dosing

5.2.1. Methylamine Defect-Healing. The sensitivity of halide perovskite thin films to organic-gas atmospheres is widely recognized, and this "soft" feature of perovskites has become the basis of engineering the microstructure/morphology of perovskite films.[60] In 2015, Zhou et al.[180] reported that $MAPbI_3$ undergoes an interesting phase/morphology transformation upon interaction with methylamine (CH_3NH_2 or MA^0) gas. Figure 36A shows a model experiment that demonstrates this unprecedented phenomenon. When two touching $MAPbI_3$ crystals are exposed to the MA^0 gas at room temperature, the surfaces of the $MAPbI_3$ crystals immediately start to "melt" until the two crystals merge into a single drop of liquid. The liquid phase is an intercalation compound of $MAPbI_3 \cdot xCH_3NH_2$, and it is stable only under the MA^0 gas. Once the MA^0 atmosphere is removed, the intercalated MA^0 molecules in the $MAPbI_3 \cdot xCH_3NH_2$ liquid are released, converting $MAPbI_3 \cdot xCH_3NH_2$ back to the $MAPbI_3$ perovskite. Note that the x value in $MAPbI_3 \cdot xCH_3NH_2$ can be dependent on the MA^0 equilibrium that is established at the gas−liquid interface. When the same phenomenon occurs in the form of thin films, the $MAPbI_3 \rightarrow MAPbI_3 \cdot xCH_3NH_2 \rightarrow MAPbI_3$ reactions are completed in only a couple of seconds. The rapidity of these transformations is most likely due to the nanoscale nature and high surface area-to-volume ratio of the thin film compared with the large and relatively isotropic single crystals of the model experiment. On the basis of the understanding of this $MAPbI_3$-MA^0 chemical interaction behavior, Zhou et al.[180] proposed a simple method (see Figure 36B) for forming a uniform, smooth $MAPbI_3$ thin film. This procedure entails placing a nominally processed rough $MAPbI_3$ film in the MA^0 gas atmosphere for one second to form a $MAPbI_3 \cdot xCH_3NH_2$ liquid film, followed by removing the film from the MA^0 gas atmosphere.[180] As shown in Figure 36C, the structural defects (e.g., pinholes) in the starting $MAPbI_3$ thin films are immediately healed after the MA^0 gas treatment. Since the phase stability of the $MAPbI_3 \cdot xCH_3NH_2$ liquid intermediate depends on the MA^0 gas atmosphere, the partial pressure P_{MA} of MA^0 gas in the atmosphere can have an important impact on the transformation behavior of $MAPbI_3$. The defect-healing occurs at a relatively high P_{MA} but not at low P_{MA}, which may be because the MA^0 gas pressure can influence the x value in $MAPbI_3 \cdot xCH_3NH_2$ and, in turn, the state (liquid or solid) of this intermediate compound.[365] In another study by Jacobs et al.,[366] the phase transition of $MAPbI_3$ thin films under a constant MA^0 gas atmosphere is studied as a function of the annealing temperature. Indeed, the transformation of the $MAPbI_3 \cdot xCH_3NH_2$ thin film from liquid to solid state occurs at a certain temperature under constant MA^0-gas atmosphere, which is consistent with the observations from Zhao et al.[365]

The type of the organic gas also has a strong impact on the defect-healing behavior of $MAPbI_3$. Zhou et al.[180] have used different gases (NH_3, $C_2H_5NH_2$, and $C_4H_9NH_2$) to treat the raw $MAPbI_3$ thin films. In the case of NH_3, an optically bleached intermediate phase is formed upon gas exposure, but the intermediate phase still maintains a solid state, and correspondingly, there is no significant morphological change after the gas treatment, consistent with an earlier report.[367] In the case of $C_2H_5NH_2$ and $C_4H_9NH_2$ gases, liquid-state intermediates form and the gas treatment results in a similar defect-healing behavior like MA^0 gas. These observations highlight the important role of the solid-to-liquid state change on the healing behavior. However, those liquid-intermediates

DOI: 10.1021/acs.chemrev.8b00318
Chem. Rev. 2019, 119, 3193−3295

derived from $C_2H_5NH_2$ and $C_4H_9NH_2$ gas intercalation cannot recrystallize to phase-pure $MAPbI_3$, presumably due to the occurrence of undesired cation-displacement reactions.

As-formed $MAPbI_3$ perovskite thin films made using the MA^0 defect-healing method exhibit several beneficial attributes such as pinhole-free morphology, preferred tet(110) orientation, extreme uniformity, and low roughness. However, one major drawback is that these films invariably contain grains with small apparent size, associated with the fast nucleation rate induced by the extremely facile self-degassing of MA^0 in the liquid intermediate. It is, however, possible to overcome this issue by manipulating the two key parameters of annealing temperature and P_{MA} in the MA^0 treatment process. In this context, Jacobs et al.[366] have proposed a 2D phase diagram that comprehensively illustrates the phase transition of $MAPbI_3$ to $MAPbI_3{\cdot}xCH_3NH_2$, which makes clear the parameters required for achieving desirable $MAPbI_3$ film microstructures. Through this effort, full-coverage $MAPbI_3$ films with apparent grain size up to several tens of micrometers can be successfully prepared. In another report by Jiang et al.,[368] the MA^0-gas treatment was performed on a smooth raw $MAPbI_3$ film at a constant high temperature of 150 °C, resulting in significant reduction in defects and apparent grain-boundary grooving.

Additives can be also introduced into the MA^0 gas treatment method to tune the grain growth of $MAPbI_3$ films. Ji et al.[138] incorporated a controlled amount of MACl into the raw $MAPbI_3$ thin film. Similar to $MAPbI_3$, MACl itself uptakes MA^0 gas molecules at room temperature and forms a liquid intermediate phase that could convert back to MACl. In this context, the addition of MACl in the raw film allows the formation of a liquid intermediate with a new composition of $MAPbI_3{\cdot}MACl{\cdot}xCH_3NH_2$, as shown in Figure 37. This intermediate phase exhibits a tailored metastability compared with $MAPbI_3{\cdot}xCH_3NH_2$. It first releases MA^0 gas and converts to a smooth solid phase of $MAPbI_3{\cdot}MACl$, which gradually converts to $MAPbI_3$ by releasing MACl at an elevated temperature (150 °C). This process appears to allow the $MAPbI_3$ grains to grow significantly (Figures 19C and 19D), with the film also inheriting the merits of the typical MA^0-gas-treated perovskite films, such as high uniformity, outstanding crystallinity, and a desirable tet(110) texture.

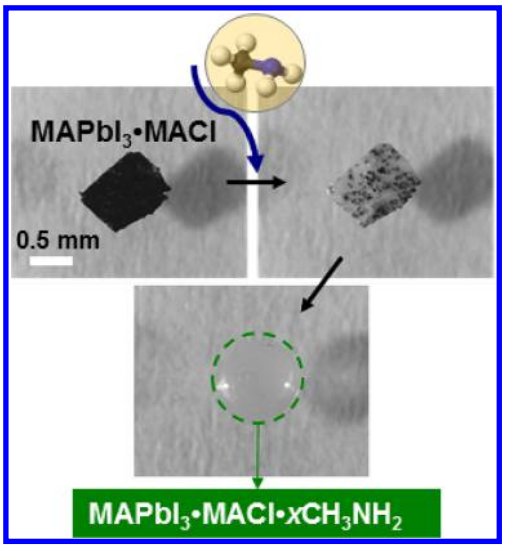

Figure 37. Optical images showing the formation of the $MAPbI_3{\cdot}MACl{\cdot}xCH_3NH_2$ liquid precursor based on the intercalation of CH_3NH_2 into the $MAPbI_3{\cdot}MACl$ solid. Adapted from ref 138. Copyright 2017 American Chemical Society.

Forming highly smooth $MAPbI_3$ perovskite thin films through the methylamine dosing method does not necessarily need to start with raw films of the $MAPbI_3$ phase. Considering that MA^0 itself can be one building block of $MAPbI_3$, the formation of $MAPbI_3$ can be achieved by performing the MA^0 treatment on inorganic $HPbI_3$ and NH_4PbI_3 films. Pang et al.[181] exposed a nominally processed rough $HPbI_3$ thin film to MA^0 gas. The first product upon the reaction of $HPbI_3$ with MA^0 gas is not $MAPbI_3$ but rather $MAPbI_3{\cdot}xCH_3NH_2$ liquid. It has been proposed that during the room-temperature $HPbI_3 \rightarrow MAPbI_3$ conversion process, excess MA^0 can be taken up as soon as the $MAPbI_3$ nucleates via the combination reaction of $HPbI_3$ and MA^0, which is responsible for the direct conversion of $HPbI_3$ to $MAPbI_3{\cdot}xCH_3NH_2$. In the next step, the $MAPbI_3{\cdot}xCH_3NH_2$ liquid rapidly (∼1 s) converts to a smooth $MAPbI_3$ film after the MA^0 gas removal. While there is a question as to whether $HPbI_3$ is a pure inorganic crystalline phase or a solvated intermediate phase ($HPbI_3{\cdot}DMF$), in this process this issue does not appear to matter. In another approach by Zong et al.,[216] NH_4PbI_3 has been studied as the starting material to react with MA^0 gas at room temperature. In this case, the first reaction that occurs is $NH_4PbI_3 + MA \rightarrow MAPbI_3 + NH_3$, where a NH_3 gas byproduct is generated. The NH_3 gas resists the excess MA^0 ingress in the as-nucleated $MAPbI_3$ until the NH_3-gas forming reaction is nearly completed. Therefore, in this process, a $MAPbI_3$ thin film with a similar morphology to NH_4PbI_3 was initially formed, which then undergoes the same morphology-phase transformation process as that of the $MAPbI_3$-MA^0 interaction. Furthermore, Raga et al.[215] have demonstrated that even starting with PbI_2, $MAPbI_3$ perovskite can form by interaction with MA^0 gas. However, moisture or solvent vapor must be present in order to provide protons to form $MAPbI_3$. The conversion behavior is similar to the NH_4PbI_3-MA^0 interaction. This is because the first reaction of PbI_2 and MA^0 gas in the moisture/solvent atmosphere has a byproduct of PbO that plays a similar role in preventing the instant ingression of MA^0 gas.

The MA^0 gas treatment method can also be extended to perovskite compositions other than pure $MAPbI_3$. Chang et al.[369] have used the same method to prepare Cs-doped $MAPbI_3$ thin films, which are significantly more stable than phase-pure $MAPbI_3$ perovskite analogs. By this method, up to 10 mol % Cs^+ cations are likely to be fully incorporated into the crystal lattice, which may enhance the moisture/light stability by forming a more symmetrical cubic perovskite structure than the tetragonal $MAPbI_3$ at room temperature. It is likely that the MA^0 dosing method can enable highly homogeneous Cs incorporation throughout the thin films, representing a potential advantage of the MA^0 gas treatment method.

5.2.2. Pyridine-Mediated Recrystallization. Similar to the MA^0 defect-healing method, treatment of a pristine $MAPbI_3$ perovskite film with pyridine vapor can also mediate the recrystallization of $MAPbI_3$ at room temperature through an optically bleached intermediate phase (Figure 38A). Jain et al.[370] have employed Raman spectroscopy and density functional theory (DFT) calculations to investigate the chemical mechanisms underlying this process. The intermediate film is a multiphase mixture consisting of MAI crystals and amorphous $PbI_2(pyridine)_2$, the latter of which arises through

DOI: 10.1021/acs.chemrev.8b00318
Chem. Rev. 2019, 119, 3193−3295

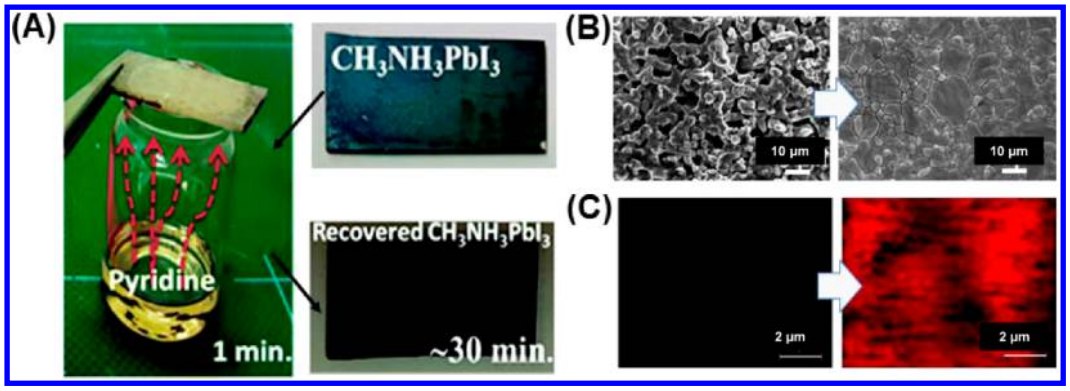

Figure 38. (A) Photographs of experiments showing the reversible interaction of $MAPbI_3$ with pyridine vapor at room temperature. (B) Top-view SEM images showing the morphology of the $MAPbI_3$ perovskite film before and after the pyridine vapor treatment. (C) PL mapping of the $MAPbI_3$ film before and after the pyridine vapor treatment. Adapted with permission from ref 370. Copyright 2016 Royal Society of Chemistry.

preferential formation of a frustrated Lewis pair with partial lone-pair electron donation from the N atom in pyridine (Lewis base) to Pb (Lewis acid). After the pyridine-induced recrystallization, the $MAPbI_3$ perovskite films exhibit improved morphology and PL (Figures 38, panels B and C), and the associated PSC performance increased from 9.5% PCE to more than 18% PCE. Hysteresis was largely suppressed, and the best PSC shows a high V_{OC} of 1.15 V.[370] The enhanced PSC performance may not only be due to the morphology healing effect but also passivation of the perovskite surfaces due to the pyridine vapor exposure. In fact, in early studies by Noel et al.[371] and deQuilettes et al.,[136] it has also been suggested that pyridine can form chemical bonds with under-coordinated Pb atoms within $MAPbI_3$ grains through the Lewis acid−base interaction noted above, passivating defects within the films. The preferential binding of pyridine molecules to Pb atoms on the exterior of $MAPbI_3$ perovskite crystals (i.e., at the grain boundaries or interfaces) has also been confirmed by Ahmed et al.[372] using DFT calculations.

5.2.3. Formamidine-Induced Perovskite Conversion. Although most research in halide perovskite thin films has thus far focused on the $MAPbI_3$ composition, $FAPbI_3$-based perovskites have emerged as a more promising composition for their improved thermal stability and extended light absorption. Converting as-formed high-quality $MAPbI_3$ perovskite films to $FAPbI_3$ directly, while preserving the original morphology, can be a promising strategy. To realize this goal, Zhou et al.[373] have adopted an organic-cation-displacement reaction of $MAPbI_3$ with formamidine ($HC(=NH)NH_2$ or FA^0) gas. The chemical reaction is illustrated in Figure 39A. In this experiment, $MAPbI_3$ films are exposed to FA^0 gas at an elevated temperature (150 °C).[373] Since the heat-treatment condition and MA^0 gas byproduct from this cation-displacement reaction resist the ingress of excess-FA^0 molecules into the as-formed $FAPbI_3$, the original morphology of the raw $MAPbI_3$ thin films is perfectly preserved in the resultant $FAPbI_3$ films (Figure 39B). The success of this morphology-preserving perovskite conversion approach is also related to the fact that, unlike ion-exchange reactions (discussed in section 5.3), this reaction is a rapid redox reaction with low reversibility, and it is solvent-free.

5.2.4. Large-Molecular Amine Gas-Induced Passivation. Large organic amine molecules are usually less successful than methylamine or pyridine for mediating reversible gas-induced transformation of $MAPbI_3$ thin films, presumably because undesirable cation-displacement reactions can occur

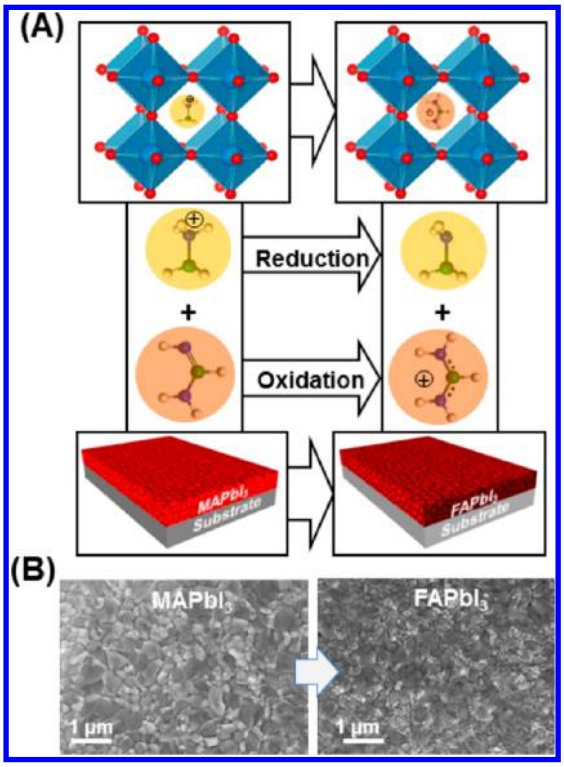

Figure 39. (A) Schematic illustration of the morphology-preserving conversion of the $MAPbI_3$ perovskite thin film into a $FAPbI_3$ perovskite film, based on the organic-cation displacement reaction of the $MAPbI_3$ perovskite with formamidine gas. (B) Top-view SEM images showing the morphology of the $MAPbI_3$ and the as-converted $FAPbI_3$ perovskite films. Adapted from ref 373. Copyright 2016 American Chemical Society.

between $MAPbI_3$ and these amine gases, resulting in the formation of stable wide-bandgap compounds that are not amenable to back-conversion to $MAPbI_3$. Nevertheless, controlled exposure of $MAPbI_3$ to these large molecular amine gases could significantly modify the surface and physical properties of the perovskite films. Wang et al.[374] annealed $FAPbI_3$ thin films in an atmosphere of benzylamine gas. The optoelectronic properties of the films are markedly improved due to the resultant surface passivation, similar to the effects of pyridine. More importantly, due to the hydrophobic nature of the phenyl functional groups, this final $FAPbI_3$ perovskite film shows considerably higher moisture tolerance (no degradation

DOI: 10.1021/acs.chemrev.8b00318
Chem. Rev. 2019, 119, 3193−3295

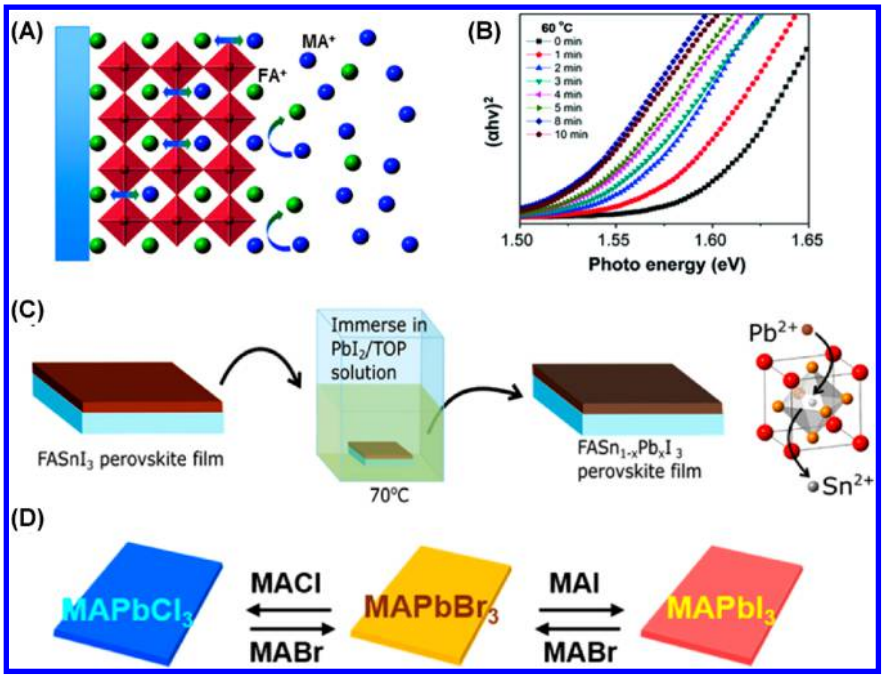

Figure 40. (A) Schematic illustration showing the mechanism of the organic-cation (A-site cation) exchange in a perovskite film placed in a solution. (B) UV−vis spectra showing the gradual conversion of the $MAPbI_3$ perovskite film to the FA^+-richer mixed-organic-cation perovskite film, along with an increase in the reaction time. Adapted with permission from ref 375. Copyright 2016 Royal Society of Chemistry. (C) Schematic illustration of the B-site cation exchange process for fabricating the mixed Pb−Sn perovskite thin films. Adapted from ref 376. Copyright 2017 American Chemical Society. (D) Schematic illustration of the perovskite interconversion based on halide (X-site) exchange reactions. Adapted from ref 377. Copyright 2015 American Chemical Society.

after >2800 h air exposure) compared to the neat $FAPbI_3$ films, which degrade rapidly over the course of a few days. An especially interesting conclusion from this study is that altering the length of the amine tethering group yields strikingly different results. Films treated with aniline (where the amine group is directly attached to the aromatic ring) and phenethylamine (where an ethyl group connects the aromatic and amine groups) fared little better than the untreated $FAPbI_3$ film in terms of environmental robustness. DFT calculations indicate that, while the packing of terminal anilinium and phenethylammonium cations on the surface of the $FAPbI_3$ perovskite crystals is irregular, the benzylammonium cations pack regularly with the benzene rings perpendicular to the perovskite surface. The calculations further indicate that water molecules penetrating the aromatic ammonium surface maintain a greater distance from the underlying Pb−I layer for the benzylammonium-functionalized surface than for the others, illustrating its superior water-repelling properties.[374]

5.3. Ion-Exchange Induced Perovskite Interconversion

The ion-exchange reaction is a synthetic concept that has been widely explored for the synthesis of III−V and/or II−VI semiconductor nanocrystals.[378,379] Ion exchange can occur upon exposure of nanocrystals to a solution containing the desired cations and/or anions, driven by mass diffusion. On the basis of the nature of the exchange, it is often used to tailor the composition of thin films or nanostructures, without significant changes in the morphology or shape. In this context, this strategy is very useful for forming new materials with compositions that are not immediately attainable via direct synthesis.[379] In halide perovskites, the activation energies for defect-mediated diffusion of the A-, B-, and X-sites are all relatively low compared with those of hard materials. Notably, the activation energies for I^- and MA^+ ions in $MAPbI_3$ are as low as 0.6 and 0.8 eV, respectively.[380,381] The ion-exchange reactions can occur for all the A-, B-, and X-sites, as shown in Figure 40 (panels A, C, and D, respectively), enabling the facile synthesis of halide perovskite thin films over a wide compositional range.

The first demonstration of ion exchange was for the X-site anions, where Pellet et al.[382] observed a strikingly rapid halide exchange in $MAPbX_3$ (X = I, Br, Cl) films. These reactions were performed by simply exposing the as-deposited $MAPbX_3$ thin films to a relatively dilute (0.05 M) solution of MAX. It was shown that all halide exchange reactions, except from bromide to iodide, can be completed within minutes, confirming the facile transport of the halide ions within the perovskite lattice. During the exchange reactions, the morphology of the perovskite can be well-preserved. Through the halide exchange shown in Figure 40D, $MAPbI_3$, $MAPbBr_3$, $MAPbCl_3$ and mixed-halide perovskite alloys can readily be formed.[382] It has since been demonstrated by others that similar halide exchange can occur in the $FAPbX_3$[383] and $CsPbX_3$[384] perovskites. Such halide exchange reactions can also be conducted using HX gases, which allow for more reliable morphology preservation.[385]

A-site ion exchange is performed mostly for the purpose of converting MA-based perovskites to FA-based based perovskites with extended light absorption and improved thermal stability. This approach can be promising and important because FA-based perovskites are relatively difficult to synthesize. Eperon et al.[386] reported the first demonstration of A-site ion-exchange for interconversion between MA-based and FA-based perovskites. By dipping thin films of $MAPbI_3$ or $FAPbI_3$ in isopropanol solutions of FAI or MAI, respectively, at room temperature, their bandgaps could be tuned between

DOI: 10.1021/acs.chemrev.8b00318
Chem. Rev. 2019, 119, 3193−3295

1.57 and 1.48 eV. The chemical conversion is uniform through the entire thin film without the formation of segregated structures/phases. It is worth noting that, through this A-site ion exchange, phase-pure $FAPbI_3$ perovskites can be deposited into mesoporous TiO_2 scaffolds. This approach has addressed a significant challenge in the PSC field, as mesoporous TiO_2 layers are important in many high-PCE PSCs, and this substrate favors the crystallization of $FAPbI_3$ in the non-perovskite polymorph when prepared by normal solution-based processing methods.[224] However, the results by Eperon et al.[386] have shown that the conversion kinetics of $MAPbI_3$ to $FAPbI_3$ are relatively sluggish, and thus a long dipping time (several hours) is required in the FAI isopropanol solution. Prolonged immersion causes severe damage to the thin film morphology due to the solubility of hybrid perovskites in isopropanol. To address this issue, Ji et al.[375] have further proposed a balanced A-site cation exchange reaction by controlling the temperature during the dipping process. As shown in Figure 40A, the MA-FA cation exchange process is expected to consist of two subprocesses. One is MA-FA cation exchange at the solid−liquid interface, and the other is the interdiffusion of FA^+ cations into the film bulk. Both subprocesses are considered thermodynamically favorable, and they are thereby controllable through tailoring of the reaction temperature. The increase in the dipping temperature will accelerate the conversion kinetics of $MAPbI_3$ to FA-based perovskites and reduce the occurrence of side reactions forming FA-based nonperovskite polymorphs. However, higher temperature also accelerates the detrimental dissolution of perovskites in isopropanol. In this context, Ji et al.[375] found that by optimizing the temperature to ∼60 °C, FA-rich thin films can form (Figure 40B) while retaining the desirable morphology of the original $MAPbI_3$ films (attributable to the balanced A-site cation exchange reaction in solution at the optimized temperature). A-site cation exchange reactions using vapor-based methods can also resolve the morphology preservation issue.[387]

Although large activation energies for B-site motion in hybrid perovskites are predicted using theory,[381] B-site cation exchange is possible. Eperon et al.[376] immersed a smooth $FASnI_3$ perovskite film (deposited using the antisolvent/solvent extraction method[150]) into a dilute solution of PbI_2 in trioctylphosphine and toluene (Figure 40C). Despite heating the mixture to 70 °C, the exchange reaction of $FASnI_3$ with PbI_2 progressed slowly over the course of days. The reaction may be interrupted during the conversion, forming stable $FASn_xPb_{1-x}I_3$ alloys with controllable Sn:Pb ratio. Once again, during the phase conversion, no segregated perovskite phases were detected.

The ion-exchange reactions play very important but "hidden" roles in the formation process of hybrid perovskites through many additive approaches. There are a few recent studies that point out ion-exchange reactions as the underlying mechanism for the formation of compact perovskite films. Li et al.[388] have studied the evolution of $MA_xFA_{1-x}PbI_3$ thin films from MA^+-ion-rich precursors. The initially formed perovskite phase from the MA^+-ion-rich precursors is MA-rich relative to the target composition, but then it is gradually converted to the target composition by solid-state ion-exchange reaction of $MA_xFA_{1-x}PbI_3$ with the solid FACl precursor. This process greatly reduces the possible formation of $MA_xFA_{1-x}PbI_3$ nonperovskite polymorphs. Unlike $MA_xFA_{1-x}PbI_3$, $MA_yFA_{1-y}PbI_3$ with a lower FA^+ content tends to crystallize in the perovskite polymorph and serves as a perovskite crystal "template" for the targeted $MA_xFA_{1-x}PbI_3$ composition.

5.4. Mechanical Compression

Halide perovskites are considered a family of mechanically "soft" materials, compared with conventional hard materials like Si and Al_2O_3. Ramirez et al.[61] have shown that $MAPbI_3$ has a Young's modulus of ∼18 GPa, hardness of ∼0.6 GPa, and fracture toughness of ∼0.2 MPa $m^{0.5}$, and other reports[58,59] have estimated similar Young's modulus and hardness values for $MAPbX_3$ (X = I, Br, Cl) as well as the all-inorganic perovskite $CsPbBr_3$. This behavior opens up the possibility to introduce significant compressive strain for tuning the formation or crystallization of halide perovskite thin films. Xiao et al.[389] have proposed, for example, simple hot-pressing as an effective post-treatment method for engineering $MAPbI_3$ films. In this method, a rough $MAPbI_3$ film full of pinholes is reconstructed to a smooth, pinhole-free thin film, greatly improving its charge-transport properties and device functionality. The improvement may be related to grain coalescence and coarsening induced by the combined effect of annealing and mechanical pressure. A cold-roll pressing method was later developed by Abdollahi Nejand et al.,[390] where the surface of the perovskite layer is first partially dissolved by exposing the film to a low-pressure DMF vapor (exploiting similar mechanisms to those at work in solvent annealing), followed by cold-roll pressing that compresses and spreads the partially dissolved perovskite. This method also transforms a nominally processed defective perovskite film to a continuous compact thin film structure. They further reported a fully solid-phase compression method, wherein ball-milled fine $MAPbI_3$ perovskite solid powders are first spray-coated onto a substrate and then subjected to hot compression.[391] Nevertheless, forming fully compact $MAPbI_3$ films using this method still represents a challenge, and PSCs made using this method show a relatively low PCE (<10%).

In addition to eliminating pinholes, the compression approach may also be useful for developing preferred crystallographic texture and increasing the grain size in the resultant $MAPbI_3$ films. In an 'indirect" demonstration, Zhu et al.[392] proposed a "face-down" annealing route for the processing of $MAPbI_3$ thin films. Here, the freshly spin-coated precursor film is placed facing down on the hot plate. In this case, it is suggested that compression of the precursor film is generated from the weight of the thick substrate during annealing and that this configuration also confines the solvent removal, resulting in $MAPbI_3$ films with strong tet(110) texture and micrometer-scale apparent grain size. Whether compression or confinement of the film is the truly important factor in this process, however, may require further exploration. While the above examples have shown the potential promise of introducing compression into perovskite processing, the mechanisms underlying the effect of compression on formation/crystallization have not yet been widely explored, and future detailed mechanistic studies are needed.

6. EFFECTS OF PRECURSOR COMPOSITION AND ADDITIVES

While the preceding discussion has largely focused on film deposition of the prototypical perovskite $MAPbI_3$, it is worthwhile to consider in more detail possible effects of precursor compositional variation away from a simple 1:1 molar ratio of MAI to PbI_2. Among several possible classes of

DOI: 10.1021/acs.chemrev.8b00318
Chem. Rev. 2019, 119, 3193−3295

such deviations, stoichiometry variations may be employed, wherein an excess of one of the precursors is added in order to manipulate film formation. Alternatively, perovskite components may be alloyed or replaced altogether with ionic species that can substitute into the perovskite, altering bulk properties and generating entirely distinct perovskite families. Such compositional modifications often require significant changes to the processing approaches relative to those used for $MAPbI_3$ in order to attain high film quality. Still further, other species may be added that do not substitute into the perovskite structure, but they may nevertheless affect film formation and have a large impact on the microstructure and/or defect population. The distinction between these latter classes, alloying components versus additives, may in some cases be ambiguous. In this section, we therefore classify the additive types according to whether they could, when considering charge-balance and approximate size requirements, substitute on the A/A′, B, or X sites in the ABX_3, A_2BX_4, $A'_2A_{n-1}B_nX_{3n+1}$, or other related perovskite structures (e.g., alkalis or monovalent cations, divalent metals, or halides/pseudohalides, respectively), or not (e.g., bulky organic molecules, water, or seed crystals such as quantum dots). It should also be emphasized that, although there are many reports of the effects of a wide range of additives on film morphology, these effects are often (though not always) presented without detailed investigation of the fundamental mechanisms through which the additive acts on film formation. Thus, it should be borne in mind that such descriptions may reflect the vagaries of how a certain process in a certain laboratory is implemented and affected, as opposed to universal truths about the interactions between the additive and perovskite system under study.

6.1. Effects of Stoichiometry on Film Formation

The effect of precursor stoichiometry can be an important factor in determining how ABX_3 and related perovskites crystallize and what secondary phases might remain in the final films. Often it is taken for granted that precursors should be combined in the final desired film stoichiometry, yet alterations to these ratios may be desirable to compensate for the loss of a volatile component, control crystallization mechanisms by way of spectator species, or to passivate interfaces or bulk defects through judicious incorporation of secondary phases.

6.1.1. BX_2-Rich Precursors. Although the presence of PbI_2 as a secondary phase in the perovskite can imply detrimental effects, either directly, by acting as an insulating layer that blocks carrier extraction at device interfaces, or indirectly, as evidence of degradation of the absorber, small excesses may be benign or even beneficial if distributed properly throughout the film. In PSCs, for example, PbI_2 should exist either along vertical grain boundaries (perpendicular to the film plane) or be thin enough at horizontal grain boundaries or interfaces to confer the benefits of passivation without blocking carriers. Chen et al.[108] identified salutary effects of a light PbI_2 grain cladding in $MAPbI_3$ films grown by the VASP process (section 4.2.3). The type I band alignment between PbI_2 and $MAPbI_3$ prevents carriers from accessing the grain boundaries, where they might recombine nonradiatively. Also, the physical separation and band bending induced by PbI_2 at grain boundaries can prevent interfacial recombination at the junctions with the TiO_2 ETL and Spiro-OMeTAD HTL.[108] Roldán-Carmona et al.[393] observed that excess PbI_2 in the precursor solution of "solvent-engineered" $MAPbI_3$ (section 4.1.2) could improve perovskite crystallinity, apparent grain size, carrier lifetime, and electron transfer to the TiO_2 ETL, contributing to an enhancement of PSC performance. Jacobsson et al.[171] observe that, contrary to the results of Roldán-Carmona et al.,[393] PbI_2 does not improve the apparent grain size of $FAPbI_3/MAPbBr_3$ prepared by solvent engineering.[171] Han et al.[394] have observed that an increase in carrier lifetime results from inclusion of excess PbI_2 in the precursor solution of $MAPbI_3$ devices prepared by solvent engineering but is not associated with any changes in morphology. Nevertheless, despite the discrepancy in morphological effects, these reports agree on the salutary effect of excess PbI_2 on PSC performance, which may signify that the benefits of grain boundary/interface passivation outweigh the effects on morphology.

The morphological discrepancy may arise due to the compositional difference among the films investigated in these reports, which most likely plays a significant role in crystallization. Ke et al.[109] found that addition of a slight excess of $Pb(SCN)_2$ to the precursor solution used in a solvent engineering process could generate, in addition to large apparent grain size, an irregular honeycomb-like network of PbI_2 deposits around them (the effects of SCN additives on grain structure will be discussed further in section 6.2.3.2). Collectively, the effects of larger grains, improved crystallinity, and passivation lead to a doubling of the PL lifetime as well as increased PSC efficiency and reduced hysteresis.[109] The strategy of improving PSC performance by adding a slight excess of the lead halide to the precursor solution appears to be generally applicable to a number of perovskite compositions, including mixed formamidinium-methylammonium lead iodide/bromide,[89] and triple-[25] or quadruple-cation absorbers.[26] A recent study by Park et al.[395] on the effects of excess PbI_2 in $(FAPbI_3)_{0.85}(MAPbBr_3)_{0.15}$ indicates that although carrier diffusion lengths are not improved by excess PbI_2, as determined by electron-beam induced current (EBIC) mapping measurements, those samples are more resistant to decay under repeated EBIC scans, possibly signifying that they possess a lower defect concentration. A further benefit of excess PbI_2 appears to be better filling of a mesoporous TiO_2 substrate, which was attributed to a reduction in the average colloid size in the precursor solution.[395]

Despite its potential to improve device performance, inclusion of PbI_2 may not be completely beneficial. While results by Liu et al.[396] concur that PbI_2 is beneficial for initial PSC performance, its presence can lead to photoinstability of $MAPbI_3$ under illumination, even in inert atmosphere. Schoonman[397] has demonstrated that lead halides can be susceptible to decomposition under UV irradiation, and the elemental iodine produced by such reaction is liable to cause the perovskite to degrade.[398] However, Liu et al.[396] demonstrate that the performance of encapsulated PSCs of similar initial efficiency (with and without added PbI_2) exhibit comparable degradation kinetics. PbI_2 photoinstability in this case may be less relevant because encapsulation can arrest device degradation not only by resisting ingress of moisture and oxygen but also by preventing decomposition products from escaping the device. While it is clear that some trade-offs (associated with retarded carrier extraction, reduced absorption, and stability concerns) will emerge from the presence of large amounts of excess PbI_2, the benefits of passivation are compelling for modest addition levels.

6.1.2. AX-Rich Precursors. While excess PbI_2 is typically understood to be an effective means of improving film quality

DOI: 10.1021/acs.chemrev.8b00318
Chem. Rev. 2019, 119, 3193−3295

through its passivation effects, there may also be some advantages to MAI-rich stoichiometries. As noted in the previous section, Jacobsson et al.[171] found that, although excess PbI_2 was a better strategy for PCE enhancement of mixed $FAPbI_3/MAPbBr_3$ PSCs prepared by solvent engineering, 10 mol % excess organic salt (as FAI) yielded more intense, spatially uniform, and longer-lived PL than that from stoichiometric or PbI_2-rich films, with improved V_{OC} of PSCs made from these films. Depth-resolved XPS (by varying the X-ray energy/penetration depth to probe composition in a range between ∼5−18 nm) and TEM measurements suggest that thin films prepared with excess PbI_2 contain some inclusions of unreacted PbI_2 within the grains, while those prepared with excess organic salt appear to be more uniform in their internal structure. Jacobsson et al.[171] have proposed that PbI_2, being considerably less soluble than the organic salt, nucleates first and is thereafter transformed by solid-state reaction with the surrounding organic salt. Thus, the enhanced luminescence may arise from a more complete transformation of the PbI_2 to perovskite in the presence of the extra organic ammonium halide. This conclusion would imply that even one-step methods may share a key characteristic of the two-step methods (i.e., diffusion of the organic ammonium halide may also be an important step affecting the crystallization kinetics). However, while Park et al.[395] have also observed PbI_2 within grains in $FAPbI_3/MAPbBr_3$ films prepared by solvent engineering via HRTEM measurements, in situ grazing incidence wide-angle X-ray scattering (WAXS) measurements indicate that PbI_2 appears only after prolonged annealing (rather than within the initial films), suggesting a precursor-solvent intermediate crystallization mechanism akin to that witnessed in formation of $MAPbI_3$ films. Further study is warranted to more fully explore this process, which is likely to be complicated by the large number of species that can participate in crystallization. It is also important to note that enhancement of the luminescence in the organic-rich films also comes at a cost. In PSCs made from the organic-rich thin films, the resulting gains in V_{OC} are offset by losses in J_{SC}, likely due to a coating of organic salt around the perovskite grains (as inferred from XPS depth profiles showing enrichment in the I:Pb elemental ratio near the film surface) that prevents carrier extraction and transport.[171]

Using a smaller excess of MAI than that explored by Jacobsson et al.[171] can provide benefits without the drawbacks noted above. Son et al.[399] argue that intergranular MAI can be beneficial in $MAPbI_3$ prepared by solvent engineering when 6 mol % excess is added to the precursor solution, having a passivating effect analogous to that of PbI_2. Cross-sectional TEM images combined with electron diffraction measurements suggest the formation of a light coating of MAI around the perovskite grains at 6 and 10 mol % excess MAI. However, it was also found that, while 6 mol % excess increases the PL lifetime, 10 mol % excess substantially reduces it relative to the stoichiometric film.[399] This feature indicates that the $MAPbI_3$ film properties are apparently very sensitive to the excess MAI and associated processing, independent of potential problems posed by carrier blocking by overly thick layers of MAI at grain boundaries. Excess MAI may contribute to iodine interstitial defects, which can be potent hole traps.[92] However, the presence of extra MAI can be easily remedied by increasing annealing temperature or time to sublime the excess, and such detrimental effects can be avoided by a proper tuning of these parameters for a given stoichiometry. In fact, the excess can be used as a buffer against the decomposition that might otherwise be induced by the final thermal anneal, allowing the film to be subject to more aggressive conditions and enlarging the grains without transforming them to PbI_2. Judicious stoichiometry choice can thus confer the benefits of the MAX treatments discussed in section 5.1.4, without requiring an additional deposition step. For example, Yang et al.[232] found that addition of a slight MAI excess (1.2:1 MAI:PbI_2) to the precursor solution used in the antisolvent/solvent extraction process (section 4.1.4), a 7:3 weight ratio of NMP and GBL as the solvent, and diethyl ether as the antisolvent, allows very large apparent grain size to develop without compromising the structure through pinhole formation.

More dramatic effects on morphology may be attained using far larger excesses of MAI, particularly with regard to the one-step spin-coating process, which tends to yield poor coverage and performance for perovskite films and devices, as discussed in section 4.1.1. While spin-coating from a stoichiometric solution of MAI and PbI_2 in DMF leads to a dendritic morphology induced by the uncontrolled growth of needle-like $MAPbI_3$·DMF crystals, the use of a 3:1 MAI:PbI_2 ratio instead gives rise to a more uniform morphology, albeit with a microstructure less compact or free of pinholes compared to typical films produced by solvent engineering or conventional two-step processes.[400,401] In terms of solution chemistry, this behavior may be explained as a result of inhibition of perovskite-solvent complex formation, since the excess MAI can compete against the solvent to coordinate with PbI_2 by providing extra I^- ions, which form coordination complexes of varying stoichiometry depending on the availability of I^-.[402]

Yan et al.[162] have undertaken a comprehensive study of the colloidal properties of DMF-based solutions produced using a range of MAI:PbI_2 stoichiometries, including both MAI-deficient and MAI-rich compositions. By examining the properties of both the precursor solutions and spin-cast films, they deduce that the stoichiometric or MAI-deficient solutions lead to the formation of rodlike colloids that are dominated by the interaction of PbI_2 with DMF. These colloids are most likely composed of PbI_2·DMF, and they inherit their rodlike shape from the crystal structure that incorporates a 1D lead halide network, as noted in section 3.1.2.1. The film morphology obtained from these solutions thus show the dendritic morphology previously discussed in section 4.1.1 (Figure 41). At higher concentrations of MAI, the coordination environment of Pb prefers structures that accommodate higher I:Pb ratios, altering the edge-sharing lead halide octahedral structure of the PbI_2·DMF or $MAPbI_3$·DMF intermediates in favor of corner-sharing octahedral networks of progressively smaller size. The size reduction of the colloids under MAI-rich conditions is confirmed by a reduction in Tyndall scattering by the solution and accompanied by more uniformly distributed and isotropic grains in the final film (Figure 41).[162] As discussed in section 3.1.2, it is possible that a large excess of MAI may also contribute to a less crystalline organic-rich intermediate phase, thereby leading to smooth morphology when precipitating from the solution. This less-crystalline intermediate serves as the matrix for final perovskite grain nucleation, leading to more even microstructure growth and more uniform coverage.

Although it can improve the microstructure relative to that obtainable from stoichiometric precursors, excess organic ammonium salt can also be time-consuming to remove,

DOI: 10.1021/acs.chemrev.8b00318
Chem. Rev. 2019, 119, 3193−3295

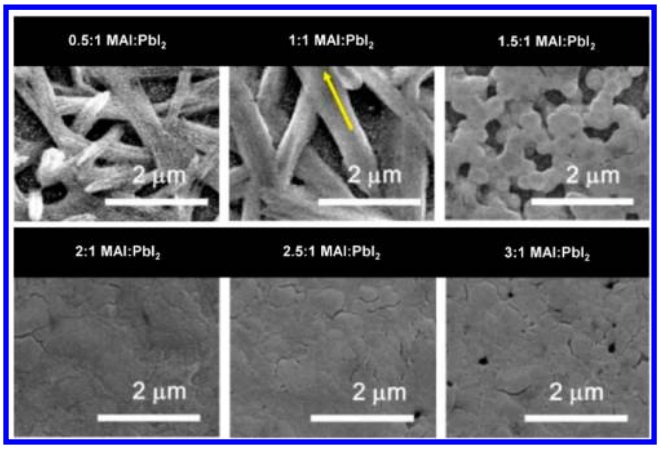

Figure 41. Top-surface SEM images showing the morphology of the $MAPbI_3$ thin films obtained by spin-coating these solutions and annealing at 100 °C. Under PbI_2-rich conditions, rodlike colloids in the solution lead to dendritic microstructure, while MAI-rich conditions interfere with Pb-solvent interactions, leading to the formation of more isotropic colloids and conformal grain coverage. Adapted from ref 162. Copyright 2015 American Chemical Society.

requiring a relatively long and higher-temperature anneal to drive it out of the film[9,175] and significantly increasing the activation energy required for perovskite crystallization.[400] While this overall behavior of such MAI-rich films has been consistently observed, some confusion seems to exist over whether the transformation into perovskite is mediated by intermediate phases other than solvent-based complexes under MAI-rich conditions. On the basis of similarities of absorption features in spectroscopic observations of the as-deposited MAI-rich films to those previously attributed to different coordination complexes of lead and iodine (PbI_{2+n}^{n-}) in solution,[403] Manser et al.[401] speculate that these features belong to an "iodoplumbate precursor" phase witnessed in the XRD patterns of the as-deposited films but do not offer a precise composition of this phase. Cao et al.[404] propose that a reduced-dimensionality $(MA)_4PbI_6$ phase can be generated under MAI-rich conditions, which has an XRD pattern closely resembling that of the "iodoplumbate precursor" identified by Manser et al.[401] This latter phase is assigned based on observations by Wakamiya et al.,[185] but importantly, they identify this phase as a hydrate, $(MA)_4PbI_6{\cdot}2H_2O$, rather than the pure $(MA)_4PbI_6$. These findings agree with a considerably older report identifying the crystal structure as being composed of isolated PbI_6 octahedra with interspersed MA^+ cations and H_2O molecules.[405] Crucially, this report also indicates that the hydrate can be decomposed to a mixture of $MAPbI_3$ and MAI by application of either heat or vacuum.[405] The presence of water molecules may, therefore, play an important role in stabilizing the structure through a scheme in which overall connectivity is mediated by hydrogen bonds linking the MA^+ cations to the H_2O molecules.

The implications of this behavior have significant bearing on understanding MAI-rich film formation, as it implies that no crystalline MAI-rich perovskite-related species may be favorable in the solid phase, at least in the absence of a mediating species such as H_2O. The "iodoplumbate precursor" may, therefore, be a "red herring" that spontaneously emerges when these films are introduced to moisture, as by exposure to humid air during X-ray or optical measurements. However, this finding also implies that the atmosphere under which these films are produced may play a crucial role in determining precursor nucleation and growth. Presumably, MAI-rich film deposition in a humid atmosphere would involve the growth of the hydrate phase as an intermediate, while deposition in an inert atmosphere would proceed via some other mechanism. To our knowledge, there are no currently available reports that explore this possibility and the potential effects on film formation. Nevertheless, spectroscopic measurements in the manner of the work of Manser et al.[401] may prove important in

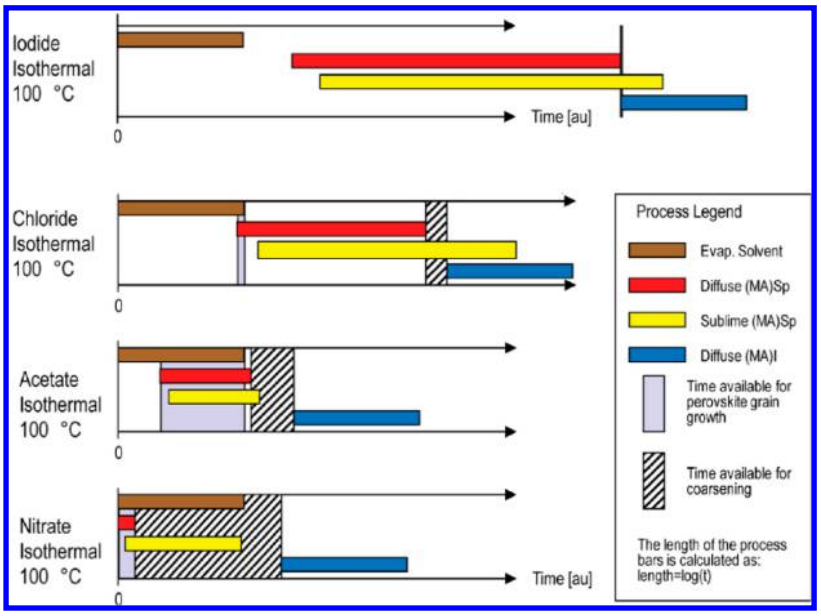

Figure 42. Processing windows for a 3:1 ratio of MAI:$PbSp_2$ precursors used in one-step spin-coating (Sp = I, Cl, OAc, NO_3). The iodide and chloride precursors leave little time for nucleation and growth of the perovskite microstructure before decomposition, while the acetate provides a much longer time window for nucleation and growth, leading to a desirable morphology. The nitrate is lost so rapidly that a continuous morphology cannot be obtained under the reaction conditions examined. Reproduced from ref 175. Copyright 2015 American Chemical Society.

DOI: 10.1021/acs.chemrev.8b00318
Chem. Rev. 2019, 119, 3193−3295

extracting further understanding of film growth under MAI-rich conditions. Such studies must be accompanied by strict control over both fabrication and measurement environments in order to prevent misunderstanding of the true nature of this process.

6.1.3. Halide/Non-Halide "Spectator" Precursors. The presence of excess MAI in the precursor solution provides an additional opportunity for control over the film growth process (i.e., since the precursor is iodide-rich), in that the lead iodide may be replaced with a lead salt of arbitrary anionic composition. Doing so can be useful whether one wishes to incorporate the secondary anion or not, since its presence can significantly modulate the behavior of the deposition process. Often, the secondary ion will not persist in the final film but act as a "spectator" (Sp^-) in an overall reaction of the form[175]

$$3MAI + PbSp_2 \rightarrow MAPbI_3 + 2MASp \quad (29)$$

As MASp is generally the most volatile component of the system, it will be driven off during the postannealing that accompanies most perovskite deposition techniques, yielding the perovskite film (or, given enough heat and time, PbI_2).[175] Moore et al.[175] compared (in the context of reaction 29) the use of four different lead salts: lead iodide, chloride, acetate, and nitrate. In each case, the as-deposited films showed mutually distinct WAXS patterns, indicating that each spectator ion promotes the formation of unique crystalline phases (which are also independent of the solvent used in the deposition). The choice of the spectator ion can have a large impact on the four different identified stages of film growth (Figure 42): solvent evaporation (labeled "Evap. Solvent" in Figure 42), which ends when the solvent is completely removed from the film; spectator diffusion ["Diffuse (MA)-Sp"], during which the spectator salt MASp diffuses out of the precursor structure, leaving behind the perovskite; spectator sublimation ["Sublime (MA)Sp"], during which the spectator salt that has diffused out of the structure evaporates from the film entirely; and MAI diffusion ["Diffuse (MA)I"], wherein MAI diffuses out of the perovskite structure, decomposing the film. Note that MAI sublimation is not considered to be an important part of this process, as decomposition has already occurred once MAI begins to diffuse out of the perovskite grains. The beginning and end of these processes can be inferred by the appearance and disappearance of peaks in the WAXS patterns (except for solvent evaporation, which is determined by thermogravimetric analysis). Note that grain "growth," as indicated in Figure 42, is conceptually different from the conventional use of the term as introduced in section 3.1.1.2. In this case, it begins with spectator diffusion and ends with whichever of spectator diffusion or solvent evaporation ends first, and it is identifiable with the time available for the nucleation of new perovskite grains from the precursor phase (although growth in the conventional sense of the already formed perovskite grains may occur during this time window as well). Grain "coarsening" is identified with the growth (in size) of already formed perovskite grains, and it is identified with the time range between the end of spectator diffusion and the beginning of MAI diffusion (i.e., the onset of decomposition).

Much useful information can be determined from careful inspection of the kinetics of these processes for different choices of the spectator ion, and by comparing the time windows available for each of the processes described above (as shown schematically in Figure 42). By fitting the time evolution of the tet(110) peak in the WAXS pattern to the JMAK equation (eqs 14 or 15) at different stages of annealing, the perovskite crystallization activation energy may be determined and is found to depend on the identity of each precursor. (However, we repeat that the empirical JMAK model may be misleading, and any associated analysis should be evaluated while keeping its limitations in mind.) This parameter may be extracted by assuming the constant K_3 to have an Arrhenius temperature dependence. The activation energy is largely affected by the speed of spectator diffusion and also to some degree on spectator sublimation if this process is relatively slow and retards the former process. In the case of MAI, the solvent evaporates completely before excess MAI begins to diffuse out of the solid precursor, restricting the time available for perovskite grain formation. Furthermore, the MAI spectator diffusion (i.e., out of the precursor phase) is followed almost immediately by MAI diffusion processes (i.e., out of the perovskite phase), leaving almost no time available for coarsening. The chloride more readily sublimes from the film, reducing the crystallization activation energy and allowing for a wider but still relatively narrow grain-coarsening window. The narrow processing windows available in the chloride and particularly the iodide systems may contribute to a greater sensitivity to the fabrication timing and overall environmental conditions. By contrast, the acetate sublimes almost concurrently with solvent evaporation and diffusion from the precursor, reducing the perovskite crystallization activation energy even further and allowing for long processing windows for both perovskite grain formation and coarsening, without risk of decomposition. The nitrate induces the lowest activation energy of the four examined, but crystallization proceeds so rapidly that a discontinuous morphology results.[175,406] The acetate precursor [in 3:1 molar ratio of MAI:$Pb(OAc)_2$] has enjoyed significant success, yielding films of more uniform microstructure when compared to those using an equivalent stoichiometry with PbI_2 or $PbCl_2$. This use of the lead acetate precursor is also broadly applicable to compositions beyond $MAPbI_3$, including those incorporating Br or FA.[407−410] Overall, the spectator precursor route appears to be a useful method of attaining reproducibly uniform perovskite films in a single step, without the capriciousness of timing and atmosphere effects to which solvent engineering can be vulnerable (so long as suitable precursors are chosen).

Of the above precursors, the chloride most frequently appears in the recent literature. Mixed iodide-chloride absorbers were introduced early in the development of PSCs,[144,193,411] boosted especially by reports that Cl addition could increase the minority carrier diffusion length relative to that of the pure iodide by an order of magnitude.[13,412] However, the question remains of whether this improvement in perovskite quality originates directly from incorporation of Cl into the lattice and concomitant trap passivation, or indirectly, through the influence of Cl on crystallite growth. Given the small size of the Cl^- ion relative to I^-, Cl has not been found to incorporate to a large enough degree to alter the unit cell of $MAPbI_3$;[413] however, remnant traces of Cl can often be found in the thin film. Early misconceptions about the degree to which Cl could incorporate into the $MAPb(I_{1-x}Cl_x)_3$ films were refuted by subsequent compositional studies showing that this fraction is quite small ([Cl]/[I] < 2%).[175,414−416]

There is no clear consensus on the location of the residual Cl, with elemental mapping studies yielding contradictory

DOI: 10.1021/acs.chemrev.8b00318
Chem. Rev. 2019, 119, 3193−3295

results that indicate retained Cl amounts and distributions are highly dependent on film processing. X-ray absorption near edge structure measurements on $MAPbI_{3-x}Cl_x$ prepared by one-step spin-coating from a 3:1 solution of MAI:$PbCl_2$ in DMF indicate that the local coordination environment of Cl in perovskite films resembles $MAPbCl_3$ more closely than either $PbCl_2$ or MACl, although the authors emphasized that this observation alone is not conclusive evidence of a preference of direct Cl for I substitution in the bulk.[416] A nano-X-ray fluorescence (nano-XRF) study on $MAPbI_3$ indicates that the distribution is heterogeneous, not only from grain to grain but even within the grains themselves.[415] In this study, the two-step dipping process (wherein PbI_2 films are dipped in a 2:1 solution of MACl:MAI in isopropanol) leads to more Cl in the final film than one-step spin-coating processes using either MACl or $PbCl_2$ as the Cl donor, both of which lead to roughly the same chlorine content. Heterogeneity of the Cl distribution was observed, however, regardless of the processing method.[415] A TOF-SIMS mapping study on $MAPbI_{3-x}Cl_x$ films prepared by VASP (in which spin-cast mixed-halide PbICl films were subjected to MAI vapor) indicates instead that the Cl congregates at grain boundaries.[174] energy-dispersive X-ray spectroscopy (EDS) mapping of $MAPbI_{3-x}Cl_x$ prepared by one-step spin-coating from a 3:1 solution of MAI:$PbCl_2$ in DMF onto a mesoporous Al_2O_3 scaffold indicates slight traces of Cl within the scaffold, while none appears to be present in the overlying capping layer,[413] consistent with the expectation that impurities are more likely to reside at grain boundaries and interfaces than within the bulk.

Although Cl does not incorporate substantially within the perovskite thin films, it does produce several notable effects on film growth, including a preferred orientation of the perovskite grains along the tet(110) plane, particularly when grown on the electron transport material TiO_2.[134,413,414,417] DFT calculations predict that the $MAPbI_3$−TiO_2 bond in particular is strengthened by interfacial Cl, and that the tet(110) plane is particularly favorable at this interface.[133] Observations of the abnormal growth of apparently very large tet(110)-oriented $MAPbI_3$ grains on TiO_2 with Cl addition, compared to the small-grain, randomly oriented pristine (no Cl added) films, further support this conclusion.[134] Wang et al.[417] have even proposed that incorporation of Cl can stabilize the cubic phase of $MAPbI_3$ on mesoporous TiO_2 substrates, based on the assignment of the two dominant peaks in the X-ray diffraction patterns of these films to the (100) and (200) planes of the cubic phase. However, these reflections could just as easily be assigned to tet(110) and tet(220) planes of the tetragonal phase, consistent with other reports,[134,413,414] and there do not appear to be any other reports corroborating this finding. It has also been reported that Cl can stabilize the perovskite phase of $CsPbI_3$,[418] perhaps through the formation of a protective layer of interfacial $CsPbCl_3$.

The presence of Cl can also dramatically impact film morphology, with a wide variety of microstructures obtained even for similar processes. An early report by Eperon et al.[419] indicates that the coverage of $MAPbI_{3-x}Cl_x$ films prepared by single-step spin-coating from a 3:1 solution of MAI:$PbCl_2$ in DMF is highly dependent on such variables as perovskite film thickness, annealing time and temperature, and thickness of the compact TiO_2 and/or mesoporous Al_2O_3 substrate. As in the case of single-step spin-coating from 1:1 MAI:PbI_2, conformal coverage is difficult to achieve, but the morphology of perovskites deposited from the chloride-containing precursor is completely different from that of the pure iodide, featuring relatively compact morphology with a few pinholes for films subjected to gentle heat treatment, which evolve into large, disconnected islands as annealing time or temperature increases.[419]

Similarly, Saliba et al.[420] have observed that slower, gentler anneals produce better surface coverage than more rapid, higher-temperature ones for films fabricated on both mesoporous and block copolymer-templated alumina scaffolds as well as planar Si substrates. Barrows et al.[421] have observed, contrarily, that annealing times well over an hour are necessary to eliminate discontinuities in the film, despite using a similar single-step spin-coating process.[419] However, a number of differences in the work of Barrows et al.[421] may be relevant: the process is conducted in air at ∼40−45% relative humidity, the substrates and solution are preheated to 90 °C prior to spin-coating (i.e., nominally hot-casting, as discussed in section 4.1.1), and the substrate is ITO/PEDOT:PSS. Of these explanations, the first two are unlikely; studies by Eperon et al.[422] and Gao et al.[423] concur that increasing relative humidity worsens surface coverage rather than improving it, while "hot-casting" tends to produce more uniform films without the need for a long postanneal.[258] It is, however, possible that substrate−film interactions may play a significant role in determining the evolution of the morphology and that the presence of moisture might facilitate either the development of pinholes/islands/poor surface coverage or more uniform films by accelerating film transformation kinetics toward the more thermodynamically stable morphology for a given chemistry of the perovskite/substrate interface. You et al.[424] have obtained similar morphology from similarly prepared films on ITO/PEDOT:PSS substrates and propose that annealing under moderate humidity can lead to a beneficial "solvent annealing" effect, as discussed further in section 6.3.1. The diversity of morphologies obtained for this nominally simple deposition technique underscore the complexity of the influence of Cl on perovskite film formation.

An especially subtle complication encountered when working with Cl precursor-derived perovskites is that the choice of Cl-containing precursor(s) used to prepare the solution can play an important role in the film formation, even though nominally identical concentrations of the precursor ions may be present in solution. Williams et al.[425] have demonstrated that films spin-cast from DMF solutions containing 3:1 molar ratios of MAI:$PbCl_2$ crystallize differently from those with a 1:2:1 ratio of MAI:MACl:PbI_2, as seen in SEM images of the final films (Figure 43, panels B and C), although in both cases the film coverage is far superior to that of the 1:1 MAI:PbI_2 precursor (Figure 43A). Additionally, the morphology of the films cast from the 3:1 MAI:$PbCl_2$ molar ratio precursor is not spatially uniform (Figure 43D), containing domains reminiscent of those from the 1:2:1 MAI:MACl:PbI_2 precursor, as well as those shown in Figure 43B. Williams et al.[425] propose that this behavior may indicate greater spatial nonuniformity in the solution itself, brought on by greater difficulty in completely breaking down $PbCl_2$ as opposed to MACl. While thermodynamics may drive the species present in solution toward the same composition in terms of ions and colloids, the kinetics of this transformation appear to be significantly altered, with solutions prepared using $PbCl_2$ favoring a less homogeneous distribution of less isotropic colloids than those using MACl (Figure 43D), providing a possible explanation for the overall morphology difference. The use of the $PbCl_2$ precursor may

DOI: 10.1021/acs.chemrev.8b00318
Chem. Rev. 2019, 119, 3193−3295

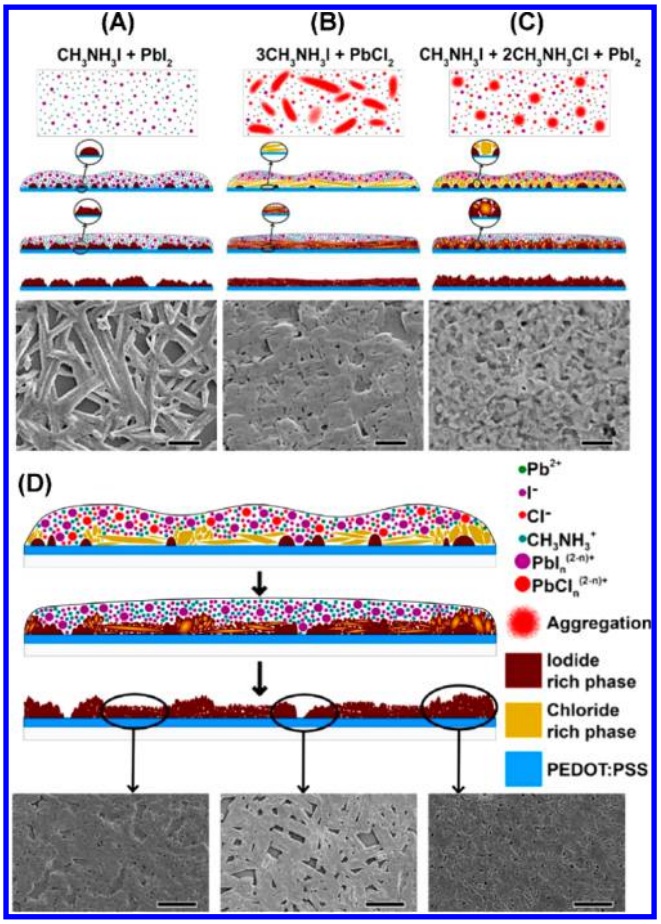

Figure 43. Schematic illustrations and top-surface SEM images of different modes of growth in $MAPbI_3$ films prepared by one-step spin-coating from DMF solutions for stoichiometric: (A) MAI:PbI_2, (B) 3:1 MAI:$PbCl_2$, and (C) 1:2:1 MAI:MACl:PbI_2. Scale bars are 2 μm in A−C. While both of the latter precursors promote improved coverage of the substrate, they lead to distinct morphologies, indicative of associated distinct colloidal species in the precursor solutions. Notably, the 3:1 MAI:$PbCl_2$ precursor leads to regions of distinct morphology at different points on the substrate (D), reflecting the diversity of colloid populations present in the solution. Scale bars are 5 μm in (D). Adapted from ref 425. Copyright 2014 American Chemical Society.

also lead to domains of greater structural coherence (though not necessarily grain size), possibly accounting for the enhanced diffusion length in the chloride-based perovskites.[425] The sensitivity of the film structure to solution preparation may thus account for the great diversity of morphologies observed in different reports, as the finer details of solution preparation and aging are generally not discussed.

Despite the wide variation in microstructures produced by single-step spin-coating from a Cl-containing precursor solution, reports tend to agree on the importance of a crystalline intermediate (or intermediates) that can reside within the film for as long as over an hour at moderate annealing temperatures (∼100 °C) based on consistently observed features in X-ray diffraction/scattering patterns, although few have made an attempt to identify the exact chemical nature of this phase or phases.[175,182,421,426−428] Williams et al.[425] have speculated that the perovskite crystal growth can be mediated by the rapid formation of a $MAPbCl_3$ intermediate phase, which is topotactically transformed to the $MAPbI_3$ structure as MACl diffuses and evolves from the structure under annealing. However, XRD studies by Unger et al.[182] and Nenon et al.[426] have indicated that, while peaks are observed at positions close to those expected for $MAPbCl_3$, there is a lack of conclusive evidence for identification of the intermediate as $MAPbCl_3$ or chloride-rich $MAPbI_{3-x}Cl_x$, or some other related phase. It is not, however, inconceivable that a small amount of $MAPbCl_3$ may remain in the film if some Cl becomes trapped, causing the perovskite to phase segregate into Cl-lean $MAPbI_{3-x}Cl_x$ and $MAPbCl_3$, but it is unlikely to play a dominant role in initial film evolution.

Alternate proposed explanations involve the influence of persistent solvent within the film, which can strongly influence crystallization in the pure iodide films, as discussed in sections 3.1.2.1 and 4.1. Moore et al.[175] and Munir et al.[252] suggest that spin-casting from MAI-rich, Cl-containing mixtures leads to some residual solvent in the film in the early stages of deposition, but that this solvent is not likely to participate within the intermediate structure. In a temperature-dependent XRD study, Nenon et al.[426] have identified $MAPbI_3$·DMF as the initial phase that forms when 3:1 MAI:$PbCl_2$ and 1:1:1 MAI:MACl:$PbCl_2$ solutions are drop-cast. They determined that it quickly converts to a different crystalline intermediate (or intermediates) and thereafter to pure $MAPbI_3$ at higher temperatures, in agreement with the reports above. Some care must be taken, however, in comparing results obtained from studies on drop-cast films against those from spin-casting, as solvent evaporation and film formation dynamics are likely to be quite different.

Although most studies do not attempt to provide a chemical formula of the Cl-containing intermediate, a recent study by Chia et al.[428] proposes that it is a 2D ⟨110⟩-oriented perovskite derivative with composition $(MA)_2PbI_2Cl_2$·MAI, in which the lead halide octahedra form corner-sharing zigzag sheets, analogous to those described by Dohner et al.[429] for the structure of (ethylenedioxy)bis(ethylammonium) lead halides ($EDBEPbX_4$). This structure differs slightly from more conventional perovskites in that a layer of MAI is presumed to lie in the gap between each pair of adjacent lead halide sheets. In the proposed structure, bonding within the sheets is mediated entirely by Pb−I bonds, while the Cl atoms reside at terminal vertices of the lead halide octahedra. Chia et al.[428] thus propose that the final perovskite structure can be straightforwardly obtained from $(MA)_2PbI_2Cl_2$·MAI via a process in which the terminal Cl atoms combine with the excess MA^+ cations and exit the film, while the I atoms intercalated between the layers replace the missing Cl atoms. Since one I atom must replace one Cl in the lead halide octahedra in each adjacent layer (for a total of two missing Cl atoms per I atom), neighboring octahedra are forced to share the I atoms, thus binding the perovskite structure together and forming the 3D corner-sharing network. A virtue of this explanation is that the 2D nature of its structure can easily explain the highly oriented nature of the final perovskite films, since the intermediate is likely to deposit with its layers preferentially parallel to the plane of the substrate. Topotactic transformation of (0k0)-oriented $(MA)_2PbI_2Cl_2$·MAI is, for example, predicted to form tet(100)-oriented $MAPbI_{3-x}Cl_x$ [by way of the (110)-oriented cubic phase].[428] Alternatively, the (021) orientation of $(MA)_2PbI_2Cl_2$·MAI can produce tet(110)-oriented $MAPbI_{3-x}Cl_x$ by way of the (100)-oriented cubic phase. Prominent peaks in the XRD and grazing-incidence X-ray scattering (GIXS) patterns of a partially

DOI: 10.1021/acs.chemrev.8b00318
Chem. Rev. 2019, 119, 3193−3295

transformed film can be assigned to (021) or (0k0) reflections of $(MA)_2PbI_2Cl_2$·MAI, suggesting they may play a significant role in the evolution of the film. Despite the explanation of Chia et al.[428] regarding the nature and function of the intermediate, there are still some open questions. The proposed crystal structure of $(MA)_2PbI_2Cl_2$·MAI was obtained not by single-crystal XRD but by fitting of the predicted GIXS pattern of a simulated crystal structure based on that of $EDBEPbX_4$. The nature of the intermediate therefore awaits confirmation by more rigorous methods. Furthermore, there are some peaks in the GIXS pattern of the intermediate film that cannot be accounted for by the simulated GIXS pattern, which may either indicate a deficiency in the proposed structure or that $(MA)_2PbI_2Cl_2$·MAI is not the only intermediate phase of relevance for the growth of $MAPbI_{3-x}Cl_x$.

A recent report by Stone et al.[430] proposes, based on grazing-incidence XRD, that the Cl-containing intermediate is based on 1D lead halide chains instead of 2D lead halide sheets and has a composition of $(MA)_2PbI_3Cl$ with excess MACl in the precursor film accounted for by amorphous MACl (most likely at surfaces or grain boundaries), rather than $(MA)_2PbI_2Cl_2$·MAI, as proposed by Chia et al.[428] The difference in proposed structures may reflect the fact that the grazing incidence XRD data of Stone et al.[430] appear to be somewhat different than the GIXS data of Chia et al.[428] (although direct comparison is further complicated by differences in the reported range of the scattering vector magnitude q), which is somewhat surprising since the films studied in both reports were prepared by similar methods using the same precursor/solvent combinations. Stone et al.[430] further suggest that extended X-ray absorption fine structure measurements can be best fit to a model of the lead halide octahedra in which I atoms reside in equatorial sites and Cl atoms (along with occasional I atoms) reside in apical sites, leading to an approximate agreement of the Pb:I:Cl stoichiometry with the proposed chemical formula (i.e., 1:3:1), although they acknowledge the assignment is not conclusive. This proposed description of the precursor film has an additional virtue when considering the kinetics of the transformation from precursor to perovskite. Comparison of in situ XRD with in situ XRF measurements of the film during annealing indicates that crystallization of the perovskite begins only once half the Cl has left the film.[430] Stone et al.[430] therefore suggest that evaporation of MACl is the rate-determining step in the transformation and that the precursor phase only begins to break down once the disordered MACl phase has been completely removed from the film.

Overall, while significant strides have been made in understanding film growth for single-step solution deposition of perovskites from Cl-containing precursors, much work remains to be done to determine the nature of this highly complex process. The reports of both Chia et al.[428] and Stone et al.[430] are important steps toward this goal but reach divergent conclusions regarding the nature of the precursor phase. Given the known complexity of these systems, it may well be that both reports are correct and that the different crystal structures proposed may be obtained depending on the subtleties of film preparation. In view of this discrepancy, growth and characterization of single crystals of one or both of the proposed phases would be extremely useful in improving the perovskite community's understanding of film deposition using Cl-based precursors.

While somewhat less commonly used in two-step processes, Cl can also be useful in templating the lead halide precursor phase in these techniques. Fan et al.[431] found that the use of different blends of PbI_2 and $PbCl_2$ in the first stage of the two-step spin-coating precursor leads to very different morphologies of both precursor and perovskite films based on the blend ratio. The variation in morphology is attributed to the formation of the mixed halide PbICl, for which the grains adopt a more needlelike habit than either the pure iodide or chloride. The blended halide morphology is more porous than either of the pure halides, allowing the perovskite grains to grow more freely and without strain (as noted in section 4.2.1). Excessive porosity can, however, lead to large-scale discontinuity and roughness of the films, and it was found that an equimolar blend of PbI_2 and $PbCl_2$ yields optimal J_{SC}, V_{OC}, and FF of the associated PSCs.[431] Yang et al.[174] have noted that using a spin-cast PbICl film as the precursor in the VASP process (section 4.2.3) can lead to enhanced apparent grain size compared to a pure PbI_2 film. Temperature-dependent XRD analysis of film transformation indicates a relatively straightforward pathway by which the PbICl is first converted into PbI_2 and thereafter to $MAPbI_{3-x}Cl_x$. The enhanced grain size may reflect the fact that the presence of Cl in the precursor delays formation of the perovskite phase considerably [the tet(110) XRD peak is evident within minutes for the pure iodide but does not build up appreciable intensity for over an hour for the PbICl precursor],[174] which may afford more time for grain coarsening. Alternatively, it may help grain growth by increasing grain boundary mobility, given its preferential location at the grain boundaries as seen in TOF-SIMS.[174] There is no evidence of any intermediate phases affecting perovskite growth in this study.

While perovskite films prepared by single-step spin-coating from Cl-based precursors were extensively reported in the early years of research on PSCs, they have become somewhat less common recently, perhaps because of the complexity and difficulty of understanding the process relative to more technically laborious but controllable techniques such as two-step deposition or solvent engineering, as well as emphasis on FA- or triple-cation based absorbers over pure MA. The long annealing times required to transform the precursors and/or intermediates to phase-pure perovskite also represent a significant disadvantage. Nevertheless, Cl-containing additives are still often employed in a less dominant role. For example, Yang et al.[277] have used an MACl additive to improve film uniformity and apparent grain size while reducing annealing time (relative to excess MAI) in high-performance doctor-bladed $MAPbI_3$ PSCs, as noted in section 4.3.1. The recent published efficiency record for PSCs derives from absorbers prepared by solvent engineering and of nominal composition $(FAPbI_3)_{0.95}(MAPbBr_3)_{0.05}$, but containing equal parts $MAPbBr_3$ and MACl by weight in the precursor solution.[265] However, no reason is given for the inclusion of MACl in this process beyond a brief admonition that device performance suffers without it, and a reference to previous work[116] that contains no mention of MACl. It may simply be that a primary benefit of Cl is indeed to passivate defects as a low-concentration impurity and increase the intrinsic carrier diffusion length of the perovskite, as suggested in early work;[13,412] however, it appears that there is still much work to be done to elucidate effects of Cl additions on perovskite film growth and properties.

DOI: 10.1021/acs.chemrev.8b00318
Chem. Rev. 2019, 119, 3193−3295

6.2. Substitutional Modifications in 3D Perovskites

While the prototypical perovskite $MAPbI_3$ has a band gap appropriate for PV energy conversion (~1.55 eV) as well as otherwise excellent physical properties, its intrinsic drawbacks mainly pertain to stability and toxicity, which pose significant challenges (also, its band gap is not suitable for either the top or bottom cell in a tandem device). Stability is a particularly important and perhaps intrinsic problem. DFT calculations predict for $MAPbI_3$ a negative formation energy[432,433] or enthalpy,[434] albeit a very low one, but some experimental results suggest that the formation enthalpy is actually positive.[102] Other experimental results indicate that the Gibbs free energy of $MAPbI_3$ formation still favors spontaneous formation of the perovskite, although with a weak driving force.[103,104] It is generally agreed that, even though reaction thermodynamics force $MAPbI_3$ to form over its precursors, this force is slight and the decomposition is difficult to avoid. This problem may be addressed by removing, at least partially, the MA cation in favor of inorganic cations (such as Cs^+) or those organic cations that have a greater affinity for the perovskite lattice and are therefore less easily removed (such as FA^+). Toxicity of the perovskite may be somewhat reduced by substituting Sn for Pb. An additional feature of this exchange is that the band gap may be lowered farther into the infrared relative to $MAPbI_3$,[101,435] enabling the construction of bottom cells in an all-perovskite tandem solar cell architecture[436] or improved capability for emitting or detecting infrared radiation. Alternatively, the band gap of halide perovskites may be tuned to span the entire visible range by varying the halide composition,[5−7] a trait useful for other optoelectronic applications such as LEDs or lasers. Although each of these families offers unique advantages over $MAPbI_3$, they are also associated with unique challenges that may affect the films during or after processing. In the sections below, these challenges will be considered, along with changes to the processing methods that may be employed to avoid them.

6.2.1. A-Site Substitution. *6.2.1.1. Formamidinium-Based Perovskites.* The formamidinium cation (FA^+) has emerged as a promising replacement for MA^+, as it can reduce the perovskite's band gap and significantly improve its thermal stability,[4,111,112,437] as well as affording the possibility for higher carrier diffusion lengths than purely MA-based perovskites;[4,12,13,116,438] in particular, carrier lifetime measurements on blended $FA_{0.55}MA_{0.45}PbI_3$ single crystals indicate that the mixed composition may have superior carrier lifetime to either of the pure compounds.[439] Although FA-based perovskites are relatively stable against thermal decomposition, they are not thermodynamically stable at room temperature, as the black perovskite phase of $FAPbI_3$ (α-$FAPbI_3$) transitions to a yellow hexagonal polymorph (δ-$FAPbI_3$) below 60 °C.[111,112] Consequently, higher annealing temperatures (usually well over 150 °C) are generally required in order to minimize the presence of the nonperovskite phase, and the resulting films will revert over time to the more favorable δ-$FAPbI_3$.[4,437] Fortunately, a simple strategy exists to improve the favorability of α-$FAPbI_3$ (i.e., alloying with other cations and anions can significantly reduce the tendency to form the yellow phase and thus enable straightforward fabrication of the FA-based perovskite films). The success of this strategy is evinced by the preponderance of high-performance PSCs (including many of the recent record-setting cells) that use FA as the majority component on the A site,[25−28,89,116,265,440,441] as well as the demonstration of high-performance FA-based PSCs with relatively good operational stability.[338,442] Jeon et al.[116] observed that the perovskite phase could be stabilized by incorporating MA and Br as partial substituents (15 mol % replacement for FA and I, respectively) in $FAPbI_3$ using the solvent engineering process (section 4.1.2). In addition to phase stability, the presence of $MAPbBr_3$ also appears to improve film morphology. Films with lower $MAPbBr_3$ content are more discontinuous, but the optimal 15 mol % concentration yields the desired compact grain structure.[116]

Other alloying components may be employed to improve the quality of FA-based films and associated devices. Lee et al.[115] found that partial substitution of Cs for FA (10 mol %) in $FAPbI_3$ prepared by solvent engineering not only improves film morphology, leading to grains that appear to be larger and more clearly defined, but also produces more favorable recombination kinetics (as measured by transient photovoltage decay). However, excessive amounts of Cs (15 mol % and above) lead to phase segregation of the nonperovskite $CsPbI_3$ phase, illustrating a limited compositional range for the $FA_{1-x}Cs_xPbI_3$ solid solution. Similar results were obtained by Yu et al.,[443] who found that 20 mol % incorporation of Cs could improve PSC operational stability and increase minority carrier lifetime in the film by an order of magnitude, as probed with TRPL. Furthermore, the annealing temperature required to achieve the black α-$FAPbI_3$ phase could be reduced from 150 to 100 °C when the precursor Cs concentration exceeds 10 mol %. Contrary to the results of Lee et al.,[115] the authors observed that the apparent grain size of the mixed-cation absorber decreases relative to the pure $FAPbI_3$ perovskite when prepared using solvent engineering, but that this effect could be mitigated by the addition of a small amount of $Pb(SCN)_2$ to the precursor solutions (effects of SCN incorporation will be further discussed in section 6.2.3.2).[443] Partial substitution of Br for I in the above system leads to more persistent problems with achieving sufficiently large apparent grain size, but these issues can be mitigated with a combination of adding $Pb(SCN)_2$ and annealing the films in DMF vapor (using the procedure described in section 5.1.2).[444]

Two factors may contribute to the enhanced thermodynamic stability and ease of formation of the mixed-cation/anion perovskites and associated films based on these materials. On one hand, the size of the FA^+ cation results in an unfavorable Goldschmidt tolerance factor[67] for the $FAPbI_3$ perovskite. Therefore, replacement of FA^+ by smaller cations such as Cs^+ or MA^+ can help to reduce the average size of the "A" cation, yielding a more favorable tolerance factor.[445] On the other hand, it has been proposed that the entropy of mixing afforded by cation blending can help stabilize the $FA_{1-x}Cs_xPbI_3$ perovskite phase relative to a two-phase mixture of the nonperovskites δ-$FAPbI_3$ and δ-$CsPbI_3$, which have dissimilar structures and are, therefore, unlikely to form solid solutions.[446,447] The latter effect may be especially potent if cations on both "A" and "B" sites are mixed; for example, Eperon et al.[276] report that both $FAPb_{0.5}Sn_{0.5}I_3$ and $FA_{0.75}Cs_{0.25}Pb_{0.5}Sn_{0.5}I_3$ films/PSCs prepared by the antisolvent/solvent extraction process are more stable in humid conditions than $FAPbI_3$ films/PSCs (especially surprising given the well-known tendency of divalent Sn to oxidize in air). The robustness of these compounds cannot be convincingly ascribed to a more favorable tolerance factor, as the ionic radii of divalent Sn and Pb differ only slightly.[448] Zong et al.[449] further note that, while that the compositional range of $FA_{1-x}Cs_xPbI_3$ is constrained to relatively low Cs

DOI: 10.1021/acs.chemrev.8b00318
Chem. Rev. 2019, 119, 3193−3295

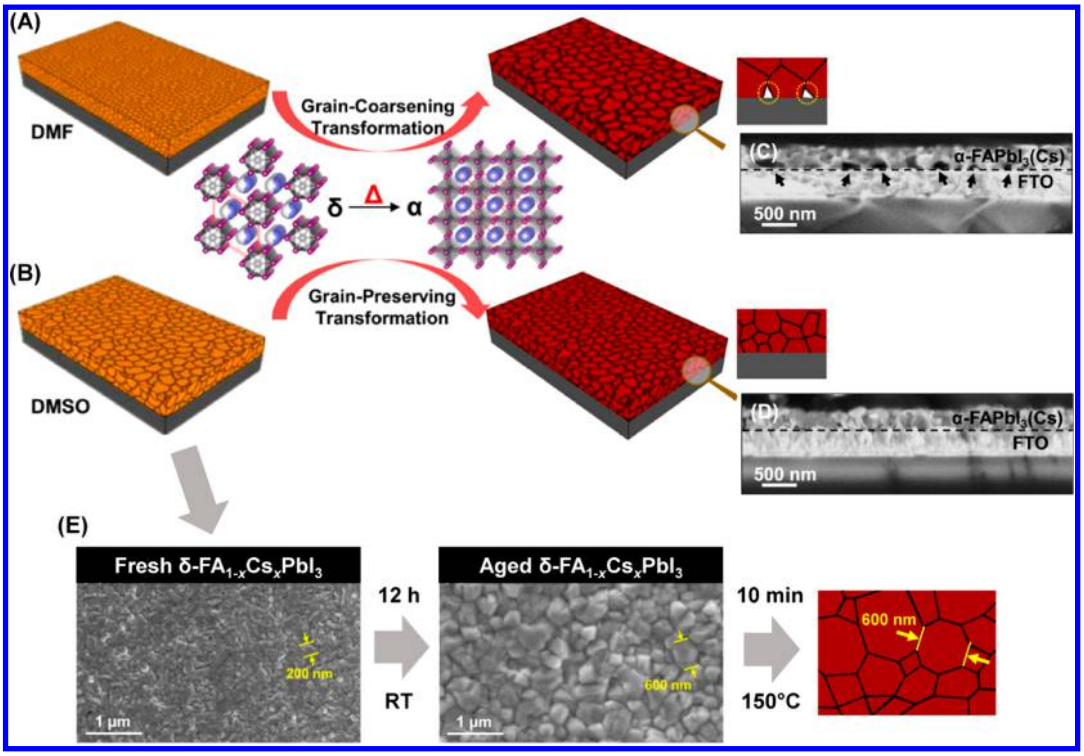

Figure 44. Schematic illustration of $FA_{1-x}Cs_xPbI_3$ films deposited from (A) DMF and (B) DMSO, and (C−D) corresponding cross-sectional SEM images. Although microstructure appears to be similar in the two cases, voids form at the interface with the substrate in the former but not the latter case when the thin film is transformed from δ-$FAPbI_3$ to α-$FAPbI_3$. (E) Top-surface SEM images show that aging of the δ-$FAPbI_3$ thin film at room temperature promotes grain growth, which carries over to the α-$FAPbI_3$ thin film after annealing. Adapted from ref 450. Copyright 2017 American Chemical Society.

concentrations by rejection of nonperovskite $CsPbI_3$, the $(FAPbI_3)_{1-x}(CsSnI_3)_x$ system is fully miscible, entirely suppressing nonperovskite impurities. The stability of this system may arise from a combination of entropic effects and a high degree of structural similarity between the $FAPbI_3$ and $CsSnI_3$ perovskite phases. It is, therefore, likely that judicious tailoring of the perovskite composition to optimize for both maximum entropy of mixing and structural compatibility will be a promising strategy for formation of high-quality mixed-cation/anion perovskite films.

Film preparation pathway and resulting morphology also play an important role in phase stability. Liu et al.[450] investigated formation of $FA_{1-x}Cs_xPbI_3$ films by the anti-solvent/solvent extraction process (section 4.1.4), finding that processing from a DMF solvent leads to interfacial voids that can significantly impair stability of the perovskite phase, while films prepared using DMSO do not suffer from these problems (Figure 44, panels A−D). The authors propose, based on observations that significant apparent grain coarsening is observed upon annealing DMF-deposited films but not within the DMSO-deposited analogs, that the simultaneous occurrence of rapid grain growth and phase conversion may promote the formation of these interfacial defects. Therefore, decoupling of these processes should lead to a more stable microstructure and prevent void formation, making the perovskite film less susceptible to degradation. Liu et al.[450] also found that, although the presence of δ-$FAPbI_3$ is generally undesirable in the final perovskite film, it, like other intermediate phases, can be useful for manipulation of the perovskite film structure/morphology. For example, after depositing δ-$FA_{1-x}Cs_xPbI_3$ from DMSO and letting the film stand in a closed Petri dish at room temperature for 12 h, the apparent grain size increased roughly 3-fold without losing its compactness (Figure 44E). The film can then be converted to an α-$FA_{1-x}Cs_xPbI_3$ film with identical overall microstructure by postannealing at 150 °C.[450]

More complicated mixtures of cations have also been successful at improving the quality of FA-based perovskite films. Saliba et al.[25] introduced a triple-cation composition, comprising a mixture of Cs^+, MA^+, and FA^+ on the "A" site and I^- and Br^- on the "X" site, which they claimed could suppress nonperovskite impurity phases present in the mixed MA-FA system. Furthermore, problems pertaining to sensitivity of the film deposition process to "hidden variables" (e.g., temperature fluctuations or residual solvent vapors) could be reduced by addition of Cs to this system.[25] PSCs from a number of laboratories using triple-cation (i.e., Cs-FA-MA) absorbers prepared by the solvent engineering process have reliably exceeded 20% PCE.[26,121,266,451] Some have reached a remarkably high FF of 84% despite very small apparent grain size (∼100 nm),[121] supporting the proposal that grain boundaries in halide perovskite films are relatively benign (if properly terminated/passivated).[14]

Precise mixing of the cations can also have a significant impact on the film processing. Matsui et al.[16] investigated the effects of varying the MA/Cs cation ratio in $(FA_{0.8}MA_{0.2-x}Cs_x)Pb(I_{0.83}Br_{0.17})_3$, finding that the presence of Cs could allow the formation of the perovskite phase at room temperature by solvent engineering, obviating entirely the need for the high-temperature processing typically necessary for FA-based perovskites. At Cs mole percentages of 10% or above, XRD peaks corresponding to $MA_2Pb_3I_8{\cdot}2DMSO$ as well as those

DOI: 10.1021/acs.chemrev.8b00318
Chem. Rev. 2019, 119, 3193−3295

indicative of δ-$FAPbI_3$ were eliminated. The authors also note that increasing the MA/Cs ratio increases the apparent grain size, though at some cost to uniformity, especially when Cs is completely removed.[16] This work sheds light on the role of Cs in the formation of the perovskite films, with Cs evidently interfering with the interactions between the perovskite precursors and the solvent. Fourier-transform infrared spectroscopy (FTIR) of the precursor solution for various concentrations of Cs suggests that hydrogen bonds between the MA^+/FA^+ cations and the Pb−I network are strengthened with the addition of Cs, allowing the generation of more spatially isotropic nuclei composed of the perovskite itself rather than a complex with the solvent. This pathway allows the perovskite to form at room temperature with a densely packed microstructure but at the cost of small apparent grain size (Figure 45). The addition of MA can alleviate this latter problem somewhat by recovering some of the interaction with the solvent, retarding crystallization and ultimately leading to films with larger grains and superior crystallinity. Matsui et al.[16] concluded that an equimolar blend of MA and Cs provides the best compromise for PSCs containing a room-temperature-deposited absorber, with PCE reaching parity with devices having the absorber annealed at 100 °C. However, Singh and Miyasaka[452] note that the processing atmosphere represents an important consideration when optimizing the cation blend and that addition of 5 mol % CsI to the precursor solution of $(FAPbI_3)_{0.83}(MAPbBr_3)_{0.17}$ deposited by a similar process but in relatively dry air (relative humidity <25%) rather than nitrogen yields optimal morphology (and PSC performance), with apparent grain size up to 1 μm.

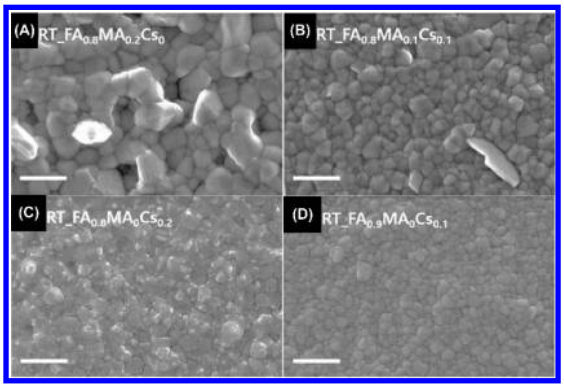

Figure 45. Top-surface SEM images of the morphology of FA-based perovskite thin films for a variety of MA and Cs compositions, before annealing. The scale bar is 500 nm in all images. Reprinted with permission from ref 16. Copyright 2017 Wiley-VCH.

Rb can also be used in place of Cs in FA-based PSCs. Gas-quenching[274] (section 4.1.3) or solvent engineering[453,454] (section 4.1.2) processes yield comparable film morphologies, although significantly higher annealing temperatures (∼150 °C) are necessary to form the black α-(FA,MA,Rb)PbI_3 phase than when Cs is used. Turren-Cruz et al.[455] report that, not only can Rb prevent the formation of δ-$FAPbI_3$ in mixed MA-FA-Rb lead iodide perovskites, it can also boost apparent grain size, mobility, and carrier lifetime, leading to high-performance PSCs in which hysteresis and other slow transients are suppressed. However, the benefits of Rb are not universally observed or agreed upon. Hu et al.[456] report that, while Cs incorporation contracts the $(FA_{0.83}MA_{0.17})Pb(I_{0.83}Br_{0.17})_3$ lattice in films prepared by solvent engineering, Rb appears to very slightly expand it, indicating that Rb is not actually incorporated into the lattice (at least, not as a substitutional cation on the "A" site), an observation corroborated by solid-state nuclear magnetic resonance measurements.[457] The lattice expansion is rationalized by noting that peaks in the XRD pattern, similar to those expected for the nonperovskite $RbPbI_3$ but shifted to slightly higher angle, may indicate that this phase also includes Br, forming $RbPb(I_{1-x}Br_x)_3$ with a predicted halide ratio matching approximately that of the $(FA_{0.83}MA_{0.17})$-$Pb(I_{0.83}Br_{0.17})_3$ precursor solution. In addition to the undesired effect of nonperovskite secondary phase formation, Rb also appears to change the composition (and, thus, material properties) of the surrounding perovskite matrix by altering its halide ratio. The competition for Br by the Rb-based phase may thus explain the expansion of the FA-perovskite phase, which may then be due to depletion of Br (relative to I) rather than any direct effect due to Rb. Hu et al.[456] posit that the affinity between Rb and Br causes the latter to leach out of the perovskite, but the lattice expansion/iodide enrichment could also be due to the fact that Rb is added to the $(FA_{0.83}MA_{0.17})$-$Pb(I_{0.83}Br_{0.17})_3$ precursor solution as RbI, which will therefore tend to increase the overall I/Br ratio in proportion to the amount of Rb. The presence of Rb also appears to exacerbate moisture sensitivity of these materials, leading to further segregation of photoinactive phases, in this case $RbPb_2I_4Br$.[456] Thus, while it appears that addition of Rb may have some benefits to perovskite film quality, these effects are far less established compared to those offered by Cs.

6.2.1.2. Cesium-Based Perovskites. Like $FAPbI_3$, $CsPbI_3$ is a more thermally stable alternative to $MAPbI_3$ with a similar bandgap (1.7 eV); however, this material and associated films also suffer from instability of the perovskite phase relative to a nonperovskite phase at room temperature, especially when exposed to ambient atmosphere.[113,114,458] From a tolerance factor perspective, $CsPbI_3$ has the opposite problem relative to $FAPbI_3$, since the Cs^+ cation is slightly too small to be integrated into the perovskite crystal structure at ambient temperatures. However, the $CsPbBr_3$ perovskite phase is stable at room temperature, as the resulting shrinkage of the anionic lattice can more easily accommodate the small Cs^+ cation on the "A" site. While substituting Br^- for I^- does increase the bandgap (∼2.25 eV for the pure bromide),[459] which is undesirable in the context of single-junction PV, blended anion mixtures can help to recover a lower band gap while maintaining the benefits of enhanced stability[117,460,461] (possibly through a confluence of improved tolerance factor and entropic effects). The larger band gap also allows $CsPbBr_3$ to emit light in the visible range, and the color of this emission can readily be tuned by alloying with Cl or I, making it a promising material for LEDs.[5]

An interesting possible resolution to $CsPbI_3$ phase instability relies on the observation that a fine-grained microstructure may actually benefit the stability of the perovskite phase. Eperon et al.[114] find that, by adding HI to a precursor solution of $CsPbI_3$ deposited by one-step spin-coating from a DMF solution, the black perovskite phase can be stabilized while the apparent grain size is reduced. This report may be interpreted in the context of studies on $CsPbI_3$ nanocrystals, which indicate that smaller crystallite size correlates with greater thermodynamic stability, possibly as the result of increasing importance of surface contributions to the overall free energy as grain size decreases.[100,462] For cases in which thermodynamics are strongly affected by surface energy, grains or

DOI: 10.1021/acs.chemrev.8b00318
Chem. Rev. 2019, 119, 3193−3295

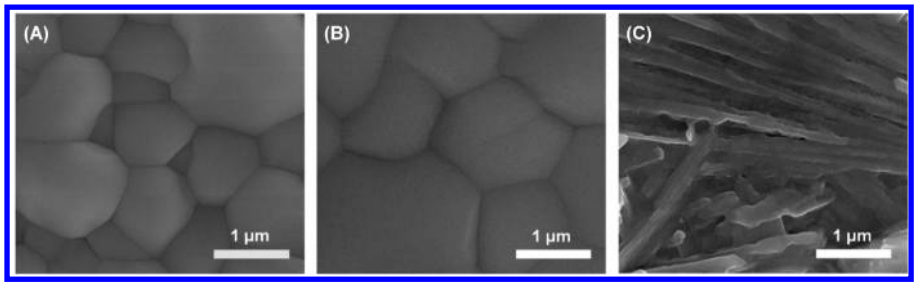

Figure 46. Top-surface SEM images showing the morphology of thin films prepared by the two-step dip-coating process: (A) $CsPbBr_3$, (B) $CsPbIBr_2$, and (C) $CsPb_{0.9}Sn_{0.1}IBr_2$. Adapted from ref 461. Copyright 2017 American Chemical Society.

nanocrystals having a more isotropic shape may become increasingly favorable due to their low surface area-to-volume ratio. Indeed, perhaps the most successful means of working with the perovskite phase of $CsPbI_3$ is to fabricate thin films from presynthesized colloidal quantum dot solutions, which display much better long-term stability of the perovskite phase.[462,463] Swarnkar et al.[462] synthesized $CsPbI_3$ quantum dots by injecting Cs-oleate in 1-octadecene (ODE) into a solution of PbI_2, oleic acid, and oleylamine in ODE. After purification, the quantum dots were dispersed in octane and spin-cast onto the substrate, after which a treatment of lead acetate or nitrate in methyl acetate induces replacement of the native ligands and improves film cohesion. Repeating the coating and ligand treatment process enables control over the film thickness. The thin films thus obtained appear to conformally coat the substrate (as judged from cross-sectional SEM images) and perform well as the active layer in PSCs and LEDs.[462] Sanehira et al.[463] find that post-treatment of such $CsPbI_3$ quantum dot films with FAI (by immersion in a solution of the salt in ethyl acetate) can improve the coupling between quantum dots, enhancing the carrier mobility without appreciably changing film morphology or properties, apart from a slight blueshift in the PL emission. PSCs fabricated using these films as absorber reach a certified PCE of 13.4%, a new record for PV devices using a quantum dot-based absorber.[24]

A unique challenge associated with Cs-rich compositions is that Cs halides are typically even less soluble than the Pb halides,[464−466] particularly CsBr,[117] which complicates traditional solution-processing methods as it can be challenging to form precursor solutions with balanced stoichiometry of the Cs and Pb (or other metal) halides at high concentrations. While it is still possible to prepare Cs-based perovskite films using traditional solvents such as DMF, or by using organic ligands to allow dispersion of perovskite quantum dots in nonpolar solvents, vapor-processing methods eliminate challenges associated with solubility, especially given that all-inorganic perovskites are significantly less sensitive to the effects of heating than hybrid analogs. Such methods, therefore, offer a facile route to the preparation of high-quality inorganic halide perovskite thin films. Hutter et al.[465] found that, while it was possible to deposit $CsPbI_3$ by solvent engineering (using a mixed DMF/DMSO solvent) and to obtain apparently large, compact grains, similar morphology could be obtained by thermal coevaporation. Furthermore, the evaporated films demonstrated vastly superior carrier lifetimes (as measured by time-resolved microwave conductivity or TRMC) as well as enhanced PV performance relative to the solvent-engineered films,[465] hinting at the possibility of detrimental solvent-precursor interactions. Frolova et al.[467] and Chen et al.[468] have likewise demonstrated that similar morphologies of $CsPbI_3$ and $CsPbI_2Br$ thin films, respectively, can be obtained along with high PV performance using thermal coevaporation.

Sequential solution deposition offers another means of managing the solubilities of the Cs and Pb halide precursors, avoiding the challenge of forming a stoichiometric balance at high concentrations. Kulbak et al.[469] demonstrated compact grains with large apparent size of $CsPbBr_3$ using a variant of the dip-coating process described in section 4.2.1, wherein first $PbBr_2$ is spin-cast from a DMF solution, which is then converted to perovskite by immersion in a warm solution of CsBr in methanol. Liang et al.[461] attained similar microstructures using essentially the same process for both $CsPbBr_3$ and $CsPbIBr_2$ but found that addition of Sn has a surprising impact on the morphology of the thin films. While the pure Pb perovskites $CsPbBr_3$ and $CsPbIBr_2$ have compact grains with apparent size over 1 μm (Figure 46, panels A and B), similar to the microstructure obtained by Kulbak et al.,[469] addition of Sn leads to a densely packed rodlike morphology (Figure 46C).[461] Nevertheless, this microstructure remains continuous (unlike the rodlike structure typically witnessed for one-step spin-coating of $MAPbI_3$, as seen in Figure 20) and evidently does not exact a penalty in any device performance parameters relative to the pure Pb analogs but rather improves J_{SC} as well as thermal and (surprisingly) environmental stability. Compact, apparently large-grain $CsPbBr_3$ perovskite films can also be obtained from the two-step spin-coating process (section 4.2.2). Duan et al.[464] first deposited $PbBr_2$ thin films as in the above examples but then spin-cast the CsBr solution onto the substrate and thereafter annealed it. Repeating this process several times generates compact grains with large apparent size predominantly composed of $CsPbBr_3$, although some impurities of CsBr-lean $CsPb_2Br_5$ and Cs-rich Cs_4PbBr_6 appear in the thin film XRD patterns. Fewer CsBr coating cycles than the optimum (4 cycles) generally lead to a $CsPb_2Br_5$-dominant film, while a higher number yield a Cs_4PbBr_6-dominant film. Even though the optimal $CsPbBr_3$ thin film contains these impurities, they evidently do not severely hurt the optoelectronic properties of the film, as HTL-free PSCs based on these films reach PCE of nearly 10%, a reasonably high value in view of the wide band gap of $CsPbBr_3$.[464]

As for the case of $MAPbI_3$ (as discussed in section 6.1), stoichiometry modulation of Cs-based perovskite films can be a useful tool for tuning film quality, particularly through the use of Cs-halide-rich precursors. Ma et al.[470] have observed that luminescence of $CsPb(I_{1-x}Br_x)_3$ films prepared by dual-source evaporation from CsBr and PbI_2 sources declines as the composition moves from CsBr-rich to PbI_2-rich, although the PL lifetime is higher for films with a balanced stoichiometry. The high PL intensity of the CsBr-rich films suggests that the

DOI: 10.1021/acs.chemrev.8b00318
Chem. Rev. 2019, 119, 3193−3295

lifetime reduction most likely reflects enhanced radiative rather than SRH recombination. PL mapping also indicates that luminescence appears to be most intense from the smallest grains for both CsBr-rich and stoichiometric films. While the microstructure is similar across each stoichiometry (compact grains, with secondary phase impurities in the off-stoichiometric films), the CsBr-rich films appear to have the smaller grains.[470] This feature may explain the strength of the overall luminescence for the CsBr-rich films, if the PL is activated by defects with strong radiative transitions at the grain surfaces, or if PL-inactive defects at the surfaces are passivated by the excess CsBr. Yantara et al.[471] further demonstrated that the PLQY and luminance of $CsPbBr_3$ LEDs prepared by simple one-step spin-coating from DMSO can be improved using a CsBr-rich precursor solution, putatively due to trap passivation as the addition of the extra CsBr does not appreciably alter the film morphology. Ling et al.[472] have examined stoichiometric and CsBr-rich $CsPbBr_3$ deposited by sequential thermal evaporation of the precursors and demonstrated improved luminescence intensity and quantum yield in the latter. They attribute the luminescence enhancement to suppression of deep trap states in favor of shallow, radiatively active states at the interface between $CsPbBr_3$ and low-dimensional Cs_4PbBr_6 generated by the excess CsBr.[472] Excess CsBr might also help to passivate bulk as well as surface defects. Cho et al.[473] found that a slight excess (1.1 times the $PbBr_2$ concentration) of CsBr in the precursor solution for one-step spin-cast $CsPbBr_3$ films enhances the current efficiency and luminance of LEDs based on these films, and they attribute this improvement to the suppression of metallic Pb defects.

6.2.1.3. Other Monovalent Cations. Although the chemical formula of the lead halide perovskites would seem to naturally accommodate alkali metals, the 3D structure at room-temperature does not easily admit even the largest non-radioactive member of this family, Cs, especially in the case of the iodide perovskites (as noted in the previous section). Nevertheless, addition of Cs in small amounts has been a successful strategy for the fabrication of high-performance PSCs (as noted in section 6.2.1.1). Therefore, the broader family of alkali-metal substitutions is a logical area of further chemical exploration. Even without substitution within the crystal structure, alkali metals can influence grain growth. Bag and Durstock[474] found that, although it did not appear to change the overall chemical composition of the film, small amounts (0−5 mol %) of NaI added to the PbI_2 precursor solution in conjunction with DMF-based solvent annealing (section 5.1.2) significantly enhances the apparent grain size and compactness of $MAPbI_3$ films prepared by the 2-step dip-coating method (section 4.2.1). Excessive amounts (>5 mol % of NaI), however, lead to formation of pinholes and voids (Figure 47). The improvement in grain structure for small amounts of NaI addition correlates with a substantial boost in PSC performance driven predominantly by an increase in J_{SC}, although optimal performance is achieved at 2 mol % Na, well below the point at which film morphology becomes discontinuous.[474] This result indicates that excessive Na incorporation may have additional detrimental effects beyond the influence on morphology.

Similar improvements in photocurrent were reported by Abdi-Jalebi et al.[475] using essentially the same two-step perovskite deposition process, though using a mesoporous rather than planar architecture. In this latter work, addition of less than 2 mol % NaI to the PbI_2 solution leads to a more

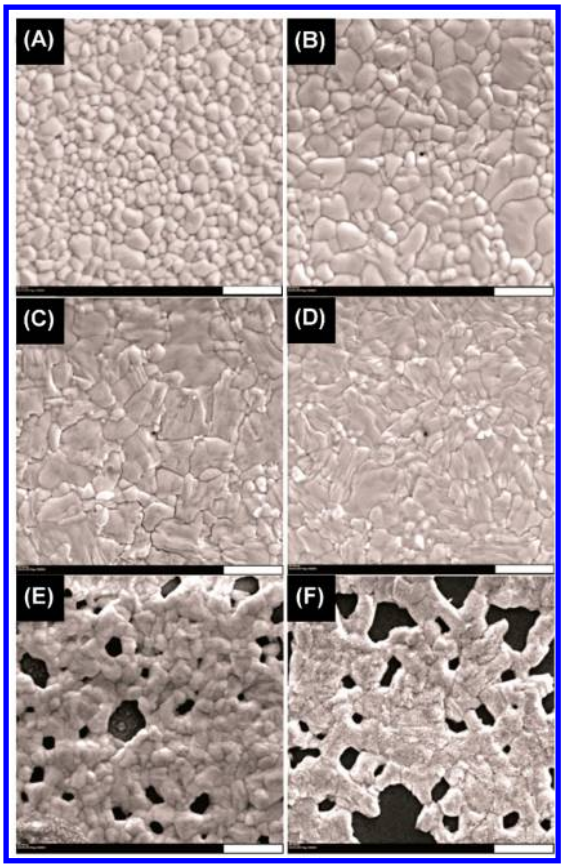

Figure 47. Top-surface SEM images of $MAPbI_3$ perovskite thin films with different NaI additions to a PbI_2 solution in the 2-step process: (A) 1 mol %, (B) 3 mol %, (C) 5 mol %, (D) 6 mol %, (E) 6 mol %, and (F) 8 mol %. While 1−3 mol % Na addition appears to lead to large, compact grains, 6 mol % leads to inconsistent coverage on the substrate, and 8 mol % results in the formation of large voids. The scale bar in all images is 2 μm. Adapted from ref 474. Copyright 2016 American Chemical Society.

porous PbI_2 precursor thin film, which aids the conversion to $MAPbI_3$ by providing pathways for the MAI to infiltrate the PbI_2 network (as discussed in section 4.2.1). However, this additive level also leads to pinholes in the perovskite capping layer, exacting a slight penalty in V_{OC}. These results are consistent with those of Bag and Durstock[474] described above, who find that the final $MAPbI_3$ films become less continuous with increasing Na incorporation, which may reflect the increasing porosity of the PbI_2 precursor film. The inferior morphology obtained by Abdi-Jalebi et al.[475] relative to that obtained by Bag and Durstock[474] may simply reflect that the $MAPbI_3$ films were solvent-annealed in the latter case but subjected to a regular thermal anneal in the former.

The benefits of Na and other alkalis (at least at low enough incorporation levels) may go beyond their influence on film morphology (i.e., alkali metals may also passivate defects). Bi et al.[476] witnessed improvement in the PCE of PSCs stored in an inert environment, driven by J_{SC}, as well as a substantial presence of Na^+ in TOF-SIMS profiles of these films/devices. The authors speculated that migration of Na^+ from the soda-lime glass substrate might passivate MA^+ vacancies at grain boundaries. Deliberate incorporation of Na by the formation of a Si/NaCl/PTAA/$MAPbI_3$ stack leads to gradual increase in the film PL lifetime, which also scales with the amount of NaCl used to form the interlayer. Control stacks without Na (either

DOI: 10.1021/acs.chemrev.8b00318
Chem. Rev. 2019, 119, 3193−3295

deliberately added or already present in the substrate), or with a thicker PTAA layer, do not display a similar change in PL lifetime. Na diffusion from the substrate is also known to have a beneficial impact in CIGS solar cells, providing well-characterized precedent for this type of phenomenon.[477,478]

Chang et al.[479] found that substituting small amounts (<1 mol %) of either Na or K could boost PL intensity and lifetime for $MAPbI_3$ films prepared by solvent engineering, with a concomitant increase in the J_{SC} and FF of associated PSCs. Although grain growth also appears to be induced by the alkali metals, this effect is only significant at incorporation levels ≥1 mol % (similar to the results observed by Bag and Durstock[474]), at which point their presence becomes detrimental to PSC performance. A subsequent study by Tang et al.[480] on K incorporation into mixed-cation $FA_{0.85}MA_{0.15}Pb(I_{0.85}Br_{0.15})_3$ (also prepared by solvent engineering) finds this system to have much higher alkali metal tolerance, with optimal PSC performance and suppressed hysteresis at 5 mol % KI addition to the perovskite solution.[480] Intriguingly, a systematic upward shift in lattice constant and downward shift in the band gap are observed for K addition levels of up to 20 mol %, although some rejection of nonperovskite phases is observed at this upper value. Abdi-Jalebi et al.[481] have shown that addition of KI to the precursor solution of $Cs_{0.06}FA_{0.79}MA_{0.15}Pb(I_{0.85}Br_{0.15})_3$ thin films prepared by solvent engineering can lead to internal PL quantum yields of ∼90% when a 5−40 mol % excess is used, although with compromised carrier mobility at levels over 10 mol %. On the basis of SEM/EDS characterization, they attribute the improved luminescence to passivating effects of a K- and Br-rich phase that decorates film surfaces and grain boundaries. They also observe a redshift of the band gap with increasing KI and propose that this behavior arises due to a preferential interaction of K with Br, which makes the bulk of the perovskite slightly more I-rich, thus lowering the band gap.[481] These findings generally agree with those of Tang et al.[480] but suggest that the effects of K addition on the perovskite lattice are indirect, rather than arising as a direct result of incorporation as an interstitial or substitutional defect (note similarity with the case of Rb incorporation,[456] as noted in section 6.2.1.1). Addition of K can also benefit inorganic $CsPbI_2Br$ perovskites prepared by one-step spin-coating, with 7.5 mol % substitution of K for Cs reportedly leading to enhanced apparent grain size, PSC performance, and operational stability.[482] While there is no clear consensus on the precise levels of light alkali metals required to attain the benefits of larger grains and defect passivation within the resulting films, it seems clear that light alkali addition is generally helpful, perhaps through the passivation effect described by Abdi-Jalebi et al.[481] The optimal alkali additive amounts will likely vary depending on the perovskite composition and deposition recipe.

Similar benefits have been observed when guanidinium [GA^+ or $C(NH_2)_3^+$] is incorporated into the precursor. De Marco et al.[483] demonstrated that partial replacement of MAI with GAI or GACl within the solution used in the second step of the two-step spin-coating process (section 4.2.2) substantially increases the PL lifetime of $MAPbI_3$ films to nearly a microsecond, a 10-fold increase relative to the pristine perovskite, in conjunction with modest improvements in apparent grain size and film roughness. The choice of GAI or GACl did not alter the conclusions of the study, suggesting that the benefits observed are intrinsic to GA incorporation rather than the choice of anion. Hou et al.[279] also observed a similar, though less drastic effect on the PL from the addition of GACl in all-mesoporous cells (as described in section 4.1.5). Jodlowski et al.[434] demonstrated that up to 25 mol % GAI can substitute into the precursor solution of $MAPbI_3$ thin films (prepared by solvent engineering) without causing phase segregation, while GA levels below this limit continuously shift the XRD peak positions. The presence of GA below the solubility limit also reportedly boosts J_{SC}, V_{OC}, FF, and thermal stability of PSCs, as well as appearing to suppress pinholes. The enthalpy of formation of the mixed MA-GA system (at 25 mol %) is calculated by DFT to be significantly lower (i.e., more negative) than that of the pure $MAPbI_3$, representing a large increase in the overall thermodynamic stability of the perovskite structure that is putatively attributable to the increased number of hydrogen bonds available in the GA-alloyed system.[434]

Monovalent noble metal cations can also be used to influence the perovskite absorber. Abdi-Jalebi et al.[475] found that <2 mol % addition of CuI, CuBr, or AgI into the PbI_2 precursor solution used in the two-step dip-coating process can help to improve the coverage of both the initial PbI_2 precursor and the final perovskite films, as well as induce a modest (for AgI) to significant (for CuI and CuBr) improvement in PSC performance. This improvement may be due to interfacial or grain boundary trap passivation. In a X-ray absorption fine structure study focused on Ag incorporation in $MAPbI_3$ prepared by solvent engineering, Chen et al.[484] found that Ag is more likely to substitute for Pb rather than MA. On the basis of Mott−Schottky analysis of capacitance−voltage measurements, Ag appears to act as an acceptor, progressively shifting the conductivity from *n*-type (pristine perovskite) to intrinsic with increasing concentration, with the Fermi level located almost exactly at midgap at 5 mol %.[484] In this study, Ag also influences the microstructure, initially increasing the apparent grain size for small doping levels (up to 1 mol %) but leading to cracks and pinholes at higher concentrations.[484] The PL lifetime of the Ag-doped perovskites increases at 0.5 mol %, but drops off thereafter, a trend mirrored in the PCEs of devices made using these films. These results suggest that Ag may passivate traps, in addition to the effects on grain structure and doping. Alternatively, it is also possible that the main benefits are solely due to microstructural improvements and that increased Ag concentration causes the trap density to compensate for the higher crystallinity and apparent grain size.

6.2.2. B-Site Substitution. *6.2.2.1. Sn-Based Perovskites.* Replacement of Pb by Sn on the "B" site is a possible strategy for achieving two desirable outcomes: reduction of toxicity and reduction of the band gap (relative to Pb-based analogs).[101,112,376,485] However, such substitution presents new challenges, including most notably the instability of divalent tin relative to the corresponding tetravalent state, rendering the perovskite highly susceptible to oxidation.[112,486,487] This tendency can lead to large trap densities, high hole concentrations, and nearly metallic conductivity in tin iodide perovskites,[486−489] with some of these effects possibly associated with Sn migration out of the lattice and reaction with oxygen to form inclusions of SnO_2 (note that if Sn^{2+} were to simply oxidize to Sn^{4+} and donate the electrons to the structure, the opposite effect might be predicted, i.e., n-type doping).[490] Sn may possibly be removed from the perovskite without large-scale perturbation of the crystal structure, generating Sn vacancies that act as acceptors. Susceptibility

DOI: 10.1021/acs.chemrev.8b00318
Chem. Rev. 2019, 119, 3193−3295

to Sn oxidation is quite troublesome for both film deposition and operation of associated optoelectronic devices and severely restricts the acceptable range of processing conditions compared to the more stable Pb-based systems (e.g., strict isolation from any exposure to possible oxidizing species is essential). Consequently, the performance of Sn-based PSCs has lagged that of the Pb-based cells, with the PCE watermark having until recently been pinned at roughly 6% since 2013.[74,486,491−493]

However, fresh advances have yielded significant improvements in film deposition and PCE. Zhao et al. used a solvent engineering method to deposit a mixed organic cation composition, $FA_xMA_{1-x}SnI_3$, which yielded a PCE of over 8%.[494] In this report, FA helps to reduce SRH recombination, as evidenced by TRPL and impedance spectroscopy, although it should still be noted that the carrier lifetimes are ∼1−5 ns, in some cases several orders of magnitude lower than those of Pb-based perovskites. Increasing the FA concentration also improves film coverage and continuity.[494] Shao et al.[495] found that a synergy of SnF_2 addition and PEA substitution could improve the crystallinity of $FASnI_3$ thin films prepared by solvent engineering, thereby reducing defect and hole concentrations and subsequently increasing the carrier lifetime as measured by TRPL. Substitution of PEAI for FAI may induce the formation of a "seed layer" of 2D $(PEA)_2SnI_4$ near the interface with the substrate that templates the growth of the overlying 3D $FASnI_3$. This templating may explain the higher crystallinity as well as the greater degree of preferred orientation evident in the PEA-assisted films relative to the purely 3D perovskite, as seen in grazing-incidence WAXS patterns. In addition, larger amounts of PEA appear to promote fusion of the grains, which may lead to greater structural cohesion of the thin film and better moisture/environmental tolerance, although substitution of more than 8 mol % PEAI leads to unacceptably rough and pinhole-containing films. With the use of the optimal substitution ratio of 8 mol % PEAI, PSCs with PCE > 9% were achieved, as of this writing the highest of any Pb-free PSC.[495] This level of performance, as well as the degree of recombination (inferred from the TRPL lifetimes), still lags those of Pb-based perovskites considerably; however, addressing the defect concentration levels appears to be an important strategy toward further improvement of Sn-based perovskite devices.

To attain high quality Sn-based halide perovskite thin films, stringent precaution must be taken to avoid exposure to air or other oxidizing species during and after film fabrication (most typically, this implies performing the processing steps in a rigorously maintained inert atmosphere glovebox). Indeed, active prevention of either Sn oxidation or loss through additives appears to be a critical strategy toward the fabrication of high-performance pure Sn perovskite films, although such approaches may also lead to unwanted morphological effects that must themselves be countered by other additives. In both of the above reports wherein PCE > 8% is reached,[494,495] SnF_2 added to the precursor solution suppresses the hole concentration and appears to aid grain growth, a commonly used strategy that has been attributed to increasing the chemical potential of Sn in the film, suppressing vacancy formation.[435,436,490,493,496] Unfortunately, SnF_2 can also phase-segregate, given the large size discrepancy between the F^- and I^- anions. This effect may, however, be mitigated by the presence of other additives. Lee et al.[497] found that adding pyrazine to the precursor solution of $FASnI_3$ prepared by solvent engineering forms a Lewis adduct with SnF_2, which disperses more homogeneously throughout the film and increases the effectiveness of SnF_2 at suppressing oxidation. It is also worthwhile to note that, in this study, the use of DMSO as a component of the precursor solution appears to be critical to the film uniformity, as solvent engineering from a pure DMF solution is unable to deliver conformal coverage. Hao et al.[498] have shown that $SnI_2{\cdot}3DMSO$ intermediate formation during one-step spin-coating of $MASnI_3$ may be a critical step to enable uniform film deposition, with subsequent conversion to compact, apparently large-grain perovskite after postannealing. Cao et al.[499] added both SnF_2 and triethylphosphine to the precursor solution of $(BA)_2(MA)_2Sn_3I_{10}$ films prepared by hot casting (as described in section 4.1.1) on substrates preheated at 120 °C. They find that SnF_2 by itself again leads to aggregation of the perovskite, forming void spaces in the films, while the films prepared using both additives exhibit significantly improved coverage, though with some small pinholes remaining.

If the benefit of adding SnF_2 is simply to increase the chemical potential of Sn, there is no particular necessity to use the fluoride as opposed to other halides. Applying this logic, Song et al.[500] used a large excess of SnI_2 to fabricate $CsSnI_3$ films and PSCs by the one-step spin-coating method, finding that a 0.4 molar ratio of CsI to SnI_2 yields the highest PCE, while cells prepared from a stoichiometric solution display neither PV nor even rectifying behavior. This observation contradicts the findings by Wang et al.,[501] who obtained a PCE of 3.31% in PSCs made from $CsSnI_3$ films derived from stoichiometric solutions. The discrepancy could be attributed to the highly compact films with uniform microstructures in this latter study, prepared using prereacted $CsSnI_3$ (using high temperature annealing in sealed tubes) and a different solvent mixture (methoxynitrile/ACN/DMF), together with optimized heat treatment. Surprisingly, the large Sn excess in the precursor solution used by Song et al.[500] does not detrimentally impact film coverage, nor are crystalline secondary phases of SnI_2 observed in the XRD patterns (at least until reaching a $CsI:SnI_2$ ratio of 0.2) or are agglomerations of Sn evident in EDS maps. It is not entirely certain where the excess SnI_2 goes in this process, but it may segregate to interfaces or grain boundaries as amorphous or very fine-grained crystalline inclusions that are not easily detected by SEM or XRD. Combining a Sn-rich stoichiometry with a reducing hydrazine atmosphere, which was previously shown to reduce the defect population and improve carrier lifetimes,[502] the authors were able to further reduce the perovskite conductivity and improve $CsSnI_3$ PSC performance to 4.8%, the highest PCE yet reported for a PSC with an all-inorganic, Sn-based absorber.[500] It bears mentioning, however, that hydrazine is an especially hazardous substance, and investigation into less dangerous reducing agents is advisable.

Sn content can also be modulated by a more counter-intuitive method. The VASP technique (as described in section 4.2.3), in which SnI_2 films are annealed in MAI vapor, reportedly may yield excess Sn in the $MASnI_3$ films rather than excess MA or I.[503] XPS measurements suggest that the extra Sn may exist as a divalent oxide or hydroxide, effectively increasing the amount of Sn^{2+} available to fill vacancies in the perovskite. This result may be explained by noting that, surprisingly, the acid/HI component of the MAI vapor does not interact strongly with the film during the VASP process (supported by the observation that annealing $SnBr_2$ films yields

DOI: 10.1021/acs.chemrev.8b00318
Chem. Rev. 2019, 119, 3193−3295

$MASnBr_3$ rather than a mixed iodide-bromide).[503] Rather, the MAI vapor may dissociate into HI and MA^0 gas, the latter of which may interact with trace moisture to produce the oxide and hydroxide species observed in the XPS spectra according to the following proposed reactions:

$$3SnI_2 + 2CH_3NH_2 + H_2O \rightarrow 2CH_3NH_3SnI_3 + SnO \quad (30)$$

$$CH_3NH_2 + H_2O \leftrightarrow CH_3NH_3OH \quad (31)$$

$$3SnI_2 + 2CH_3NH_3OH \rightarrow 2CH_3NH_3SnI_3 + Sn(OH)_2 \quad (32)$$

These chemical reactions, yielding either oxide or hydroxide, generate two moles of perovskite and one of the oxide/hydroxide for every three moles of SnI_2, thus accounting for the excess Sn. The authors also tested exposure of the SnX_2 films to MA^0 gas and obtained similar results to the MAI anneal, suggesting that the above-proposed reaction scheme holds some validity. Similar behavior has also been observed for PbI_2,[215] as discussed in section 5.2.1. Accordingly, PSCs prepared from the Sn-rich films deposited by VASP may outperform those in which the absorber is deposited by one-step spin-coating from a stoichiometric precursor solution.[503]

As a final note, mixed Pb/Sn compositions are also of significant interest. Although the band gap of $MASnI_3$ is substantially lower than that of $MAPbI_3$, anomalous reduction of the band gap occurs for intermediate $MAPb_{1-x}Sn_xI_3$ compositions, enabling collection of infrared emission with wavelengths of as long as 1060 nm.[101,485] The minimum band gap occurs for slightly Sn-rich compositions but varies little across a broad compositional range ($x \approx 0.25-0.75$), over which it is approximately 1.2 eV.[101,485] The band gap of $FAPb_{1-x}Sn_xI_3$ obeys a similar trend.[376] The tunable reduction in the band gap makes these compositions attractive either for use as the bottom cell in tandem photovoltaic devices[276,436] or PSCs with optimal band gap stipulated by the Shockley-Queisser limit.[504] An additional prospective benefit is that mixed Pb/Sn PSCs are reported to exhibit comparable or even improved operational stability relative to those based on pure Pb absorbers.[276] Leijtens et al.[505] propose that compositions with 50% or less Sn are stabilized against oxidation by a mechanism in which the presence of Pb interferes with the formation of the volatile decomposition product SnI_4, forcing oxidation of Sn to occur along a less kinetically favorable pathway that instead produces I_2. Thus, replacement of Sn with Pb is speculated to have a dual protective effect that reduces environmental susceptibility not only by lessening the content of vulnerable species but also by retarding the oxidation kinetics of the remaining Sn. The increased robustness of the mixed Pb−Sn perovskites is also evident by the fact that the efficiency of PSCs using these films as the absorber significantly outstrips that of the pure Sn perovskites, with several reports exceeding 17%.[436,504,506] Despite the increased oxidation resistance conferred by the presence of Pb, reports of high-performance mixed Pb−Sn PSCs tend to employ antioxidants such as SnF_2[276,436,504,506] or ascorbic acid[507] and, in general, emphasize the importance of avoiding Sn oxidation at every stage of fabrication. As in the case of the pure-Sn perovskites, deposition strategies developed for high-quality Pb-based perovskite films generally transfer well to the mixed compositions, with antisolvent extraction[276] and solvent engineering[436,504,506,507] both being effective strategies for the deposition of compact and conformal films.

6.2.2.2. Other Divalent B Site Cations. By analogy to replacement of MA^+ on the A site with a Group 1 or 11 metal, Pb^{2+} in the B site may potentially be substituted by a Group 2 or 12 metal or potentially any other divalent transition metal. Sr^{2+} appears to be a particularly popular choice,[120,508−511] perhaps due to having essentially the same size as Pb^{2+} in a 6-fold coordination environment.[512] The size similarity between Sr^{2+} and Pb^{2+} also makes assessment of the degree of incorporation challenging, as XRD pattern shifts cannot be convincingly used for this purpose.[510] Pérez-del-Rey et al.[120] have shown that addition of 2 mol % excess SrI_2 to a 3:1 mixture of MAI and $Pb(OAc)_2{\cdot}3H_2O$ in DMF, used in a one-step spin-coating recipe, leads to much smoother films with significantly reduced apparent grain size but also much longer charge carrier lifetime (as measured by TRMC). XPS and X-ray absorption measurements of the films show an unexpected enhancement of the Sr/Pb ratio relative to the precursor stoichiometry as well as an oxygen peak that is not present in the pristine $MAPbI_3$, indicating possible enrichment of Sr at the film surface, perhaps in the form of a strontium oxide, carbonate, or acetate crust. The extent of Sr incorporation into the bulk is not known. Sr-alloyed $MAPbI_3$ PSCs can evidently reach 85% FF, an astoundingly high value nearly at the theoretical limit,[120] making the understanding of how Sr interacts with the perovskite framework of particular interest. Conceivably, the small apparent grain size may be explained by pinning of the grain boundaries by Sr impurities, which should become more confining as Sr content in the film increases. This crust, if it indeed exists, presumably also passivates the grain boundaries/surfaces, as evidenced by the enhancement of the TRMC lifetime and FF.

Substitution of other alkaline earth metals can also lead to some interesting results. In a study by Chan et al.[509] on the effects of Mg, Ca, Sr, and Ba in $MAPbI_{3-x}Cl_x$ films prepared by one-step spin-coating from a DMF solution, while incorporation of the first three metals leads to small apparent grain size (as well as broad XRD peaks) and pinholes, Ba leads to apparent grain size and XRD peak broadness similar to that of the pristine perovskite and a more compact microstructure. A systematic redshift in the band gap and shift of the tet(110) peak in the perovskite XRD pattern to lower angles occur with increasing Ba content, suggesting that Ba may substitute within the perovskite lattice.[509] Overall, 3 mol % Ba (added as BaI_2 in the precursor solution) yields the highest performing PSCs, with an average PCE of 14.0% compared to 11.8% for those prepared using the pristine perovskite. Although it is reasonable to claim that the superior morphology of the Ba-alloyed perovskite film enables better performance, this study did not further elaborate on why Ba is more effective than the other alkaline earths. It is also worthwhile to note that the low performance and nonideal morphology of the pristine perovskite film may simply reflect a lack of optimization of the fabrication process, and that the benefits of Ba may not be relevant at a higher level of performance or in systems where the pristine perovskite already has full coverage over the substrate.

Group 12 metals (especially Cd) also exhibit some interesting behavior when incorporated in perovskite films. While Navas et al.[513] predicted that a solid solution of $MAPb_{1-x}Cd_xI_3$ could persist up to $x = 0.5$, subsequent study revealed that, at levels above $x = 0.01$, the perovskite phase segregates into $MAPbI_3$, $(MA)_2CdI_4$, and PbI_2.[514] The presence of Cd can also increase the apparent grain size and

DOI: 10.1021/acs.chemrev.8b00318
Chem. Rev. 2019, 119, 3193−3295

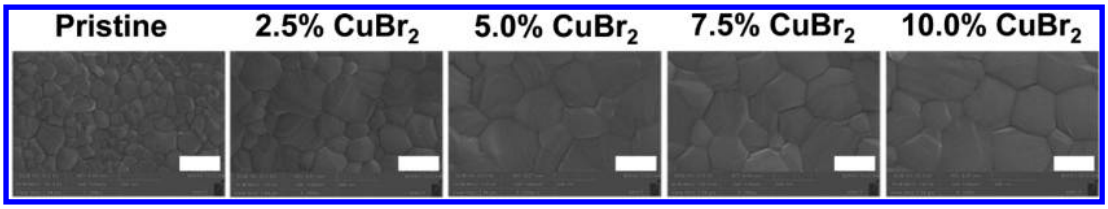

Figure 48. Top-surface SEM images showing enhancement of grain growth in $MAPbI_3$ perovskite thin films prepared by solvent engineering, reportedly enabled by the formation of a liquid $CuBr_2$-containing intermediate. All scale bars 500 nm. Reprinted from ref 519. Copyright 2016 Elsevier.

carrier lifetime of $MAPbI_3$ films, although reports differ on whether the lifetime is boosted modestly[514] or more substantially.[515] Cd incorporation can be a "double-edged sword"; while the above effects can benefit PSC performance,[515] Cd has been observed to diffuse from a CdS ETL into the $MAPbI_3$ perovskite absorber during film processing, leading to the generation of insulating $(MA)_2CdI_4$ and PbI_2 at the interface and effectively blocking the device current.[514,516] Watthage et al.[515] indicate that $(MA)_2CdI_4$ may play a crucial role in the enlargement of the grains by acting as a flux for the interaction between solid PbI_2 films and MAI in solution during the two-step process and/or by promoting Ostwald ripening of the perovskite grains. It may be the case that similar processes are at work for Cd-doped films prepared by solvent engineering,[514] which possess nearly identical grain structure to the Cd-doped two-step films despite the substantial differences in processing. However, it has not been determined whether colloidal $(MA)_2CdI_4$ species are present in the one-step precursor solution, as they are when $CdCl_2$ is added to a solution of MAI in isopropanol for the two-step process,[515] and further work is needed to elucidate the details of this reaction. Incorporation of mercury (by substituting HgI_2 for PbI_2 in the precursor solution of $MAPbI_3$ prepared by solvent engineering) can lead to similar effects to those of Cd, with small amounts (up to 10 mol %) boosting apparent grain size and PSC performance (although hysteresis also increases). However, larger amounts lead to the emergence of large pinholes and phase segregation of the nonperovskite $MAHgI_3$.[517] Given the chemical similarity between Hg and Cd, it is conceivable that they may have similar effects on film growth; however, the details of the interaction are likely to be different, as $(MA)_2CdI_4$ seems to be more likely to form under typical perovskite processing conditions compared to $MACdI_3$.[514]

Williams et al.[245] have undertaken a study of the effects of four transition metals (Mn, Fe, Co, and Ni), added in the form of divalent halides to replace PbI_2 in $MAPbI_3$, and observe that although pure films drop-cast from a solution of $MAPbI_3$ in DMSO tend to grow with a rodlike morphology characteristic of conversion from a perovskite-DMSO complex, addition of any of the four metals favors direct precipitation of the perovskite, leading to more isotropic morphology. Evidently, the presence of the transition metals interferes with formation of the perovskite-solvent complex, as indicated by the enhanced resistance of the transition metal-alloyed films to bleaching when exposed to DMSO vapor (which would indicate the formation of the light-colored perovskite-DMSO complex). A reasonably large amount of each of the above metals may be incorporated into the films without rejection of secondary phases (according to XRD patterns), with the solubility limit appearing to lie between 10 and 25 at %. A slight increase in the lattice parameters indicates that these metals may not directly substitute for Pb (given the smaller sizes of the substituted atoms), and the nature of their distribution in the lattice remains ambiguous. An additional effect of the presence of the transition metals, as discussed in section 3.5, is a response to magnetic fields (as may be encountered when annealing films on a stirring hot plate). For Fe-alloyed films, stronger magnetic fields appear to induce larger grains but also lead to twinning, and the resultant films display inferior optoelectronic properties, causing a clear reduction in PSC J_{SC}, FF, and PCE.[245] Although the carrier lifetime as measured by TRPL is reduced (at 10 at % alloying level), the PL intensity of the Mn-alloyed film is enhanced 3-fold relative to the pristine perovskite, indicating that its presence stimulates radiative recombination. These results, as well as others predicting that introduction of Mn does not introduce deep trap levels,[518] indicate that Mn may be a productive transition metal for inclusion in order to attain improved morphology. Furthermore, its effects on radiative recombination are certainly deserving of further study, as this feature may enable the production of brighter and more efficient near-infrared LEDs.

Besides the transition metal additives described above, Jahandar et al.[519] find that addition of $CuBr_2$ to the precursor solution for $MAPbI_3$ films prepared by solvent engineering can increase the apparent grain size substantially, perhaps through the formation of a $CuBr_2$·DMSO intermediate that melts during the postdeposition anneal, allowing the grains to grow by Ostwald ripening in the presence of this liquid phase. Significant improvement in PCE accompanies this growth, attributed in part to an increase in the hole concentration (as inferred from a Mott−Schottky analysis of capacitance−voltage data), which does indeed track the PCE well for all levels of $CuBr_2$ incorporation. However, the rather small reported (~2-fold) increase in carrier concentration (from 8×10^{16} to 1.6×10^{17} cm^{-3}) does not explain by itself the 2 orders of magnitude drop in the perovskite sheet resistance. Presumably, the dramatic improvement in the grain structure improves the effective mobility in the perovskite as well as the carrier concentration. However, the grain structure does not change substantially above 5 mol % $CuBr_2$ (Figure 48), which coincides with the maximum PCE, and it may be that the PCE drops due to rejection of Cu- or $CuBr_2$-rich secondary phases for $CuBr_2$ incorporation levels above this value, which might interfere with carrier extraction.

6.2.2.3. Double Perovskites. An alternative means of removing Pb from the perovskite structure is to replace it with equal proportions of monovalent and trivalent metals, ideally those that are isoelectronic to Pb^{2+} or Sn^{2+}, such as Bi^{3+}, Sb^{3+}, In^{+}, or Tl^{+} (although the latter two are compromised, respectively, by instability of the monovalent oxidation state and toxicity), forming structures with a rock salt-type ordering of the monovalent and trivalent metal octahedra that are

DOI: 10.1021/acs.chemrev.8b00318
Chem. Rev. 2019, 119, 3193−3295

frequently termed "double perovskites."[520−522] A number of such compositions (both inorganic and hybrid organic−inorganic) have been recently reported, including $Cs_2AgBiBr_6$[520,521] and $Cs_2AgBiBr_6$:Tl,[523] $Cs_2AgBiCl_6$,[521,522] $Cs_2AgInCl_6$,[524] $(MA)_2AgBiBr_6$,[525] $(MA)_2TlBiBr_6$,[526] rare earth-containing $(MA)_2KYCl_6$ and $(MA)_2KGdCl_6$,[527] and quasi-2D $(BA)_4AgBiBr_8$ and $(BA)_2CsAgBiBr_7$.[528] Although the double perovskites represent a large and diverse subfamily of halide perovskites, the only composition that has thus far received significant attention for thin-film optoelectronics is $Cs_2AgBiBr_6$, owing to its enhanced thermal and environmental resistance[520,521] relative to hybrid perovskites such as $MAPbI_3$, as well as long carrier lifetimes exceeding 1 μs in thin films.[529] A significant drawback of $Cs_2AgBiBr_6$ in the context of PV, however, is its large (>2 eV) and indirect band gap,[520,521] and DFT calculations indicate that the maximum attainable PCE from PSCs based on this compound is no more than 8%.[530] Nonetheless, multiple reports[531,532] of PCE exceeding 2% and V_{OC} ∼1 V in $Cs_2AgBiBr_6$ solar cells make them among the highest-performing Pb/Sn-free halide perovskite absorbers, despite their poor absorption, further attesting to their high electronic quality.

A number of strategies developed for the deposition of other halide perovskites have been readily applied to $Cs_2AgBiBr_6$ thin films. Despite the challenges associated with dissolving CsBr (as discussed in section 6.2.1.2), as well as AgBr and $BiBr_3$,[531] most of these methods are based on single-step spin-coating. In the first report of $Cs_2AgBiBr_6$ thin film deposition, Greul et al.[531] compared the solubility of $Cs_2AgBiBr_6$ in hydrobromic acid, DMF, DMSO, and NMP and found DMSO to be by far the best solvent (solubility limit ∼0.6 M compared to ≤0.1 M for the others). Using a hot-casting approach (as discussed in section 4.1.1) in which both the substrate and solution were heated prior to spin-coating, they observed enhanced optical absorption of the films with increasing preheating temperature. This effect was attributed to faster evaporation of the solvent, resulting in an overall greater amount of material deposited on the substrate. However, excessive preheating led to formation of an extremely rough capping layer of large crystallites on the surface of the mesoporous TiO_2 substrate, perhaps due to excessively rapid precipitation of the perovskite, and was associated with a loss in J_{SC} and PCE of solar cells using the $Cs_2AgBiBr_6$ as absorber. Heating to 75 °C was found to be optimal for maximizing photovoltaic performance. Greul et al.[531] also found a postdeposition thermal anneal to be important to ensure film purity. Although XRD patterns of the as-deposited films are dominated by peaks belonging to the double perovskite, AgBr and $Cs_3Bi_2Br_9$ impurities could only be removed by annealing the films at or above 250 °C, with 285 °C providing optimal PCE of the associated PSCs. Using a similar recipe that includes a 5 Pa vacuum drying step between spin-coating and annealing to improve coverage, Lei et al.[533] obtained reasonably compact films on planar Si/SiO_2 substrates, although some pinholes appear to be present. Solvent engineering techniques have also been employed for deposition of double perovskites with reasonable success. Gao et al.[532] report that washing the substrate with isopropanol during spinning yielded smoother and less hazy films than those that were unwashed, or washed with other antisolvents such as ethanol, methanol, toluene, or chlorobenzene. The optimized films appear to have a smooth microstructure composed of large, compact grains without evidence of impurities, although the existence of several peaks in the PL spectrum (in contrast with the single broad peak that is usually observed[520,529,531]) of the films remains unexplained, and could indicate the presence of secondary phases that are not detectable by XRD. These phases might arise from differential precipitation rates of the perovskite precursors upon interaction with the antisolvent; further work is needed to clarify the origin of these unusual optical features. Pantaler et al.[534] find that using chlorobenzene as the antisolvent in the solvent engineering process can yield a smooth and compact capping layer of $Cs_2AgBiBr_6$ deposited on mesoporous TiO_2 substrates, in comparison with the highly discontinuous capping layer obtained by Greul et al.[531] using the hot-casting method. Despite the successes of hot-casting and solvent engineering, simple one-step spin-coating may be adequate for producing high-quality $Cs_2AgBiBr_6$ films, at least on planar substrates. Ning et al.[535] report the fabrication of phase-pure, compact films with reasonably large apparent grain size on ITO/compact TiO_2 substrates by spin-coating from a 0.5 M solution prepared by dissolving presynthesized crystals in DMSO. This result suggests that formation of $Cs_2AgBiBr_6$ is less likely to be complicated by the effects of precursor-solvent intermediate phases, as in the case of $MAPbI_3$.[536]

Recently, Ju et al.[537] discovered a new type of Pb-free Ti-based double perovskite, Cs_2TiX_6, where every other Ti (at the B-site) is missing and the V_{Ti} are ordered. They synthesized powders of Cs_2TiI_6, $Cs_2TiI_4Br_2$, $Cs_2TiI_2Br_4$, and Cs_2TiBr_6 and measured optical bandgaps of 1.02, 1.15, 1.38, and 1.78 eV, respectively. Subsequently, Chen et al.[538] prepared thin films of Cs_2TiBr_6 using the two-step vapor-based method for PSCs with possible tandem-PVs application in mind. These thin films show balanced and long lifetimes of photogenerated electrons and holes, and the initial champion PSC has a PCE of 3.3%.

6.2.3. X-Site Substitution. *6.2.3.1. Bromide.* Br is a frequently used alloying element in perovskite thin films, forming a portion of the halide component in many high-performance PSCs and LEDs, including all of the record-setting PSCs plotted on the National Renewable Energy Laboratory's "Best Research-Cell Efficiencies" chart except the earliest.[24,26−28,116,148,265] Early introduction of Br into PV absorbers was motivated by reports that the moisture tolerance of $MAPbI_3$ could be improved substantially by its incorporation.[148,539] Alloying of Br and I provides a means of tuning the band gap. As the proportion of Br increases relative to that of I, the band gap does as well, a trend that holds for a variety of perovskite systems, including $MAPb(I_{1-x}Br_x)_3$,[539] $MASn(I_{1-x}Br_x)_3$,[491] $FAPb(I_{1-x}Br_x)_3$,[4] and $CsSn(I_{1-x}Br_x)_3$.[540] This tunability is desirable for many other optoelectronic applications, as the range of band gaps accessible in these systems encompasses values appropriate for top cells in tandem PV systems or LEDs and lasers spanning colors from infrared through green. Hoke et al.,[118] however, determined that exposure of $MAPb(I_{1-x}Br_x)_3$ films to illumination induces phase segregation into iodide- and bromide-rich regions for intermediate x values (ranging from ∼0.2−0.6), which has also been directly observed in $MAPb(I_{0.6}Br_{0.4})_3$ through chemical mapping by EDS.[541,542] A corresponding reduction in the band-to-band PL peak intensity is also observed, while a PL peak presumably corresponding to the iodide-rich x = 0.2 phase grows in its place. This effect appears to be reversible, and the single-phase mixed-halide perovskite is recovered after removal from the light.[118] The increase in V_{OC} deficit in

DOI: 10.1021/acs.chemrev.8b00318
Chem. Rev. 2019, 119, 3193−3295

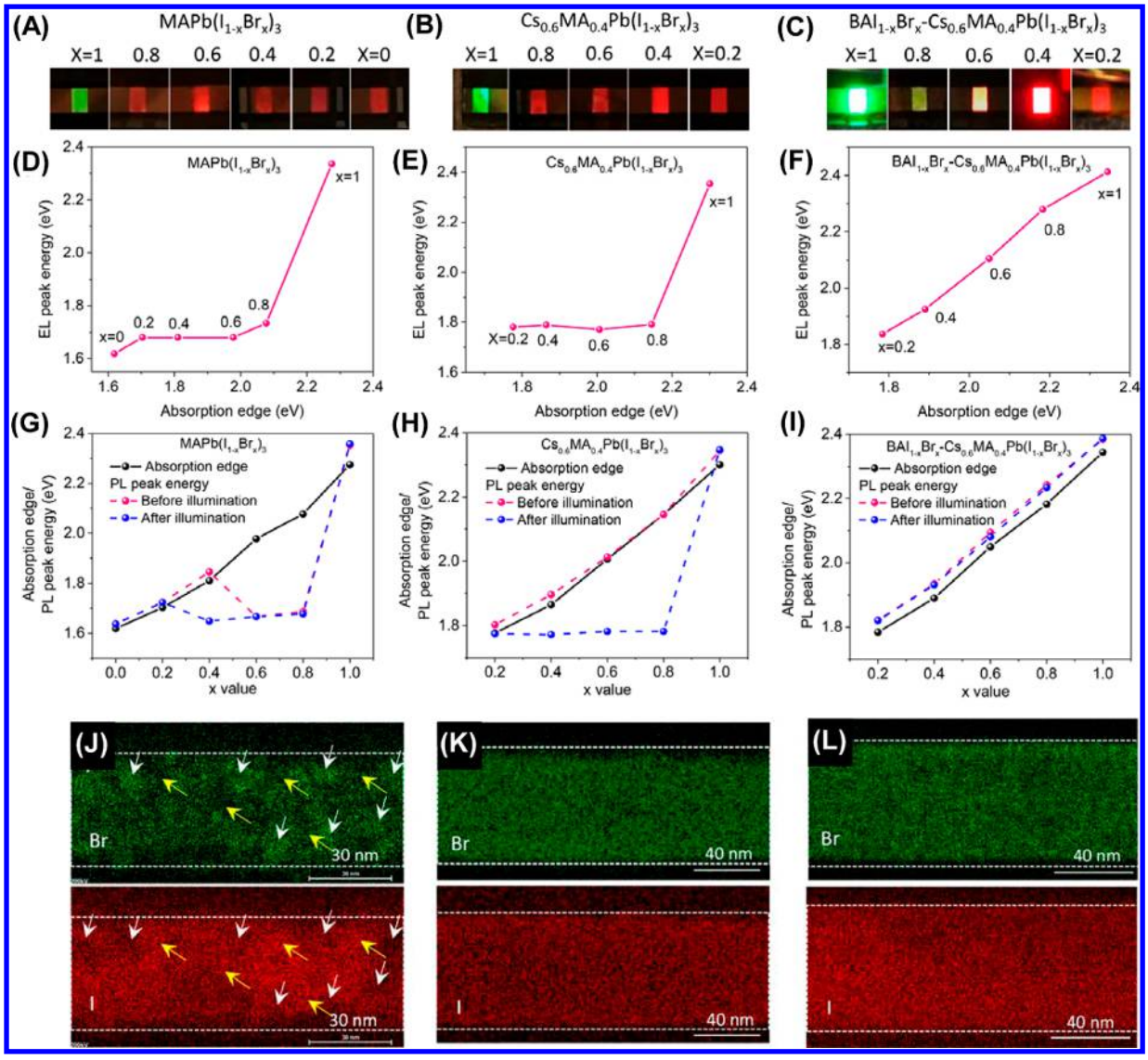

Figure 49. Optical and photophysical behavior of (A, D, G, and J) $MAPb(I_{1-x}Br_x)_3$, (B, E, H, and K) $Cs_{0.6}MA_{0.4}Pb(I_{1-x}Br_x)_3$, and (C, F, I, and L) $BAI_{1-x}Br_x$-alloyed $Cs_{0.6}MA_{0.4}Pb(I_{1-x}Br_x)_3$. (A−C) Photographs of LEDs for various Br contents x, which generally display red electroluminescence for all ratios except the pure bromide, with the exception of those using the BA-alloyed perovskite, for which the color smoothly varies from red to green as the composition transitions from I-rich to Br-rich. (D−F) Peak electroluminescence of the above LEDs as a function of the absorption edge, which displays the same color pinning for the MA and Cs/MA perovskites despite a smooth variation of the absorption edge with Br content. (G−I) Absorption edge and peak PL energy as a function of Br content; while the absorption edge scales more or less linearly with composition, pinning of the PL peak in the mixed I/Br compositions is progressively alleviated by transitioning from pure MA to Cs/MA to BA-alloyed Cs/MA perovskites. (J−L) SEM/EDS elemental maps of the above perovskites at $x = 0.4$, wherein segregation into I- and Br-rich regions is evident for the MA perovskite but not the others. Adapted from ref 542. Copyright 2017 American Chemical Society.

$MAPb(I_{1-x}Br_x)_3$ thin film devices with Br content is thus most easily explained by a carrier funneling effect (also observed in other tunable-band gap perovskite systems such as the Ruddlesden−Popper series),[31] in which photogenerated carriers preferentially migrate to the regions of lowest band gap (in this case, the iodide-rich regions), losing energy in the process. The available V_{OC} is, therefore, constrained by this lowest band gap value, which may be significantly lower than the nominal band gap of the single-phase mixed-halide perovskite. This behavior is not exclusive to the $MAPb(I_{1-x}Br_x)_3$ system, as Niezgoda et al.[543] also observe similar effects in $CsPbBrI_2$.

Compositional segregation is obviously undesirable in the context of many optoelectronic applications and undermines the tunability of mixed iodide-bromide films, as certain band gaps may be functionally inaccessible for devices operated in high-illumination environments. It is, therefore, useful to explore possible processing strategies to mitigate or control this effect. Prevention of halide migration is perhaps the most straightforward way of reducing the susceptibility to phase segregation. Yoon et al.[544] found that phase segregation kinetics can be strongly suppressed in $MAPb(I_{1-x}Br_x)_3$ films spin-cast from DMF, simply by employing a halide-deficient precursor solution (Pb:halide ratio of 1:2.4). Although a high density of halide vacancies enhances the diffusivity of Br^- and I^- anions, the scarcity of these anions means they evidently must travel farther through the lattice to reach I- or Br-rich domains. While Yoon et al.[544] provide a possible pathway to reduce halide phase segregation, a 20% deficiency of the halogen represents a rather dramatic departure from ideal

DOI: 10.1021/acs.chemrev.8b00318
Chem. Rev. 2019, 119, 3193−3295

stoichiometry and likely implies other detrimental impacts on film properties.

Alternatively, Xiao et al.[542] have applied larger organic cations to stabilize the mixed phase. Noting that the apparent grain size of $MAPbI_3$ films prepared by the solvent engineering process (section 4.1.2) can be strongly reduced by the addition of *n*-butylammonium halide (BAI/BABr),[32] Xiao et al. added 20 mol % excess BA halide to the mixed iodide-bromide perovskite to form compositions with approximate formula $BAI_{1-x}Br_x$-$Cs_{0.6}MA_{0.4}Pb(I_{1-x}Br_x)_3$.[542] Addition of the BA halide in this manner results in very fine apparent grain size (~10 nm in diameter) presumably terminated by a BA-rich surface layer. Such small crystallites are less favorable for phase segregation, in part due to the relatively large amount of energy required to create new surfaces at the phase boundaries. While the absorption edge does not change upon illumination and scales linearly with Br composition, the photo- and electroluminescence peak energies are pinned at roughly the values corresponding to the I-rich $x = 0.2$ perovskite, unless BA is added to the perovskite precursor, in which case the linear dependence of the emission peak on halide content is recovered (Figure 49, panels A−I). This effect could also be witnessed in chemical mapping of the illuminated films by EDS, which shows clear segregation into I-rich and Br-rich domains in a pure $MAPb(I_{1-x}Br_x)_3$ thin film and homogeneous distribution of these elements in the BA-alloyed Cs/MA films (Figure 49J-L). Phase segregation in the Cs/MA perovskites is not evident in the EDS images, indicating that Cs alleviates phase segregation to some degree; however, pinning of the luminescence reveals that it cannot do so completely. Only with BA addition can the tunability of the mixed iodide-bromide thin films be recovered, allowing for continuous color variation (as well as enhanced electroluminescence) in LEDs and linear increase in V_{OC} with bromide content in PSCs.[542]

Another complication that arises when working with Br-containing perovskites is that the size/chemical difference between the Br^- and I^- anions has important consequences for film formation. "One-step" spin-coating of $MAPbBr_3$ or Br-rich compositions tends to yield isolated, large, and well-faceted crystals scattered over the surface of the substrate[163,545] rather than continuous, compact films or the dendritic structure often found in one-step spin-cast $MAPbI_3$ films. Even deposition techniques that are more reliable for obtaining high-quality $MAPbI_3$ films such as antisolvent/solvent extraction[275] or two-step dip coating[546] lead to rougher and less continuous films when applied to the Br-rich system. A key observation noted by Zhou et al.[275] is that the reduced size of the Br^- ion relative to I^- results in a higher diffusivity of the bromide, enhancing the relative growth rate of the perovskite grains over nucleation and accounting for the favorability of large, dispersed crystals over compact grains. In order to overcome this problem, strategies must be devised that allow nucleation to be decoupled from growth. Zhou et al.[275] increased nucleation rates in the antisolvent/solvent extraction process by agitating the antisolvent bath and more rapidly extracting solvent from the film, thereby increasing the saturation ratio. Yu et al.[545] reduced the size and increased the density of $MAPbBr_3$ crystallites in films spin-cast in a single step from DMF by adding hydrobromic acid to the solution. The improved morphology can be attributed to the increased viscosity of the acidified solution, which reduces the diffusivity of solutes and thereby suppresses the growth rate of perovskite nuclei.

Giesbrecht et al.[126] were able to obtain continuous $MAPbBr_3$ films using conventional solvent engineering as well as a one-step spin-coating recipe using a 3:1 molar ratio of $MABr:Pb(OAc)_2$. The former films possess the small, densely packed grain structure typical of solvent-engineered films, demonstrating that the rapid introduction of antisolvent is sufficient to overcome the diffusivity-enhanced growth. Films produced by the latter process are characterized by what appear to be very large (~1−10 μm) but shapeless grains with strong preferred orientation favoring the (00*l*) planes. The large apparent grain size was ascribed to the production of excess methylammonium acetate, which may dissociate into liquid (acetic acid) and gaseous species (MA^0), promoting Ostwald ripening of the perovskite grains.[126] The compactness and formlessness of the grains are somewhat surprising in view of the tendency for $MAPbBr_3$ to crystallize as dispersed, cubic crystals with clear facets. Curiously, the length of time taken to spin the substrate appears to be extremely important. Films produced using a spin dwell time of 30 s do indeed comprise scattered cubic crystals of relatively uniform size, with large voids between them, but a longer dwell time of 3 min yields the apparently large, shapeless grain microstructure described above.[126] The reasons for this difference were not explored, but the formation of apparently large, flat, highly oriented grains is suggestive of the formation of a layered intermediate phase that may be topotactically converted to perovskite by the postdeposition treatment (as discussed for the case of Cl precursors discussed in section 6.1.3). Alternatively, as discussed in section 3.4, the formation of very large grains with preferred orientation may be evidence of secondary grain coarsening, in which the (001) face of the perovskite crystallites possesses a strong affinity for the TiO_2 substrate. However, further study of the influence of the precursors on the crystallite growth will be necessary to better understand this process.

Another means of avoiding the challenges posed by the high diffusivity of Br^- in solution is to reject solution-based in favor of vapor deposition approaches. Giesbrecht et al.[126] used a conventional VASP process to react MABr with spin-cast $PbBr_2$ thin films, obtaining compact, reasonably large apparent grain size on the order of 1 μm, though with random crystallographic orientation that contrasts strongly with the (00*l*)-oriented films produced using the $Pb(OAc)_2$/MABr precursor (one-step spin-coating approach described earlier). This result suggests that the larger grains obtained by the one-step spin-coating method may indeed be due in part to the refluxing effect of the liquefied precursors. Along similar lines, Leyden et al.[313] used a conventional CVD process to deposit MABr onto thermally evaporated $PbBr_2$ films, obtaining $MAPbBr_3$ films of compact microstructure whose apparent grain size can be tuned by changing the substrate temperature, with larger grains resulting from higher temperatures. We may conclude by observing that the difficulties in obtaining continuous films of bromide-rich perovskites differ from the pure iodides in degree but not in kind. That is, it is still important to favor nucleation over growth in order to prevent the formation of large and dispersed crystallites rather than compact grains, but the comparatively high diffusivity of Br- makes this dynamic slightly more challenging to achieve. Nevertheless, processes that aggressively stimulate nucleation, such as solvent engineering, or retard growth, such as vapor deposition processes, offer straightforward resolutions to this challenge.

DOI: 10.1021/acs.chemrev.8b00318
Chem. Rev. 2019, 119, 3193−3295

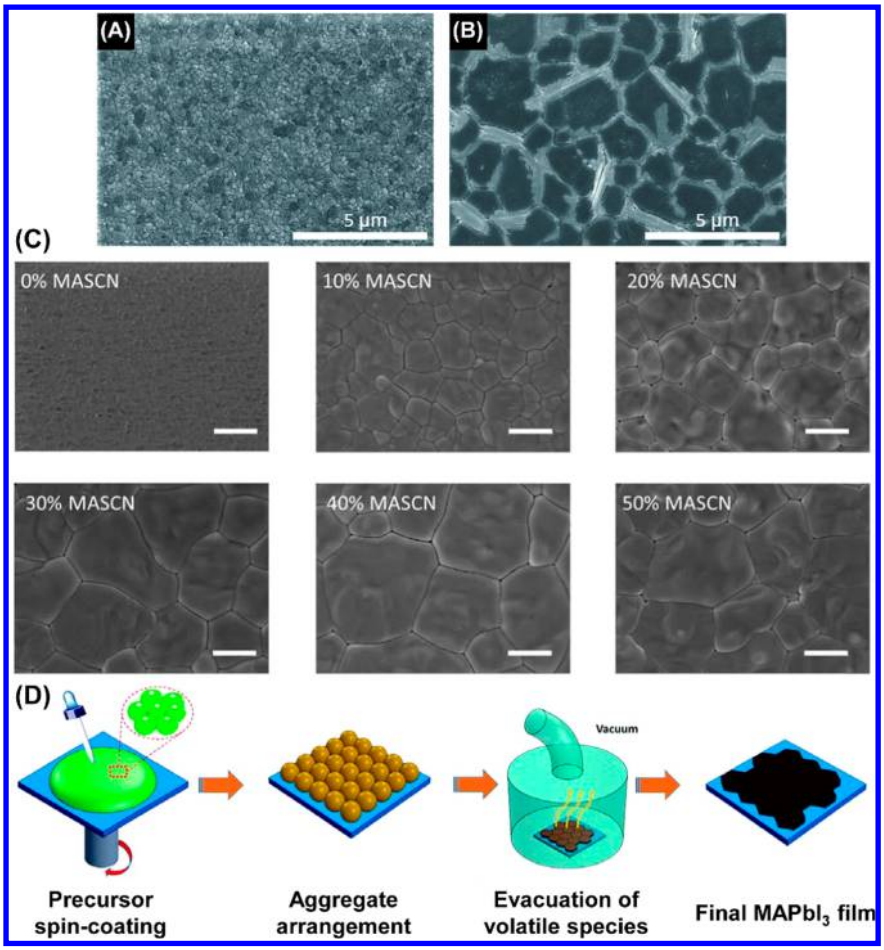

Figure 50. Top-surface SEM images showing the morphologies of $MAPbI_3$ films deposited by solvent engineering (A) without and (B) with 5 mol % $Pb(SCN)_2$ in the precursor solution, demonstrating a large increase in apparent grain size (after annealing) upon addition of thiocyanate, as well as large deposits of PbI_2 at the grain boundaries that may passivate the surfaces there. Reprinted with permission from ref 109. Copyright 2016 Wiley-VCH. (C) Top-surface SEM images of $MAPbI_3$ films deposited by solvent engineering (without annealing) with varying amounts of MASCN in the precursor solution. (D) Proposed scheme for the formation of large grains derived from SCN-stimulated aggregates, in which the aggregates arrange themselves on the substrate and are subsequently transformed into perovskite grains by exposure to vacuum. Adapted with permission from ref 15. Copyright 2017 Royal Society of Chemistry.

6.2.3.2. Thiocyanate. Early interest in the thiocyanate (SCN^-) anion was stimulated by the prospect of its substitution for I^- in the 3D $MAPbI_3$ structure and possible benefit to stability.[547,548] Subsequent studies on single crystals conclude that, rather than substituting for I^- in $MAPbI_3$ (to any significant degree), SCN^- induces a layered structure with chemical formula $(MA)_2PbI_2(SCN)_2$.[549] This structure is akin to the 2D $n = 1$ member of the Ruddlesden−Popper series (Figures 2 and 3), except that the SCN^- ions reside at apical sites in the lead-halide/pseudohalide octahedra, with iodine ions occupying the equatorial (bridging) sites, thus accommodating the asymmetry of the SCN^- ion.[549] Ganose et al.[550] suggest, based on DFT calculations, that this structure would be more stable than the $MAPbI_3$ system but that it should still possess a band gap equivalent to that of $MAPbI_3$, echoing the claims of prior experimental reports. More comprehensive studies reveal that the band gap of $(MA)_2PbI_2(SCN)_2$ falls above 2 eV, rather than at 1.6 eV, as previously claimed.[551,552] Analysis of the discrepancy between the UV−vis and PL spectra led to the discovery of efficient generation of triplet excitons in this material, with the lower energy phosphorescent emission originating from the triplet population.[552] Although the wide band gap and large out-of-plane carrier effective mass of $(MA)_2PbI_2(SCN)_2$ do not make it a particularly attractive candidate for PV, it may find other applications as an efficient triplet sensitizer.

Although the thiocyanate anion has not so far proven particularly useful in substituting for I^- as a significant component within 3D perovskites (or within successful device structures), it can be usefully employed as an additive to boost film grain size and device performance.[15,109,443,444] Ke et al.[109] proposed a mechanism by which a small amount of $Pb(SCN)_2$ (5 mol % relative to the targeted $MAPbI_3$) can react with $MAPbI_3$ precursors to form gaseous products (e.g., HSCN and CH_3NH_2) and leave behind a small amount of unreacted PbI_2. These gases may facilitate recrystallization of the nascent perovskite crystallites as they evolve within the film, leading to large apparent grain size (>1 μm on average) (Figure 50, panels A and B). There is no indication from either XPS or FTIR of a significant concentration of remnant SCN in the films, supporting the hypothesis of the loss of HSCN via vapor phase evolution. Further, use of an excess of the lead salt relative to the organic cation leads to a PbI_2 cladding around the surfaces of the grains (Figure 50B) that may passivate these regions. This processing approach appears to apply beyond the

DOI: 10.1021/acs.chemrev.8b00318
Chem. Rev. 2019, 119, 3193−3295

$MAPbI_3$ system, with similar results having been obtained for FA-based compositions as well.[443,444,553]

Thiocyanates need not be introduced as a lead salt. One of the disadvantages of the approach described above is that introduction of SCN is intrinsically linked to added Pb. Therefore, the amount of SCN that can be added will be limited by the level of PbI_2 incorporation that can be tolerated within the film before this secondary phase degrades film structure/performance. Han et al.[15] recently demonstrated that large apparent grain size, compact spin-cast $MAPbI_3$ films can be attained through the use of a much larger (tens of mol % excess relative to the targeted $MAPbI_3$) addition of MASCN (Figure 50C). Furthermore, this desirable microstructure can be formed entirely at room temperature, with only a simple vacuum drying step necessary after the deposition to drive off the residual solvent and excess MASCN, which most likely decomposes into gaseous HSCN and CH_3NH_2 (another prospective pathway leads to CH_3SCN and NH_3) under the influence of the vacuum.[15] While there is no heating involved in the process, the presence of SCN^- ions in the precursor solution leads to the formation of large aggregates whose size directly correlates with the apparent size of the grains in the final film, suggesting that these aggregates transform into the grains during deposition and vacuum treatment (Figure 50D). PSCs produced by this method exhibit PCE exceeding 18%, likely owing to the high crystallinity of the film as well as long carrier lifetime (~1 μs).

6.3. Other Additives for 3D Perovskites

6.3.1. Water and Aqueous Acids. Although exposure to moisture is widely understood to be detrimental to Sn/Pb-based halide perovskites, a number of studies have investigated the potential beneficial impacts of water on perovskite film formation. Since the organic components (e.g., MA^+ and FA^+) in hybrid perovskites are highly hygroscopic, humidity or moisture can play a significant role in their crystallization processes. The effect depends on the perovskite compositions, their precursor phases, and the fabrication methods. Early studies regarding the influence of humidity on perovskite processing focused on the well-known Cl-containing precursor solution containing a 3:1 molar ratio of MAI:$PbCl_2$. Eperon et al.[422] performed a systematic study on the effects of moisture on the $MAPbI_3$ thin films derived from the chlorine-containing precursor and found that higher humidity atmospheres allow faster film formation, leading to a tailored film morphology and significantly improved PL properties, with higher V_{OC} in corresponding PSC devices. In a different effort, You et al.[424] achieved $MAPbI_3$ thin films that exhibit a combination of merits such as outstanding film coverage, large apparent grain size, high carrier mobility, and long carrier lifetimes. In these two studies, it is highly likely that water vapor influences the sublimation or decomposition of the MACl byproduct, modulating the crystallization behavior of the final $MAPbI_3$ film. This hypothesis is supported by the results of Cronin et al.,[554] who have studied the effects of ambient humidity on the optimum annealing time of $MAPbI_3$ films from Cl-containing precursors and conclude that higher humidity accelerates growth of the perovskite grains.

In the case of one-step processing of $MAPbI_3$ films, Gao et al.[423] determined that ambient humidity has separate effects for the spin-coating and annealing steps. They have concluded that, for the spin-coating step, humidity can reduce the supersaturation, resulting in reduced nucleation density and less conformal films prepared either by deposition from a 1:1 solution of MAI:PbI_2 or a 3:1 solution of MAI:$PbCl_2$. For the thermal-annealing step, however, the presence of humidity slows the crystallization process, yielding higher-crystallinity films as inferred from XRD measurements (note, however, that this conclusion only applies to films prepared using the Cl-containing precursor, while films made from the pure iodide precursor crystallize so quickly that differences in the kinetics could not readily be observed.) It is, therefore, reasonable to posit that water acts as a solvent for the perovskite precursors, and the presence of water vapor thus tends to retard crystallization at all steps of the deposition process. Under this interpretation, humidity is, therefore, undesirable during spin-coating, where a high level of supersaturation is desired to yield a uniform film, but desirable during annealing, where slowing the pace of crystallization ultimately yields higher crystallinity and presumably more defect-free films.

It is interesting to note that the observations of Gao et al.[423] regarding the effects of humidity on perovskite crystallization speed directly contradict those of Eperon et al.,[422] who demonstrate that humidity speeds up crystallization rather than slowing it down. This discrepancy is especially puzzling since the films are prepared using essentially the same processing recipe and also that equally plausible mechanisms can be invoked to explain the observations (i.e., in the former, solvating effects of water vapor slow the reaction between the precursors, while in the latter, ambient water vapor coordinates to the excess organic halide and helps to remove it from the film). It is conceivable, however, that the discrepancy may arise from differences in the flow of the ambient atmosphere. In a more stagnant environment, initial evolution of MA^0 gas, HCl, and/or MACl might build up a high partial pressure of these species in the immediate vicinity of the film, retarding further escape and, therefore, also slowing perovskite formation. In a higher-flow atmosphere, the excess organic halide can be more efficiently removed, allowing more rapid crystallization to occur. However, such details are difficult to measure accurately and are frequently omitted from experimental descriptions. This example further highlights the difficulty in establishing, based on device results, whether a proposed processing change is a generally important improvement or whether the change simply improves the device performance for a very specific set of experimental conditions.

For two-step $MAPbI_3$ film deposition methods, humidity appears to influence the crystallization in a different way. Gangishetty et al.[555] show that the crystallite size in as-deposited $MAPbI_3$ thin films increases with increase in humidity. At low relative humidity, small cubic crystallites with large gaps between them are formed, while at higher humidity, larger perovskite crystals with better connectivity are observed. A mechanistic study by Xu et al.[556] suggests that moisture activates the reaction between PbI_2 and MAX, which facilitates the formation of phase-pure $MAPbI_3$, and also allows the tailoring of the crystallization kinetics. Furthermore, Jeong et al.[557] have found that humidity also influences the solution deposition of stacked MAI and PbI_2 layers and thus the final morphology of $MAPbI_3$ films after the precursor interdiffusion reaction.

The processing of $FAPbI_3$ thin films fabricated by solvent engineering also depends on humidity, as shown by Wozny et al.[437] The relative humidity strongly affects the morphology of the as-formed $FAPbI_3$ films. A controlled low humidity environment contributes to the formation of compact,

DOI: 10.1021/acs.chemrev.8b00318
Chem. Rev. 2019, 119, 3193−3295

pinhole-free thin films, whereas high humidity leads to pinhole defects. These results are further supported by a later study by Aguiar et al.,[558] who have observed similar pinhole formation when synthesizing $FAPbI_3$ with moisture exposure using in situ TEM (i.e., perhaps related to the effect of humidity on the nonperovskite-to-perovskite conversion kinetics during $FAPbI_3$ processing). Humidity can also impact the perovskite crystallization through synergy with other substances. For example, Rong et al.[280] have demonstrated a moisture-induced transformation process of $MAPbI_3$ for fabricating printable mesoporous triple-layer PSCs. In this study, moisture synergizes with an ammonium chloride (NH_4Cl) additive in the starting $MAPbI_3$ precursor, forming an intermediate $CH_3NH_3X{\cdot}NH_4PbX_3(H_2O)_2$ (X = I or Cl) phase, which converts to high-quality $MAPbI_3$ crystallites with a preferred tet(110) orientation after annealing.

Water can also be added directly to the precursor solution in order to impact film formation. For example, Gong et al.[559] found that a 2% by volume mixture of water in DMF appears to significantly enhance the surface coverage of $MAPbI_{3-x}Cl_x$ prepared by the one-step spin-coating process, increasing apparent grain size and reducing pinhole density. Wu et al.[560] found that using a 2 wt % mixture of water in DMF enhances dissolution of PbI_2 for use in the two-step spin-coating process, with large voids in the PbI_2 precursor films arising when too little or too much water is used. The $MAPbI_3$ films subsequently prepared from the optimal PbI_2 recipe display compact grains with large apparent size, while the discontinuities in the PbI_2 films prepared with too little or too much water propagate to the final $MAPbI_3$ films. A subsequent study by Chiang et al.[561] revealed that adding H_2O to the MAI solution as well further enhances the apparent grain size, perhaps allowing the MAI to penetrate further into the PbI_2 film, or accelerating the perovskite synthesis reaction, as proposed by Xu et al.[556] Addition of water to the precursor solutions in this manner combined with exposure of the PbI_2-MAI-H_2O precursor film to DMF vapor prior to the final anneal further enhance apparent grain size, while maintaining a compact morphology. It thus appears that water can, in appropriate concentration, effectively contribute to "solvent annealing" of the perovskite (as discussed in section 5.1.2), improving the grain structure and possibly also healing bulk defects. In all cases, however, the amount of water must be tightly controlled in order to avoid detrimental effects, as excessive exposure leads to the familiar problems of film and device degradation.[562]

Water introduction may alternatively occur as a byproduct of the addition of other species employed to affect film processing. A notable category is acids, which are often commercially supplied as aqueous solutions. Heo et al.[563] added hydriodic acid to a precursor solution of $MAPbI_3$ prepared by one-step spin-coating from DMF or DMSO solutions, finding that uniform films with good coverage can be obtained, in contrast with the dendritic morphology typically associated with this method when acid-free precursors are used. While the authors attribute the success of this method to the role of HI in preventing $MAPbI_3$ decomposition, it is possible that the uniform morphology can be obtained because, analogous to the case of excess MAI, the acid donates I^- species that compete with the solvent for coordination to dissolved Pb^{2+} and enable the formation of smaller, more perovskite-like colloids,[162] thus avoiding formation of the dendritic film structure induced by growth of perovskite-solvent intermediates. A more recent study focusing on the effects of HI and HBr on the crystallization of $FA_{0.83}Cs_{0.17}Pb(I_{0.8}Br_{0.2})_3$ reaches a similar conclusion, finding that the presence of hydrohalic acids can mediate the size and dispersion of the colloidal species.[164] As discussed in section 3.1.2, these species can serve as preferential nucleation sites by lowering of the heterogeneous nucleation free energy (per eqs 5 and 6). On the basis of this observation, aging of the solution is likely an important parameter. Insufficiently aged solutions contain large populations of colloids, which lead to a high density of nucleation sites and therefore to compact but apparently fine-grained structures. Increasing solution aging allows the acid to slowly dissolve the colloids, leading to sparser nucleation sites and apparently larger grains, although those that have aged for too long evidently lead to pinhole formation.[164]

Other acids can play a beneficial role. Hypophosphorous acid (H_3PO_2), used as a stabilizer in commercial solutions of HI (a precursor used in the synthesis of MAI), has also been reported to improve grain structure, luminescence, and device performance, with benefits ascribed to either more controlled crystallization via $Pb(H_2PO_2)_2$ intermediates[564] or to suppression of electronic defects.[565] In both cases, it is noted that performance of PSCs suffers when ultrapure MAI is used as a precursor (as obtained through purification of the as-synthesized MAI by recrystallization), suggesting that H_3PO_2 may serve a hidden function in other literature reports, in which the film deposition involves unpurified MAI (typically made by reacting MA with HI containing a small amount of H_3PO_2). Noel et al.[566] found that addition of formic acid (HCOOH) to DMF solutions of MAI and $PbCl_2$ can dissolve colloids, as in the case of hydrohalic acids, leading to more uniform and more crystalline films. Counterintuitively, addition of HCOOH tends to drive the solution pH higher rather than lower. This effect is presumed to be a result of acceleration of DMF hydrolysis (due to the presence of traces of water) by the acid, yielding as products HCOOH and dimethylamine (DMA). As DMA is a stronger base than HCOOH is an acid, the pH rises. The presence of DMA is thought to increase the solubility of the perovskite precursors in the same way as MA^0 gas, as discussed in section 4.1.1, and Noel et al.[566] have determined that bubbling DMA gas through the solution has similar effects on the colloid population as the addition of HCOOH. An additional advantage of the use of this relatively weak acid is that it does not introduce excess halide or phosphorus into the films, simplifying the processing environment compared with other acids. Both $MAPbI_{3-x}Cl_x$ and $(FAPbI_3)_{0.83}(MAPbBr_3)_{0.17}$ devices processed using HCOOH display high V_{OC}; the latter reach 1.21 V, corresponding to a V_{OC} deficit ($= E_g/q - V_{OC}$) of 360 mV, among the lowest values yet observed.[566]

6.3.2. Organic Molecules. Perovskite crystallization processes can be strongly mediated by the presence of molecular spectator species and associated intermediate phases, besides the more ionic additives (as discussed in other components of section 6) and solvent complexes (as discussed throughout section 4). The great breadth and diversity of organic molecules virtually guarantees that at least some of them will, if used properly, play a beneficial role, even if they cannot be expected to participate in the perovskite lattice due to large size and/or lack of suitable tethering groups. Early reports focused on the use of alkyl halides to mediate precursor-solvent interactions, with 1,8-diiodooctane

DOI: 10.1021/acs.chemrev.8b00318
Chem. Rev. 2019, 119, 3193−3295

(DIO) found to improve the morphology and carrier extraction of $MAPbI_{3-x}Cl_x$ films and PSCs, likely as a consequence of improved solubility due to Pb chelation by the additive (due to the Pb···I attraction).[567] These conclusions were found to apply more broadly to a variety of alkyl halides, with improved morphology and performance extending to films produced using the dichlorinated, dibrominated, and diiodinated butane analogs of DIO.[568] Strikingly, the additive can also influence the film composition since the halogens in the additive are relatively labile. $MAPbI_{3-x}Cl_x$ films whose composition differs in no important way from those prepared using the conventional 3:1 MAI:$PbCl_2$ stoichiometry could be obtained from mixtures of MACl, $PbCl_2$, and a large excess of 1,4-diiodobutane.[568]

In analogy to the solvent complexes discussed in section 3.1.2.1, Lewis acid−base interactions can also be used to manipulate film formation. Thiourea (TU) is a Lewis base and can therefore coordinate to Pb, forming intermediates that appear to significantly enlarge the grains of $MAPbI_3$[569] and $FAPbI_3$[570] films, although the exact mechanism remains obscure. The perovskite-TU affinity can even be used to synergistically insert Cu(TU)I adducts into grain boundaries via the solvent engineering method, by codissolving CuI and TU along with the perovskite (in this case $MAPbI_{3-x}Cl_x$) precursors.[571] It is proposed that the perovskite grains are then clad in a coating of the Cu(TU)I adduct, which behaves similarly to CuI in terms of electronic properties, prospectively creating a bulk heterojunction between the intrinsic or *n*-type perovskite and the *p*-type Cu(TU)I coating. This coating also evidently passivates the grain boundaries, both reducing the trap density and moving their energetic location further from midgap, as inferred by admittance spectroscopy. This hypothesis is supported by compositional measurements, for example, inductively coupled plasma atomic emission spectroscopy and FTIR, that indicate the presence of Cu and thiourea in the film, respectively, and EDS measurements that indicate that Cu is localized in the grain boundaries, although it is not unambiguously proven that Cu(TU)I survives as the original adduct or decomposes upon incorporation into the film. Another Lewis base, ascorbic acid (AA), can be useful not for the influence it has on grain growth but as an antioxidant in Sn-containing perovskites. Xu et al.[36] found that ambient stability of low-band gap $MA_{0.5}FA_{0.5}Pb_{0.5}Sn_{0.5}I_3$ perovskites can be improved by AA incorporation, leading to high-detectivity ($>10^{12}$ Jones) near-infrared photodetectors and high PCE $MAPb_{0.5}Sn_{0.5}I_3$ PSCs.[507] For both types of devices, AA appears to serve as a more effective antioxidant than the commonly used additive SnF_2. This observation may prove to be an exciting development in improving the viability of Sn-based perovskite films and devices.

Finally, the $CsPbI_3$ perovskite phase has also been reported to be stabilized by the addition of sulfobetaine zwitterions, which significantly reduces the apparent grain size relative to pristine $CsPbI_3$ for films prepared by the solvent engineering process.[572] Dynamic light scattering measurements indicate that the zwitterions interfere with the PbI_2-DMSO interaction, leading to the formation of much smaller colloidal particles that result in the deposition of a practically amorphous film. As in the case where HI is added to the $CsPbI_3$ precursor solution (see section 6.2.1.2),[114] the smaller grains induced by the presence of the zwitterions may be more stable as a result of increased importance of the surface free energy relative to the bulk, favoring the more symmetric perovskite over the nonperovskite structure.[572]

6.3.3. Quantum Dots. A final means of controlling crystallization of the 3D perovskite is to introduce quantum dots (QDs) into the precursor solution to act as preferential heterogeneous nucleation sites, whose size and distribution can be used to tune the perovskite film grain structure. Li et al.[183] used MAI-capped PbS quantum dots to template film growth, with 1 wt % inclusion in the $MAPbI_{3-x}Cl_x$ precursor solution yielding an optimal morphology (i.e., apparently large, compact grains). Along similar lines, Ngo et al.[184] incorporated PbS/CdS core/shell quantum dots into solvent-engineered $MAPbI_3$ films, not only improving the apparent grain size but also modulating the PL and electroluminescence spectra of the QD-perovskite films and LEDs constructed using those films (i.e., a broad infrared emission peak appears in addition to the characteristic band-to-band luminescence of the $MAPbI_3$ matrix). It should be noted that some of the grain growth observed in the latter case may be due to the presence of Cd, which may have leached out of the QD shell, as evidenced by the telltale appearance of $(MA)_2CdI_4$[514] in SEM images of the perovskite film structure. Overall, these results are intriguing, as they point the way toward opportunities for fabrication of more complex photonic and optoelectronic structures.

6.4. Low-Dimensional Perovskites

6.4.1. Low-Dimensional Hybrid Perovskites/Large Organic Cation Incorporation. While 3D perovskites (i.e., those whose crystal structure exhibits three-dimensional connectivity of the metal halide octahedra) are the most actively studied systems for film deposition and device integration, layered perovskites (section 2.1; Figures 2 and 3) offer much greater flexibility for materials design (i.e., ability to incorporate larger and potentially functional organic cations) and provide unique opportunities and challenges for film deposition. In the case of particularly large organic moieties, their disparate chemical nature relative to the inorganic framework requires the application of unconventional deposition methods that can blend the structural components yet avoid damage to the organic part (e.g., see section 4.1.6). As observed in sections 2.1 and 2.3.2.2, one of the more general challenges associated with the layered perovskites is the control of crystallographic orientation such that the layers are either vertical or horizontal with respect to the substrate (for applications or measurements where charge transport is important). In PSCs, for example, since current collection occurs in a direction perpendicular to the substrate, the most effective configuration would be for the perovskite layers to orient perpendicular to the substrate.

Use of the quasi-2D Ruddlesden−Popper phases rather than the purely 2D compositions offers one pathway for addressing crystallographic orientation within deposited films, as more 3D-like structures are less likely to prefer a configuration in which the perovskite layers lie flat relative to the substrate. Cao et al.[70] observed that, for $(BA)_2(MA)_{n-1}Pb_nI_{3n+1}$ films produced by one-step spin-coating, only for the purely 2D structure (n = 1) do the perovskite layers lie completely flat on the substrate, with XRD patterns displaying only the (00*l*) reflections. As n increases, crystallite growth perpendicular to the layers becomes increasingly favorable due to the growing influence of the MA cations. For n = 2, the "off-axis" XRD peaks are only barely visible but are completely dominant for larger values of n, indicating predominantly vertical orientation of the layers.[70]

DOI: 10.1021/acs.chemrev.8b00318
Chem. Rev. 2019, 119, 3193−3295

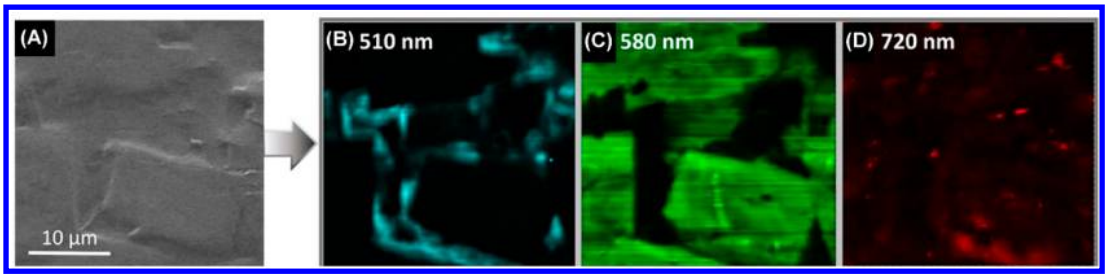

Figure 51. (A) Top-surface SEM image and (B−D) CL maps of a spin-cast "n = 2" $(PEA)_2MAPb_2I_7$ thin film, displaying luminescence from (B) n = 1, (C) n = 2, and (D) large-n Ruddlesden−Popper phases, thereby demonstrating the phase impure nature of the film. Adapted from ref 72. Copyright 2017 American Chemical Society.

Tsai et al.[73] compared the X-ray diffraction and scattering patterns of spin-cast $(BA)_2(MA)_3Pb_4I_{13}$ (n = 4) films, finding that although the perovskite grains are randomly oriented when fabricated on room-temperature substrates, hot-casting (as discussed in section 4.1.1) enables the formation of strongly oriented films with layers perpendicular to the substrate and provides for efficient conduction of current across the plane of the film. Chen et al.[152] have proposed that the vertical layer orientation in these materials originates from heterogeneous nucleation of the grains at the liquid−gas interface, rather than at the liquid-substrate interface, or homogeneously within the solution. This interpretation is driven by observations of crust formation over the surface of a drop of precursor solution as it dries on a hot plate, indicating that solution supersaturation occurs predominantly near the surface and providing for an independence of the crystallization behavior with regard to substrate type (even including mesoporous substrates).[152] Obtaining the vertical perovskite layer orientation using nominal n = 4 compositions has thus far been a fairly successful strategy for the fabrication of PSCs with enhanced moisture/environmental stability, although their PCE still lags that of the 3D perovskites by a considerable margin.[73,573−576]

It should be noted that the nominal target compositions of the Ruddlesden−Popper perovskites (specified by the layer number n) typically do not accurately reflect the actual phases present in the resulting films. Often, these compositions are targeted by blending the precursors in the desired stoichiometry prior to deposition; yet, the films so obtained contain inclusions of Ruddlesden−Popper perovskites of other layer thicknesses (higher or lower n).[31,72] The distribution of such phases can be especially important for device operation as their relative band alignment favors funneling of excited carriers to the phase with the lowest band gap.[31] Photo- and electroluminescence of such mixed-phase thin films may be "contaminated" or even dominated by contributions from phases with different n relative to the target phase. In this regard, the luminescence of Ruddlesden−Popper perovskite films can be a more sensitive phase composition determination approach than techniques such as XRD, which can be misleading (due in part to the changing preferred orientation as n increases). For example, a recent report by Tsai et al.[577] indicates that phase-pure $(BA)_2(MA)_{n\text{-}1}Pb_nI_{3n+1}$ Ruddlesden−Popper films can be obtained by dissolving presynthesized single crystals of the desired composition in DMF and hot-casting the resulting solution as described in section 4.1.1. However, the resulting films are evidently not phase-pure, as their electroluminescence spectra possess multiple peaks in some cases. Moreover, the positions of these peaks disagree with earlier work by Stoumpos et al.,[578] who performed PL measurements on $(BA)_2(MA)_{n\text{-}1}Pb_nI_{3n+1}$ single crystals and found the resulting spectra to possess single, sharp, and well-defined peaks. With the assumption that the data obtained from the single crystals are representative of a truly phase-pure material, reconciling the above results indicates that the "n = 2" films are dominated by luminescence from phases corresponding to n = 3 and 4, while higher-n films are mostly dominated by luminescence from n > 4. Although the XRD patterns are dominated by peaks of the desired phase, even small inclusions of the lower-band gap phases that are below the threshold of detection by XRD can have a large effect on the luminescence due to the carrier funneling effect described by Yuan et al.[31]

Stoumpos et al.[578] have also noted that, in order to obtain a high yield of corresponding $(BA)_2(MA)_{n-1}Pb_nI_{3n+1}$ single crystals, it is necessary to use a deficiency of BA in the starting solution, due to the different solubility characteristics of the 3D and 2D perovskite components. In view of these results, it is not surprising that spin-coating solutions prepared by dissolution of single crystals might not yield phase-pure films and that achieving such films might require finer control over the stoichiometry as well as careful attention to the impact of a given combination of precursors and solvents. Note that while photo- and electroluminescence measurements can be useful at detecting the presence of contaminant phases, they are bulk-averaged measurements and do not help to unravel the microstructural details. However, Cortecchia et al.[72] have performed SEM/CL measurements on "n = 2" $(PEA)_2MAPb_2I_7$ films spin-cast in a single step from a DMSO solution, and found that, although the grains are dominated by luminescence from the true n = 2 phase, the surfaces are decorated with regions corresponding to other values of n (Figure 51). While detailed mechanistic insight into how different growth conditions promote a different phase distribution was not probed in this study, it serves as a useful proof-of-concept for further exploration of CL mapping as a tool for understanding these phenomena.

Although the layered hybrid perovskites represent an interesting area in their own right, incorporation of the large organic cation can be beneficial even in very small amounts that do not substantially perturb the 3D structure, not only because the hydrophobicity of commonly used functional groups such as alkyl chains or aromatic rings can protect the structure from attack by moisture[579,580] but also by suppressing ion-migration and stabilizing the overall structure. These beneficial effects appear to remedy many of the problems afflicting the various perovskite family members. Stability of $MAPbI_3$ films against damp heat has been reported to improve with ethylammonium (EA^+) alloying, without significant

DOI: 10.1021/acs.chemrev.8b00318
Chem. Rev. 2019, 119, 3193−3295

impact on the grain structure, along with a substantial boost to the carrier lifetime, from 300 to 2000 ns.[581] Wang et al.[582] have also found that MA-EA alloying does not substantially alter the grain structure but in this study the additive appears to degrade PV performance at all levels investigated. Chen et al.[583] observed that addition of small amounts of PEA into the $MAPbI_3$ precursor solution results in films and PSCs in which the presence of PEA is hardly detectable, except by somewhat ambiguous changes in infrared absorption spectra, yet the films are much more resistant to hysteresis and humidity-induced degradation compared to the pristine $MAPbI_3$ films. The authors attribute this effect to the formation of a 2D $(PEA)_2PbI_4$ cladding around the $MAPbI_3$ grains, protecting against moisture ingress and inhibiting iodide migration. Amino acid halides have also found use in improving the environmental stability of $MAPbI_3$ films and PSCs, particularly in the all-mesoporous architectures discussed in section 4.1.5 [e.g., 5-ammoniumvaleric acid iodide (5-AVAI)], have been employed to improve carrier lifetime and better anchor the perovskite to the mesoporous scaffold.[278] The reported benefits of the amino acid may also be due in part to the formation of a phase mixture of 2D (incorporating the large 5-AVA^+ cation) and 3D perovskites, wherein the former can help to passivate interfaces and also protect the latter against damage by moisture ingress. Solar modules using the all-mesoporous architecture and 5-AVAI additive are able to maintain their PCE for over a year in ambient conditions without any evidence of degradation.[584] As noted in section 6.2.3.1, Xiao et al.[542] demonstrated that reduction of apparent grain size by addition of excess BAI and/or BABr could play an especially important role in mixed iodide-bromide films (i.e., the smaller grain size reportedly leads to a significant reduction in light-induced phase-segregation into iodide-rich and bromide-rich regions).

Large organic cations can also allay phase instability in both FA- and Cs-based perovskite films (as discussed in section 6.2.1). Li et al.[580] found that inclusion of PEA (~5 mol %) in the FAI solution used in the two-step spin-coating process prevents reversion of α-$FAPbI_3$ to the nonperovskite phase in ambient air with 40% relative humidity, presumably by a similar mechanism to that described earlier involving PEA localized at grain boundaries. Incorporation of PEA not only allows the film to become more moisture resistant but also may provide an inherent stabilizing force against the layer translation necessary to convert $FAPbI_3$ to the nonperovskite phase.[580] PEA also appears to improve the crystallinity of the $FAPbI_3$ perovskite, as inferred from a boost in the intensity of the XRD patterns upon its addition.[580] Similarly, Fu et al.[585] found that PEA- and oleylamine (OA)-derived cations both stabilize perovskite phases of $CsPbI_3$, although OA induces the formation of the cubic α-$CsPbI_3$ perovskite phase while PEA appears to favor a slightly distorted orthorhombic β-$CsPbI_3$ perovskite phase (Figure 52A). These cations additionally improve the film morphology considerably. The pure, nonperovskite $CsPbI_3$ film is highly discontinuous, but the OA- and PEA-alloyed films comprise compact grains with small apparent size (although some pinholes are still present in the former film), as shown in Figure 52 (panels B−D). The OA- and PEA-alloyed films display good phase stability when encapsulated samples are stored in air over a period of 4 months, with no sign of degradation in the XRD pattern and UV−vis spectrum of the PEA sample and with only very minimal loss in absorbance for the OA sample.[585] Zhang et al.[586] have also found that addition of the divalent en^{2+} cation can both lower the formation temperature as well as stabilize the perovskite phase of $CsPbI_3$, possibly as a result of apparent grain size reduction and improved intragranular cohesion as a result of cross-linking behavior provided by the en^{2+} cation.

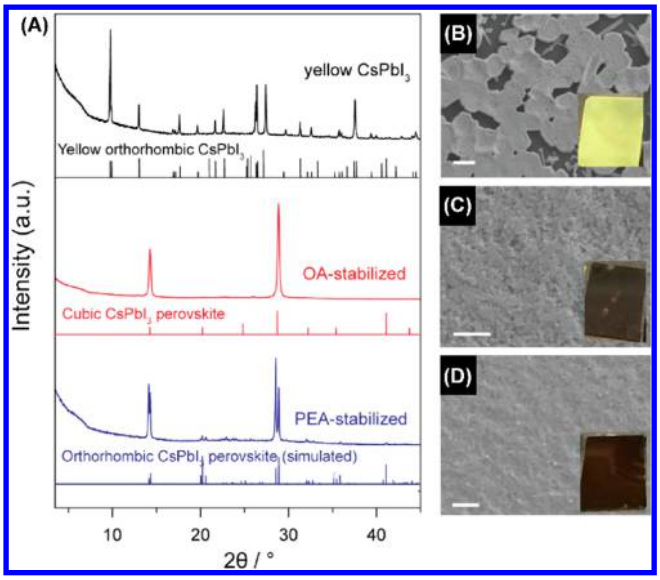

Figure 52. (A) XRD patterns of pristine, OA, and PEA-stabilized $CsPbI_3$. Corresponding top-surface SEM images of (B) pristine, (C) OA-stabilized, and (D) PEA-stabilized $CsPbI_3$ thin films. Insets: photographs of the respective thin films. All scale bars 1 μm. Adapted from ref 585. Copyright 2017 American Chemical Society.

Alloying of the large organic cations can also be employed to protect the Sn-based perovskite films against oxidation. Cao et al.[499] found that PSCs prepared using the Ruddlesden−Popper $(BA)_2(MA)_2Sn_4I_{13}$ perovskite films are significantly more stable in air than analogous $MASnI_3$ films/devices, presumably due to the increased hydrophobicity (and therefore resistance to moisture ingress) of the films due to the presence of the BA-cation alkyl chains. Ruddlesden−Popper perovskites, $(PEA)_2(FA)_{n-1}Sn_nI_{3n+1}$, formed using a PEA:FA ratio of 20% in the precursor solution, also appear to be more stable than pristine $FASnI_3$ films, with less Sn^{4+} evident in the former's XPS spectrum as well as considerably more stable PSC performance.[492] This effect may be partly attributable to an intrinsically higher enthalpy of decomposition by oxidation of the system as the layer number n decreases (*i.e.*, more 2D systems are more stable). However, the improved stability may also arise because addition of PEA induces the growth of a smoother, more tightly packed grain structure (compared to the 3D system) that more efficiently resists ingress of oxidizing species, in addition to the protection conferred by the hydrophobic phenyl rings.[492] Even smaller amounts of the large organic cation can be beneficial. As noted in section 6.2.2.1, Shao et al.[495] observed that 8−12 mol % replacement of FA with PEA in the $(PEA)_2(FA)_{n-1}Sn_nI_{3n+1}$ precursor solution appears to "fuse" grain boundaries, possibly obstructing diffusion channels that would otherwise form along them, although larger amounts lead to pinhole formation. Accordingly, PSCs prepared using 8 mol % PEA outperform the pristine $FASnI_3$ in all device performance parameters, as well as stability.

6.4.2. Low-Dimensional All-Inorganic Perovskites. While low-dimensional perovskites formed by the addition of

DOI: 10.1021/acs.chemrev.8b00318
Chem. Rev. 2019, 119, 3193−3295

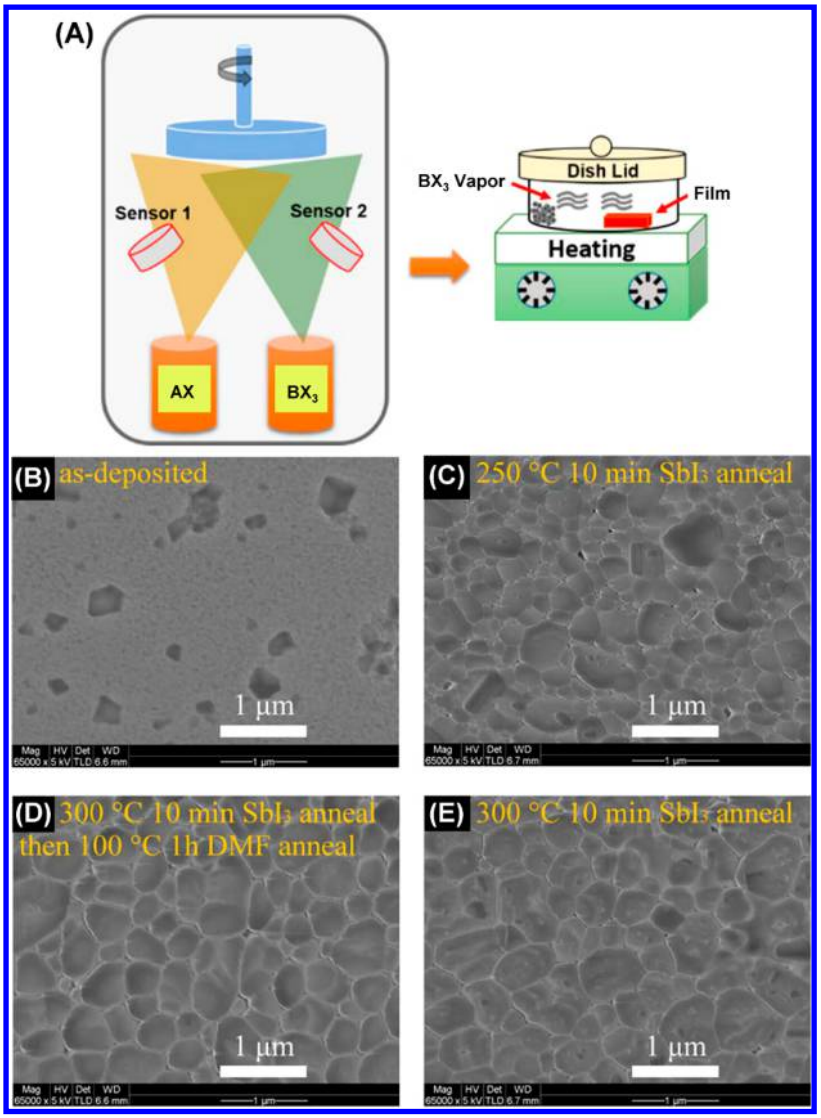

Figure 53. (A) Schematic illustration of the two-step evaporation method used to deposit low-dimensional all-inorganic perovskite thin films. Adapted from ref 590. Copyright 2018 American Chemical Society. (B) Top-surface SEM images of the microstructures of $Cs_3Sb_2I_9$ obtained by this method: (B) as-deposited film and (C−E) coarsened microstructure under various annealing conditions. Adapted from ref 589. Copyright 2015 American Chemical Society.

large organic cations tend to be the most heavily studied, all-inorganic compositions have also been pursued. These structures require (and accommodate) somewhat different processing approaches than those typically used for the hybrid perovskites. Strictly inorganic precursors tend to behave somewhat differently than organic-based analogs; for example, CsI is relatively insoluble compared even to PbI_2, as noted in section 6.2.1.2, while many of the other metal halide precursors involved in the formation of lower-dimensional perovskites (e.g., SnI_4, SbI_3, BiI_3, $TiBr_4$) are comparatively volatile. Thus, sequential or two-step vapor deposition techniques (similar to those discussed in sections 4.2.3 and 4.2.4) may be more attractive for this class of materials than solution-based methods, although there are some reports of film synthesis via these latter techniques. For example, Park et al.[587] deposited $Cs_3Bi_2I_9$ films (with dimer nonperovskite rather than layered perovskite crystal structure) by single-step spin-coating, although the coverage was not especially uniform. Harikesh et al.[588] deposited the layered perovskite $Rb_3Sb_2I_9$ by a solvent-engineering recipe, wherein loss of volatile SbI_3 was compensated by adding SbI_3 to the toluene antisolvent, which also improves film coverage. In the two-step vapor deposition approach, one or both of the precursors are thermally evaporated in the first step and the resulting film is thereafter annealed in an atmosphere of the more volatile halide (e.g., SbI_3 or BiI_3), as shown in Figure 53A. The approach further benefits from the fact that the inorganic components of the layered perovskites are unlikely to thermally decompose at the temperatures used for annealing. Saparov et al.[589] reported that $Cs_3Sb_2I_9$ thin films with large apparent grain size (Figure 53, panels B−E) could be obtained by coevaporating CsI and SbI_3 and thereafter annealing the resulting film at ∼300 °C in SbI_3 vapor (in a nitrogen-filled glovebox). In this manner, quick reaction of the precursors yields films with large and compact grains. Importantly, relatively random crystallographic grain orientation, such that cross-plane transport is not compromised by the directions with unfavorable electrical mobility, can be obtained by depositing only CsI during the thermal evaporation step and thereafter annealing in preheated SbI_3 vapor.[589] The details of the vapor annealing process play a

DOI: 10.1021/acs.chemrev.8b00318
Chem. Rev. 2019, 119, 3193−3295

critical role in obtaining an optimized film. The annealing temperature dictates the grain size and film continuity (Figure 53, panels B−E), with too low of a temperature leading to small apparent grain size and too high of a temperature inducing pin holes. Quenching the film at too high of a temperature may result in loss of SbI_3 from the film (especially the surface region), while cooling the film to near ambient temperature before removing from the SbI_3 atmosphere may result in unwanted condensation of excess SbI_3 on the film surface. The optimal procedure reportedly involves cooling the film to 200 °C, followed by quenching.[589] Khazaee et al.[590] have also reported that a variant of this process can be used to grow films of $Rb_3Bi_2I_9$ (as well as the 3D nonperovskite $AgBi_2I_7$), wherein a postanneal under BiI_3 vapor appears to substantially enlarge the grains relative to the as-deposited films produced by coevaporation, without leading to pinhole formation. The two-step approach has also been used for "zero-dimensional" (BX_6 octahedra are completely isolated from one another) perovskites including Cs_2SnI_6[591] and Cs_2TiBr_6.[538] Annealing thermally evaporated CsI films in SnI_4 vapor at 190 °C yields phase-pure Cs_2SnI_6 films with a compact grain structure, which is challenging to achieve by solution methods due to the low solubility of the precursors in common polar solvents.[591] Chen et al.[538] applied similar methods to the synthesis of Cs_2TiBr_6, annealing thermally evaporated CsBr thin films in $TiBr_4$ vapor at 200 °C for 24 h. By doing so, they obtain films with compact grain structure and PL lifetime of ∼24 ns.

7. SUBSTRATE-PEROVSKITE INTERACTIONS

An important factor in determining the growth of a thin film is the substrate, which not only influences wetting or distribution of the precursors but also can perform chemistry on the film during or after its formation, thereby affecting electrical properties and morphology. The substrate choice can, therefore, have profound effects on the needs for successful film deposition and on the ultimate film properties or device performance. The need to understand substrate−film dynamics is especially acute in the case of the halide perovskites, as their facile reactivity can lead to unexpected interactions with the substrate.

7.1. Impact of Substrate on Film Nucleation and Growth

7.1.1. Effects of Substrate Geometry. One key factor influencing substrate−film interaction during film growth relates to the choice of planar versus mesoporous substrate configuration (e.g., in the design of a solar cell, LED, or other device architecture, as discussed in section 2.2). An important ongoing question regarding the mesoporous architecture revolves around whether the perovskite is the same within and outside of the pores (i.e., as in a capping layer overlying the mesoporous layer or as in a distinct active layer on a planar substrate). Early studies indicated that $MAPbI_3$ infiltrated within mesoporous TiO_2 is largely amorphous (although aging improves crystallinity)[592,593] yet possesses strong PL when compared with an analogous bulk perovskite sample, in addition to yielding a blue shift of the absorption onset.[592] A blue shift in the absorption and PL spectra for perovskite confined in mesoporous Al_2O_3 scaffolds relative to that grown on a flat substrate has also been observed.[413,594] An explanation offered for this phenomenon is that the mesoporous structure induces a random ordering of the MA^+ cations, which are otherwise consistently more ordered on a flat substrate. This difference may lead to a shift in the energetics of the excitonic transition, accounting for the blue shift in the optical spectra.[413] Listorti et al.[88] suggest that the crystal structure of perovskite infiltrated into the mesoporous structure differs from perovskite deposited on planar substrates regardless of substrate chemistry (also noting a familiar blue shift in the mesoporous perovskite) and that the diffusion length in the former is inferior to that in the latter. As observed in section 3.3, crystallization within the pores of the scaffold can lead to tensile strain within the perovskite grains,[87] providing an alternate possible explanation for the modification of the optical properties of the mesoporous films.

The morphology of the capping layer itself, however, can be influenced by the mesoporous layer. The higher surface area available on mesoporous substrates is claimed to lead to a higher density of nucleation sites, leading to enhancement of coverage but also reduction in grain size, an effect that carries over into the capping layer (the grain size within the pores themselves is obviously limited by the average pore size).[87,163,595] In alignment with this observation, greater scaffold porosity leads to smaller grains in the capping layer, again presumably because the greater density of nucleation sites stimulates more heterogeneous nucleation.[595] The dimensionality of the component nanostructures within the mesoporous framework can also influence grain size, with nanoparticles leading to flatter surfaces and fewer nucleation sites and therefore larger apparent grain size, and nanowires leading to rougher surfaces, higher nucleation densities, and smaller apparent grain size.[596] The thickness of such nanowire layers also appears to have an impact (i.e., greater thickness of the mesoporous nanowire layer leads to higher nucleation density for nanowires and hence smaller apparent grain size), despite a roughly constant capping layer thickness.[597] This effect may, however, be more related to the increased structural complexity of the nanowire network, rather than any direct effects pertaining to thickness. Pascoe et al.[598] observed that the texturing of the capping layer can be sensitive to both the nature of the substrate as well as precursor solution concentration, finding that rough although mostly conformal $MAPbI_3$ layers could be obtained via the gas-quenching technique, when depositing high concentration solutions on mesoporous TiO_2 substrates. Curiously, this effect appeared to be specific to the above set of experimental parameters and could not be duplicated when using low-concentration precursors, a planar substrate, or a mesoporous Al_2O_3 scaffold, which yielded instead a flatter, compact morphology characteristic of typical films produced by solvent engineering or gas-quenching. This result may reflect a particular affinity between the perovskite and TiO_2, wherein the perovskite growth is more closely templated by the TiO_2 than analogous Al_2O_3; however, this difference was left largely unexplored.

A mesoporous scaffold may be a particularly advantageous substrate for 2D perovskites. The isotropic nature of the pore network should allow the perovskite grains to crystallize without any preferred orientation with respect to the layer axis, thus mitigating their tendency to present a barrier to electric current across the plane of the film, as discussed in section 2.1. Indeed, Safdari et al.[599] show that alkyldiammonium lead iodide perovskite films (alkyl groups: butyl, hexyl, and octyl) spin-coated onto mesoporous TiO_2 substrates exhibit XRD patterns resembling the powder patterns of the equivalent ground bulk materials, as opposed to the group of evenly spaced peaks characteristic of a single set of crystallographic

DOI: 10.1021/acs.chemrev.8b00318
Chem. Rev. 2019, 119, 3193−3295

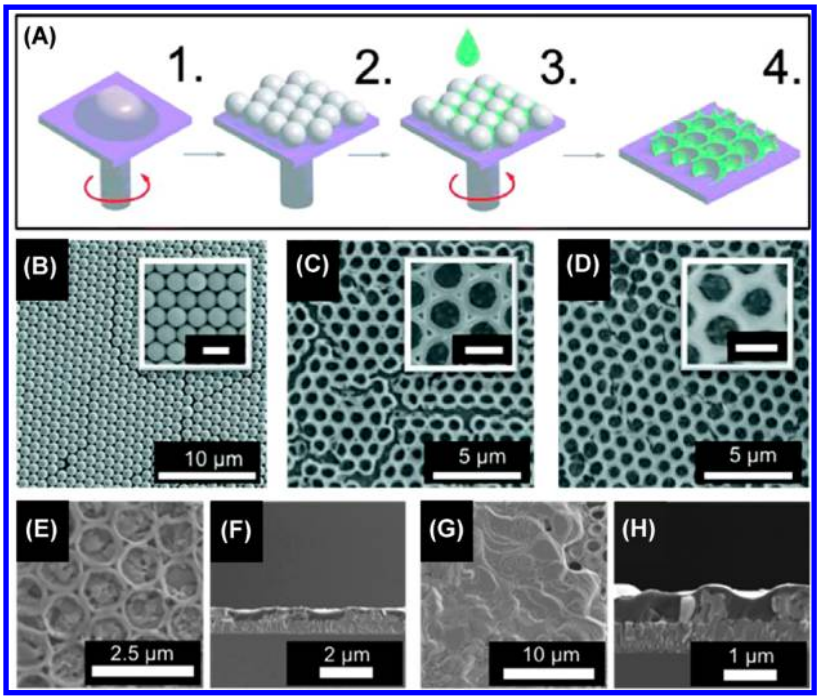

Figure 54. (A) Schematic illustration of the formation of microstructured oxide scaffolds: the oxide precursor is deposited onto a monolayer of polystyrene spheres, then calcined to burn off the spheres, leaving behind a honeycomb-like network of the oxide. Top-surface SEM images of nanostructures: (B) hexagonal arrangement of polystyrene sphere monolayer, (C) final TiO_2, and (D) SiO_2 nanostructures. (E and G) Top-view and (F and H) cross-sectional SEM images of $MAPbI_{3-x}Cl_x$ deposited onto the scaffold using (E and F) 20 and (G and H) 40 wt % precursor solutions. Reprinted with permission from ref 601. Copyright 2015 Royal Society of Chemistry.

planes parallel to the perovskite layers. Similarly, Sanehira et al.[600] have demonstrated that $(BA)_2PbI_4$ films with significant vertical orientation of the layers can be grown on TiO_2 nanowire substrates. These reports illustrate that mesostructured substrates may prove useful for improving the functionality of 2D perovskite devices for which good cross-plane charge transport is necessary.

A more extreme example of the use of a microstructured layer to template the growth is provided by Hörantner et al.,[601] who patterned a semiperiodic honeycomb-structured mesoporous layer (TiO_2 or SiO_2) by first depositing a monolayer of polystyrene (PS) spheres (diameter ~1 μm) followed by the metal oxide precursor, then sintering the structure at 500 °C to burn off the organic components, leaving the metal oxide behind (Figure 54, panels A−D). The perovskite is then infiltrated into the network by one-step spin-coating from a 3:1 solution of MAI:$PbCl_2$ in DMF (Figure 54, panels E−H). Semitransparent PSCs using such SiO_2 and TiO_2 microstructures perform favorably relative to those with a planar structure and a noncontinuous perovskite layer (allowing light transmission through the voids in the film), since it maintains transparency without shunt path formation between the HTL and ETL.[601,602] Similar success has been achieved using an anodized Al_2O_3 layer with pillar-shaped cavities into which the perovskite is infiltrated.[603] Zheng et al.[604] noted an added benefit, in that such TiO_2 microstructures could also reduce reflective losses in PSCs. This technique can also be applied to patterning of organic transport layers. The PS spheres can be dispersed in PEDOT:PSS ink, which is then spin-cast onto the substrate; the PS spheres are then removed from the film by washing with a nonpolar solvent.[605] Zhang et al.[605] find that perovskite films fabricated on such films display enhanced crystallinity and apparent grain size and that associated PSCs perform better than those fabricated on planar PEDOT:PSS layers. Hu et al.[606] find not only that light harvesting is improved in PSCs based on micropatterned PEDOT:PSS, as for analogous TiO_2 layers, but that such PEDOT:PSS films also display enhanced flexural robustness, enabling the production of flexible PSCs with superior performance and longevity.

7.1.2. Effects of Surface Chemistry. Perovskite-substrate interactions can be highly important in influencing film nucleation. Given that the perovskite precursors will only dissolve in highly polar solvents, which have a strong affinity for hydrophilic surfaces, substrate surface energy may modulate perovskite nucleation. Yang et al.,[607] for example, tuned the wetting properties of SnO_2 by depositing a self-assembled aminosilane monolayer on top of it. By itself, UV-treated SnO_2 is highly hydrophilic, but deposition of the monolayer increases the contact angle, allowing for an increase in the apparent grain size of perovskite films deposited on the treated substrates.[607] Singh et al.[608] observed that treating the TiO_2 surface with potassium bis(trifluoromethanesulfonyl)-imide (K-TFSI) greatly increases the apparent grain size of triple-cation perovskite films prepared by solvent engineering. The larger grains may arise from enhanced substrate-perovskite bonding enabled by residual sulfate groups left on the TiO_2 surface, although further investigation is needed to explore the details of this mechanism.

Some care must be taken in choosing a substrate or surface modification, as an excessively hydrophobic surface may preclude deposition of the perovskite altogether or at least induce significant dewetting that leads to pinhole or void formation. Lee et al.[609] encountered such problems when depositing $MAPbI_3$ on poly(*N*,*N*′-bis(4-butylphenyl)-*N*,*N*′-bis(phenyl)benzidine) (poly-TPD), a hydrophobic HTL,

DOI: 10.1021/acs.chemrev.8b00318
Chem. Rev. 2019, 119, 3193−3295

leading to significant defects in film continuity. Film morphology was improved by inserting a nominally *n*-type layer of poly[(9,9-bis(3′-(*N*,*N*-dimethylamino)propyl)-2,7-fluorene)-*alt*-2,7-(9,9-dioctylfluorene)] (PFN), which possesses both hydrophobic and hydrophilic functional groups, allowing it to bind to the PTPD substrate as well as the perovskite. This interlayer leads to complete coverage of the perovskite film, albeit with much smaller apparent grain size, as may be expected from the increased probability of nucleation on the substrate. Surprisingly, the *n*-type nature of the PFN interlayer does not appear to interfere with hole extraction by the HTL.[609]

The propensity of the perovskite to be excluded from especially hydrophobic regions of the substrate can be an advantage, and it has been exploited to form intricately patterned thin films. For example, Kagan et al.[610] were able to partition $(PEA)_2SnI_4$ films by predepositing a pattern of alkyl-based inks with head groups chosen to bond to the substrate using a silicone stamp then spin-coating the perovskite precursor on top (Figure 55, panels A−C). The perovskite

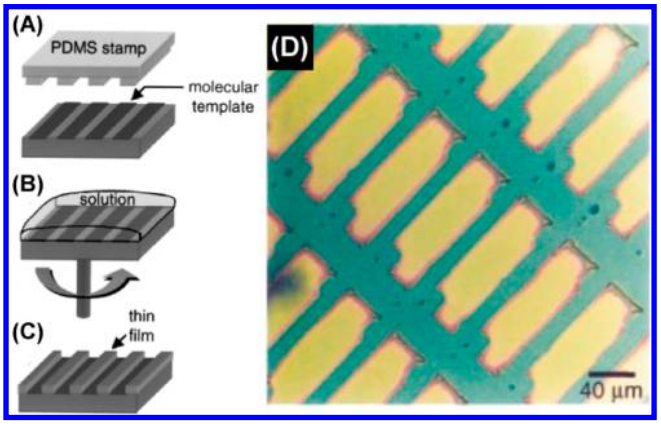

Figure 55. (A−C) Schematic illustration of complex feature patterning by PDMS stamping and (D) optical microscope image of $(PEA)_2SnI_4$ (light regions) on a ZrO_2 substrate. Reprinted with permission from ref 610. Copyright 2001 AIP Publishing.

deposits only where the substrate is left exposed, allowing for the creation of complex patterns such as zig-zagged lines, curves, and dots, with a micrometer-scale feature resolution (Figure 55D). The patterned perovskite can then be used to prepare low-leakage thin-film transistors.[610] Along similar lines, Wu et al.[611] lithographically patterned Al_2O_3 and hydrophobic poly-TPD layers, such that $MAPbI_3$ could be deposited only inside a regular array of trenches in the Al_2O_3, and these films were integrated into semitransparent PSCs. Feng et al.[612] used a Si micropillar array with hydrophobic fluorinated alkyl chains on the sides of the pillars and bare Si top surfaces to grow $MAPbBr_3$ films on only the latter. The resulting square microplates could then be transferred to a substrate to form a laser array with components of uniform size and controllable spacing and distribution. Geske et al.[613] have observed an interesting effect, wherein a regular microstructure can be obtained in $MAPbI_3$ and $MAPbBr_3$ films fabricated on Si/SiO_2 substrates on which a square array of Au dots is deposited. The dot spacing determines the structure of an array of perovskite domains in the resulting films, which resemble the morphology obtained by typical hot casting methods but also inheriting the regularity of the underlying Au dot pattern. It is interesting to note that these films are fabricated not exactly by the hot-casting process described in section 4.1.1 but rather by single-step spin-coating followed by a rapid hot plate anneal (10 s at 180 and 200 °C for $MAPbI_3$ and $MAPbBr_3$, respectively);[613] this process nevertheless seems to lead to similar morphology as preheating the substrate and solution. In the case of $MAPbI_3$, while these domains are referred to as grains, they are probably not grains, as evidenced by their internal structure (as discussed in section 4.1.1) and more likely arise from Rayleigh-Bénard convection cells.[263] These cells may be present during the anneal before the solvent (which contains DMSO in both cases—i.e., likely to persist within the film after spin-coating) is expelled from the film during annealing. Optical microscope images of $MAPbI_3$ grown on uniform Si/SiO_2 and $Si/SiO_2/Au$ substrates indicate that the films wet much more easily on the former than the latter.[613] Thus, the structure of the patterned films may arise from an outward flow of the precursors away from the Au dots toward the exposed oxide. It is more difficult to determine whether the domains equate to grains in the $MAPbBr_3$ films, as they are more strongly faceted, smoother, and possess much greater preferred orientation than the analogous $MAPbI_3$ films.[613] This behavior is consistent with that described in section 6.2.3.1, in which it is typically much easier to obtain large and well-faceted crystallites in $MAPbBr_3$ than in $MAPbI_3$. Despite the uncertainty regarding the films' true grain structure, these results are an interesting example of how patterning of the substrate can be used to induce topographical ordering of the overlying film.

Vapor-deposited perovskite film characteristics can also be affected by the substrate chemistry, as discussed in section 3.1.3. In a recent review, Ávila et al.[195] note that, while $MAPbI_3$ can form quickly and cleanly when deposited on organic substrates such as polyethylenimine or PEDOT:PSS, an interfacial buffer layer builds up on oxides, although the nature of this layer is dependent on the individual chemistry of the oxide. On MoO_3 and ITO, OH groups may contribute to MAI decomposition, reducing adhesion. On the (110) face of TiO_2, an MAI-rich buffer layer is reported to form, while on ZnO the buffer appears to be PbI_2-rich. This observation offers some implications for the tailoring of film/device interfaces, wherein the chemistry of the perovskite buffer layer can be controlled (or removed altogether) by the application of thin interfacial layers. However, more work remains to be done to provide a concrete understanding of these relatively complex growth processes and substrate−film interactions.

7.1.3. Epitaxy. Although the halide perovskites are widely renowned for their defect resistance, it can nevertheless be advantageous to limit the opportunities for defect formation. Epitaxial film growth has proven to be crucial for the fabrication of high-quality III−V optoelectronic devices and thus may hold some promise for improvement of perovskite films as well, not only for the potential for fabrication of single crystal thin film devices but also for physical property measurements less contaminated by the effects of grain boundaries or bulk defects. As discussed in section 3.1.1.2, perovskite formation is typically assumed to occur via the island/Volmer−Weber growth mechanism. However, suitable choice of the substrate can instead promote layer-by-layer/Frank-van der Merwe growth, facilitating the formation of single-crystal thin films. Wang et al.[614] demonstrated epitaxial growth of $CsSnBr_3$ on the (100) face of a NaCl single crystal by thermal coevaporation of CsBr and $SnBr_2$, enabled by the low lattice mismatch between these materials (a = 5.80 Å for

DOI: 10.1021/acs.chemrev.8b00318
Chem. Rev. 2019, 119, 3193−3295

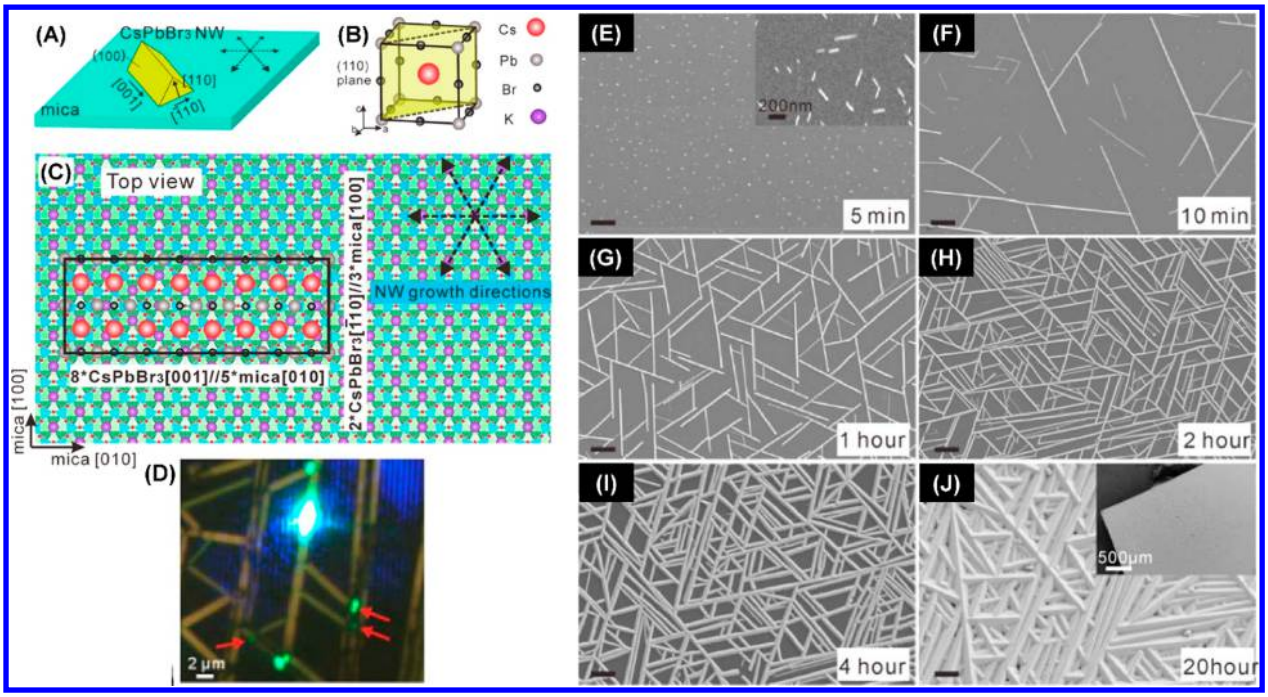

Figure 56. Schematic illustrations of (A and B) growth of $CsPbBr_3$ nanocrystals on a phlogopite mica substrate and (C) interfacial lattice arrangement of the $CsPbBr_3$ crystals relative to the hexagonal mica substrate. (D) Waveguiding behavior in the nanowires, as evidenced by PL emission from the ends of the wires. (E−J) Top-surface SEM images of the nanowires grown for various durations. Given enough time, the nanocrystals grow together and form a largely continuous thin film. Adapted from ref 618. Copyright 2017 American Chemical Society.

$CsSnBr_3$ and 5.64 Å for NaCl, leading to a compressive mismatch of −2.8%). High ionicity of the substrate appears to be important in ensuring a strong bond with the film, as substrates with similar lattice mismatch but more covalent bonding character, such as Ge or InP, lead to polycrystalline rather than single-crystal thin films (illustrating the challenge of avoiding Volmer−Weber growth). In situ reflection of high-energy electron diffraction (RHEED) measurements of the perovskite film indicate that the growth method favors layer-by-layer/Frank-van der Merwe deposition, providing additional evidence of the strong bond with the substrate.[614]

A similar study focused on the deposition of $CsSnBr_3$ and $CsPbBr_3$ thin films by chemical vapor deposition (CVD) onto freshly cleaved NaCl crystals, finding that the greater lattice mismatch from the latter compound leads to some notable changes in the growth behavior compared to the Sn compound.[615] Optical microscope images indicate that $CsPbBr_3$ films appear to favor Volmer−Weber growth, as evidenced by a flakelike microstructure for thinner films. This island growth mechanism need not impede the formation of single-crystal thin films, however, if it is well-controlled. For slower nucleation rates, the orientation of these nanocrystalline flakes is heterogeneous, but increasing the nucleation rate leads to a consistent orientation of the flakes. Uniform several-micrometers-thick films without evidence of grain boundaries can thus be obtained from the coalescence of the uniformly oriented island crystallites, illustrating that Frank-van der Merwe growth is not strictly necessary for the formation of epitaxial films. Note that similar Volmer−Weber growth has also been observed for vapor-phase epitaxy of $CsPbBr_3$ on $SrTiO_3$. In this case, continuous single-crystal thin films were recovered by increasing the growth temperature.[616] These single-crystal films can serve as useful platforms for study of photophysics, such as in-depth analysis of TRPL spectra. Removal of the crystal surfaces/grain boundaries leads to an increase in the PL lifetime from 0.47 to 30 ns when probed on a single crystal film rather than a discontinuous flakelike film on NaCl substrates.[615] In this study, a rapid shift of the PL peak energy from slightly above the band gap to the band gap over the first few seconds after excitation is taken as evidence of radiative recombination of hot carriers, putatively enabled by the high crystal quality of the epitaxial film.[615] Additionally, a small oscillation is seen in the TRPL decay curve of a relatively thick film, which may be an indication of the photo-Dember effect,[617] wherein the mismatched mobilities of the photogenerated electrons and holes lead to a restoring dipole electric field as the carriers diffuse from the excitation point. This field induces a time-dependent oscillation in the joint density of electrons and holes, and, therefore, also in the radiative recombination rate. While more work may be necessary to confirm this hypothesis, it is clear that the high quality of epitaxial single-crystal thin films affords unique opportunities for the study of physical phenomena that might otherwise be obscured by materials defects (although it should be noted that apparent single crystal grains within epitaxial films may still contain defects such as twin boundaries and substitutional defects from diffused substrate atoms).

While growth of epitaxial perovskite films proceeds most straightforwardly on substrates with similar structural motifs (e.g., NaCl or $SrTiO_3$), the use of other substrates with less obvious structural connection to the perovskite can also yield interesting results. Chen et al.[618] investigated the CVD growth of $CsPbBr_3$ on mica. As a result of the large lattice mismatch, $CsPbBr_3$ does not easily form conformal films but rather prefers to form rodlike nanostructures comprising right triangular prismatic crystals oriented with the (110) planes parallel to the substrate and the (001) facets exposed (Figure 56, panels A−C) (note that these planes correspond to the

DOI: 10.1021/acs.chemrev.8b00318
Chem. Rev. 2019, 119, 3193−3295

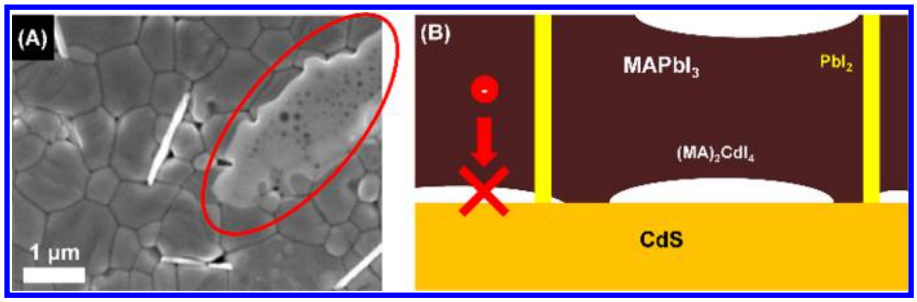

Figure 57. (A) Top-surface SEM image showing the formation of $(MA)_2CdI_4$ (circled in red) and PbI_2 (bright rods/flakes) in $MAPbI_3$ films deposited on CdS. Adapted from ref 514. Copyright 2016 American Chemical Society. (B) Schematic illustration of electron blocking by insulating $(MA)_2CdI_4$ near the $MAPbI_3$/CdS interface.

cubic $CsPbBr_3$ phase). The crystals are distributed with random position but a relatively coherent orientation that reflects the hexagonal symmetry of the underlying mica substrate, with most nanocrystals intersecting one another at 60° angles, as shown in Figure 56 (panels E−J). For sufficiently long growth times (∼1 day), the nanocrystal network will eventually coalesce into a conformal film, though it still retains significant roughness (Figure 56J). The nanocrystal networks so produced display strong band-to-band PL as well as waveguiding behavior, as evidenced by observations of PL emission from the ends of the nanorods as well as at the point of excitation (Figure 56D).[618]

7.2. Interdiffusion between Perovskite and the Substrate

The substrate can influence the perovskite through more than just surface chemistry. If it possesses mobile ions, these may diffuse into the perovskite, potentially changing its properties. This behavior may be beneficial; for example, Bi et al.[476] observed a gradual improvement in the PCE of PSCs stored over a period of several days, with TOF-SIMS depth profiling of the perovskite film suggesting that the absorber was enriched in sodium. These results were interpreted as Na^+ ions having migrated from the soda-lime glass substrate into the perovskite, passivating grain boundaries and boosting photocurrent.[476] Similar behavior has been noted in copper indium gallium selenide (CIGS) solar cells (although these are processed at much higher temperature).[477,478] Small amounts of Cd diffusing from an underlying CdS ETL have also been shown to increase apparent grain size[514] and perhaps improve device performance.[516] However, larger Cd incorporation levels lead to secondary phase formation, as described in the next section, which can clearly be detrimental. Such behavior is not commonly observed for other transport materials; however, it is prudent when considering new candidate ETLs or HTLs to allow for the possibility of such interdiffusion and associated potential effects on device performance.

Qin et al.[619] found that the hexavalent Cr component of a sputtered CrO_x HTL can be detrimental, with XPS depth profiling indicating that Cr^{6+} ions could migrate into the overlying perovskite film. Once in the perovskite film, the Cr^{6+} might oxidize iodide or otherwise reduce PSC performance, though the exact mechanism has not been conclusively elucidated. It appears that incorporating Cu into the Cr sputtering target can lead to a more stable HTL, possibly through the formation of more stable $CuCrO_2$ phases, and the extent of Cr diffusion into the perovskite deposited on the CrO_x:Cu HTL was significantly lessened.[619] It has also been proposed that fullerene-based molecules such as PCBM (an ETL candidate) can be driven into perovskite grain boundaries by a mild anneal at 100 °C.[620] The fullerenes are thought to passivate grain boundaries and reduce the trap density there, based on observations of a blue shift in the PL spectra of the treated films (signifying a reduction in shallow defects), as well as results of thermal admittance and impedance spectroscopies. Although the presence of fullerenes at grain boundaries has yet to be confirmed, it is possible that deposition of perovskite onto a fullerene-coated surface followed by a conventional anneal might allow similar benefits to be reaped.

7.3. Interfacial Chemical Reactions

There are a number of electron and hole transport materials (i.e., potential substrates for perovskite films) that, instead of (or in addition to) gently releasing mobile ions into the perovskite, react at the interface to produce secondary phases. CdS is one such material, whose tendency to react with $MAPbI_3$ appears to be exacerbated by excessively high annealing temperatures.[514] Sufficient diffusion of Cd in the perovskite may lead to phase segregation of a $MAPb_{1-x}Cd_xI_3$ solid solution into insulating $(MA)_2CdI_4$ and PbI_2 (Figure 57). Alternatively, dissociation of MAI can result in the reaction of HI with CdS to produce H_2S and CdI_2. The gaseous species formed by these reactions, CH_3NH_2 and H_2S, evolve from the film, leaving behind insulating CdI_2. Regardless of which reaction pathway predominates, the end result is likely to be the same [i.e., formation of insulating phases (CdI_2, PbI_2, and/or $(MA)_2CdI_4$) that can block carrier extraction near the CdS interface].[514]

Another material that can react rapidly with $MAPbI_3$ upon annealing is ZnO, which appears to catalyze decomposition of the perovskite into PbI_2 rather than forming other secondary phases.[621] Yang et al.[621] have suggested that the basic ZnO readily deprotonates the MA^+ cation, promoting loss of the organic component. Despite this problem, ZnO remains a possible candidate for room-temperature fabrication of PSCs,[622] as decomposition appears to be a significant problem primarily when the perovskite film is annealed. MoO_3 is a prospective hole extraction layer due to its deep work function; however, Liu et al.[623] observed that the proportion of Mo^{5+} to Mo^{6+} detected by XPS in MoO_3 films evaporated onto the perovskite surface is highest near the interface (i.e., for very thin MoO_3 films), dropping off precipitously as the thickness of the MoO_3 layer increases. A concomitant depletion of iodine from the perovskite at the interface with increased MoO_3 thickness, as quantified by the I:Pb ratio in the XPS spectra, suggests that a redox reaction takes place at the interface, wherein iodide in the perovskite oxidizes to form volatile elemental iodine, which leaves the film. The electrons

DOI: 10.1021/acs.chemrev.8b00318
Chem. Rev. 2019, 119, 3193−3295

released by oxidation of I^- reduce Mo in the overlying film, explaining the enhancement of Mo^{5+} near the interface.

Another prospective HTL, CuSCN, may react with $MAPbI_3$ via a halide-exchange reaction to form Cu and Pb iodides and volatile MASCN, which then escapes the film. However, capping the entire device structure with PMMA prevents egress of the decomposition products, inhibiting further interfacial reaction.[624] The above examples illustrate the high chemical activity of the perovskite and the need to optimize substrate−film interfaces, not only for film structure and device performance but also for intrinsic stability and inertness of the layers relative to one another.

7.4. Impact of Substrate on Film Electrical Properties

Another interesting and potentially important effect of the substrate is on the perovskite film work function. Miller et al.[82] observed that $MAPbI_3$ film carrier type tends to follow that of the substrate. Those films fabricated on intrinsic or n-type substrates tend to be n-type, while those on p-type substrates tend to be intrinsic or weakly p-type. Similar behavior was recorded by Schulz et al.[81] when comparing $MAPbI_3$ films fabricated on n-type TiO_2 and p-type NiO_x, possibly indicating a means of tuning the band bending in perovskite devices. These observations may simply reflect the low intrinsic carrier and trap state density within the perovskite film, which might otherwise screen substrate influences. These results, as well as the absence of any especially compelling evidence of a strong dependence of PSC performance on the absorber work function or carrier density, suggest that the ETL and HTL may play a more significant role in establishing the built-in electric field than the perovskite does.

8. CONCLUSIONS

Halide perovskites offer an unprecedented opportunity to unite outstanding optoelectronic properties with facile and low-temperature processing methods. While the soft nature of these materials may be integral to the excellent material properties that make them so attractive for photovoltaics and other optoelectronic applications,[625] as well as the ability to fabricate films via low-temperature processing,[1] it also implies unique challenges for film deposition, such as unexpected and unwanted chemical reactions or the possibility of decomposition. In spite of these challenges, there are a wide range of techniques by which high-quality films can be obtained. Regardless of whether considering solution- or vapor-phase approaches, most successful film deposition techniques rely on independently controlling the nucleation and growth processes. Rapid nucleation of the perovskite (or intermediate phase) allows uniform coverage of the substrate and avoids the formation of detrimental microstructural defects such as voids and pinholes. The high grain boundary density often obtained from these processes can be alleviated either by crystallizing the perovskite from an intermediate precursor phase, or through a suitable thermal, optical, or chemical post-treatment to induce grain growth. Given the small energies involved for processes that have significant influence over film formation, one ongoing challenge for the field involves deconvolving how subtle chemical variations can impact the nucleation and growth processes. Such variations might arise from interactions between the precursors and the solvent or other features of the processing environment, or from the presence of an additive used to manipulate film growth. Many of the mechanistic effects of such additives (including those discussed in this review) are poorly understood, and what works well for a certain process in a given laboratory may not extrapolate to a different context. Nevertheless, the fact that so many atomic and molecular species may be added into the precursor feedstock and lead to benign or beneficial effects on perovskite film structure and properties is a testament to the remarkable defect tolerance of this family of materials.

It should be stressed that, although many deposition techniques can successfully produce high-quality films, reaching performance levels comparable to those of record-setting devices requires careful attention to details at every stage of the processing, including those that are not commonly emphasized/reported. The processing atmosphere is one such variable that can play an important role. Although perovskites are commonly fabricated in inert-atmosphere gloveboxes, such systems typically only control moisture and oxygen levels and may trap solvents in the glovebox atmosphere that may have a significant but difficult-to-characterize impact on processing. By contrast, while processing in air carries the risk of exposing films to moisture, it can more safely be assumed that the composition of ambient air in a well-ventilated lab (or better yet, cleanroom) is more consistent (neglecting possible changes in humidity, which can be readily measured and/or controlled) than a heavily used N_2- or Ar-filled glovebox, particularly if a wide variety of solvents is routinely used there. Similar considerations apply to the vacuum systems used in vapor processing, as routine deposition of many different materials in the same chamber carries a substantial risk of cross-contamination, which may adversely affect film quality. Another potential complicating factor is temperature (i.e., many processes are performed at "room temperature," which is by nature an imprecise term that may imply any temperature in the range of approximately 20 to 30 °C). One should not discount the possible effects of such temperature fluctuations unless it is possible to show conclusively that the system under study does not vary with such excursions; Saliba et al.,[626] for example, have noted that a process optimized for the deposition of high-performance triple cation PSCs yields low-efficiency devices if the glovebox temperature exceeds 28 °C during perovskite deposition. In the case of deliberate heating using hot plates or ovens, temperature distributions, thermal gradients, and efficacy of heat transfer can have profound influence on the quality of the thin films. Purity of the chemicals used in processing could also affect deposition greatly; while low-purity PbI_2, for example, might yield devices with decent device performance, these results are almost certain to be nonreproducible from batch to batch of chemicals, relative to higher grades. Even nominally high-purity chemicals may still only be assayed with respect to metal purity but contain substantial oxide, water, or other chemical species that might interfere with solubility or otherwise alter processing. Finally, cleaning and handling of the substrates and films at each step of the process should be performed with extreme care to minimize the effects of adventitious contaminants, either as impurities on the atomic scale or as larger defects such as dust particles. Without proper attention to what may seem to be trivial details, even the most reliable process may fail to yield the intended results (either gaining insights about film deposition/properties or achieving reproducible high-performance devices).

Although a staggering amount of research has been performed on halide perovskite fabrication in the past few years, there remain a number of productive avenues for further

DOI: 10.1021/acs.chemrev.8b00318
Chem. Rev. 2019, 119, 3193−3295

study in view of the many uncertainties that can affect perovskite film deposition processes. For example, although the research community has gained much important knowledge concerning the chemistry of several important perovskite-solvent combinations, there is much room to explore the behavior of both the well-known systems as well as less conventional ones (e.g., $MAPbI_3$ in MA/ACN,[257] 2ME,[256] or the DMSO/ethylene glycol blend[292,293] used in RIR-MAPLE). Recent studies have highlighted the importance of carefully investigating the colloidal properties of solutions from a temporal as well as compositional perspective. In this regard, precursor solutions can age rapidly, with important consequences for the reproducibility of the films deposited from them, which can vary widely based on the specific system under consideration.[106,164,627] Studies that focus on the colloidal behavior of perovskite precursors are, therefore, likely to be of great value to the field, especially given the wide range of possible compositions beyond $MAPbI_3$, for which this aspect of film formation remains largely unexplored. Other "invisible" factors brought on by interactions between precursors and solvents may change the composition of the final thin film in ways that may be difficult to detect yet that may be consequential for device operation or film properties.[106] While there are a number of studies that probe the effects of solvent in the processing atmosphere (and emphasize the importance of controlling it),[126,190,245,502] they tend to focus on solvents that are often used in perovskite deposition but not necessarily on others that may be commonly found in a frequently used glovebox. Studies focusing on subtle yet important interactions that can influence film deposition will therefore be of high value to the halide perovskite field on both a scientific and technological level.

Beyond the focus on solution processing, precursor-substrate interactions can also be highly important in determining thin film morphology and composition as well as device performance,[96,195,196] but understanding of the details of these interactions is superficial in many cases and deserves further attention. This need is especially acute for vapor-deposited halide perovskite films, for which growth mechanics are still relatively obscure and for which substrate-perovskite interaction presumably dominates the deposition process. A particularly important effect of the substrate, interfacial strain, has been a known factor in the transformation of metal halide precursor films to perovskite during two-step processes[202] but also recently has become recognized as an important consideration for thin film deposition in one-step processes as well,[628,629] particularly in view of the large thermal expansion coefficient[630−632] of halide perovskites. Controlling this effect will be of critical importance, especially as efforts to optimize PSCs for long-term stability gain prominence. Finally, our experimental understanding of defect populations in halide perovskites and how these relate to processing conditions has largely focused on grain size and grain boundary density. Even in this latter category there is much room for scientific exploration; however, studies focused on connections between these and other microstructural defects and processing are currently lacking. It is remarkable that such rapid strides have been made in perovskite device functionality without a thorough reckoning of these materials properties. As the research community grapples with the effects of diminishing returns on perovskite film/device performance, however, it will become imperative to take these considerations into account.

In summary, halide perovskites, as "soft semiconductors," represent an emerging class of revolutionary materials. The unique advantages of these substances are accompanied by unique challenges in thin film deposition, resulting from the ease with which they can thermally degrade or interact with a wide variety of substances/surfaces. Although halide perovskite reactivity poses significant issues for their fabrication and handling, it also affords great flexibility in how they can be processed and how their properties can be controlled. Indeed, as a great number of thin-film deposition approaches have been presented in this review, rather than trying to distinguish which are the "best" approaches for depositing halide perovskite films, it is worth appreciating that one of the truly remarkable aspects of this materials family is that so many completely different approaches (both solution- and vacuum-based) can give rise to outstanding semiconductor films. The recent profusion of optoelectronic devices with excellent performance based on halide perovskite thin film active layers, using a wide range of compositions, architectures, and processing methods, attests to this versatility. While we predict that halide perovskites will remain an active field of research for many years to come, the lessons learned concerning their processing may also be applicable to other important emerging materials families with similar "soft" chemical, mechanical, and optoelectronic characteristics.

AUTHOR INFORMATION

Corresponding Authors

*E-mail: nitin_padture@brown.edu.
*E-mail: david.mitzi@duke.edu.

ORCID

Nitin P. Padture: 0000-0001-6622-8559
David B. Mitzi: 0000-0001-5189-4612

Notes

The authors declare no competing financial interest.

Biographies

Wiley A. Dunlap-Shohl is a Ph.D. candidate and Chambers Scholar in David Mitzi's group at Duke University. He earned an A.B. in Physics and Engineering Sciences in 2012 and a B.E. with a concentration in mechanical design in 2013 from Dartmouth College. Before joining the Mitzi group at Duke in 2014, he briefly worked at Victor Technologies in West Lebanon, NH, on the design of plasma cutting equipment, and at General Compression in Newton, MA, testing prototype compressed-air energy storage technology. His current research interests are focused on the development of novel processing techniques for the deposition of hybrid perovskite thin films and on studying the interfacial interactions of perovskites with other materials used in the construction of solar cells and related optoelectronic devices.

Yuanyuan (Alvin) Zhou joined Brown University as Assistant Professor (Research) of Engineering in July 2016. He received his Ph.D. in Engineering from Brown University in June 2016. He holds a B.S. in Materials Science & Engineering from Xi'an Jiaotong University and dual M.S. degrees in Materials Science & Engineering from Xi'an Jiaotong University and in Chemistry from Korea Research Institute of Chemical Technology. He also has worked as an intern at the National Renewable Energy Laboratory from Oct. 2014 to May 2016. Dr. Zhou's research focuses on probing composition-microstructure−property-performance relationships of new-generation functional inorganic materials including perovskites and developing

DOI: 10.1021/acs.chemrev.8b00318
Chem. Rev. 2019, 119, 3193−3295

high-performance photovoltaics, optoelectronics, and electrochemical devices. He has published over 55 journal papers.

Nitin P. Padture is the Otis E. Randall University Professor of Engineering and Director of the Institute for Molecular and Nanoscale Innovation at Brown University. He received his B.Tech. in Metallurgical Engineering from the Indian Institute of Technology–Bombay (1985), M.S. in Ceramic Engineering from Alfred University (1987), and Ph.D. in Materials Science & Engineering from Lehigh University (1991). Padture was a postdoctoral researcher at the National Institute for Standards and Technology for three years (1991–1994), and then served on the faculty of University of Connecticut for ten years (1995–2004). Prior to joining Brown University in 2012, he was College of Engineering Distinguished Professor and founding Director of the NSF-funded Materials Research Science & Engineering Center at the Ohio State University. Padture's research interests are in broad areas of advanced structural ceramics/coatings/composites and functional nanomaterials/devices, with applications ranging from jet engines to nanoelectronics to solar cells. He is author or coauthor of about 220 publications, which have been cited widely. An elected fellow of American Association for the Advancement of Science, Padture is Editor of the international journals, *Acta Materialia* and *Scripta Materialia*.

David B. Mitzi is the Simon Family Professor of Engineering at Duke University, with appointments to the Department of Mechanical Engineering and Materials Science and the Department of Chemistry. He received his B.S. in Electrical Engineering and Engineering Physics from Princeton University in 1985 and his Ph.D. in Applied Physics from Stanford University in 1990. Prior to joining the faculty at Duke in 2014, Dr. Mitzi spent 23 years at IBM's T.J. Watson Research Center, where his focus was on the search for and application of new electronic materials, including organic–inorganic hybrid perovskites and inorganic materials for photovoltaic, LED, transistor and memory applications. For his final five years at IBM, he served as manager for the Photovoltaic Science and Technology Department, where he initiated and managed a multicompany program to develop a low-cost, high-throughput approach to deposit thin-film chalcogenide-based absorber layers for high-efficiency solar cells. Dr. Mitzi's current research interests involve making emerging solar energy conversion materials more effective, cost-efficient, and competitive for the energy market. He has been elected a fellow of the Materials Research Society (MRS) and has authored or coauthored more than 200 papers and book chapters.

ACKNOWLEDGMENTS

W.A.D-S. and D.B.M. thank the Office of Naval Research (Award N00014-17-1-2207) and the Office of Energy Efficiency and Renewable Energy (EERE), U.S. Department of Energy (Award DE-EE0006712) for financial support. W.A.D.-S. also gratefully acknowledges the support from the Fitzpatrick Institute for Photonics John T. Chambers Scholarship. Y.Z. and N.P.P. thank the National Science Foundation (Award OIA-1538893) and the Office of Naval Research (Award N00014-17-1-2232) for financial support. All opinions expressed in this paper are the authors' and do not necessarily reflect the policies and views of ONR, DOE, or NSF. Neither the United States Government nor any agency thereof, nor any of their employees, makes any warranty, express or implied, or assumes any legal liability or responsibility for the accuracy, completeness, or usefulness of any information, apparatus, product, or process disclosed, or represents that its use would not infringe privately owned rights. Reference herein to any specific commercial product, process, or service by trade name, trademark, manufacturer, or otherwise does not necessarily constitute or imply its endorsement, recommendation, or favoring by the United States Government or any agency thereof. The views and opinions of authors expressed herein do not necessarily state or reflect those of the United States Government or any agency thereof.

REFERENCES

(1) Egger, D. A.; Bera, A.; Cahen, D.; Hodes, G.; Kirchartz, T.; Kronik, L.; Lovrincic, R.; Rappe, A. M.; Reichman, D. R.; Yaffe, O. What Remains Unexplained about the Properties of Halide Perovskites? *Adv. Mater.* **2018**, *30*, No. e1800691.

(2) Knutson, J.; Martin, J. D.; Mitzi, D. B. Tuning the Band Gap in Hybrid Tin Iodide Perovskite Semiconductors Using Structural Templating. *Inorg. Chem.* **2005**, *44*, 4699–4705.

(3) Fang, Y.; Dong, Q.; Shao, Y.; Yuan, Y.; Huang, J. Highly Narrowband Perovskite Single-Crystal Photodetectors Enabled by Surface-Charge Recombination. *Nat. Photonics* **2015**, *9*, 679–686.

(4) Eperon, G. E.; Stranks, S. D.; Menelaou, C.; Johnston, M. B.; Herz, L. M.; Snaith, H. J. Formamidinium Lead Trihalide: a Broadly Tunable Perovskite for Efficient Planar Heterojunction Solar Cells. *Energy Environ. Sci.* **2014**, *7*, 982–988.

(5) Song, J.; Li, J.; Li, X.; Xu, L.; Dong, Y.; Zeng, H. Quantum Dot Light-Emitting Diodes Based on Inorganic Perovskite Cesium Lead Halides ($CsPbX_3$). *Adv. Mater.* **2015**, *27*, 7162–7167.

(6) Hu, H.; Salim, T.; Chen, B.; Lam, Y. M. Molecularly Engineered Organic-Inorganic Hybrid Perovskite with Multiple Quantum Well Structure for Multicolored Light-Emitting Diodes. *Sci. Rep.* **2016**, *6*, 33546.

(7) Wang, N.; Cheng, L.; Ge, R.; Zhang, S.; Miao, Y.; Zou, W.; Yi, C.; Sun, Y.; Cao, Y.; Yang, R.; et al. Perovskite Light-Emitting Diodes Based on Solution-Processed Self-Organized Multiple Quantum Wells. *Nat. Photonics* **2016**, *10*, 699–704.

(8) Mante, P. A.; Stoumpos, C. C.; Kanatzidis, M. G.; Yartsev, A. Electron-Acoustic Phonon Coupling in Single Crystal $CH_3NH_3PbI_3$ Perovskites Revealed by Coherent Acoustic Phonons. *Nat. Commun.* **2017**, *8*, 14398.

(9) Wehrenfennig, C.; Eperon, G. E.; Johnston, M. B.; Snaith, H. J.; Herz, L. M. High Charge Carrier Mobilities and Lifetimes in Organolead Trihalide Perovskites. *Adv. Mater.* **2014**, *26*, 1584–1589.

(10) Reid, O. G.; Yang, M.; Kopidakis, N.; Zhu, K.; Rumbles, G. Grain-Size-Limited Mobility in Methylammonium Lead Iodide Perovskite Thin Films. *ACS Energy Lett.* **2016**, *1*, 561–565.

(11) Green, M. A.; Ho-Baillie, A.; Snaith, H. J. The Emergence of Perovskite Solar Cells. *Nat. Photonics* **2014**, *8*, 506–514.

(12) Xing, G.; Mathews, N.; Sun, S.; Lim, S. S.; Lam, Y. M.; Grätzel, M.; Mhaisalkar, S.; Sum, T. C. Long-Range Balanced Electron- and Hole-Transport Lengths in Organic-Inorganic $CH_3NH_3PbI_3$. *Science* **2013**, *342*, 344–347.

(13) Stranks, S. D.; Eperon, G. E.; Grancini, G.; Menelaou, C.; Alcocer, M. J.; Leijtens, T.; Herz, L. M.; Petrozza, A.; Snaith, H. J. Electron-Hole Diffusion Lengths Exceeding 1 Micrometer in an Organometal Trihalide Perovskite Absorber. *Science* **2013**, *342*, 341–344.

(14) Yin, W. J.; Shi, T.; Yan, Y. Unique Properties of Halide Perovskites as Possible Origins of the Superior Solar Cell Performance. *Adv. Mater.* **2014**, *26*, 4653–4658.

(15) Han, Q.; Bai, Y.; Liu, J.; Du, K.-Z.; Li, T.; Ji, D.; Zhou, Y.; Cao, C.; Shin, D.; Ding, J.; et al. Additive Engineering for High-Performance Room-Temperature-Processed Perovskite Absorbers with Micron-Size Grains and Microsecond-Range Carrier Lifetimes. *Energy Environ. Sci.* **2017**, *10*, 2365–2371.

(16) Matsui, T.; Seo, J. Y.; Saliba, M.; Zakeeruddin, S. M.; Grätzel, M. Room-Temperature Formation of Highly Crystalline Multication Perovskites for Efficient, Low-Cost Solar Cells. *Adv. Mater.* **2017**, *29*, 1606258.

(17) Mitzi, D. B.; Chondroudis, K.; Kagan, C. R. Organic-Inorganic Electronics. *IBM J. Res. Dev.* **2001**, *45*, 29–45.

DOI: 10.1021/acs.chemrev.8b00318
Chem. Rev. 2019, 119, 3193–3295

(18) Kagan, C. R.; Mitzi, D. B.; Dimitrakopoulos, C. D. Organic-Inorganic Hybrid Materials as Semiconducting Channels in Thin-Film Field-Effect Transistors. *Science* **1999**, *286*, 945−947.
(19) Mitzi, D. B.; Dimitrakopoulos, C. D.; Kosbar, L. L. Structurally Tailored Organic-Inorganic Perovskites: Optical Properties and Solution-Processed Channel Materials for Thin-Film Transistors. *Chem. Mater.* **2001**, *13*, 3728−3740.
(20) Mitzi, D. B.; Dimitrakopoulos, C. D.; Rosner, J.; Medeiros, D. R.; Xu, Z.; Noyan, C. Hybrid Field-Effect Transistor Based on a Low-Temperature Melt-Processed Channel Layer. *Adv. Mater.* **2002**, *14*, 1772−1776.
(21) Era, M.; Morimoto, S.; Tsutsui, T.; Saito, S. Organic - Inorganic Heterostructure Electroluminescent Device Using a Layered Perovskite Semiconductor $(C_6H_5C_2H_4NH_3)_2PbI_4$. *Appl. Phys. Lett.* **1994**, *65*, 676−678.
(22) Hattori, T.; Taira, T.; Era, M.; Tsutsui, T.; Saito, S. Highly Efficient Electroluminescence from a Heterostructure Device Combined with Emissive Layered-Perovskite and an Electron-Transporting Organic Compound. *Chem. Phys. Lett.* **1996**, *254*, 103−108.
(23) Chondroudis, K.; Mitzi, D. B. Electroluminescence from an Organic-Inorganic Perovskite Incorporating a Quaterthiophene Dye within Lead Halide Perovskite Layers. *Chem. Mater.* **1999**, *11*, 3028−3030.
(24) Best Research Cell Efficiencies. National Renewable Energy Laboratory. https://www.nrel.gov/pv/assets/images/efficiency-chart-20180716.jpg (accessed Aug 12, 2018).
(25) Saliba, M.; Matsui, T.; Seo, J. Y.; Domanski, K.; Correa-Baena, J. P.; Nazeeruddin, M. K.; Zakeeruddin, S. M.; Tress, W.; Abate, A.; Hagfeldt, A.; et al. Cesium-Containing Triple Cation Perovskite Solar Cells: Improved Stability, Reproducibility and High Efficiency. *Energy Environ. Sci.* **2016**, *9*, 1989−1997.
(26) Saliba, M.; Matsui, T.; Domanski, K.; Seo, J.-Y.; Ummadisingu, A.; Zakeeruddin, S. M.; Correa-Baena, J.-P.; Tress, W.; Abate, A.; Hagfeldt, A.; et al. Incorporation of Rubidium Cations into Perovskite Solar Cells Improves Photovoltaic Performance. *Science* **2016**, *354*, 206−209.
(27) Yang, W. S.; Noh, J. H.; Jeon, N. J.; Kim, Y. C.; Ryu, S.; Seo, J.; Seok, S. I. High-Performance Photovoltaic Perovskite Layers Fabricated through Intramolecular Exchange. *Science* **2015**, *348*, 1234−1237.
(28) Yang, W. S.; Park, B.-W.; Jung, E. H.; Jeon, N. J.; Kim, Y. C.; Lee, D. U.; Shin, S. S.; Seo, J.; Kim, E. K.; Noh, J. H.; et al. Iodide Management in Formamidinium-Lead-Halide-Based Perovskite Layers for Efficient Solar Cells. *Science* **2017**, *356*, 1376−1379.
(29) Shin, S. S.; Yeom, E. J.; Yang, W. S.; Hur, S.; Kim, M. G.; Im, J.; Seo, J.; Noh, J. H.; Seok, S. I. Colloidally Prepared La-Doped $BaSnO_3$ Electrodes for Efficient, Photostable Perovskite Solar Cells. *Science* **2017**, *356*, 167−171.
(30) Cho, H.; Jeong, S.-H.; Park, M.-H.; Wolf, C.; Lee, C.-L.; Heo, J. H.; Sadhanala, A.; Myoung, N.; Yoo, S.; Im, S. H.; et al. Overcoming the Electroluminescence Efficiency Limitations of Perovskite Light-Emitting Diodes. *Science* **2015**, *350*, 1222−1225.
(31) Yuan, M.; Quan, L. N.; Comin, R.; Walters, G.; Sabatini, R.; Voznyy, O.; Hoogland, S.; Zhao, Y.; Beauregard, E. M.; Kanjanaboos, P.; et al. Perovskite Energy Funnels for Efficient Light-Emitting Diodes. *Nat. Nanotechnol.* **2016**, *11*, 872−877.
(32) Xiao, Z.; Kerner, R. A.; Zhao, L.; Tran, N. L.; Lee, K. M.; Koh, T.-W.; Scholes, G. D.; Rand, B. P. Efficient Perovskite Light-Emitting Diodes Featuring Nanometre-Sized Crystallites. *Nat. Photonics* **2017**, *11*, 108−115.
(33) Zhang, L.; Yang, X.; Jiang, Q.; Wang, P.; Yin, Z.; Zhang, X.; Tan, H.; Yang, Y. M.; Wei, M.; Sutherland, B. R.; et al. Ultra-Bright and Highly Efficient Inorganic Based Perovskite Light-Emitting Diodes. *Nat. Commun.* **2017**, *8*, 15640.
(34) Sutherland, B. R.; Sargent, E. H. Perovskite Photonic Sources. *Nat. Photonics* **2016**, *10*, 295−302.
(35) García de Arquer, F. P.; Gong, X.; Sabatini, R. P.; Liu, M.; Kim, G. H.; Sutherland, B. R.; Voznyy, O.; Xu, J.; Pang, Y.; Hoogland, S.; et al. Field-Emission from Quantum-Dot-in-Perovskite Solids. *Nat. Commun.* **2017**, *8*, 14757.
(36) Xu, X.; Chueh, C.-C.; Jing, P.; Yang, Z.; Shi, X.; Zhao, T.; Lin, L. Y.; Jen, A. K.-Y. High-Performance Near-IR Photodetector Using Low-Bandgap $MA_{0.5}FA_{0.5}Pb_{0.5}Sn_{0.5}I_3$ Perovskite. *Adv. Funct. Mater.* **2017**, *27*, 1701053.
(37) Kim, Y. C.; Kim, K. H.; Son, D.-Y.; Jeong, D.-N.; Seo, J.-Y.; Choi, Y. S.; Han, I. T.; Lee, S. Y.; Park, N.-G. Printable Organometallic Perovskite Enables Large-Area, Low-Dose X-Ray Imaging. *Nature* **2017**, *550*, 87−91.
(38) Wei, H.; Fang, Y.; Mulligan, P.; Chuirazzi, W.; Fang, H.-H.; Wang, C.; Ecker, B. R.; Gao, Y.; Loi, M. A.; Cao, L.; et al. Sensitive X-Ray Detectors Made of Methylammonium Lead Tribromide Perovskite Single Crystals. *Nat. Photonics* **2016**, *10*, 333−339.
(39) Wei, H.; DeSantis, D.; Wei, W.; Deng, Y.; Guo, D.; Savenije, T. J.; Cao, L.; Huang, J. Dopant Compensation in Alloyed $CH_3NH_3PbBr_{3-x}Cl_x$ Perovskite Single Crystals for Gamma-Ray Spectroscopy. *Nat. Mater.* **2017**, *16*, 826−833.
(40) Xing, G.; Mathews, N.; Lim, S. S.; Yantara, N.; Liu, X.; Sabba, D.; Grätzel, M.; Mhaisalkar, S.; Sum, T. C. Low-Temperature Solution-Processed Wavelength-Tunable Perovskites for Lasing. *Nat. Mater.* **2014**, *13*, 476−480.
(41) Zhu, H.; Fu, Y.; Meng, F.; Wu, X.; Gong, Z.; Ding, Q.; Gustafsson, M. V.; Trinh, M. T.; Jin, S.; Zhu, X.-Y. Lead Halide Perovskite Nanowire Lasers with Low Lasing Thresholds and High Quality Factors. *Nat. Mater.* **2015**, *14*, 636−642.
(42) Mirershadi, S.; Ahmadi-Kandjani, S.; Zawadzka, A.; Rouhbakhsh, H.; Sahraoui, B. Third Order Nonlinear Optical Properties of Organometal Halide Perovskite by Means of the Z-scan Technique. *Chem. Phys. Lett.* **2016**, *647*, 7−13.
(43) Johnson, J. C.; Li, Z.; Ndione, P. F.; Zhu, K. Third-Order Nonlinear Optical Properties of Methylammonium Lead Halide Perovskite Films. *J. Mater. Chem. C* **2016**, *4*, 4847−4852.
(44) Yi, J.; Miao, L.; Li, J.; Hu, W.; Zhao, C.; Wen, S. Third-Order Nonlinear Optical Response of $CH_3NH_3PbI_3$ Perovskite in the Mid-Infrared Regime. *Opt. Mater. Express* **2017**, *7*, 3894−3901.
(45) Zhang, C.; Sun, D.; Vardeny, Z. V. Multifunctional Optoelectronic-Spintronic Device Based on Hybrid Organometal Trihalide Perovskites. *Adv. Energy Mater.* **2017**, *3*, 1600426.
(46) Willett, R. D.; Jardine, F. H.; Rouse, I.; Wong, R. J.; Landee, C. P.; Numata, M. Crystal Structure, Magnetic Susceptibility, and EPR Study of Bis-(β-alaninium) Tetrachlorocuprate(II): Spin-Diffusion Effects in a Two-Dimensional Square Planar Ferromagnet with Anisotropic and Antisymmetric Exchange. *Phys. Rev. B: Condens. Matter Mater. Phys.* **1981**, *24*, 5372−5381.
(47) Smith, M. D.; Pedesseau, L.; Kepenekian, M.; Smith, I. C.; Katan, C.; Even, J.; Karunadasa, H. I. Decreasing the Electronic Confinement in Layered Perovskites through Intercalation. *Chem. Sci.* **2017**, *8*, 1960−1968.
(48) Even, J.; Pedesseau, L.; Katan, C. Understanding Quantum Confinement of Charge Carriers in Layered 2D Hybrid Perovskites. *ChemPhysChem* **2014**, *15*, 3733−3741.
(49) Hong, X.; Ishihara, T.; Nurmikko, A. V. Dielectric Confinement Effect on Excitons in PbI_4-Based Layered Semiconductors. *Phys. Rev. B: Condens. Matter Mater. Phys.* **1992**, *45*, 6961−6964.
(50) Dammak, T.; Koubaa, M.; Boukheddaden, K.; Bougzhala, H.; Mlayah, A.; Abid, Y. Two-Dimensional Excitons and Photoluminescence Properties of the Organic/Inorganic $(4\text{-}FC_6H_4C_2H_4NH_3)_2[PbI_4]$ Nanomaterial. *J. Phys. Chem. C* **2009**, *113*, 19305−19309.
(51) Niesner, D.; Wilhelm, M.; Levchuk, I.; Osvet, A.; Shrestha, S.; Batentschuk, M.; Brabec, C.; Fauster, T. Giant Rashba Splitting in $CH_3NH_3PbBr_3$ Organic-Inorganic Perovskite. *Phys. Rev. Lett.* **2016**, *117*, 126401.
(52) Wang, T.; Daiber, B.; Frost, J. M.; Mann, S. A.; Garnett, E. C.; Walsh, A.; Ehrler, B. Indirect to Direct Bandgap Transition in Methylammonium Lead Halide Perovskite. *Energy Environ. Sci.* **2017**, *10*, 509−515.

DOI: 10.1021/acs.chemrev.8b00318
Chem. Rev. 2019, 119, 3193−3295

(53) Zhai, Y.; Baniya, S.; Zhang, C.; Li, J.; Haney, P.; Sheng, C.-X.; Ehrenfreund, E.; Vardeny, Z. V. Giant Rashba Splitting in 2D Organic-Inorganic Halide Perovskites Measured by Transient Spectroscopies. *Sci. Adv.* **2017**, *3*, No. e1700704.
(54) Kepenekian, M.; Robles, R.; Katan, C.; Sapori, D.; Pedesseau, L.; Even, J. Rashba and Dresselhaus Effects in Hybrid Organic-Inorganic Perovskites: From Basics to Devices. *ACS Nano* **2015**, *9*, 11557−11567.
(55) Zheng, F.; Tan, L. Z.; Liu, S.; Rappe, A. M. Rashba Spin-Orbit Coupling Enhanced Carrier Lifetime in $CH_3NH_3PbI_3$. *Nano Lett.* **2015**, *15*, 7794−7800.
(56) Kepenekian, M.; Even, J. Rashba and Dresselhaus Couplings in Halide Perovskites: Accomplishments and Opportunities for Spintronics and Spin-Orbitronics. *J. Phys. Chem. Lett.* **2017**, *8*, 3362−3370.
(57) Yaffe, O.; Guo, Y.; Tan, L. Z.; Egger, D. A.; Hull, T.; Stoumpos, C. C.; Zheng, F.; Heinz, T. F.; Kronik, L.; Kanatzidis, M. G.; et al. Local Polar Fluctuations in Lead Halide Perovskite Crystals. *Phys. Rev. Lett.* **2017**, *118*, 136001.
(58) Sun, S.; Fang, Y.; Kieslich, G.; White, T. J.; Cheetham, A. K. Mechanical Properties of Organic−Inorganic Halide Perovskites, $CH_3NH_3PbX_3$ (X = I, Br and Cl), by Nanoindentation. *J. Mater. Chem. A* **2015**, *3*, 18450−18455.
(59) Rakita, Y.; Cohen, S. R.; Kedem, N. K.; Hodes, G.; Cahen, D. Mechanical Properties of $APbX_3$ (A = Cs or CH_3NH_3; X = I or Br) Perovskite Single Crystals. *MRS Commun.* **2015**, *5*, 623−629.
(60) Zhou, Y.; Padture, N. P. Gas-Induced Formation/Transformation of Organic−Inorganic Halide Perovskites. *ACS Energy Lett.* **2017**, *2*, 2166−2176.
(61) Ramirez, C.; Yadavalli, S. K.; Garces, H. F.; Zhou, Y.; Padture, N. P. Thermo-Mechanical Behavior of Organic-Inorganic Halide Perovskites for Solar Cells. *Scr. Mater.* **2018**, *150*, 36−41.
(62) Mitzi, D. B. Synthesis, Structure, and Properties of Organic-Inorganic Perovskites and Related Materials. In *Progress in Inorganic Chemistry*, Karlin, K. D., Ed.; John Wiley & Sons, Inc.: 1999; Vol. *48*.
(63) Saparov, B.; Mitzi, D. B. Organic-Inorganic Perovskites: Structural Versatility for Functional Materials Design. *Chem. Rev.* **2016**, *116*, 4558−4596.
(64) Mitzi, D. B. Templating and Structural Engineering in Organic−Inorganic Perovskites. *J. Chem. Soc., Dalton Trans.* **2001**, 1−12.
(65) Frost, J. M.; Walsh, A. What Is Moving in Hybrid Halide Perovskite Solar Cells? *Acc. Chem. Res.* **2016**, *49*, 528−535.
(66) Svane, K. L.; Forse, A. C.; Grey, C. P.; Kieslich, G.; Cheetham, A. K.; Walsh, A.; Butler, K. T. How Strong Is the Hydrogen Bond in Hybrid Perovskites? *J. Phys. Chem. Lett.* **2017**, *8*, 6154−6159.
(67) Goldschmidt, V. M. Die Gesetze der Krystallochemie. *Naturwissenschaften* **1926**, *14*, 477−485.
(68) Li, C.; Lu, X.; Ding, W.; Feng, L.; Gao, Y.; Guo, Z. Formability of ABX_3 (X = F, Cl, Br, I) Halide Perovskites. *Acta Crystallogr., Sect. B: Struct. Sci.* **2008**, *64*, 702−707.
(69) Mao, L.; Ke, W.; Pedesseau, L.; Wu, Y.; Katan, C.; Even, J.; Wasielewski, M. R.; Stoumpos, C. C.; Kanatzidis, M. G. Hybrid Dion-Jacobson 2D Lead Iodide Perovskites. *J. Am. Chem. Soc.* **2018**, *140*, 3775−3783.
(70) Cao, D. H.; Stoumpos, C. C.; Farha, O. K.; Hupp, J. T.; Kanatzidis, M. G. 2D Homologous Perovskites as Light-Absorbing Materials for Solar Cell Applications. *J. Am. Chem. Soc.* **2015**, *137*, 7843−7850.
(71) Venkatesan, N. R.; Labram, J. G.; Chabinyc, M. L. Charge-Carrier Dynamics and Crystalline Texture of Layered Ruddlesden−Popper Hybrid Lead Iodide Perovskite Thin Films. *ACS Energy Lett.* **2018**, *3*, 380−386.
(72) Cortecchia, D.; Lew, K. C.; So, J.-K.; Bruno, A.; Soci, C. Cathodoluminescence of Self-Organized Heterogeneous Phases in Multidimensional Perovskite Thin Films. *Chem. Mater.* **2017**, *29*, 10088−10094.
(73) Tsai, H.; Nie, W.; Blancon, J.-C.; Stoumpos, C. C.; Asadpour, R.; Harutyunyan, B.; Neukirch, A. J.; Verduzco, R.; Crochet, J. J.; Tretiak, S.; et al. High-Efficiency Two-Dimensional Ruddlesden-Popper Perovskite Solar Cells. *Nature* **2016**, *536*, 312−316.
(74) Ke, W.; Stoumpos, C. C.; Spanopoulos, I.; Mao, L.; Chen, M.; Wasielewski, M. R.; Kanatzidis, M. G. Efficient Lead-Free Solar Cells Based on Hollow {en}$MASnI_3$ Perovskites. *J. Am. Chem. Soc.* **2017**, *139*, 14800−14806.
(75) Ke, W.; Stoumpos, C. C.; Zhu, M.; Mao, L.; Spanopoulos, I.; Liu, J.; Kontsevoi, O. Y.; Chen, M.; Sarma, D.; Zhang, Y.; et al. Enhanced Photovoltaic Performance and Stability with a New Type of Hollow 3D Perovskite {en}$FASnI_3$. *Sci. Adv.* **2017**, *3*, No. e1701293.
(76) Xie, H.; Liu, X.; Lyu, L.; Niu, D.; Wang, Q.; Huang, J.; Gao, Y. Effects of Precursor Ratios and Annealing on Electronic Structure and Surface Composition of $CH_3NH_3PbI_3$ Perovskite Films. *J. Phys. Chem. C* **2016**, *120*, 215−220.
(77) Wang, Q.; Shao, Y.; Xie, H.; Lyu, L.; Liu, X.; Gao, Y.; Huang, J. Qualifying Composition Dependent p and n Self-doping in $CH_3NH_3PbI_3$. *Appl. Phys. Lett.* **2014**, *105*, 163508.
(78) Song, D.; Cui, P.; Wang, T.; Wei, D.; Li, M.; Cao, F.; Yue, X.; Fu, P.; Li, Y.; He, Y.; et al. Managing Carrier Lifetime and Doping Property of Lead Halide Perovskite by Postannealing Processes for Highly Efficient Perovskite Solar Cells. *J. Phys. Chem. C* **2015**, *119*, 22812−22819.
(79) Emara, J.; Schnier, T.; Pourdavoud, N.; Riedl, T.; Meerholz, K.; Olthof, S. Impact of Film Stoichiometry on the Ionization Energy and Electronic Structure of $CH_3NH_3PbI_3$ Perovskites. *Adv. Mater.* **2016**, *28*, 553−559.
(80) Schulz, P.; Edri, E.; Kirmayer, S.; Hodes, G.; Cahen, D.; Kahn, A. Interface Energetics in Organo-Metal Halide Perovskite-Based Photovoltaic Cells. *Energy Environ. Sci.* **2014**, *7*, 1377−1381.
(81) Schulz, P.; Whittaker-Brooks, L. L.; MacLeod, B. A.; Olson, D. C.; Loo, Y.-L.; Kahn, A. Electronic Level Alignment in Inverted Organometal Perovskite Solar Cells. *Adv. Mater. Interfaces* **2015**, *2*, 1400532.
(82) Miller, E. M.; Zhao, Y.; Mercado, C. C.; Saha, S. K.; Luther, J. M.; Zhu, K.; Stevanović, V.; Perkins, C. L.; van de Lagemaat, J. Substrate-Controlled Band Positions in $CH_3NH_3PbI_3$ Perovskite Films. *Phys. Chem. Chem. Phys.* **2014**, *16*, 22122−22130.
(83) Minemoto, T.; Murata, M. Device Modeling of Perovskite Solar Cells Based on Structural Similarity with Thin Film Inorganic Semiconductor Solar Cells. *J. Appl. Phys.* **2014**, *116*, No. 054505.
(84) Minemoto, T.; Murata, M. Theoretical Analysis on Effect of Band Offsets in Perovskite Solar Cells. *Sol. Energy Mater. Sol. Cells* **2015**, *133*, 8−14.
(85) Jiang, C.-S.; Yang, M.; Zhou, Y.; To, B.; Nanayakkara, S. U.; Luther, J. M.; Zhou, W.; Berry, J. J.; van de Lagemaat, J.; Padture, N. P.; et al. Carrier Separation and Transport in Perovskite Solar Cells Studied by Nanometre-Scale Profiling of Electrical Potential. *Nat. Commun.* **2015**, *6*, 8397.
(86) O'Regan, B. C.; Grätzel, M. A Low-Cost, High-Efficiency Solar Cell Based on Dye-Sensitized Colloidal TiO_2 Films. *Nature* **1991**, *353*, 737−739.
(87) Zhou, Y.; Vasiliev, A. L.; Wu, W.; Yang, M.; Pang, S.; Zhu, K.; Padture, N. P. Crystal Morphologies of Organolead Trihalide in Mesoscopic/Planar Perovskite Solar Cells. *J. Phys. Chem. Lett.* **2015**, *6*, 2292−2297.
(88) Listorti, A.; Juarez-Perez, E. J.; Frontera, C.; Roiati, V.; Garcia-Andrade, L.; Colella, S.; Rizzo, A.; Ortiz, P.; Mora-Sero, I. Effect of Mesostructured Layer upon Crystalline Properties and Device Performance on Perovskite Solar Cells. *J. Phys. Chem. Lett.* **2015**, *6*, 1628−1637.
(89) Bi, D.; Tress, W.; Dar, M. I.; Gao, P.; Luo, J.; Renevier, C.; Schenk, K.; Abate, A.; Giordano, F.; Correa Baena, J.-P.; et al. Efficient Luminescent Solar Cells Based on Tailored Mixed-Cation Perovskites. *Sci. Adv.* **2016**, *2*, No. e1501170.
(90) Li, D.; Dong, G.; Li, W.; Wang, L. High Performance Organic-Inorganic Perovskite-Optocoupler Based on Low-Voltage and Fast Response Perovskite Compound Photodetector. *Sci. Rep.* **2015**, *5*, 7902.

DOI: 10.1021/acs.chemrev.8b00318
Chem. Rev. 2019, 119, 3193−3295

(91) Sutherland, B. R.; Johnston, A. K.; Ip, A. H.; Xu, J.; Adinolfi, V.; Kanjanaboos, P.; Sargent, E. H. Sensitive, Fast, and Stable Perovskite Photodetectors Exploiting Interface Engineering. *ACS Photonics* **2015**, *2*, 1117−1123.
(92) Meggiolaro, D.; Motti, S. G.; Mosconi, E.; Barker, A. J.; Ball, J.; Perini, C. A. R.; Deschler, F.; Petrozza, A.; De Angelis, F. Iodine Chemistry Determines the Defect Tolerance of Lead-Halide Perovskites. *Energy Environ. Sci.* **2018**, *11*, 702−713.
(93) Yuan, Y.; Huang, J. Ion Migration in Organometal Trihalide Perovskite and Its Impact on Photovoltaic Efficiency and Stability. *Acc. Chem. Res.* **2016**, *49*, 286−293.
(94) Snaith, H. J.; Abate, A.; Ball, J. M.; Eperon, G. E.; Leijtens, T.; Noel, N. K.; Stranks, S. D.; Wang, J. T.; Wojciechowski, K.; Zhang, W. Anomalous Hysteresis in Perovskite Solar Cells. *J. Phys. Chem. Lett.* **2014**, *5*, 1511−1515.
(95) Sherkar, T. S.; Momblona, C.; Gil-Escrig, L.; Ávila, J.; Sessolo, M.; Bolink, H. J.; Koster, L. J. A. Recombination in Perovskite Solar Cells: Significance of Grain Boundaries, Interface Traps, and Defect Ions. *ACS Energy Lett.* **2017**, *2*, 1214−1222.
(96) Patel, J. B.; Wong-Leung, J.; Van Reenen, S.; Sakai, N.; Wang, J. T. W.; Parrott, E. S.; Liu, M.; Snaith, H. J.; Herz, L. M.; Johnston, M. B. Influence of Interface Morphology on Hysteresis in Vapor-Deposited Perovskite Solar Cells. *Adv. Electron. Mater.* **2017**, *3*, 1600470.
(97) Weber, S. A. L.; Hermes, I. M.; Turren-Cruz, S.-H.; Gort, C.; Bergmann, V. W.; Gilson, L.; Hagfeldt, A.; Graetzel, M.; Tress, W.; Berger, R. How the Formation of Interfacial Charge Causes Hysteresis in Perovskite Solar Cells. *Energy Environ. Sci.* **2018**, *11*, 2404.
(98) Gagliardi, A.; Abate, A. Mesoporous Electron-Selective Contacts Enhance the Tolerance to Interfacial Ion Accumulation in Perovskite Solar Cells. *ACS Energy Lett.* **2018**, *3*, 163−169.
(99) Xiao, Z.; Yuan, Y.; Shao, Y.; Wang, Q.; Dong, Q.; Bi, C.; Sharma, P.; Gruverman, A.; Huang, J. Giant Switchable Photovoltaic Effect in Organometal Trihalide Perovskite Devices. *Nat. Mater.* **2015**, *14*, 193−198.
(100) Protesescu, L.; Yakunin, S.; Bodnarchuk, M. I.; Krieg, F.; Caputo, R.; Hendon, C. H.; Yang, R. X.; Walsh, A.; Kovalenko, M. V. Nanocrystals of Cesium Lead Halide Perovskites ($CsPbX_3$, X = Cl, Br, and I): Novel Optoelectronic Materials Showing Bright Emission with Wide Color Gamut. *Nano Lett.* **2015**, *15*, 3692−3696.
(101) Ogomi, Y.; Morita, A.; Tsukamoto, S.; Saitho, T.; Fujikawa, N.; Shen, Q.; Toyoda, T.; Yoshino, K.; Pandey, S. S.; Ma, T.; et al. $CH_3NH_3Sn_xPb_{1-x}I_3$ Perovskite Solar Cells Covering up to 1060 nm. *J. Phys. Chem. Lett.* **2014**, *5*, 1004−1011.
(102) Nagabhushana, G. P.; Shivaramaiah, R.; Navrotsky, A. Direct Calorimetric Verification of Thermodynamic Instability of Lead Halide Hybrid Perovskites. *Proc. Natl. Acad. Sci. U. S. A.* **2016**, *113*, 7717−7721.
(103) Brenner, T. M.; Rakita, Y.; Orr, Y.; Klein, E.; Feldman, I.; Elbaum, M.; Cahen, D.; Hodes, G. Conversion of Single Crystalline PbI_2 to $CH_3NH_3PbI_3$: Structural Relations and Transformation Dynamics. *Chem. Mater.* **2016**, *28*, 6501−6510.
(104) Ivanov, I. L.; Steparuk, A. S.; Bolyachkina, M. S.; Tsvetkov, D. S.; Safronov, A. P.; Zuev, A. Y. Thermodynamics of Formation of Hybrid Perovskite-Type Methylammonium Lead Halides. *J. Chem. Thermodyn.* **2018**, *116*, 253−258.
(105) Lee, M. V.; Raga, S. R.; Kato, Y.; Leyden, M. R.; Ono, L. K.; Wang, S.; Qi, Y. Transamidation of Dimethylformamide during Alkylammonium Lead Triiodide Film Formation for Perovskite Solar Cells. *J. Mater. Res.* **2017**, *32*, 45−55.
(106) Dou, B.; Wheeler, L. M.; Christians, J. A.; Moore, D. T.; Harvey, S. P.; Berry, J. J.; Barnes, F. S.; Shaheen, S. E.; van Hest, M. F. A. M. Degradation of Highly Alloyed Metal Halide Perovskite Precursor Inks: Mechanism and Storage Solutions. *ACS Energy Lett.* **2018**, *3*, 979−985.
(107) Zhao, L.; Kerner, R. A.; Xiao, Z.; Lin, Y. L.; Lee, K. M.; Schwartz, J.; Rand, B. P. Redox Chemistry Dominates the Degradation and Decomposition of Metal Halide Perovskite Optoelectronic Devices. *ACS Energy Lett.* **2016**, *1*, 595−602.
(108) Chen, Q.; Zhou, H.; Song, T.-B.; Luo, S.; Hong, Z.; Duan, H.-S.; Dou, L.; Liu, Y.; Yang, Y. Controllable Self-Induced Passivation of Hybrid Lead Iodide Perovskites toward High Performance Solar Cells. *Nano Lett.* **2014**, *14*, 4158−4163.
(109) Ke, W.; Xiao, C.; Wang, C.; Saparov, B.; Duan, H.-S.; Zhao, D.; Xiao, Z.; Schulz, P.; Harvey, S. P.; Liao, W.; et al. Employing Lead Thiocyanate Additive to Reduce the Hysteresis and Boost the Fill Factor of Planar Perovskite Solar Cells. *Adv. Mater.* **2016**, *28*, 5214−5221.
(110) Patel, J. B.; Lin, Q.; Zadvorna, O.; Davies, C. L.; Herz, L. M.; Johnston, M. B. Photocurrent Spectroscopy of Perovskite Solar Cells Over a Wide Temperature Range from 15 to 350 K. *J. Phys. Chem. Lett.* **2018**, *9*, 263−268.
(111) Koh, T. M.; Fu, K.; Fang, Y.; Chen, S.; Sum, T. C.; Mathews, N.; Mhaisalkar, S. G.; Boix, P. P.; Baikie, T. Formamidinium-Containing Metal-Halide: An Alternative Material for Near-IR Absorption Perovskite Solar Cells. *J. Phys. Chem. C* **2014**, *118*, 16458−16462.
(112) Stoumpos, C. C.; Malliakas, C. D.; Kanatzidis, M. G. Semiconducting Tin and Lead Iodide Perovskites with Organic Cations: Phase Transitions, High Mobilities, and Near-Infrared Photoluminescent Properties. *Inorg. Chem.* **2013**, *52*, 9019−9038.
(113) Dastidar, S.; Hawley, C. J.; Dillon, A. D.; Gutierrez-Perez, A. D.; Spanier, J. E.; Fafarman, A. T. Quantitative Phase-Change Thermodynamics and Metastability of Perovskite-Phase Cesium Lead Iodide. *J. Phys. Chem. Lett.* **2017**, *8*, 1278−1282.
(114) Eperon, G. E.; Paternò, G. M.; Sutton, R. J.; Zampetti, A.; Haghighirad, A. A.; Cacialli, F.; Snaith, H. J. Inorganic Caesium Lead Iodide Perovskite Solar Cells. *J. Mater. Chem. A* **2015**, *3*, 19688−19695.
(115) Lee, J.-W.; Kim, D.-H.; Kim, H.-S.; Seo, S.-W.; Cho, S. M.; Park, N.-G. Formamidinium and Cesium Hybridization for Photo- and Moisture-Stable Perovskite Solar Cell. *Adv. Energy Mater.* **2015**, *5*, 1501310.
(116) Jeon, N. J.; Noh, J. H.; Yang, W. S.; Kim, Y. C.; Ryu, S.; Seo, J.; Seok, S. I. Compositional Engineering of Perovskite Materials for High-Performance Solar Cells. *Nature* **2015**, *517*, 476−480.
(117) Sutton, R. J.; Eperon, G. E.; Miranda, L.; Parrott, E. S.; Kamino, B. A.; Patel, J. B.; Hörantner, M. T.; Johnston, M. B.; Haghighirad, A. A.; Moore, D. T.; et al. Bandgap-Tunable Cesium Lead Halide Perovskites with High Thermal Stability for Efficient Solar Cells. *Adv. Energy Mater.* **2016**, *6*, 1502458.
(118) Hoke, E. T.; Slotcavage, D. J.; Dohner, E. R.; Bowring, A. R.; Karunadasa, H. I.; McGehee, M. D. Reversible Photo-Induced Trap Formation in Mixed-Halide Hybrid Perovskites for Photovoltaics. *Chem. Sci.* **2015**, *6*, 613−617.
(119) Ciesielski, R.; Schäfer, F.; Hartmann, N. F.; Giesbrecht, N.; Bein, T.; Docampo, P.; Hartschuh, A. Grain Boundaries Act as Solid Walls for Charge Carrier Diffusion in Large Crystal MAPI Thin Films. *ACS Appl. Mater. Interfaces* **2018**, *10*, 7974−7981.
(120) Pérez-Del-Rey, D.; Forgács, D.; Hutter, E. M.; Savenije, T. J.; Nordlund, D.; Schulz, P.; Berry, J. J.; Sessolo, M.; Bolink, H. J. Strontium Insertion in Methylammonium Lead Iodide: Long Charge Carrier Lifetime and High Fill-Factor Solar Cells. *Adv. Mater.* **2016**, *28*, 9839−9845.
(121) Stolterfoht, M.; Wolff, C. M.; Amir, Y.; Paulke, A.; Perdigón-Toro, L.; Caprioglio, P.; Neher, D. Approaching the Fill Factor Shockley−Queisser Limit in Stable, Dopant-Free Triple Cation Perovskite Solar Cells. *Energy Environ. Sci.* **2017**, *10*, 1530−1539.
(122) Huang, J.; Shao, Y.; Dong, Q. Organometal Trihalide Perovskite Single Crystal: A New Next Wave of Materials for 25% Efficiency Photovoltaics and Applications Beyond? *J. Phys. Chem. Lett.* **2015**, *6*, 3218−3227.
(123) Wang, Q.; Chen, B.; Liu, Y.; Deng, Y.; Bai, Y.; Dong, Q.; Huang, J. Scaling Behavior of Moisture-Induced Grain Degradation in Polycrystalline Hybrid Perovskite Thin Films. *Energy Environ. Sci.* **2017**, *10*, 516−522.
(124) Rolston, N.; Printz, A. D.; Tracy, J. M.; Weerasinghe, H. C.; Vak, D.; Haur, L. J.; Priyadarshi, A.; Mathews, N.; Slotcavage, D. J.;

DOI: 10.1021/acs.chemrev.8b00318
Chem. Rev. 2019, 119, 3193−3295

McGehee, M. D.; et al. Effect of Cation Composition on the Mechanical Stability of Perovskite Solar Cells. *Adv. Energy Mater.* **2018**, *8*, 1702116.
(125) Rolston, N.; Watson, B. L.; Bailie, C. D.; McGehee, M. D.; Bastos, J. P.; Gehlhaar, R.; Kim, J.-E.; Vak, D.; Mallajosyula, A. T.; Gupta, G.; et al. Mechanical Integrity of Solution-Processed Perovskite Solar Cells. *Extreme Mech. Lett.* **2016**, *9*, 353−358.
(126) Giesbrecht, N.; Schlipf, J.; Oesinghaus, L.; Binek, A.; Bein, T.; Müller-Buschbaum, P.; Docampo, P. Synthesis of Perfectly Oriented and Micrometer-Sized $MAPbBr_3$ Perovskite Crystals for Thin-Film Photovoltaic Applications. *ACS Energy Lett.* **2016**, *1*, 150−154.
(127) Jiang, C.; Zhang, P. Crystalline Orientation Dependent Photoresponse and Heterogeneous Behaviors of Grain Boundaries in Perovskite Solar Cells. *J. Appl. Phys.* **2018**, *123*, No. 083105.
(128) Kutes, Y.; Zhou, Y.; Bosse, J. L.; Steffes, J.; Padture, N. P.; Huey, B. D. Mapping the Photoresponse of $CH_3NH_3PbI_3$ Hybrid Perovskite Thin Films at the Nanoscale. *Nano Lett.* **2016**, *16*, 3434−3441.
(129) Leblebici, S. Y.; Leppert, L.; Li, Y.; Reyes-Lillo, S. E.; Wickenburg, S.; Wong, E.; Lee, J.; Melli, M.; Ziegler, D.; Angell, D. K.; et al. Facet-Dependent Photovoltaic Efficiency Variations in Single Grains of Hybrid Halide Perovskite. *Nat. Energy* **2016**, *1*, 16093.
(130) Docampo, P.; Hanusch, F. C.; Giesbrecht, N.; Angloher, P.; Ivanova, A.; Bein, T. Influence of the Orientation of Methylammonium Lead Iodide Perovskite Crystals on Solar Cell Performance. *APL Mater.* **2014**, *2*, 081508.
(131) Chen, A. Z.; Foley, B. J.; Ma, J. H.; Alpert, M. R.; Niezgoda, J. S.; Choi, J. J. Crystallographic Orientation Propagation in Metal Halide Perovskite Thin Films. *J. Mater. Chem. A* **2017**, *5*, 7796−7800.
(132) Dong, Q.; Yuan, Y.; Fang, Y.; Wang, Q.; Huang, J.; Shao, Y. Abnormal Crystal Growth in $CH_3NH_3PbI_{3-x}Cl_x$ Using a Multi-Cycle Solution Coating Process. *Energy Environ. Sci.* **2015**, *8*, 2464−2470.
(133) Mosconi, E.; Ronca, E.; De Angelis, F. First-Principles Investigation of the TiO_2/Organohalide Perovskites Interface: The Role of Interfacial Chlorine. *J. Phys. Chem. Lett.* **2014**, *5*, 2619−2625.
(134) Bouchard, M.; Hilhorst, J.; Pouget, S.; Alam, F.; Mendez, M.; Djurado, D.; Aldakov, D.; Schülli, T.; Reiss, P. Direct Evidence of Chlorine-Induced Preferential Crystalline Orientation in Methylammonium Lead Iodide Perovskites Grown on TiO_2. *J. Phys. Chem. C* **2017**, *121*, 7596−7602.
(135) Yun, J. S.; Ho-Baillie, A.; Huang, S.; Woo, S. H.; Heo, Y.; Seidel, J.; Huang, F.; Cheng, Y.-B.; Green, M. A. Benefit of Grain Boundaries in Organic-Inorganic Halide Planar Perovskite Solar Cells. *J. Phys. Chem. Lett.* **2015**, *6*, 875−880.
(136) deQuilettes, D. W.; Vorpahl, S. M.; Stranks, S. D.; Nagaoka, H.; Eperon, G. E.; Ziffer, M. E.; Snaith, H. J.; Ginger, D. S. Impact of Microstructure on Local Carrier Lifetime in Perovskite Solar Cells. *Science* **2015**, *348*, 683−686.
(137) Yang, M.; Zeng, Y.; Li, Z.; Kim, D.-H.; Jiang, C.-S.; van de Lagemaat, J.; Zhu, K. Do Grain Boundaries Dominate Non-Radiative Recombination in $CH_3NH_3PbI_3$ Perovskite Thin Films? *Phys. Chem. Chem. Phys.* **2017**, *19*, 5043−5050.
(138) Ji, F.; Pang, S.; Zhang, L.; Zong, Y.; Cui, G.; Padture, N. P.; Zhou, Y. Simultaneous Evolution of Uniaxially Oriented Grains and Ultralow-Density Grain-Boundary Network in $CH_3NH_3PbI_3$ Perovskite Thin Films Mediated by Precursor Phase Metastability. *ACS Energy Lett.* **2017**, *2*, 2727−2733.
(139) Zong, Y.; Zhou, Y.; Zhang, Y.; Li, Z.; Zhang, L.; Ju, M.-G.; Chen, M.; Pang, S.; Zeng, X. C.; Padture, N. P. Continuous Grain-Boundary Functionalization for High-Efficiency Perovskite Solar Cells with Exceptional Stability. *Chem.* **2018**, *4*, 1404−1415.
(140) Hermes, I. M.; Bretschneider, S. A.; Bergmann, V. W.; Li, D.; Klasen, A.; Mars, J.; Tremel, W.; Laquai, F.; Butt, H.-J.; Mezger, M.; et al. Ferroelastic Fingerprints in Methylammonium Lead Iodide Perovskite. *J. Phys. Chem. C* **2016**, *120*, 5724−5731.
(141) Rothmann, M. U.; Li, W.; Zhu, Y.; Bach, U.; Spiccia, L.; Etheridge, J.; Cheng, Y.-B. Direct Observation of Intrinsic Twin Domains in Tetragonal $CH_3NH_3PbI_3$. *Nat. Commun.* **2017**, *8*, 14547.
(142) Kim, T. W.; Uchida, S.; Matsushita, T.; Cojocaru, L.; Jono, R.; Kimura, K.; Matsubara, D.; Shirai, M.; Ito, K.; Matsumoto, H.; et al. Self-Organized Superlattice and Phase Coexistence inside Thin Film Organometal Halide Perovskite. *Adv. Mater.* **2018**, *30*, 1705230.
(143) Zhou, Y.; Game, O. S.; Pang, S.; Padture, N. P. Microstructures of Organometal Trihalide Perovskites for Solar Cells: Their Evolution from Solutions and Characterization. *J. Phys. Chem. Lett.* **2015**, *6*, 4827−4839.
(144) Lee, M. M.; Teuscher, J.; Miyasaka, T.; Murakami, T. N.; Snaith, H. J. Efficient Hybrid Solar Cells Based on Meso-Superstructured Organometal Halide Perovskites. *Science* **2012**, *338*, 643−647.
(145) Zhao, Y.; Zhu, K. Solution-Chemistry Engineering Toward High-Efficiency Perovskite Solar Cells. *J. Phys. Chem. Lett.* **2014**, *5*, 4175−4186.
(146) Jung, H. S.; Park, N.-G. Perovskite Solar Cells: From Materials to Devices. *Small* **2015**, *11*, 10−25.
(147) Saidaminov, M. I.; Abdelhady, A. L.; Murali, B.; Alarousu, E.; Burlakov, V. M.; Peng, W.; Dursun, I.; Wang, L.; He, Y.; Maculan, G.; et al. High-Quality Bulk Hybrid Perovskite Single Crystals within Minutes by Inverse Temperature Crystallization. *Nat. Commun.* **2015**, *6*, 7586.
(148) Jeon, N. J.; Noh, J. H.; Kim, Y. C.; Yang, W. S.; Ryu, S.; Seok, S. I. Solvent Engineering for High-Performance Inorganic-Organic Hybrid Perovskite Solar Cells. *Nat. Mater.* **2014**, *13*, 897−903.
(149) Xiao, M.; Huang, F.; Huang, W.; Dkhissi, Y.; Zhu, Y.; Etheridge, J.; Gray-Weale, A.; Bach, U.; Cheng, Y.-B.; Spiccia, L. A Fast Deposition-Crystallization Procedure for Highly Efficient Lead Iodide Perovskite Thin-Film Solar Cells. *Angew. Chem., Int. Ed.* **2014**, *53*, 9898−9903.
(150) Zhou, Y.; Yang, M.; Wu, W.; Vasiliev, A. L.; Zhu, K.; Padture, N. P. Room-Temperature Crystallization of Hybrid-Perovskite Thin Films via Solvent−Solvent Extraction for High-Performance Solar Cells. *J. Mater. Chem. A* **2015**, *3*, 8178−8184.
(151) De Yoreo, J. J.; Gilbert, P. U. P. A.; Sommerdijk, N. A. J. M.; Penn, R. L.; Whitelam, S.; Joester, D.; Zhang, H.; Rimer, J. D.; Navrotsky, A.; Banefield, J. F.; et al. Crystallization by Particle Attachment in Synthetic, Biogenic, and Geologic Environments. *Science* **2015**, *349*, aaa6760.
(152) Chen, A. Z.; Shiu, M.; Ma, J. H.; Alpert, M. R.; Zhang, D.; Foley, B. J.; Smilgies, D.-M.; Lee, S.-H.; Choi, J. J. Origin of Vertical Orientation in Two-Dimensional Metal Halide Perovskites and its Effect on Photovoltaic Performance. *Nat. Commun.* **2018**, *9*, 1336.
(153) Nielsen, A. E. *Kinetics of Precipitation*; Pergamon: Oxford, UK, 1964.
(154) Brinker, C. J.; Scherer, G. W. *Sol-Gel Science*; Academic Press: New York, NY, USA, 1990.
(155) Adamson, A. W.; Gast, A. P. *Physical Chemistry of Surfaces*; Wiley: New York, NY, 1997.
(156) Ring, T. A. *Fundamentals of Ceramic Powder Processing and Synthesis*; Academic Publishers: New York, NY, 1996.
(157) LaMer, V. K.; Dinegar, R. H. Theory, Production, and Mechanism of Formation of Monodispersed Hydrosols. *J. Am. Chem. Soc.* **1950**, *72*, 4847−4854.
(158) Sun, Y. Controlled Synthesis of Colloidal Silver Nanoparticles in Organic Solutions: Empirical Rules for Nucleation Engineering. *Chem. Soc. Rev.* **2013**, *42*, 2497−2511.
(159) Rahaman, M. N. *Ceramic Processing and Sintering*; Marcel Dekker Inc.: New York, NY, 2007.
(160) Kingery, W. D.; Bowen, H. K.; Uhlmann, D. R. *Introduction to Ceramics*, 2nd ed.; Wiley Interscience: New York, 1976.
(161) Porter, D. A.; Easterling, K. E. *Phase Transformations Metals and Alloys*; Van Nostrand Reinhold (International) Co. Ltd.: Berkshire, England, 1981.
(162) Yan, K.; Long, M.; Zhang, T.; Wei, Z.; Chen, H.; Yang, S.; Xu, J. Hybrid Halide Perovskite Solar Cell Precursors: Colloidal Chemistry and Coordination Engineering behind Device Processing for High Efficiency. *J. Am. Chem. Soc.* **2015**, *137*, 4460−4468.

DOI: 10.1021/acs.chemrev.8b00318
Chem. Rev. 2019, 119, 3193−3295

(163) Tidhar, Y.; Edri, E.; Weissman, H.; Zohar, D.; Hodes, G.; Cahen, D.; Rybtchinski, B.; Kirmayer, S. Crystallization of Methyl Ammonium Lead Halide Perovskites: Implications for Photovoltaic Applications. *J. Am. Chem. Soc.* **2014**, *136*, 13249−13256.
(164) McMeekin, D. P.; Wang, Z.; Rehman, W.; Pulvirenti, F.; Patel, J. B.; Noel, N. K.; Johnston, M. B.; Marder, S. R.; Herz, L. M.; Snaith, H. J. Crystallization Kinetics and Morphology Control of Formamidinium-Cesium Mixed-Cation Lead Mixed-Halide Perovskite via Tunability of the Colloidal Precursor Solution. *Adv. Mater.* **2017**, *29*, 1607039.
(165) Burschka, J.; Pellet, N.; Moon, S.-J.; Humphry-Baker, R.; Gao, P.; Nazeeruddin, M. K.; Grätzel, M. Sequential Deposition as a Route to High-Performance Perovskite-Sensitized Solar Cells. *Nature* **2013**, *499*, 316−319.
(166) Kashchiev, D. *Nucleation: Basic Theory and Applications*; Butterworth-Heinemann: Boston, MA, 2000.
(167) Mitzi, D. B. Organic-Inorganic Perovskites Containing Trivalent Metal Halide Layers: the Templating Influence of the Organic Cation Layer. *Inorg. Chem.* **2000**, *39*, 6107−6113.
(168) Stevenson, J.; Sorenson, B.; Subramaniam, V. H.; Raiford, J.; Khlyabich, P. P.; Loo, Y.-L.; Clancy, P. Mayer Bond Order as a Metric of Complexation Effectiveness in Lead Halide Perovskite Solutions. *Chem. Mater.* **2017**, *29*, 2435−2444.
(169) Li, T.; Pan, Y.; Wang, Z.; Xia, Y.; Chen, Y.; Huang, W. Additive Engineering for Highly Efficient Organic−Inorganic Halide Perovskite Solar Cells: Recent Advances and Perspectives. *J. Mater. Chem. A* **2017**, *5*, 12602−12652.
(170) Ahn, N.; Son, D.-Y.; Jang, I.-H.; Kang, S. M.; Choi, M.; Park, N.-G. Highly Reproducible Perovskite Solar Cells with Average Efficiency of 18.3% and Best Efficiency of 19.7% Fabricated via Lewis Base Adduct of Lead(II) Iodide. *J. Am. Chem. Soc.* **2015**, *137*, 8696−8699.
(171) Jacobsson, T. J.; Correa-Baena, J.-P.; Halvani Anaraki, E.; Philippe, B.; Stranks, S. D.; Bouduban, M. E.; Tress, W.; Schenk, K.; Teuscher, J.; Moser, J.-E.; et al. Unreacted PbI_2 as a Double-Edged Sword for Enhancing the Performance of Perovskite Solar Cells. *J. Am. Chem. Soc.* **2016**, *138*, 10331−10343.
(172) Venables, J. A.; Spiller, G. D. T.; Hanbücken, M. Nucleation and Growth of Thin Films. *Rep. Prog. Phys.* **1984**, *47*, 399−459.
(173) Zheng, Y. C.; Yang, S.; Chen, X.; Chen, Y.; Hou, Y.; Yang, H. G. Thermal-Induced Volmer-Weber Growth Behvaior for Planar Heterojunction Perovskites Solar Cells. *Chem. Mater.* **2015**, *27*, 5116−5121.
(174) Yang, B.; Keum, J.; Ovchinnikova, O. S.; Belianinov, A.; Chen, S.; Du, M. H.; Ivanov, I. N.; Rouleau, C. M.; Geohegan, D. B.; Xiao, K. Deciphering Halogen Competition in Organometallic Halide Perovskite Growth. *J. Am. Chem. Soc.* **2016**, *138*, 5028−5035.
(175) Moore, D. T.; Sai, H.; Tan, K. W.; Smilgies, D.-M.; Zhang, W.; Snaith, H. J.; Wiesner, U.; Estroff, L. A. Crystallization Kinetics of Organic-Inorganic Trihalide Perovskites and the Role of the Lead Anion in Crystal Growth. *J. Am. Chem. Soc.* **2015**, *137*, 2350−2358.
(176) Ummadisingu, A.; Grätzel, M. Revealing the Detailed Path of Sequential Deposition for Metal Halide Perovskite Formation. *Sci. Adv.* **2018**, *4*, No. e1701402.
(177) Davidovich, R. L.; Stavila, V.; Marinin, D. V.; Voit, E. I.; Whitmire, K. H. Stereochemistry of Lead(II) Complexes with Oxygen Donor Ligands. *Coord. Chem. Rev.* **2009**, *253*, 1316−1352.
(178) Moore, D. T.; Tan, K. W.; Sai, H.; Barteau, K. P.; Wiesner, U.; Estroff, L. A. Direct Crystallization Route to Methylammonium Lead Iodide Perovskite from an Ionic Liquid. *Chem. Mater.* **2015**, *27*, 3197−3199.
(179) Foley, B. J.; Girard, J.; Sorenson, B. A.; Chen, A. Z.; Niezgoda, J. S.; Alpert, M. A.; Harper, A. F.; Smilgies, D.-M.; Clancy, P.; Saidi, W. A.; et al. Controlling Nucleation, Growth, and Orientation of Metal Halide Perovskite Thin Films with Rationally Selected Additives. *J. Mater. Chem. A* **2017**, *5*, 113−123.
(180) Zhou, Z.; Wang, Z.; Zhou, Y.; Pang, S.; Wang, D.; Xu, H.; Liu, Z.; Padture, N. P.; Cui, G. Methylamine-Gas-Induced Defect-Healing Behavior of $CH_3NH_3PbI_3$ Thin Films for Perovskite Solar Cells. *Angew. Chem., Int. Ed.* **2015**, *54*, 9705−9709.
(181) Pang, S.; Zhou, Y.; Wang, Z.; Yang, M.; Krause, A. R.; Zhou, Z.; Zhu, K.; Padture, N. P.; Cui, G. Transformative Evolution of Organolead Triiodide Perovskite Thin Films from Strong Room-Temperature Solid-Gas Interaction between $HPbI_3$-CH_3NH_2 Precursor Pair. *J. Am. Chem. Soc.* **2016**, *138*, 750−753.
(182) Unger, E. L.; Bowring, A. R.; Tassone, C. J.; Pool, V. L.; Gold-Parker, A.; Cheacharoen, R.; Stone, K. H.; Hoke, E. T.; Toney, M. F.; McGehee, M. D. Chloride in Lead Chloride-Derived Organo-Metal Halides for Perovskite-Absorber Solar Cells. *Chem. Mater.* **2014**, *26*, 7158−7165.
(183) Li, S.-S.; Chang, C.-H.; Wang, Y.-C.; Lin, C.-W.; Wang, D.-Y.; Lin, J.-C.; Chen, C.-C.; Sheu, H.-S.; Chia, H.-C.; Wu, W.-R.; et al. Intermixing-Seeded Growth for High-Performance Planar Heterojunction Perovskite Solar Cells Assisted by Precursor-Capped Nanoparticles. *Energy Environ. Sci.* **2016**, *9*, 1282−1289.
(184) Ngo, T. T.; Suarez, I.; Sanchez, R. S.; Martinez-Pastor, J. P.; Mora-Sero, I. Single Step Deposition of an Interacting Layer of a Perovskite Matrix with Embedded Quantum Dots. *Nanoscale* **2016**, *8*, 14379−14383.
(185) Wakamiya, A.; Endo, M.; Sasamori, T.; Tokitoh, N.; Ogomi, Y.; Hayase, S.; Murata, Y. Reproducible Fabrication of Efficient Perovskite-based Solar Cells: X-ray Crystallographic Studies on the Formation of $CH_3NH_3PbI_3$ Layers. *Chem. Lett.* **2014**, *43*, 711−713.
(186) Miyamae, H.; Numahata, Y.; Nagata, M. The Crystal Structure of Lead(II) Iodide-Dimethylsulphoxide(1/2), $PbI_2(dmso)_2$. *Chem. Lett.* **1980**, *9*, 663−664.
(187) Hao, F.; Stoumpos, C. C.; Liu, Z.; Chang, R. P.; Kanatzidis, M. G. Controllable Perovskite Crystallization at a Gas-Solid Interface for Hole Conductor-Free Solar Cells with Steady Power Conversion Efficiency over 10%. *J. Am. Chem. Soc.* **2014**, *136*, 16411−16419.
(188) Guo, Y.; Shoyama, K.; Sato, W.; Matsuo, Y.; Inoue, K.; Harano, K.; Liu, C.; Tanaka, H.; Nakamura, E. Chemical Pathways Connecting Lead(II) Iodide and Perovskite via Polymeric Plumbate(II) Fiber. *J. Am. Chem. Soc.* **2015**, *137*, 15907−15914.
(189) Rong, Y.; Tang, Z.; Zhao, Y.; Zhong, X.; Venkatesan, S.; Graham, H.; Patton, M.; Jing, Y.; Guloy, A. M.; Yao, Y. Solvent Engineering Towards Controlled Grain Growth in Perovskite Planar Heterojunction Solar Cells. *Nanoscale* **2015**, *7*, 10595−10599.
(190) Kerner, R. A.; Zhao, L.; Xiao, Z.; Rand, B. P. Ultrasmooth Metal Halide Perovskite Thin Films via Sol−Gel Processing. *J. Mater. Chem. A* **2016**, *4*, 8308−8315.
(191) Li, B.; Li, M.; Fei, C.; Cao, G.; Tian, J. Colloidal Engineering for Monolayer $CH_3NH_3PbI_3$ Films toward High Performance Perovskite Solar Cells. *J. Mater. Chem. A* **2017**, *5*, 24168−24177.
(192) Era, M.; Hattori, T.; Taira, T.; Tsutsui, T. Self-Organized Growth of PbI-Based Layered Perovskite Quantum Well by Dual-Source Vapor Deposition. *Chem. Mater.* **1997**, *9*, 8−10.
(193) Liu, M.; Johnston, M. B.; Snaith, H. J. Efficient Planar Heterojunction Perovskite Solar Cells by Vapour Deposition. *Nature* **2013**, *501*, 395−398.
(194) Xu, H.; Wu, Y.; Xu, F.; Zhu, J.; Ni, C.; Wang, W.; Hong, F.; Xu, R.; Xu, F.; Huang, J.; et al. Grain Growth Study of Perovskite Thin Films Prepared by Flash Evaporation and its Effect on Solar Cell Performance. *RSC Adv.* **2016**, *6*, 48851−48857.
(195) Ávila, J.; Momblona, C.; Boix, P. P.; Sessolo, M.; Bolink, H. J. Vapor-Deposited Perovskites: The Route to High-Performance Solar Cell Production? *Joule* **2017**, *1*, 431−442.
(196) Olthof, S.; Meerholz, K. Substrate Dependent Electronic Structure and Film Formation of $MAPbI_3$ Perovskites. *Sci. Rep.* **2017**, *7*, 40267.
(197) Zhou, X.; Li, X.; Liu, Y.; Huang, F.; Zhong, D. Interface Electronic Properties of Co-evaporated $MAPbI_3$ on ZnO(0001): In Situ X-ray Photoelectron Spectroscopy and Ultraviolet Photoelectron Spectroscopy Study. *Appl. Phys. Lett.* **2016**, *108*, 121601.
(198) Xu, H.; Wu, Y.; Cui, J.; Ni, C.; Xu, F.; Cai, J.; Hong, F.; Fang, Z.; Wang, W.; Zhu, J.; et al. Formation and Evolution of the

DOI: 10.1021/acs.chemrev.8b00318
Chem. Rev. 2019, 119, 3193−3295

Unexpected PbI_2 Phase at Interface During the Growth of Evaporated Perovskite Films. *Phys. Chem. Chem. Phys.* **2016**, *18*, 18607−18613.
(199) Liang, K.; Mitzi, D. B.; Prikas, M. T. Synthesis and Characterization of Organic-Inorganic Perovskite Thin Films Prepared Using a Versatile Two-Step Dipping Technique. *Chem. Mater.* **1998**, *10*, 403−411.
(200) Xiao, Z.; Bi, C.; Shao, Y.; Dong, Q.; Wang, Q.; Yuan, Y.; Wang, C.; Gao, Y.; Huang, J. Efficient, High Yield Perovskite Photovoltaic Devices Grown by Interdiffusion of Solution-Processed Precursor Stacking Layers. *Energy Environ. Sci.* **2014**, *7*, 2619−2623.
(201) Chen, Q.; Zhou, H.; Hong, Z.; Luo, S.; Duan, H.-S.; Wang, H.-H.; Liu, Y.; Li, G.; Yang, Y. Planar Heterojunction Perovskite Solar Cells via Vapor-Assisted Solution Process. *J. Am. Chem. Soc.* **2014**, *136*, 622−625.
(202) Schlipf, J.; Docampo, P.; Schaffer, C. J.; Körstgens, V.; Biessmann, L.; Hanusch, F.; Giesbrecht, N.; Bernstorff, S.; Bein, T.; Müller-Buschbaum, P. A Closer Look into Two-Step Perovskite Conversion with X-Ray Scattering. *J. Phys. Chem. Lett.* **2015**, *6*, 1265−1269.
(203) Zhou, Y.; Yang, M.; Vasiliev, A. L.; Garces, H. F.; Zhao, Y.; Wang, D.; Pang, S.; Zhu, K.; Padture, N. P. Growth Control of Compact $CH_3NH_3PbI_3$ Thin Films via Enhanced Solid-State Precursor Reaction for Efficient Planar Perovskite Solar Cells. *J. Mater. Chem. A* **2015**, *3*, 9249−9256.
(204) Wu, Y.; Islam, A.; Yang, X.; Qin, C.; Liu, J.; Zhang, K.; Peng, W.; Han, L. Retarding the Crystallization of PbI_2 for Highly Reproducible Planar-Structured Perovskite Solar Cells via Sequential Deposition. *Energy Environ. Sci.* **2014**, *7*, 2934−2938.
(205) Liu, T.; Hu, Q.; Wu, J.; Chen, K.; Zhao, L.; Liu, F.; Wang, C.; Lu, H.; Jia, S.; Russell, T.; et al. Mesoporous PbI_2 Scaffold for High-Performance Planar Heterojunction Perovskite Solar Cells. *Adv. Energy Mater.* **2016**, *6*, 1501890.
(206) Zhang, H.; Mao, J.; He, H.; Zhang, D.; Zhu, H. L.; Xie, F.; Wong, K. S.; Grätzel, M.; Choy, W. C. H. A Smooth $CH_3NH_3PbI_3$ Film via a New Approach for Forming the PbI_2 Nanostructure Together with Strategically High CH_3NH_3I Concentration for High Efficient Planar-Heterojunction Solar Cells. *Adv. Energy Mater.* **2015**, *5*, 1501354.
(207) Tu, Y.; Wu, J.; He, X.; Guo, P.; Wu, T.; Luo, H.; Liu, Q.; Wang, K.; Lin, J.; Huang, M.; et al. Solvent Engineering for Forming Stonehenge-like PbI_2 Nano-Structures Towards Efficient Perovskite Solar Cells. *J. Mater. Chem. A* **2017**, *5*, 4376−4383.
(208) Zhou, Y.; Yang, M.; Kwun, J.; Game, O. S.; Zhao, Y.; Pang, S.; Padture, N. P.; Zhu, K. Intercalation Crystallization of Phase-Pure α-HC-$(NH_2)_2PbI_3$ Upon Microstructurally Engineered PbI_2 Thin Films for Planar Perovskite Solar Cells. *Nanoscale* **2016**, *8*, 6265−6272.
(209) Zhang, T.; Yang, M.; Zhao, Y.; Zhu, K. Controllable Sequential Deposition of Planar $CH_3NH_3PbI_3$ Perovskite Films via Adjustable Volume Expansion. *Nano Lett.* **2015**, *15*, 3959−3963.
(210) Liu, J.; Shirai, Y.; Yang, X.; Yue, Y.; Chen, W.; Wu, Y.; Islam, A.; Han, L. High-Quality Mixed-Organic-Cation Perovskites from a Phase-Pure Non-Stoichiometric Intermediate $(FAI)_{1-x}$-PbI_2 for Solar Cells. *Adv. Mater.* **2015**, *27*, 4918−4923.
(211) Li, W.; Fan, J.; Li, J.; Mai, Y.; Wang, L. Controllable Grain Morphology of Perovskite Absorber Film by Molecular Self-Assembly toward Efficient Solar Cell Exceeding 17%. *J. Am. Chem. Soc.* **2015**, *137*, 10399−10405.
(212) Hu, H.; Wang, D.; Zhou, Y.; Zhang, J.; Lv, S.; Pang, S.; Chen, X.; Liu, Z.; Padture, N. P.; Cui, G. Vapour-Based Processing of Hole-Conductor-Free $CH_3NH_3PbI_3$ Perovskite/C_{60} Fullerene Planar Solar Cells. *RSC Adv.* **2014**, *4*, 28964−28967.
(213) Hsiao, S.-Y.; Lin, H.-L.; Lee, W.-H.; Tsai, W.-L.; Chiang, K.-M.; Liao, W.-Y.; Ren-Wu, C.-Z.; Chen, C.-Y.; Lin, H.-W. Efficient All-Vacuum Deposited Perovskite Solar Cells by Controlling Reagent Partial Pressure in High Vacuum. *Adv. Mater.* **2016**, *28*, 7013−7019.
(214) Li, G.; Ho, J. Y. L.; Wong, M.; Kwok, H.-S. Low Cost, High Throughput and Centimeter-Scale Fabrication of Efficient Hybrid Perovskite Solar Cells by Closed Space Vapor Transport. *Phys. Status Solidi RRL* **2016**, *10*, 153−157.
(215) Raga, S. R.; Ono, L. K.; Qi, Y. Rapid Perovskite Formation by CH_3NH_2 Gas-Induced Intercalation and Reaction of PbI_2. *J. Mater. Chem. A* **2016**, *4*, 2494−2500.
(216) Zong, Y.; Zhou, Y.; Ju, M.; Garces, H. F.; Krause, A. R.; Ji, F.; Cui, G.; Zeng, X. C.; Padture, N. P.; Pang, S. Thin-Film Transformation of NH_4PbI_3 to $CH_3NH_3PbI_3$ Perovskite: A Methylamine-Induced Conversion-Healing Process. *Angew. Chem., Int. Ed.* **2016**, *55*, 14723−14727.
(217) Jo, Y.; Oh, K. S.; Kim, M.; Kim, K.-H.; Lee, H.; Lee, C.-W.; Kim, D. S. High Performance of Planar Perovskite Solar Cells Produced from PbI_2(DMSO) and PbI_2(NMP) Complexes by Intramolecular Exchange. *Adv. Mater. Interfaces* **2016**, *3*, 1500768.
(218) Grätzel, M. The Light and Shade of Perovskite Solar Cells. *Nat. Mater.* **2014**, *13*, 838−842.
(219) Scherer, G. W. Crystallization in Pores. *Cem. Concr. Res.* **1999**, *29*, 1347−1358.
(220) Scherer, G. W. Stress from Crystallization of Salt. *Cem. Concr. Res.* **2004**, *34*, 1613−1624.
(221) Scherer, G. W., Factors Affecting Crystallization Pressure. In *Proceedings of International RILEM TC 186-ISA Workshop*; Scrivener, K., Skalny, J., Eds.; RILEM Publications S.A.R.L.: Bagneux, France, 2004; Vol. *35*, pp 139−154.
(222) Steiger, M. Crystal Growth in Porous Materials - I: The Crystallization Pressure of Large Crystals. *J. Cryst. Growth* **2005**, *282*, 455−469.
(223) Steiger, M. Crystal Growth in Porous Materials - II: Influence of Crystal Size on the Crystallization Pressure. *J. Cryst. Growth* **2005**, *282*, 470−481.
(224) Wang, Z.; Zhou, Y.; Pang, S.; Xiao, Z.; Zhang, J.; Chai, W.; Xu, H.; Liu, Z.; Padture, N. P.; Cui, G. Additive-Modulated Evolution of $HC(NH_2)_2PbI_3$ Black Polymorph for Mesoscopic Perovskite Solar Cells. *Chem. Mater.* **2015**, *27*, 7149−7155.
(225) Zhou, Y.; Kwun, J.; Garces, H. F.; Pang, S.; Padture, N. P. Observation of Phase-Retention Behavior of the $HC(NH_2)_2PbI_3$ Black Perovskite Polymorph Upon Mesoporous TiO_2 Scaffolds. *Chem. Commun.* **2016**, *52*, 7273−7275.
(226) Luque, A.; Hegedus, S. *Handbook of Photovoltaic Science and Engineering*; Wiley: New York, NY, 2011.
(227) Yadavalli, S. K.; Zhou, Y.; Padture, N. P. Exceptional Grain Growth in Formamidinium Lead Iodide Perovskite Thin Films Induced by the δ-to-α Phase Transformation. *ACS Energy Lett.* **2018**, *3*, 63−64.
(228) Thompson, C. V. Grain Growth in Thin Films. *Annu. Rev. Mater. Sci.* **1990**, *20*, 245−268.
(229) Lawn, B. R. *Fracture of Brittle Solids*, 2nd ed.; Cambridge University Press: Cambridge, U.K., 1993.
(230) Voorhees, P. W. Ostwald Ripening of Two-Phase Mixtures. *Annu. Rev. Mater. Sci.* **1992**, *22*, 197−215.
(231) Readey, D. W. *Kinetics in Materials Science and Engineering*; CRC Press: Boca Raton, FL, 2017.
(232) Yang, M.; Zhou, Y.; Zeng, Y.; Jiang, C.-S.; Padture, N. P.; Zhu, K. Square-Centimeter Solution-Processed Planar $CH_3NH_3PbI_3$ Perovskite Solar Cells with Efficiency Exceeding 15%. *Adv. Mater.* **2015**, *27*, 6363−6370.
(233) Jang, J.; Oh, J. Y.; Kim, S. K.; Choi, Y. J.; Yoon, S. Y.; Kim, C. O. Electric-Field-Enhanced Crystallization of Amorphous Silicon. *Nature* **1998**, *395*, 481−483.
(234) Tai, C. Y.; Wu, C.-K.; Chang, M.-C. Effects of Magnetic Field on the Crystallization of $CaCO_3$ Using Permanent Magnets. *Chem. Eng. Sci.* **2008**, *63*, 5606−5612.
(235) Vijayan, R.; Swathi, K.; Narayan, K. S. Synergistic Effects of Electric-Field-Assisted Annealing and Thermal Annealing in Bulk Heterojunction Solar Cells. *ACS Appl. Mater. Interfaces* **2017**, *9*, 19436−19445.
(236) Rakita, Y.; Bar-Elli, O.; Meirzadeh, E.; Kaslasi, H.; Peleg, Y.; Hodes, G.; Lubomirsky, I.; Oron, D.; Ehre, D.; Cahen, D. Tetragonal $CH_3NH_3PbI_3$ is Ferroelectric. *Proc. Natl. Acad. Sci. U. S. A.* **2017**, *114*, E5504−E5512.

DOI: 10.1021/acs.chemrev.8b00318
Chem. Rev. 2019, 119, 3193−3295

(237) Whitfield, P. S.; Herron, N.; Guise, W. E.; Page, K.; Cheng, Y. Q.; Milas, I.; Crawford, M. K. Structures, Phase Transitions and Tricritical Behavior of the Hybrid Perovskite Methyl Ammonium Lead Iodide. *Sci. Rep.* **2016**, *6*, 35685.
(238) Lychev, A. P.; Rudenko, Y. S.; Cheremisin, A. I. Effect of Electric Field on Crystallization. *Russ. Phys. J.* **1977**, *20*, 441−440.
(239) Kuznetsov, D. A.; Hodorowicz, S.; Krymova, W. G. Wave Mechanism of the Effect of External Fields on Crystallization. *Krist. Tech.* **1979**, *14*, 671−675.
(240) Shyu, J.-J.; Chen, Y.-H. Effect of Electric Field on the Crystallization of Lead Titanate in a Glass. *J. Mater. Sci.* **2004**, *39*, 159−163.
(241) Hammadi, Z.; Veesler, S. New Approaches on Crystallization Under Electric Field. *Prog. Biophys. Mol. Biol.* **2009**, *101*, 38−44.
(242) Revalor, E.; Hammadi, Z.; Astier, J.-P.; Grossier, R.; Garcia, E.; Hoff, C.; Furuta, K.; Okustu, T.; Morin, R.; Veesler, S. Usual and Unusual Crystallization from Solution. *J. Cryst. Growth* **2010**, *312*, 939−946.
(243) Zhang, C.-C.; Wang, Z.-K.; Li, M.; Liu, Z.-Y.; Yang, J.-E.; Yang, Y.-G.; Gao, X.-Y.; Ma, H. Electric-Field Assisted Perovskite Crystallization for High-Performance Solar Cells. *J. Mater. Chem. A* **2018**, *6*, 1161−1170.
(244) Wang, H.; Lei, J.; Gao, F.; Yang, Z.; Yang, D.; Jiang, J.; Li, J.; Hu, X.; Ren, X.; Liu, B.; et al. Magnetic Field-Assisted Perovskite Film Preparation for Enhanced Performance of Solar Cells. *ACS Appl. Mater. Interfaces* **2017**, *9*, 21756−21762.
(245) Williams, S. T.; Rajagopal, A.; Jo, S. B.; Chueh, C.-C.; Tang, T. F. L.; Kraeger, A.; Jen, A. K.-Y. Realizing a New Class of Hybrid Organic−Inorganic Multifunctional Perovskite. *J. Mater. Chem. A* **2017**, *5*, 10640−10650.
(246) Poindexter, J. R.; Hoye, R. L. Z.; Nienhaus, L.; Kurchin, R. C.; Morishige, A. E.; Looney, E. E.; Osherov, A.; Correa-Baena, J. P.; Lai, B.; Bulović, V.; et al. High Tolerance to Iron Contamination in Lead Halide Perovskite Solar Cells. *ACS Nano* **2017**, *11*, 7101−7109.
(247) Ummadisingu, A.; Steier, L.; Seo, J.-Y.; Matsui, T.; Abate, A.; Tress, W.; Grätzel, M. The Effect of Illumination on the Formation of Metal Halide Perovskite Films. *Nature* **2017**, *545*, 208−212.
(248) Kojima, A.; Teshima, K.; Shirai, Y.; Miyasaka, T. Organometal Halide Perovskites as Visible-Light Sensitizers for Photovoltaic Cells. *J. Am. Chem. Soc.* **2009**, *131*, 6050−6051.
(249) Im, J.-H.; Kim, H.-S.; Park, N.-G. Morphology-Photovoltaic Property Correlation in Perovskite Solar Cells: One-Step versus Two-Step Deposition of $CH_3NH_3PbI_3$. *APL Mater.* **2014**, *2*, 081510.
(250) Li, Y.; He, X.-L.; Ding, B.; Gao, L.-L.; Yang, G.-J.; Li, C.-X.; Li, C.-J. Realizing Full Coverage of Perovskite Film on Substrate Surface during Solution Processing: Characterization and Elimination of Uncovered Surface. *J. Power Sources* **2016**, *320*, 204−211.
(251) Wang, Q.; Shao, Y.; Dong, Q.; Xiao, Z.; Yuan, Y.; Huang, J. Large Fill-Factor Bilayer Iodine Perovskite Solar Cells Fabricated by a Low-Temperature Solution-Process. *Energy Environ. Sci.* **2014**, *7*, 2359−2365.
(252) Munir, R.; Sheikh, A. D.; Abdelsamie, M.; Hu, H.; Yu, L.; Zhao, K.; Kim, T.; El Tall, O.; Li, R.; Smilgies, D.-M.; et al. Hybrid Perovskite Thin-Film Photovoltaics: In Situ Diagnostics and Importance of the Precursor Solvate Phases. *Adv. Mater.* **2017**, *29*, 1604113.
(253) Li, Y.; Zhao, Z.; Lin, F.; Cao, X.; Cui, X.; Wei, J. In Situ Observation of Crystallization of Methylammonium Lead Iodide Perovskite from Microdroplets. *Small* **2017**, *13*, 1604125.
(254) Ding, B.; Gao, L.; Liang, L.; Chu, Q.; Song, X.; Li, Y.; Yang, G.; Fan, B.; Wang, M.; Li, C.; et al. Facile and Scalable Fabrication of Highly Efficient Lead Iodide Perovskite Thin-Film Solar Cells in Air Using Gas Pump Method. *ACS Appl. Mater. Interfaces* **2016**, *8*, 20067−20073.
(255) Li, X.; Bi, D.; Yi, C.; Decoppet, J.-D.; Luo, J.; Zakeeruddin, S. M.; Hagfeldt, A.; Grätzel, M. A Vacuum Flash−Assisted Solution Process for High-Efficiency Large-Area Perovskite Solar Cells. *Science* **2016**, *353*, 58−62.
(256) Hendriks, K. H.; van Franeker, J. J.; Bruijnaers, B. J.; Anta, J. A.; Wienk, M. M.; Janssen, R. A. J. 2-Methoxyethanol as a New Solvent for Processing Methylammonium Lead Halide Perovskite Solar Cells. *J. Mater. Chem. A* **2017**, *5*, 2346−2354.
(257) Noel, N. K.; Habisreutinger, S. N.; Wenger, B.; Klug, M. T.; Hörantner, M. T.; Johnston, M. B.; Nicholas, R. J.; Moore, D. T.; Snaith, H. J. A Low Viscosity, Low Boiling Point, Clean Solvent System for the Rapid Crystallisation of Highly Specular Perovskite Films. *Energy Environ. Sci.* **2017**, *10*, 145−152.
(258) Nie, W.; Tsai, H.; Asadpour, R.; Blancon, J.-C.; Neukirch, A. J.; Gupta, G.; Crochet, J. J.; Chhowalla, M.; Tretiak, S.; Alam, M. A.; et al. High-Efficiency Solution-Processed Perovskite Solar Cells with Millimeter-Scale Grains. *Science* **2015**, *347*, 522−525.
(259) Bi, C.; Wang, Q.; Shao, Y.; Yuan, Y.; Xiao, Z.; Huang, J. Non-Wetting Surface-Driven High-Aspect-Ratio Crystalline Grain Growth for Efficient Hybrid Perovskite Solar Cells. *Nat. Commun.* **2015**, *6*, 7747.
(260) Eperon, G. E.; Burlakov, V. M.; Goriely, A.; Snaith, H. J. Neutral Color Semitransparent Microstructured Perovskite Solar Cells. *ACS Nano* **2014**, *8*, 591−598.
(261) Deng, Y.; Peng, E.; Shao, Y.; Xiao, Z.; Dong, Q.; Huang, J. Scalable Fabrication of Efficient Organolead Trihalide Perovskite Solar Cells with Doctor-Bladed Active Layers. *Energy Environ. Sci.* **2015**, *8*, 1544−1550.
(262) Liu, T.; Zhou, Y.; Hu, Q.; Chen, K.; Zhang, Y.; Yang, W.; Wu, J.; Ye, F.; Luo, D.; Zhu, K.; et al. Fabrication of Compact and Stable Perovskite Films with Optimized Precursor Composition in the Fast-Growing Procedure. *Sci. China Mater.* **2017**, *60*, 608−616.
(263) Deng, Y.; Wang, Q.; Yuan, Y.; Huang, J. Vividly Colorful Hybrid Perovskite Solar Cells by Doctor-Blade Coating with Perovskite Photonic Nanostructures. *Mater. Horiz.* **2015**, *2*, 578−583.
(264) Wu, W.-Q.; Wang, Q.; Fang, Y.; Shao, Y.; Tang, S.; Deng, Y.; Lu, H.; Liu, Y.; Li, T.; Yang, Z.; et al. Molecular Doping Enabled Scalable Blading of Efficient Hole-Transport-Layer-Free Perovskite Solar Cells. *Nat. Commun.* **2018**, *9*, 1625.
(265) Jeon, N. J.; Na, H.; Jung, E. H.; Yang, T.-Y.; Lee, Y. G.; Kim, G.; Shin, H.-W.; Seok, S. I.; Lee, J.; Seo, J. A Fluorene-Terminated Hole-Transporting Material for Highly Efficient and Stable Perovskite Solar Cells. *Nat. Energy* **2018**, *3*, 682−689.
(266) Ye, T.; Petrović, M.; Peng, S.; Yoong, J. L.; Vijila, C.; Ramakrishna, S. Enhanced Charge Carrier Transport and Device Performance Through Dual-Cesium Doping in Mixed-Cation Perovskite Solar Cells with Near Unity Free Carrier Ratios. *ACS Appl. Mater. Interfaces* **2017**, *9*, 2358−2368.
(267) Paek, S.; Schouwink, P.; Athanasopoulou, E. N.; Cho, K. T.; Grancini, G.; Lee, Y.; Zhang, Y.; Stellacci, F.; Nazeeruddin, M. K.; Gao, P. From Nano- to Micrometer Scale: The Role of Antisolvent Treatment on High Performance Perovskite Solar Cells. *Chem. Mater.* **2017**, *29*, 3490−3498.
(268) Bai, Y.; Xiao, S.; Hu, C.; Zhang, T.; Meng, X.; Li, Q.; Yang, Y.; Wong, K. S.; Chen, H.; Yang, S. A Pure and Stable Intermediate Phase is Key to Growing Aligned and Vertically Monolithic Perovskite Crystals for Efficient PIN Planar Perovskite Solar Cells with High Processibility and Stability. *Nano Energy* **2017**, *34*, 58−68.
(269) Tu, Y.; Wu, J.; He, X.; Guo, P.; Luo, H.; Liu, Q.; Lin, J.; Huang, M.; Huang, Y.; Fan, L.; et al. Controlled Growth of $CH_3NH_3PbI_3$ Films towards Efficient Perovskite Solar Cells by Varied-Stoichiometric Intermediate Adduct. *Appl. Surf. Sci.* **2017**, *403*, 572−577.
(270) Xiao, S.; Bai, Y.; Meng, X.; Zhang, T.; Chen, H.; Zheng, X.; Hu, C.; Qu, Y.; Yang, S. Unveiling a Key Intermediate in Solvent Vapor Postannealing to Enlarge Crystalline Domains of Organometal Halide Perovskite Films. *Adv. Funct. Mater.* **2017**, *27*, 1604944.
(271) Bu, T.; Wu, L.; Liu, X.; Yang, X.; Zhou, P.; Yu, X.; Qin, T.; Shi, J.; Wang, S.; Li, S.; et al. Synergic Interface Optimization with Green Solvent Engineering in Mixed Perovskite Solar Cells. *Adv. Energy Mater.* **2017**, *7*, 1700576.
(272) Liu, J.; Ozaki, M.; Yakumaru, S.; Handa, T.; Nishikubo, R.; Kanemitsu, Y.; Saeki, A.; Murata, Y.; Murdey, R.; Wakamiya, A. Lead-

DOI: 10.1021/acs.chemrev.8b00318
Chem. Rev. 2019, 119, 3193−3295

Free Solar Cells based on Tin Halide Perovskite Films with High Coverage and Improved Aggregation. *Angew. Chem., Int. Ed.* **2018**, *57*, 13221.
(273) Huang, F.; Dkhissi, Y.; Huang, W.; Xiao, M.; Benesperi, I.; Rubanov, S.; Zhu, Y.; Lin, X.; Jiang, L.; Zhou, Y.; et al. Gas-Assisted Preparation of Lead Iodide Perovskite Films Consisting of a Monolayer of Single Crystalline Grains for High Efficiency Planar Solar Cells. *Nano Energy* **2014**, *10*, 10−18.
(274) Zhang, M.; Yun, J. S.; Ma, Q.; Zheng, J.; Lau, C. F. J.; Deng, X.; Kim, J.; Kim, D.; Seidel, J.; Green, M. A.; et al. High-Efficiency Rubidium-Incorporated Perovskite Solar Cells by Gas Quenching. *ACS Energy Lett.* **2017**, *2*, 438−444.
(275) Zhou, Y.; Yang, M.; Game, O. S.; Wu, W.; Kwun, J.; Strauss, M. A.; Yan, Y.; Huang, J.; Zhu, K.; Padture, N. P. Manipulating Crystallization of Organolead Mixed-Halide Thin Films in Antisolvent Baths for Wide-Bandgap Perovskite Solar Cells. *ACS Appl. Mater. Interfaces* **2016**, *8*, 2232−2237.
(276) Eperon, G. E.; Leijtens, T.; Bush, K. A.; Prasanna, R.; Green, T.; Wang, J. T.-W.; McMeekin, D. P.; Volonakis, G.; Milot, R. L.; May, R.; et al. Perovskite-Perovskite Tandem Photovoltaics with Optimized Bandgaps. *Science* **2016**, *354*, 861.
(277) Yang, M.; Li, Z.; Reese, M. O.; Reid, O. G.; Kim, D. H.; Siol, S.; Klein, T. R.; Yan, Y.; Berry, J. J.; van Hest, M. F. A. M.; et al. Perovskite Ink with Wide Processing Window for Scalable High-Efficiency Solar Cells. *Nat. Energy* **2017**, *2*, 17038.
(278) Mei, A.; Li, X.; Liu, L.; Ku, Z.; Liu, T.; Rong, Y.; Xu, M.; Hu, M.; Chen, J.; Yang, Y.; et al. A Hole-Conductor-Free, Fully Printable Mesoscopic Perovskite Solar Cell with High Stability. *Science* **2014**, *345*, 295−298.
(279) Hou, X.; Hu, Y.; Liu, H.; Mei, A.; Li, X.; Duan, M.; Zhang, G.; Rong, Y.; Han, H. Effect of Guanidinium on Mesoscopic Perovskite Solar Cells. *J. Mater. Chem. A* **2017**, *5*, 73−78.
(280) Rong, Y.; Hou, X.; Hu, Y.; Mei, A.; Liu, L.; Wang, P.; Han, H. Synergy of Ammonium Chloride and Moisture on Perovskite Crystallization for Efficient Printable Mesoscopic Solar Cells. *Nat. Commun.* **2017**, *8*, 14555.
(281) Xu, X.; Liu, Z.; Zuo, Z.; Zhang, M.; Zhao, Z.; Shen, Y.; Zhou, H.; Chen, Q.; Yang, Y.; Wang, M. Hole Selective NiO Contact for Efficient Perovskite Solar Cells with Carbon Electrode. *Nano Lett.* **2015**, *15*, 2402−2408.
(282) Calió, L.; Momblona, C.; Gil-Escrig, L.; Kazim, S.; Sessolo, M.; Sastre-Santos, Á.; Bolink, H. J.; Ahmad, S. Vacuum Deposited Perovskite Solar Cells Employing Dopant-Free Triazatruxene as the Hole Transport Material. *Sol. Energy Mater. Sol. Cells* **2017**, *163*, 237−241.
(283) Lin, Q.; Armin, A.; Nagiri, R. C. R.; Burn, P. L.; Meredith, P. Electro-Optics of Perovskite Solar Cells. *Nat. Photonics* **2015**, *9*, 106−112.
(284) Momblona, C.; Gil-Escrig, L.; Bandiello, E.; Hutter, E. M.; Sessolo, M.; Lederer, K.; Blochwitz-Nimoth, J.; Bolink, H. J. Efficient Vacuum Deposited p-i-n and n-i-p Perovskite Solar Cells Employing Doped Charge Transport Layers. *Energy Environ. Sci.* **2016**, *9*, 3456−3463.
(285) Chen, C.-W.; Kang, H.-W.; Hsiao, S.-Y.; Yang, P.-F.; Chiang, K.-M.; Lin, H.-W. Efficient and Uniform Planar-Type Perovskite Solar Cells by Simple Sequential Vacuum Deposition. *Adv. Mater.* **2014**, *26*, 6647−6652.
(286) Pérez-Del-Rey, D.; Boix, P. P.; Sessolo, M.; Hadipour, A.; Bolink, H. J. Interfacial Modification for High Efficiency Vapor Phase Deposited Perovskite Solar Cells Based on Metal-Oxide Buffer Layer. *J. Phys. Chem. Lett.* **2018**, *9*, 1041−1046.
(287) Mitzi, D. B.; Prikas, M. T.; Chondroudis, K. Thin Film Deposition of Organic-Inorganic Hybrid Materials Using a Single Source Thermal Ablation Technique. *Chem. Mater.* **1999**, *11*, 542−544.
(288) Chondroudis, K.; Mitzi, D. B.; Brock, P. Effect of Thermal Annealing on the Optical and Morphological Properties of (AETH)-PbX_4 (X = Br, I) Perovskite Films Prepared Using Single Source Thermal Ablation. *Chem. Mater.* **2000**, *12*, 169−175.
(289) Mitzi, D. B.; Chondroudis, K.; Kagan, C. R. Design, Structure, and Optical Properties of Organic-Inorganic Perovskites Containing an Oligothiophene Chromophore. *Inorg. Chem.* **1999**, *38*, 6246−6256.
(290) Longo, G.; Gil-Escrig, L.; Degen, M. J.; Sessolo, M.; Bolink, H. J. Perovskite Solar Cells Prepared by Flash Evaporation. *Chem. Commun.* **2015**, *51*, 7376−7378.
(291) Bansode, U.; Naphade, R.; Game, O.; Agarkar, S.; Ogale, S. Hybrid Perovskite Films by a New Variant of Pulsed Excimer Laser Deposition: A Room-Temperature Dry Process. *J. Phys. Chem. C* **2015**, *119*, 9177−9185.
(292) Barraza, E. T.; Dunlap-Shohl, W. A.; Mitzi, D. B.; Stiff-Roberts, A. D. Deposition of Methylammonium Lead Triiodide by Resonant Infrared Matrix-Assisted Pulsed Laser Evaporation. *J. Electron. Mater.* **2018**, *47*, 917−926.
(293) Dunlap-Shohl, W. A.; Barraza, E. T.; Barrette, A.; Gundogdu, K.; Stiff-Roberts, A. D.; Mitzi, D. B. $MAPbI_3$ Solar Cells with Absorber Deposited by Resonant Infrared Matrix-Assisted Pulsed Laser Evaporation. *ACS Energy Lett.* **2018**, *3*, 270−275.
(294) Bansode, U.; Ogale, S. On-Axis Pulsed Laser Deposition of Hybrid Perovskite Films for Solar Cell and Broadband Photo-Sensor Applications. *J. Appl. Phys.* **2017**, *121*, 133107.
(295) Pate, R.; Stiff-Roberts, A. D. The Impact of Laser-Target Absorption Depth on the Surface and Internal Morphology of Matrix-Assisted Pulsed Laser Evaporated Conjugated Polymer Thin Films. *Chem. Phys. Lett.* **2009**, *477*, 406−410.
(296) Xiao, Y.; Han, G.; Zhou, H.; Wu, J. An Efficient Titanium Foil Based Perovskite Solar Cell: Using a Titanium Dioxide Nanowire Array Anode and Transparent Poly(3,4-ethylenedioxythiophene) Electrode. *RSC Adv.* **2016**, *6*, 2778−2784.
(297) Xiao, Y.; Han, G.; Wu, J.; Lin, J.-Y. Efficient Bifacial Perovskite Solar Cell Based on a Highly Transparent Poly(3,4-ethylenedioxythiophene) as the p-Type Hole-Transporting Material. *J. Power Sources* **2016**, *306*, 171−177.
(298) Chen, Y.-X.; Ge, Q.-Q.; Shi, Y.; Liu, J.; Xue, D.-J.; Ma, J.-Y.; Ding, J.; Yan, H.-J.; Hu, J.-S.; Wan, L. J. General Space-Confined On-Substrate Fabrication of Thickness-Adjustable Hybrid Perovskite Single-Crystalline Thin Films. *J. Am. Chem. Soc.* **2016**, *138*, 16196−16199.
(299) Chen, Z.; Dong, Q.; Liu, Y.; Bao, C.; Fang, Y.; Lin, Y.; Tang, S.; Wang, Q.; Xiao, X.; Bai, Y.; et al. Thin Single Crystal Perovskite Solar Cells to Harvest Below-Bandgap Light Absorption. *Nat. Commun.* **2017**, *8*, 1890.
(300) Li, T.; Dunlap-Shohl, W. A.; Han, Q.; Mitzi, D. B. Melt Processing of Hybrid Organic−Inorganic Lead Iodide Layered Perovskites. *Chem. Mater.* **2017**, *29*, 6200−6204.
(301) Mitzi, D. B.; Medeiros, D. R.; DeHaven, P. W. Low-Temperature Melt Processing of Organic-Inorganic Hybrid Films. *Chem. Mater.* **2002**, *14*, 2839−2841.
(302) Mitzi, D. Synthesis, Crystal Structure, and Optical and Thermal Properties of $(C_4H_9NH_3)_2MI_4$ (M = Ge, Sn, Pb). *Chem. Mater.* **1996**, *8*, 791−800.
(303) Harms, H. A.; Tetreault, N.; Pellet, N.; Bensimon, M.; Grätzel, M. Mesoscopic Photosystems for Solar Light Harvesting and Conversion: Facile and Reversible Transformation of Metal-Halide Perovskites. *Faraday Discuss.* **2014**, *176*, 251−269.
(304) Li, H.; Cao, K.; Cui, J.; Liu, S.; Qiao, X.; Shen, Y.; Wang, M. 14.7% Efficient Mesoscopic Perovskite Solar Cells Using Single Walled Carbon Nanotubes/Carbon Composite Counter Electrodes. *Nanoscale* **2016**, *8*, 6379−6385.
(305) Zhou, Y.; Yang, M.; Kwun, J.; Game, O. S.; Zhao, Y.; Pang, S.; Padture, N. P.; Zhu, K. Intercalation Crystallization of Phase-Pure α-$HC(NH_2)_2PbI_3$ upon Microstructurally Engineered PbI_2 Thin Films for Planar Perovskite Solar Cells. *Nanoscale* **2016**, *8*, 6265−6270.
(306) Im, J.-H.; Jang, I.-H.; Pellet, N.; Grätzel, M.; Park, N.-G. Growth of $CH_3NH_3PbI_3$ Cuboids with Controlled Size for High-Efficiency Perovskite Solar Cells. *Nat. Nanotechnol.* **2014**, *9*, 927−932.
(307) Xiao, L.; Xu, J.; Luan, J.; Zhang, B.; Tan, Z.; Yao, J.; Dai, S. Achieving Mixed Halide Perovskite via Halogen Exchange during

DOI: 10.1021/acs.chemrev.8b00318
Chem. Rev. 2019, 119, 3193−3295

Vapor-Assisted Solution Process for Efficient and Stable Perovskite Solar Cells. *Org. Electron.* **2017**, *50*, 33−42.
(308) Li, Y.; Cooper, J. K.; Buonsanti, R.; Giannini, C.; Liu, Y.; Toma, F. M.; Sharp, I. D. Fabrication of Planar Heterojunction Perovskite Solar Cells by Controlled Low-Pressure Vapor Annealing. *J. Phys. Chem. Lett.* **2015**, *6*, 493−499.
(309) Chen, J.; Xu, J.; Xiao, L.; Zhang, B.; Dai, S.; Yao, J. Mixed-Organic-Cation $(FA)_x(MA)_{1-x}PbI_3$ Planar Perovskite Solar Cells with 16.48% Efficiency via a Low-Pressure Vapor-Assisted Solution Process. *ACS Appl. Mater. Interfaces* **2017**, *9*, 2449−2458.
(310) Leyden, M. R.; Ono, L. K.; Raga, S. R.; Kato, Y.; Wang, S.; Qi, Y. High Performance Perovskite Solar Cells by Hybrid Chemical Vapor Deposition. *J. Mater. Chem. A* **2014**, *2*, 18742−18745.
(311) Leyden, M. R.; Lee, M. V.; Raga, S. R.; Qi, Y. Large Formamidinium Lead Trihalide Perovskite Solar Cells Using Chemical Vapor Deposition with High Reproducibility and Tunable Chlorine Concentrations. *J. Mater. Chem. A* **2015**, *3*, 16097−16103.
(312) Leyden, M. R.; Jiang, Y.; Qi, Y. Chemical Vapor Deposition Grown Formamidinium Perovskite Solar Modules with High Steady State Power and Thermal Stability. *J. Mater. Chem. A* **2016**, *4*, 13125−13132.
(313) Leyden, M. R.; Meng, L.; Jiang, Y.; Ono, L. K.; Qiu, L.; Juarez-Perez, E. J.; Qin, C.; Adachi, C.; Qi, Y. Methylammonium Lead Bromide Perovskite Light-Emitting Diodes by Chemical Vapor Deposition. *J. Phys. Chem. Lett.* **2017**, *8*, 3193−3198.
(314) Yin, J.; Qu, H.; Cao, J.; Tai, H.; Li, J.; Zheng, N. Vapor-Assisted Crystallization Control Toward High Performance Perovskite Photovoltaics with over 18% Efficiency in the Ambient Atmosphere. *J. Mater. Chem. A* **2016**, *4*, 13203−13210.
(315) Lee, W.-H.; Chen, C.-Y.; Li, C.-S.; Hsiao, S.-Y.; Tsai, W.-L.; Huang, M.-J.; Cheng, C.-H.; Wu, C.-I.; Lin, H.-W. Boosting Thin-Film Perovskite Solar Cell Efficiency through Vacuum-Deposited Sub-Nanometer Small-Molecule Electron Interfacial Layers. *Nano Energy* **2017**, *38*, 66−71.
(316) Chen, H.; Wei, Z.; Zheng, X.; Yang, S. A Scalable Electrodeposition Route to the Low-Cost, Versatile and Controllable Fabrication of Perovskite Solar Cells. *Nano Energy* **2015**, *15*, 216−226.
(317) Koza, J. A.; Hill, J. C.; Demster, A. C.; Switzer, J. A. Epitaxial Electrodeposition of Methylammonium Lead Iodide Perovskites. *Chem. Mater.* **2016**, *28*, 399−405.
(318) Luo, P.; Zhou, S.; Liu, Z.; Xia, W.; Sun, L.; Cheng, J.; Xu, C.; Lu, Y. A Novel Transformation Route from PbS to $CH_3NH_3PbI_3$ for Fabricating Curved and Large-Area Perovskite Films. *Chem. Commun.* **2016**, *52*, 11203−11206.
(319) Li, Z.; Klein, T. R.; Kim, D. H.; Yang, M.; Berry, J. J.; van Hest, M. F. A. M.; Zhu, K. Scalable Fabrication of Perovskite Solar Cells. *Nat. Rev. Mater.* **2018**, *3*, 18017.
(320) Kim, J. H.; Williams, S. T.; Cho, N.; Chueh, C.-C.; Jen, A. K.-Y. Enhanced Environmental Stability of Planar Heterojunction Perovskite Solar Cells Based on Blade-Coating. *Adv. Energy Mater.* **2015**, *5*, 1401229.
(321) Yang, Z.; Chueh, C.-C.; Zuo, F.; Kim, J. H.; Liang, P.-W.; Jen, A. K.-Y. High-Performance Fully Printable Perovskite Solar Cells via Blade-Coating Technique under the Ambient Condition. *Adv. Energy Mater.* **2015**, *5*, 1500328.
(322) Li, Y.-F.; Sheng, Y.-J.; Tsao, H.-K. Evaporation Stains: Suppressing the Coffee-Ring Effect by Contact Angle Hysteresis. *Langmuir* **2013**, *29*, 7802−7811.
(323) Gao, Y.; Tobing, L. Y. M.; Kiffer, A.; Zhang, D. H.; Dang, C.; Demir, H. V. Azimuthally Polarized, Circular Colloidal Quantum Dot Laser Beam Enabled by a Concentric Grating. *ACS Photonics* **2016**, *3*, 2255−2261.
(324) Deng, Y.; Zheng, X.; Bai, Y.; Wang, Q.; Zhao, J.; Huang, J. Surfactant-Controlled Ink Drying Enables High-Speed Deposition of Perovskite Films for Efficient Photovoltaic Modules. *Nat. Energy* **2018**, *3*, 560−566.
(325) Vak, D.; Hwang, K.; Faulks, A.; Jung, Y.-S.; Clark, N.; Kim, D.-Y.; Wilson, G. J.; Watkins, S. E. 3D Printer Based Slot-Die Coater as a Lab-to-Fab Translation Tool for Solution-Processed Solar Cells. *Adv. Energy Mater.* **2015**, *5*, 1401539.
(326) Hwang, K.; Jung, Y.-S.; Heo, Y.-J.; Scholes, F. H.; Watkins, S. E.; Subbiah, J.; Jones, D. J.; Kim, D.-Y.; Vak, D. Toward Large Scale Roll-to-Roll Production of Fully Printed Perovskite Solar Cells. *Adv. Mater.* **2015**, *27*, 1241−1247.
(327) Schmidt, T. M.; Larsen-Olsen, T. T.; Carlé, J. E.; Angmo, D.; Krebs, F. C. Upscaling of Perovskite Solar Cells: Fully Ambient Roll Processing of Flexible Perovskite Solar Cells with Printed Back Electrodes. *Adv. Energy Mater.* **2015**, *5*, 1500569.
(328) Cotella, G.; Baker, J.; Worsley, D.; De Rossi, F.; Pleydell-Pearce, C.; Carnie, M.; Watson, T. One-Step Deposition by Slot-Die Coating of Mixed Lead Halide Perovskite for Photovoltaic Applications. *Sol. Energy Mater. Sol. Cells* **2017**, *159*, 362−369.
(329) He, M.; Li, B.; Cui, X.; Jiang, B.; He, Y.; Chen, Y.; O'Neil, D.; Szymanski, P.; Ei-Sayed, M. A.; Huang, J.; et al. Meniscus-Assisted Solution Printing of Large-Grained Perovskite Films for High-Efficiency Solar Cells. *Nat. Commun.* **2017**, *8*, 16045.
(330) Ye, F.; Chen, H.; Xie, F.; Tang, W.; Yin, M.; He, J.; Bi, E.; Wang, Y.; Yang, X.; Han, L. Soft-Cover Deposition of Scaling-Up Uniform Perovskite Thin Films for High Cost-Performance Solar Cells. *Energy Environ. Sci.* **2016**, *9*, 2295−2301.
(331) Barrows, A. T.; Pearson, A. J.; Kwak, C. K.; Dunbar, A. D. F.; Buckley, A. R.; Lidzey, D. G. Efficient Planar Heterojunction Mixed-Halide Perovskite Solar Cells Deposited via Spray-Deposition. *Energy Environ. Sci.* **2014**, *7*, 2944−2950.
(332) Heo, J. H.; Lee, M. H.; Jang, M. H.; Im, S. H. Highly efficient $CH_3NH_3PbI_{3-x}Cl_x$ Mixed Halide Perovskite Solar Cells Prepared by Re-dissolution and Crystal Grain Growth via Spray Coating. *J. Mater. Chem. A* **2016**, *4*, 17636−17642.
(333) Peng, X.; Yuan, J.; Shen, S.; Gao, M.; Chesman, A. S. R.; Yin, H.; Cheng, J.; Zhang, Q.; Angmo, D. Perovskite and Organic Solar Cells Fabricated by Inkjet Printing: Progress and Prospects. *Adv. Funct. Mater.* **2017**, *27*, 1703704.
(334) Li, S.-G.; Jiang, K.-J.; Su, M.-J.; Cui, X.-P.; Huang, J.-H.; Zhang, Q.-Q.; Zhou, X.-Q.; Yang, L.-M.; Song, Y.-L. Inkjet Printing of $CH_3NH_3PbI_3$ on a Mesoscopic TiO_2 Film for Highly Efficient Perovskite Solar Cells. *J. Mater. Chem. A* **2015**, *3*, 9092−9097.
(335) Mathies, F.; Abzieher, T.; Hochstuhl, A.; Glaser, K.; Colsmann, A.; Paetzold, U. W.; Hernandez-Sosa, G.; Lemmer, U.; Quintilla, A. Multipass Inkjet Printed Planar Methylammonium Lead Iodide Perovskite Solar Cells. *J. Mater. Chem. A* **2016**, *4*, 19207−19213.
(336) Liang, C.; Li, P.; Gu, H.; Zhang, Y.; Li, F.; Song, Y.; Shao, G.; Mathews, N.; Xing, G. One-Step Inkjet Printed Perovskite in Air for Efficient Light Harvesting. *Solar RRL* **2018**, *2*, 1700217.
(337) Berry, J. J.; van de Lagemaat, J.; Al-Jassim, M. M.; Kurtz, S.; Yan, Y.; Zhu, K. Perovskite Photovoltaics: The Path to a Printable Terawatt-Scale Technology. *ACS Energy Lett.* **2017**, *2*, 2540−2544.
(338) Christians, J. A.; Schulz, P.; Tinkham, J. S.; Schloemer, T. H.; Harvey, S. P.; Tremolet de Villers, B. J.; Sellinger, A.; Berry, J. J.; Luther, J. M. Tailored Interfaces of Unencapsulated Perovskite Solar Cells for >1,000 h Operational Stability. *Nat. Energy* **2018**, *3*, 68−74.
(339) Gil-Escrig, L.; Momblona, C.; La-Placa, M.-G.; Boix, P. P.; Sessolo, M.; Bolink, H. J. Vacuum Deposited Triple-Cation Mixed-Halide Perovskite Solar Cells. *Adv. Energy Mater.* **2018**, *8*, 1703506.
(340) Zhu, W.; Bao, C.; Wang, Y.; Li, F.; Zhou, X.; Yang, J.; Lv, B.; Wang, X.; Yu, T.; Zou, Z. Coarsening of One-Step Deposited Organolead Triiodide Perovskite Films via Ostwald Ripening for High Efficiency Planar-Heterojunction Solar Cells. *Dalton Trans.* **2016**, *45*, 7856−7865.
(341) Zhou, Q.; Jin, Z.; Li, H.; Wang, J. Enhancing Performance and Uniformity of $CH_3NH_3PbI_{3-x}Cl_x$ Perovskite Solar Cells by Air-Heated-Oven Assisted Annealing under Various Humidities. *Sci. Rep.* **2016**, *6*, 21257.
(342) Troughton, J.; Carnie, M. J.; Davies, M. L.; Charbonneau, C.; Jewell, E. H.; Worsley, D. A.; Watson, T. M. Photonic Flash-Annealing of Lead Halide Perovskite Solar Cells in 1 ms. *J. Mater. Chem. A* **2016**, *4*, 3471−3476.

DOI: 10.1021/acs.chemrev.8b00318
Chem. Rev. 2019, 119, 3193−3295

(343) Lavery, B. W.; Kumari, S.; Konermann, H.; Draper, G. L.; Spurgeon, J.; Druffel, T. Intense Pulsed Light Sintering of $CH_3NH_3PbI_3$ Solar Cells. *ACS Appl. Mater. Interfaces* **2016**, *8*, 8419−8426.
(344) Pool, V. L.; Dou, B.; Van Campen, D. G.; Klein-Stockert, T. R.; Barnes, F. S.; Shaheen, S. E.; Ahmad, M. I.; van Hest, M. F. A. M. M.; Toney, M. F. Thermal Engineering of $FAPbI_3$ Perovskite Material via Radiative Thermal Annealing and In Situ XRD. *Nat. Commun.* **2017**, *8*, 14075.
(345) Druffel, T.; Dharmadasa, R.; Lavery, B. W.; Ankireddy, K. Intense Pulsed Light Processing for Photovoltaic Manufacturing. *Sol. Energy Mater. Sol. Cells* **2018**, *174*, 359−369.
(346) Troughton, J.; Charbonneau, C.; Carnie, M. J.; Davies, M. L.; Worsley, D. A.; Watson, T. A. Rapid Processing of Perovskite Solar Cells in Under 2.5 seconds. *J. Mater. Chem. A* **2015**, *3*, 9123−9127.
(347) Hooper, K.; Carnie, M.; Charbonneau, C.; Watson, T. Near Infrared Radiation as a Rapid Heating Technique for TiO_2 Films on Glass Mounted Dye Sensitized Solar Cells. *Int. J. Photoenergy* **2014**, *2014*, 953623.
(348) Sanchez, S.; Hua, X.; Phung, N.; Steiner, U.; Abate, A. Flash Infrared Annealing for Anti-Solvent-Free Highly Efficient Perovskite Solar Cells. *Adv. Energy Mater.* **2018**, *8*, 1702915.
(349) Amendola, V.; Fortunati, I.; Marega, C.; Abdelhady, A. L.; Saidaminov, M. I.; Bakr, O. M. High-Purity Hybrid Organolead Halide Perovskite Nanoparticles Obtained by Pulsed-Laser Irradiation in Liquid. *ChemPhysChem* **2017**, *18*, 1047−1054.
(350) Jeon, T.; Jin, H. M.; Lee, S. H.; Lee, J. M.; Park, H. I.; Kim, M. K.; Lee, K. J.; Shin, B.; Kim, S. O. Laser Crystallization of Organic−Inorganic Hybrid Perovskite Solar Cells. *ACS Nano* **2016**, *10*, 7907−7914.
(351) Dou, B.; Pool, V. L.; Toney, M. F.; van Hest, M. F. A. M. Radiative Thermal Annealing/in Situ X-ray Diffraction Study of Methylammonium Lead Triiodide: Effect of Antisolvent, Humidity, Annealing Temperature Profile, and Film Substrates. *Chem. Mater.* **2017**, *29*, 5931−5941.
(352) Cao, Q.; Yang, S.; Gao, Q.; Lei, L.; Yu, Y.; Shao, J.; Liu, Y. Fast and Controllable Crystallization of Perovskite Films by Microwave Irradiation Process. *ACS Appl. Mater. Interfaces* **2016**, *8*, 7854−7861.
(353) Xiao, Z.; Dong, Q.; Bi, C.; Shao, Y.; Yuan, Y.; Huang, J. Solvent Annealing of Perovskite-Induced Crystal Growth for Photovoltaic-Device Efficiency Enhancement. *Adv. Mater.* **2014**, *26*, 6503−6509.
(354) Sinturel, C.; Vayer, M.; Morris, M.; Hillmyer, M. A. Solvent Vapor Annealing of Block Polymer Thin Films. *Macromolecules* **2013**, *46*, 5399−5415.
(355) Liu, J.; Gao, C.; He, X.; Ye, Q.; Ouyang, L.; Zhuang, D.; Liao, C.; Mei, J.; Lau, W. Improved Crystallization of Perovskite Films by Optimized Solvent Annealing for High Efficiency Solar Cell. *ACS Appl. Mater. Interfaces* **2015**, *7*, 24008−24015.
(356) Liu, C.; Wang, K.; Yi, C.; Shi, X.; Smith, A. W.; Gong, X.; Heeger, A. J. Efficient Perovskite Hybrid Photovoltaics via Alcohol-Vapor Annealing Treatment. *Adv. Funct. Mater.* **2016**, *26*, 101−110.
(357) Sun, X.; Zhang, C.; Chang, J.; Yang, H.; Xi, H.; Lu, G.; Chen, D.; Lin, Z.; Lu, X.; Zhang, J.; et al. Mixed-Solvent-Vapor Annealing of Perovskite for Photovoltaic Device Efficiency Enhancement. *Nano Energy* **2016**, *28*, 417−425.
(358) Xie, F. X.; Zhang, D.; Su, H.; Ren, X.; Wong, K. S.; Grätzel, M.; Choy, W. C. H. Vacuum-Assisted Thermal Annealing of $CH_3NH_3PbI_3$ for Highly Stable and Efficient Perovskite Solar Cells. *ACS Nano* **2015**, *9*, 639−646.
(359) Gao, L.-L.; Liang, L.-S.; Song, X.-X.; Ding, B.; Yang, G.-J.; Fan, B.; Li, C.-X.; Li, C.-J. Preparation of Flexible Perovskite Solar Cells by a Gas Pump Drying Method on a Plastic Substrate. *J. Mater. Chem. A* **2016**, *4*, 3704−3710.
(360) Yang, M.; Zhang, T.; Schulz, P.; Li, Z.; Li, G.; Kim, D. H.; Guo, N.; Berry, J. J.; Zhu, K.; Zhao, Y. Facile Fabrication of Large-Grain $CH_3NH_3PbI_{3-x}Br_x$ Films for High-Efficiency Solar Cells via CH_3NH_3Br-Selective Ostwald Ripening. *Nat. Commun.* **2016**, *7*, 12305.
(361) Dualeh, A.; Gao, P.; Seok, S. I.; Nazeeruddin, M. K.; Grätzel, M. Thermal Behavior of Methylammonium Lead-Trihalide Perovskite Photovoltaic Light Harvesters. *Chem. Mater.* **2014**, *26*, 6160−6164.
(362) Khadka, D. B.; Shirai, Y.; Yanagida, M.; Masuda, T.; Miyano, K. Enhancement in Efficiency and Optoelectronic Quality of Perovskite Thin Films Annealed in MACl Vapor. *Sustainable Energy Fuels* **2017**, *1*, 755−766.
(363) Tosun, B. S.; Hillhouse, H. W. Enhanced Carrier Lifetimes of Pure Iodide Hybrid Perovskite via Vapor-Equilibrated Re-Growth (VERG). *J. Phys. Chem. Lett.* **2015**, *6*, 2503−2508.
(364) Xie, F.; Chen, C.-C.; Wu, Y.; Li, X.; Cai, M.; Liu, X.; Yang, X.; Han, L. Vertical Recrystallization for Highly Efficient and Stable Formamidinium-Based Inverted-Structure Perovskite Solar Cells. *Energy Environ. Sci.* **2017**, *10*, 1942−1949.
(365) Zhao, T.; Williams, S. T.; Chueh, C.-C.; deQuilettes, D. W.; Liang, P.-W.; Ginger, D. S.; Jen, A. K.-Y. Design Rules for the Broad Application of Fast (<1 s) Methylamine Vapor Based, Hybrid Perovskite Post Deposition Treatments. *RSC Adv.* **2016**, *6*, 27475−27484.
(366) Jacobs, D. L.; Zang, L. Thermally Induced Recrystallization of $MAPbI_3$ Perovskite under Methylamine Atmosphere: An Approach to Fabricating Large Uniform Crystalline Grains. *Chem. Commun.* **2016**, *52*, 10743−10746.
(367) Zhao, Y.; Zhu, K. Optical Bleaching of Perovskite $CH_3NH_3PbI_3$ Through Room-Temperature Phase Transformation Induced by Ammonia. *Chem. Commun.* **2014**, *50*, 1605−1607.
(368) Jiang, Y.; Juarez-Perez, E. J.; Ge, Q.; Wang, S.; Leyden, M. R.; Ono, L. K.; Raga, S. R.; Hu, J.; Qi, Y. Post-Annealing of $MAPbI_3$ Perovskite Films with Methylamine for Efficient Perovskite Solar Cells. *Mater. Horiz.* **2016**, *3*, 548−555.
(369) Chang, Y.; Wang, L.; Zhang, J.; Zhou, Z.; Li, C.; Chen, B.; Etgar, L.; Cui, G.; Pang, S. CH_3NH_2 Gas Induced (110) Preferred Cesium-Containing Perovskite Films with Reduced PbI_6 Octahedron Distortion and Enhanced Moisture Stability. *J. Mater. Chem. A* **2017**, *5*, 4803−4808.
(370) Jain, S. M.; Qiu, Z.; Häggman, L.; Mirmohades, M.; Johansson, M. B.; Edvinsson, T.; Boschloo, G. Frustrated Lewis Pair-Mediated Recrystallization of $CH_3NH_3PbI_3$ for Improved Optoelectronic Quality and High Voltage Planar Perovskite Solar Cells. *Energy Environ. Sci.* **2016**, *9*, 3770−3782.
(371) Noel, N. K.; Abate, A.; Stranks, S. D.; Parrott, E.; Burlakov, V.; Goriely, A.; Snaith, H. J. Enhanced Photoluminescence and Solar Cell Performance via Lewis Base Passivation of Organic-Inorganic Lead Halide Perovskites. *ACS Nano* **2014**, *8*, 9815−9821.
(372) Ahmed, G. H.; Yin, J.; Bose, R.; Sinatra, L.; Alarousu, E.; Yengel, E.; AlYami, N. M.; Saidaminov, M. I.; Zhang, Y.; Hedhili, M. N.; et al. Pyridine-Induced Dimensionality Change in Hybrid Perovskite Nanocrystals. *Chem. Mater.* **2017**, *29*, 4393−4400.
(373) Zhou, Y.; Yang, M.; Pang, S.; Zhu, K.; Padture, N. P. Exceptional Morphology-Preserving Evolution of Formamidinium Lead Triiodide Perovskite Thin Films via Organic-Cation Displacement. *J. Am. Chem. Soc.* **2016**, *138*, 5535−5538.
(374) Wang, F.; Geng, W.; Zhou, Y.; Fang, H.-H.; Tong, C.-J.; Loi, M. A.; Liu, L.-M.; Zhao, N. Phenylalkylamine Passivation of Organolead Halide Perovskites Enabling High-Efficiency and Air-Stable Photovoltaic Cells. *Adv. Mater.* **2016**, *28*, 9986−9992.
(375) Ji, F.; Wang, L.; Pang, S.; Gao, P.; Xu, H.; Xie, G.; Zhang, J.; Cui, G. A Balanced Cation Exchange Reaction toward Highly Uniform and Pure Phase $FA_{1-x}MA_xPbI_3$ Perovskite Films. *J. Mater. Chem. A* **2016**, *4*, 14437−14443.
(376) Eperon, G. E.; Ginger, D. S. B-Site Metal Cation Exchange in Halide Perovskites. *ACS Energy Lett.* **2017**, *2*, 1190−1196.
(377) Jang, D. M.; Park, K.; Kim, D. H.; Park, J.; Shojaei, F.; Kang, H. S.; Ahn, J.-P.; Lee, J. W.; Song, J. K. Reversible Halide Exchange Reaction of Organometal Trihalide Perovskite Colloidal Nanocrystals for Full-Range Band Gap Tuning. *Nano Lett.* **2015**, *15*, 5191−5199.

DOI: 10.1021/acs.chemrev.8b00318
Chem. Rev. 2019, 119, 3193−3295

(378) Beberwyck, B. J.; Surendranath, Y.; Alivisatos, A. P. Cation Exchange: A Versatile Tool for Nanomaterials Synthesis. *J. Phys. Chem. C* **2013**, *117*, 19759−19770.
(379) De Trizio, L.; Manna, L. Forging Colloidal Nanostructures via Cation Exchange Reactions. *Chem. Rev.* **2016**, *116*, 10852−10887.
(380) Game, O. S.; Buchsbaum, G. J.; Zhou, Y.; Padture, N. P.; Kingon, A. I. Ions Matter: Description of the Anomalous Electronic Behavior in Methylammonium Lead Halide Perovskite Devices. *Adv. Funct. Mater.* **2017**, *27*, 1606584.
(381) Eames, C.; Frost, J. M.; Barnes, P. R.; O'Regan, B. C.; Walsh, A.; Islam, M. S. Ionic Transport in Hybrid Lead Iodide Perovskite Solar Cells. *Nat. Commun.* **2015**, *6*, 7497.
(382) Pellet, N.; Teuscher, J.; Maier, J.; Grätzel, M. Transforming Hybrid Organic Inorganic Perovskites by Rapid Halide Exchange. *Chem. Mater.* **2015**, *27*, 2181−2188.
(383) Hills-Kimball, K.; Nagaoka, Y.; Cao, C.; Chaykovsky, E.; Chen, O. Synthesis of Formamidinium Lead Halide Perovskite Nanocrystals Through Solid−Liquid−Solid Cation Exchange. *J. Mater. Chem. C* **2017**, *5*, 5680−5684.
(384) Guhrenz, C.; Benad, A.; Ziegler, C.; Haubold, D.; Gaponik, N.; Eychmuller, A. Solid-State Anion Exchange Reactions for Color Tuning of $CsPbX_3$ Perovskite Nanocrystals. *Chem. Mater.* **2016**, *28*, 9033−9040.
(385) Chen, K.; Deng, X.; Goddard, R.; Tuysuz, H. Pseudomorphic Transformation of Organometal Halide Perovskite Using the Gaseous Hydrogen Halide Reaction. *Chem. Mater.* **2016**, *28*, 5530−5537.
(386) Eperon, G. E.; Beck, C. E.; Snaith, H. J. Cation Exchange for Thin Film Lead Iodide Perovskite Interconversion. *Mater. Horiz.* **2016**, *3*, 63−71.
(387) Zhou, Z.; Pang, S.; Ji, F.; Zhang, B.; Cui, G. The Fabrication of Formamidinium Lead Iodide Perovskite Thin Films via Organic Cation Exchange. *Chem. Commun.* **2016**, *52*, 3828−3831.
(388) Li, G.; Zhang, T.; Guo, N.; Xu, F.; Qian, X.; Zhao, Y. Ion-Exchange-Induced 2D−3D Conversion of $HMA_{1-x}FA_xPbI_3Cl$ Perovskite into a High-Quality $MA_{1-x}FA_xPbI_3$ Perovskite. *Angew. Chem., Int. Ed.* **2016**, *55*, 13460−13464.
(389) Xiao, J.; Yang, Y.; Xu, X.; Shi, J.; Zhu, L.; Lv, S.; Wu, H.; Luo, Y.; Li, D.; Meng, Q. Pressure-Assisted $CH_3NH_3PbI_3$ Morphology Reconstruction to Improve the High Performance of Perovskite Solar Cells. *J. Mater. Chem. A* **2015**, *3*, 5289−5293.
(390) Abdollahi Nejand, B.; Gharibzadeh, S.; Ahmadi, V.; Shahverdi, H. R. New Scalable Cold-Roll Pressing for Post-treatment of Perovskite Microstructure in Perovskite Solar Cells. *J. Phys. Chem. C* **2016**, *120*, 2520−2528.
(391) Abdollahi Nejand, B.; Gharibzadeh, S.; Ahmadi, V.; Shahverdi, H. R. Novel Solvent-Free Perovskite Deposition in Fabrication of Normal and Inverted Architectures of Perovskite Solar Cells. *Sci. Rep.* **2016**, *6*, 33649.
(392) Zhu, W.; Kang, L.; Yu, T.; Lv, B.; Wang, Y.; Chen, X.; Wang, X.; Zhou, Y.; Zou, Z. Facile Face-Down Annealing Triggered Remarkable Texture Development in $CH_3NH_3PbI_3$ Films for High-Performance Perovskite Solar Cells. *ACS Appl. Mater. Interfaces* **2017**, *9*, 6104−6113.
(393) Roldán-Carmona, C.; Gratia, P.; Zimmermann, I.; Grancini, G.; Gao, P.; Graetzel, M.; Nazeeruddin, M. K. High Efficiency Methylammonium Lead Triiodide Perovskite Solar Cells: the Relevance of Non-Stoichiometric Precursors. *Energy Environ. Sci.* **2015**, *8*, 3550−3556.
(394) Han, Q.; Ding, J.; Bai, Y.; Li, T.; Ma, J.-Y.; Chen, Y.-X.; Zhou, Y.; Liu, J.; Ge, Q.-Q.; Chen, J.; et al. Carrier Dynamics Engineering for High-Performance Electron-Transport-Layer-Free Perovskite Photovoltaics. *Chem.* **2018**, *4*, 2405.
(395) Park, B.-W.; Kedem, N.; Kulbak, M.; Lee, D. Y.; Yang, W. S.; Jeon, N. J.; Seo, J.; Kim, G.; Kim, K. J.; Shin, T. J.; et al. Understanding how Excess Lead Iodide Precursor Improves Halide Perovskite Solar Cell Performance. *Nat. Commun.* **2018**, *9*, 3301.
(396) Liu, F.; Dong, Q.; Wong, M. K.; Djurišić, A. B.; Ng, A.; Ren, Z.; Shen, Q.; Surya, C.; Chan, W. K.; Wang, J.; et al. Is Excess PbI_2 Beneficial for Perovskite Solar Cell Performance? *Adv. Energy Mater.* **2016**, *6*, 1502206.
(397) Schoonman, J. Organic−Inorganic Lead Halide Perovskite Solar Cell Materials: A Possible Stability Problem. *Chem. Phys. Lett.* **2015**, *619*, 193−195.
(398) Wang, S.; Jiang, Y.; Juarez-Perez, E. J.; Ono, L. K.; Qi, Y. Accelerated Degradation of Methylammonium Lead Iodide Perovskites Induced by Exposure to Iodine Vapour. *Nat. Energy* **2017**, *2*, 16195.
(399) Son, D.-Y.; Lee, J.-W.; Choi, Y. J.; Jang, I.-H.; Lee, S.; Yoo, P. J.; Shin, H.; Ahn, N.; Choi, M.; Kim, D.; et al. Self-Formed Grain Boundary Healing Layer for Highly Efficient $CH_3NH_3PbI_3$ Perovskite Solar Cells. *Nat. Energy* **2016**, *1*, 16081.
(400) Khlyabich, P. P.; Loo, Y.-L. Crystalline Intermediates and Their Transformation Kinetics during the Formation of Methylammonium Lead Halide Perovskite Thin Films. *Chem. Mater.* **2016**, *28*, 9041−9048.
(401) Manser, J. S.; Reid, B.; Kamat, P. V. Evolution of Organic−Inorganic Lead Halide Perovskite from Solid-State Iodoplumbate Complexes. *J. Phys. Chem. C* **2015**, *119*, 17065−17073.
(402) Sharenko, A.; Mackeen, C.; Jewell, L.; Bridges, F.; Toney, M. F. Evolution of Iodoplumbate Complexes in Methylammonium Lead Iodide Perovskite Precursor Solutions. *Chem. Mater.* **2017**, *29*, 1315−1320.
(403) Stamplecoskie, K. G.; Manser, J. S.; Kamat, P. V. Dual Nature of the Excited State in Organic−Inorganic Lead Halide Perovskites. *Energy Environ. Sci.* **2015**, *8*, 208−215.
(404) Cao, J.; Jing, X.; Yan, J.; Hu, C.; Chen, R.; Yin, J.; Li, J.; Zheng, N. Identifying the Molecular Structures of Intermediates for Optimizing the Fabrication of High-Quality Perovskite Films. *J. Am. Chem. Soc.* **2016**, *138*, 9919−9926.
(405) Vincent, B. V.; Robertson, K. N.; Cameron, T. S.; Knop, O. Alkylammonium Lead Halides. Part 1. Isolated PbI_6^{4-} Ions in $(CH_3NH_3)_4PbI_6$-$2H_2O$. *Can. J. Chem.* **1987**, *65*, 1042−1046.
(406) Moore, D. T.; Sai, H.; Tan, K. W.; Estroff, L. A.; Wiesner, U. Impact of the Organic Halide Salt on Final Perovskite Composition for Photovoltaic Applications. *APL Mater.* **2014**, *2*, 081802.
(407) Zhang, W.; Saliba, M.; Moore, D. T.; Pathak, S. K.; Hörantner, M. T.; Stergiopoulos, T.; Stranks, S. D.; Eperon, G. E.; Alexander-Webber, J. A.; Abate, A.; et al. Ultrasmooth Organic-Inorganic Perovskite Thin-Film Formation and Crystallization for Efficient Planar Heterojunction Solar Cells. *Nat. Commun.* **2015**, *6*, 6142.
(408) Bai, S.; Sakai, N.; Zhang, W.; Wang, Z.; Wang, J. T.-W.; Gao, F.; Snaith, H. J. Reproducible Planar Heterojunction Solar Cells Based on One-Step Solution-Processed Methylammonium Lead Halide Perovskites. *Chem. Mater.* **2017**, *29*, 462−473.
(409) Zhao, L.; Luo, D.; Wu, J.; Hu, Q.; Zhang, W.; Chen, K.; Liu, T.; Liu, Y.; Zhang, Y.; Liu, F.; et al. High-Performance Inverted Planar Heterojunction Perovskite Solar Cells Based on Lead Acetate Precursor with Efficiency Exceeding 18%. *Adv. Funct. Mater.* **2016**, *26*, 3508−3514.
(410) Luo, D.; Zhao, L.; Wu, J.; Hu, Q.; Zhang, Y.; Xu, Z.; Liu, Y.; Liu, T.; Chen, K.; Yang, W.; et al. Dual-Source Precursor Approach for Highly Efficient Inverted Planar Heterojunction Perovskite Solar Cells. *Adv. Mater.* **2017**, *29*, 1604758.
(411) Ball, J. M.; Lee, M. M.; Hey, A.; Snaith, H. J. Low-Temperature Processed Meso-Superstructured to Thin-Film Perovskite Solar Cells. *Energy Environ. Sci.* **2013**, *6*, 1739−1743.
(412) Suarez, B.; Gonzalez-Pedro, V.; Ripolles, T. S.; Sanchez, R. S.; Otero, L.; Mora-Sero, I. Recombination Study of Combined Halides (Cl, Br, I) Perovskite Solar Cells. *J. Phys. Chem. Lett.* **2014**, *5*, 1628−1635.
(413) Grancini, G.; Marras, S.; Prato, M.; Giannini, C.; Quarti, C.; De Angelis, F.; De Bastiani, M.; Eperon, G. E.; Snaith, H. J.; Manna, L.; et al. The Impact of the Crystallization Processes on the Structural and Optical Properties of Hybrid Perovskite Films for Photovoltaics. *J. Phys. Chem. Lett.* **2014**, *5*, 3836−3842.
(414) Colella, S.; Mosconi, E.; Fedeli, P.; Listorti, A.; Gazza, F.; Orlandi, F.; Ferro, P.; Besagni, T.; Rizzo, A.; Calestani, G.; et al.

DOI: 10.1021/acs.chemrev.8b00318
Chem. Rev. 2019, 119, 3193−3295

$MAPbI_{3-x}Cl_x$ Mixed Halide Perovskite for Hybrid Solar Cells: The Role of Chloride as Dopant on the Transport and Structural Properties. *Chem. Mater.* **2013**, *25*, 4613−4618.
(415) Luo, Y.; Gamliel, S.; Nijem, S.; Aharon, S.; Holt, M.; Stripe, B.; Rose, V.; Bertoni, M. I.; Etgar, L.; Fenning, D. P. Spatially Heterogeneous Chlorine Incorporation in Organic−Inorganic Perovskite Solar Cells. *Chem. Mater.* **2016**, *28*, 6536−6543.
(416) Pool, V. L.; Gold-Parker, A.; McGehee, M. D.; Toney, M. F. Chlorine in $PbCl_2$-Derived Hybrid-Perovskite Solar Absorbers. *Chem. Mater.* **2015**, *27*, 7240−7243.
(417) Wang, Q.; Lyu, M.; Zhang, M.; Yun, J. H.; Chen, H.; Wang, L. Transition from the Tetragonal to Cubic Phase of Organohalide Perovskite: The Role of Chlorine in Crystal Formation of $CH_3NH_3PbI_3$ on TiO_2 Substrates. *J. Phys. Chem. Lett.* **2015**, *6*, 4379−4384.
(418) Dastidar, S.; Egger, D. A.; Tan, L. Z.; Cromer, S. B.; Dillon, A. D.; Liu, S.; Kronik, L.; Rappe, A. M.; Fafarman, A. T. High Chloride Doping Levels Stabilize the Perovskite Phase of Cesium Lead Iodide. *Nano Lett.* **2016**, *16*, 3563−3570.
(419) Eperon, G. E.; Burlakov, V. M.; Docampo, P.; Goriely, A.; Snaith, H. J. Morphological Control for High Performance, Solution-Processed Planar Heterojunction Perovskite Solar Cells. *Adv. Funct. Mater.* **2014**, *24*, 151−157.
(420) Saliba, M.; Tan, K. W.; Sai, H.; Moore, D. T.; Scott, T.; Zhang, W.; Estroff, L. A.; Wiesner, U.; Snaith, H. J. Influence of Thermal Processing Protocol upon the Crystallization and Photovoltaic Performance of Organic−Inorganic Lead Trihalide Perovskites. *J. Phys. Chem. C* **2014**, *118*, 17171−17177.
(421) Barrows, A. T.; Lilliu, S.; Pearson, A. J.; Babonneau, D.; Dunbar, A. D. F.; Lidzey, D. G. Monitoring the Formation of a $CH_3NH_3PbI_{3-x}Cl_x$ Perovskite during Thermal Annealing Using X-Ray Scattering. *Adv. Funct. Mater.* **2016**, *26*, 4934−4942.
(422) Eperon, G. E.; Habisreutinger, S. N.; Leijtens, T.; Bruijnaers, B. J.; van Franeker, J. J.; deQuilettes, D. W.; Pathak, S.; Sutton, R. J.; Grancini, G.; Ginger, D. S.; et al. The Importance of Moisture in Hybrid Lead Halide Perovskite Thin Film Fabrication. *ACS Nano* **2015**, *9*, 9380−9393.
(423) Gao, H.; Bao, C.; Li, F.; Yu, T.; Yang, J.; Zhu, W.; Zhou, X.; Fu, G.; Zou, Z. Nucleation and Crystal Growth of Organic−Inorganic Lead Halide Perovskites under Different Relative Humidity. *ACS Appl. Mater. Interfaces* **2015**, *7*, 9110−9117.
(424) You, J.; Yang, Y.; Hong, Z.; Song, T.-B.; Meng, L.; Liu, Y.; Jiang, C.; Zhou, H.; Chang, W.-H.; Li, G.; et al. Moisture Assisted Perovskite Film Growth for High Performance Solar Cells. *Appl. Phys. Lett.* **2014**, *105*, 183902.
(425) Williams, S. T.; Zuo, F.; Chueh, C.-C.; Liao, C.-Y.; Liang, P.-W.; Jen, A. K.-Y. Role of Chloride in the Morphological Evolution of Organo-Lead Halide Perovskite Thin Films. *ACS Nano* **2014**, *8*, 10640−10654.
(426) Nenon, D. P.; Christians, J. A.; Wheeler, L. M.; Blackburn, J. L.; Sanehira, E. M.; Dou, B.; Olsen, M. L.; Zhu, K.; Berry, J. J.; Luther, J. M. Structural and Chemical Evolution of Methylammonium Lead Halide Perovskites during Thermal Processing from Solution. *Energy Environ. Sci.* **2016**, *9*, 2072−2082.
(427) Yang, Y.; Feng, S.; Li, M.; Xu, W.; Yin, G.; Wang, Z.; Sun, B.; Gao, X. Annealing Induced Re-crystallization in $CH_3NH_3PbI_{3-x}Cl_x$ for High Performance Perovskite Solar Cells. *Sci. Rep.* **2017**, *7*, 46724.
(428) Chia, H.-C.; Sheu, H.-S.; Hsiao, Y.-Y.; Li, S.-S.; Lan, Y.-K.; Lin, C.-Y.; Chang, J.-W.; Kuo, Y.-C.; Chen, C.-H.; Weng, S.-C.; et al. Critical Intermediate Structure that Directs the Crystalline Texture and Surface Morphology of Organo-Lead Trihalide Perovskite. *ACS Appl. Mater. Interfaces* **2017**, *9*, 36897−36906.
(429) Dohner, E. R.; Jaffe, A.; Bradshaw, L. R.; Karunadasa, H. I. Intrinsic White-Light Emission from Layered Hybrid Perovskites. *J. Am. Chem. Soc.* **2014**, *136*, 13154−13157.
(430) Stone, K. H.; Gold-Parker, A.; Pool, V. L.; Unger, E. L.; Bowring, A. R.; McGehee, M. D.; Toney, M. F.; Tassone, C. J. Transformation from Crystalline Precursor to Perovskite in $PbCl_2$-Derived $MAPbI_3$. *Nat. Commun.* **2018**, *9*, 3458.
(431) Fan, L.; Ding, Y.; Luo, J.; Shi, B.; Yao, X.; Wei, C.; Zhang, D.; Wang, G.; Sheng, Y.; Chen, Y.; et al. Elucidating the Role of Chlorine in Perovskite Solar Cells. *J. Mater. Chem. A* **2017**, *5*, 7423−7432.
(432) Frost, J. M.; Butler, K. T.; Brivio, F.; Hendon, C. H.; van Schilfgaarde, M.; Walsh, A. Atomistic Origins of High Performance in Hybrid Halide Perovskite Solar Cells. *Nano Lett.* **2014**, *14*, 2584−2590.
(433) Buin, A.; Pietsch, P.; Xu, J.; Voznyy, O.; Ip, A. H.; Comin, R.; Sargent, E. H. Materials Processing Routes to Trap-Free Halide Perovskites. *Nano Lett.* **2014**, *14*, 6281−6286.
(434) Jodlowski, A. D.; Roldán-Carmona, C.; Grancini, G.; Salado, M.; Ralaiarisoa, M.; Ahmad, S.; Koch, N.; Camacho, L.; de Miguel, G.; Nazeeruddin, M. K. Large Guanidinium Cation Mixed with Methylammonium in Lead Iodide Perovskites for 19% Efficient Solar Cells. *Nat. Energy* **2017**, *2*, 972−979.
(435) Liao, W.; Zhao, D.; Yu, Y.; Shrestha, N.; Ghimire, K.; Grice, C. R.; Wang, C.; Xiao, Y.; Cimaroli, A. J.; Ellingson, R. J.; et al. Fabrication of Efficient Low-Bandgap Perovskite Solar Cells by Combining Formamidinium Tin Iodide with Methylammonium Lead Iodide. *J. Am. Chem. Soc.* **2016**, *138*, 12360−12363.
(436) Zhao, D.; Yu, Y.; Wang, C.; Liao, W.; Shrestha, N.; Grice, C. R.; Cimaroli, A. J.; Guan, L.; Ellingson, R. J.; Zhu, K.; et al. Low-Bandgap Mixed Tin−Lead Iodide Perovskite Absorbers with Long Carrier Lifetimes for All-Perovskite Tandem Solar Cells. *Nat. Energy* **2017**, *2*, 17018.
(437) Wozny, S.; Yang, M.; Nardes, A. M.; Mercado, C. C.; Ferrere, S.; Reese, M. O.; Zhou, W.; Zhu, K. Controlled Humidity Study on the Formation of Higher Efficiency Formamidinium Lead Triiodide-Based Solar Cells. *Chem. Mater.* **2015**, *27*, 4814−4820.
(438) Zhumekenov, A. A.; Saidaminov, M. I.; Haque, M. A.; Alarousu, E.; Sarmah, S. P.; Murali, B.; Dursun, I.; Miao, X.-H.; Abdelhady, A. L.; Wu, T.; et al. Formamidinium Lead Halide Perovskite Crystals with Unprecedented Long Carrier Dynamics and Diffusion Length. *ACS Energy Lett.* **2016**, *1*, 32−37.
(439) Li, W.-G.; Rao, H.-S.; Chen, B.-X.; Wang, X.-D.; Kuang, D.-B. A Formamidinium−Methylammonium Lead Iodide Perovskite Single Crystal Exhibiting Exceptional Optoelectronic Properties and Long-Term Stability. *J. Mater. Chem. A* **2017**, *5*, 19431−19438.
(440) McMeekin, D. P.; Sadoughi, G.; Rehman, W.; Eperon, G. E.; Saliba, M.; Hörantner, M. T.; Haghighirad, A.; Sakai, N.; Korte, L.; Rech, B.; et al. A Mixed-Cation Lead Mixed-Halide Perovskite Absorber for Tandem Solar Cells. *Science* **2016**, *351*, 151−155.
(441) Jiang, Q.; Zhang, L.; Wang, H.; Yang, X.; Meng, J.; Liu, H.; Yin, Z.; Wu, J.; Zhang, X.; You, J. Enhanced Electron Extraction Using SnO_2 for High-Efficiency Planar-Structure $HC(NH_2)_2PbI_3$-Based Perovskite Solar Cells. *Nat. Energy* **2017**, *2*, 16177.
(442) Bush, K. A.; Palmstrom, A. F.; Yu, Z. J.; Boccard, M.; Cheacharoen, R.; Mailoa, J. P.; McMeekin, D. P.; Hoye, R. L. Z.; Bailie, C. D.; Leijtens, T.; et al. 23.6%-Efficient Monolithic Perovskite/Silicon Tandem Solar Cells with Improved Stability. *Nat. Energy* **2017**, *2*, 17009.
(443) Yu, Y.; Wang, C.; Grice, C. R.; Shrestha, N.; Chen, J.; Zhao, D.; Liao, W.; Cimaroli, A. J.; Roland, P. J.; Ellingson, R. J.; et al. Improving the Performance of Formamidinium and Cesium Lead Triiodide Perovskite Solar Cells using Lead Thiocyanate Additives. *ChemSusChem* **2016**, *9*, 3288−3297.
(444) Yu, Y.; Wang, C.; Grice, C. R.; Shrestha, N.; Zhao, D.; Liao, W.; Guan, L.; Awni, R. A.; Meng, W.; Cimaroli, A. J.; et al. Synergistic Effects of Lead Thiocyanate Additive and Solvent Annealing on the Performance of Wide-Bandgap Perovskite Solar Cells. *ACS Energy Lett.* **2017**, *2*, 1177−1182.
(445) Li, Z.; Yang, M.; Park, J.-S.; Wei, S.-H.; Berry, J. J.; Zhu, K. Stabilizing Perovskite Structures by Tuning Tolerance Factor: Formation of Formamidinium and Cesium Lead Iodide Solid-State Alloys. *Chem. Mater.* **2016**, *28*, 284−292.
(446) Yi, C.; Luo, J.; Meloni, S.; Boziki, A.; Ashari-Astani, N.; Grätzel, C.; Zakeeruddin, S. M.; Röthlisberger, U.; Grätzel, M. Entropic Stabilization of Mixed A-Cation ABX_3 Metal Halide

DOI: 10.1021/acs.chemrev.8b00318
Chem. Rev. 2019, 119, 3193−3295

Perovskites for High Performance Perovskite Solar Cells. *Energy Environ. Sci.* **2016**, *9*, 656−662.
(447) Syzgantseva, O. A.; Saliba, M.; Grätzel, M.; Röthlisberger, U. Stabilization of the Perovskite Phase of Formamidinium Lead Triiodide by Methylammonium, Cs, and/or Rb Doping. *J. Phys. Chem. Lett.* **2017**, *8*, 1191−1196.
(448) Yoder, C. H. Appendix 3: Metallic, Covalent, and Ionic Radii. In *Ionic Compounds: Applications of Chemistry to Mineralogy*; John Wiley & Sons, Inc.: Hoboken, NJ, 2006.
(449) Zong, Y.; Wang, N.; Zhang, L.; Ju, M.-G.; Zeng, X. C.; Sun, X. W.; Zhou, Y.; Padture, N. P. Homogenous Alloys of Formamidinium Lead Triiodide and Cesium Tin Triiodide for Efficient Ideal-Bandgap Perovskite Solar Cells. *Angew. Chem., Int. Ed.* **2017**, *56*, 12658−12662.
(450) Liu, T.; Zong, Y.; Zhou, Y.; Yang, M.; Li, Z.; Game, O. S.; Zhu, K.; Zhu, R.; Gong, Q.; Padture, N. P. High-Performance Formamidinium-Based Perovskite Solar Cells via Microstructure-Mediated δ-to-α Phase Transformation. *Chem. Mater.* **2017**, *29*, 3246−3250.
(451) Tan, H.; Jain, A.; Voznyy, O.; Lan, X.; García de Arquer, F. P.; Fan, J. Z.; Quintero-Bermudez, R.; Yuan, M.; Zhang, B.; Zhao, Y.; et al. Efficient and Stable Solution-Processed Planar Perovskite Solar Cells via Contact Passivation. *Science* **2017**, *355*, 722−726.
(452) Singh, T.; Miyasaka, T. Stabilizing the Efficiency Beyond 20% with a Mixed Cation Perovskite Solar Cell Fabricated in Ambient Air under Controlled Humidity. *Adv. Energy Mater.* **2018**, *8*, 1700677.
(453) Park, Y. H.; Jeong, I.; Bae, S.; Son, H. J.; Lee, P.; Lee, J.; Lee, C.-H.; Ko, M. J. Inorganic Rubidium Cation as an Enhancer for Photovoltaic Performance and Moisture Stability of $HC(NH_2)_2PbI_3$ Perovskite Solar Cells. *Adv. Funct. Mater.* **2017**, *27*, 1605988.
(454) Duong, T.; Mulmudi, H. K.; Shen, H.; Wu, Y.; Barugkin, C.; Mayon, Y. O.; Nguyen, H. T.; Macdonald, D.; Peng, J.; Lockrey, M.; et al. Structural Engineering Using Rubidium Iodide as a Dopant under Excess Lead Iodide Conditions for High Efficiency and Stable Perovskites. *Nano Energy* **2016**, *30*, 330−340.
(455) Turren-Cruz, S.-H.; Saliba, M.; Mayer, M. T.; Juárez-Santiesteban, H.; Mathew, X.; Nienhaus, L.; Tress, W.; Erodici, M. P.; Sher, M.-J.; Bawendi, M. G.; et al. Enhanced Charge Carrier Mobility and Lifetime Suppress Hysteresis and Improve Efficiency in Planar Perovskite Solar Cells. *Energy Environ. Sci.* **2018**, *11*, 78−86.
(456) Hu, Y.; Aygüler, M. F.; Petrus, M. L.; Bein, T.; Docampo, P. Impact of Rubidium and Cesium Cations on the Moisture Stability of Multiple-Cation Mixed-Halide Perovskites. *ACS Energy Lett.* **2017**, *2*, 2212−2218.
(457) Kubicki, D. J.; Prochowicz, D.; Hofstetter, A.; Zakeeruddin, S. M.; Grätzel, M.; Emsley, L. Phase Segregation in Cs-, Rb- and K-Doped Mixed-Cation $(MA)_x(FA)_{1-x}PbI_3$ Hybrid Perovskites from Solid-State NMR. *J. Am. Chem. Soc.* **2017**, *139*, 14173−14180.
(458) Luo, P.; Xia, W.; Zhou, S.; Sun, L.; Cheng, J.; Xu, C.; Lu, Y. Solvent Engineering for Ambient-Air-Processed, Phase-Stable $CsPbI_3$ in Perovskite Solar Cells. *J. Phys. Chem. Lett.* **2016**, *7*, 3603−3608.
(459) Stoumpos, C. C.; Malliakas, C. D.; Peters, J. A.; Liu, Z.; Sebastian, M.; Im, J.; Chasapis, T. C.; Wibowo, A. C.; Chung, D. Y.; Freeman, A. J.; et al. Crystal Growth of the Perovskite Semiconductor $CsPbBr_3$: A New Material for High-Energy Radiation Detection. *Cryst. Growth Des.* **2013**, *13*, 2722−2727.
(460) Zhou, W.; Zhao, Y.; Zhou, X.; Fu, R.; Li, Q.; Zhao, Y.; Liu, K.; Yu, D.; Zhao, Q. Light-Independent Ionic Transport in Inorganic Perovskite and Ultrastable Cs-Based Perovskite Solar Cells. *J. Phys. Chem. Lett.* **2017**, *8*, 4122−4128.
(461) Liang, J.; Zhao, P.; Wang, C.; Wang, Y.; Hu, Y.; Zhu, G.; Ma, L.; Liu, J.; Jin, Z. $CsPb_{0.9}Sn_{0.1}IBr_2$ Based All-Inorganic Perovskite Solar Cells with Exceptional Efficiency and Stability. *J. Am. Chem. Soc.* **2017**, *139*, 14009−14012.
(462) Swarnkar, A.; Marshall, A. R.; Sanehira, E. M.; Chernomordik, B. D.; Moore, D. T.; Christians, J. A.; Chakrabarti, T.; Luther, J. M. Quantum Dot−Induced Phase Stabilization of α-$CsPbI_3$ Perovskite for High-Efficiency Photovoltaics. *Science* **2016**, *354*, 92−95.
(463) Sanehira, E. M.; Marshall, A. R.; Christians, J. A.; Harvey, S. P.; Ciesielski, P. N.; Wheeler, L. M.; Schulz, P.; Lin, L. Y.; Beard, M. C.; Luther, J. M. Enhanced Mobility $CsPbI_3$ Quantum Dot Arrays for Record-Efficiency, High-Voltage Photovoltaic Cells. *Sci. Adv.* **2017**, *3*, No. eaao4204.
(464) Duan, J.; Zhao, Y.; He, B.; Tang, Q. High-Purity Inorganic Perovskite Films for Solar Cells with 9.72% Efficiency. *Angew. Chem., Int. Ed.* **2018**, *57*, 3787−3791.
(465) Hutter, E. M.; Sutton, R. J.; Chandrashekar, S.; Abdi-Jalebi, M.; Stranks, S. D.; Snaith, H. J.; Savenije, T. J. Vapour-Deposited Cesium Lead Iodide Perovskites: Microsecond Charge Carrier Lifetimes and Enhanced Photovoltaic Performance. *ACS Energy Lett.* **2017**, *2*, 1901−1908.
(466) Beal, R. E.; Slotcavage, D. J.; Leijtens, T.; Bowring, A. R.; Belisle, R. A.; Nguyen, W. H.; Burkhard, G. F.; Hoke, E. T.; McGehee, M. D. Cesium Lead Halide Perovskites with Improved Stability for Tandem Solar Cells. *J. Phys. Chem. Lett.* **2016**, *7*, 746−751.
(467) Frolova, L. A.; Anokhin, D. V.; Piryazev, A. A.; Luchkin, S. Y.; Dremova, N. N.; Stevenson, K. J.; Troshin, P. A. Highly Efficient All-Inorganic Planar Heterojunction Perovskite Solar Cells Produced by Thermal Coevaporation of CsI and PbI_2. *J. Phys. Chem. Lett.* **2017**, *8*, 67−72.
(468) Chen, C.-Y.; Lin, H.-Y.; Chiang, K.-M.; Tsai, W.-L.; Huang, Y.-C.; Tsao, C.-S.; Lin, H.-W. All-Vacuum-Deposited Stoichiometrically Balanced Inorganic Cesium Lead Halide Perovskite Solar Cells with Stabilized Efficiency Exceeding 11%. *Adv. Mater.* **2017**, *29*, 1605290.
(469) Kulbak, M.; Cahen, D.; Hodes, G. How Important Is the Organic Part of Lead Halide Perovskite Photovoltaic Cells? Efficient $CsPbBr_3$ Cells. *J. Phys. Chem. Lett.* **2015**, *6*, 2452−2456.
(470) Ma, Q.; Huang, S.; Chen, S.; Zhang, M.; Lau, C. F. J.; Lockrey, M. N.; Mulmudi, H. K.; Shan, Y.; Yao, J.; Zheng, J.; et al. The Effect of Stoichiometry on the Stability of Inorganic Cesium Lead Mixed-Halide Perovskites Solar Cells. *J. Phys. Chem. C* **2017**, *121*, 19642−19649.
(471) Yantara, N.; Bhaumik, S.; Yan, F.; Sabba, D.; Dewi, H. A.; Mathews, N.; Boix, P. P.; Demir, H. V.; Mhaisalkar, S. Inorganic Halide Perovskites for Efficient Light-Emitting Diodes. *J. Phys. Chem. Lett.* **2015**, *6*, 4360−4364.
(472) Ling, Y.; Tan, L.; Wang, X.; Zhou, Y.; Xin, Y.; Ma, B.; Hanson, K.; Gao, H. Composite Perovskites of Cesium Lead Bromide for Optimized Photoluminescence. *J. Phys. Chem. Lett.* **2017**, *8*, 3266−3271.
(473) Cho, H.; Wolf, C.; Kim, J. S.; Yun, H. J.; Bae, J. S.; Kim, H.; Heo, J.-M.; Ahn, S.; Lee, T.-W. High-Efficiency Solution-Processed Inorganic Metal Halide Perovskite Light-Emitting Diodes. *Adv. Mater.* **2017**, *29*, 1700579.
(474) Bag, S.; Durstock, M. F. Large Perovskite Grain Growth in Low-Temperature Solution-Processed Planar p-i-n Solar Cells by Sodium Addition. *ACS Appl. Mater. Interfaces* **2016**, *8*, 5053−5057.
(475) Abdi-Jalebi, M.; Dar, M. I.; Sadhanala, A.; Senanayak, S. P.; Franckevičius, M.; Arora, N.; Hu, Y.; Nazeeruddin, M. K.; Zakeeruddin, S. M.; Grätzel, M.; et al. Impact of Monovalent Cation Halide Additives on the Structural and Optoelectronic Properties of $CH_3NH_3PbI_3$ Perovskite. *Adv. Energy Mater.* **2016**, *6*, 1502472.
(476) Bi, C.; Zheng, X.; Chen, B.; Wei, H.; Huang, J. Spontaneous Passivation of Hybrid Perovskite by Sodium Ions from Glass Substrates: Mysterious Enhancement of Device Efficiency Revealed. *ACS Energy Lett.* **2017**, *2*, 1400−1406.
(477) Kronik, L.; Cahen, D.; Schock, H. W. Effects of Sodium on Polycrystalline $Cu(In,Ga)Se_2$ and Its Solar Cell Performance. *Adv. Mater.* **1998**, *10*, 31−36.
(478) Rudmann, D.; da Cunha, A. F.; Kaelin, M.; Kurdesau, F.; Zogg, H.; Tiwari, A. N.; Bilger, G. Efficiency Enhancement of $Cu(In,Ga)Se_2$ Solar Cells Due to Post-Deposition Na Incorporation. *Appl. Phys. Lett.* **2004**, *84*, 1129−1131.
(479) Chang, J.; Lin, Z.; Zhu, H.; Isikgor, F. H.; Xu, Q.-H.; Zhang, C.; Hao, Y.; Ouyang, J. Enhancing the Photovoltaic Performance of Planar Heterojunction Perovskite Solar Cells by Doping the Perovskite Layer with Alkali Metal Ions. *J. Mater. Chem. A* **2016**, *4*, 16546−16552.

DOI: 10.1021/acs.chemrev.8b00318
Chem. Rev. 2019, 119, 3193−3295

(480) Tang, Z.; Bessho, T.; Awai, F.; Kinoshita, T.; Maitani, M. M.; Jono, R.; Murakami, T. N.; Wang, H.; Kubo, T.; Uchida, S.; et al. Hysteresis-Free Perovskite Solar Cells Made of Potassium-Doped Organometal Halide Perovskite. *Sci. Rep.* **2017**, *7*, 12183.
(481) Abdi-Jalebi, M.; Andaji-Garmaroudi, Z.; Cacovich, S.; Stavrakas, C.; Philippe, B.; Richter, J. M.; Alsari, M.; Booker, E. P.; Hutter, E. M.; Pearson, A. J.; et al. Maximizing and Stabilizing Luminescence from Halide Perovskites with Potassium Passivation. *Nature* **2018**, *555*, 497−501.
(482) Nam, J. K.; Chai, S. U.; Cha, W.; Choi, Y. J.; Kim, W.; Jung, M. S.; Kwon, J.; Kim, D.; Park, J. H. Potassium Incorporation for Enhanced Performance and Stability of Fully Inorganic Cesium Lead Halide Perovskite Solar Cells. *Nano Lett.* **2017**, *17*, 2028−2033.
(483) De Marco, N.; Zhou, H.; Chen, Q.; Sun, P.; Liu, Z.; Meng, L.; Yao, E. P.; Liu, Y.; Schiffer, A.; Yang, Y. Guanidinium: A Route to Enhanced Carrier Lifetime and Open-Circuit Voltage in Hybrid Perovskite Solar Cells. *Nano Lett.* **2016**, *16*, 1009−1016.
(484) Chen, Q.; Chen, L.; Ye, F.; Zhao, T.; Tang, F.; Rajagopal, A.; Jiang, Z.; Jiang, S.; Jen, A. K.-Y.; Xie, Y.; et al. Ag-Incorporated Organic-Inorganic Perovskite Films and Planar Heterojunction Solar Cells. *Nano Lett.* **2017**, *17*, 3231−3237.
(485) Hao, F.; Stoumpos, C. C.; Chang, R. P. H.; Kanatzidis, M. G. Anomalous Band Gap Behavior in Mixed Sn and Pb Perovskites Enables Broadening of Absorption Spectrum in Solar Cells. *J. Am. Chem. Soc.* **2014**, *136*, 8094−8099.
(486) Noel, N. K.; Stranks, S. D.; Abate, A.; Wehrenfennig, C.; Guarnera, S.; Haghighirad, A.-A.; Sadhanala, A.; Eperon, G. E.; Pathak, S. K.; Johnston, M. B.; et al. Lead-Free Organic−Inorganic Tin Halide Perovskites for Photovoltaic Applications. *Energy Environ. Sci.* **2014**, *7*, 3061.
(487) Mitzi, D. B.; Feild, C. A.; Schlesinger, Z.; Laibowitz, R. B. Transport, Optical, and Magnetic Properties of the Conducting Halide Perovskite $CH_3NH_3SnI_3$. *J. Solid State Chem.* **1995**, *114*, 159−163.
(488) Mitzi, D. B.; Liang, K. Synthesis, Resistivity, and Thermal Properties of the Cubic Perovskite $NH_2CH = NH_2SnI_3$ and Related Systems. *J. Solid State Chem.* **1997**, *134*, 376−381.
(489) Takahashi, Y.; Hasegawa, H.; Takahashi, Y.; Inabe, T. Hall Mobility in Tin Iodide Perovskite $CH_3NH_3SnI_3$: Evidence for a Doped Semiconductor. *J. Solid State Chem.* **2013**, *205*, 39−43.
(490) Gupta, S.; Cahen, D.; Hodes, G. How SnF_2 Impacts the Material Properties of Lead-Free Tin Perovskites. *J. Phys. Chem. C* **2018**, *122*, 13926−13936.
(491) Hao, F.; Stoumpos, C. C.; Cao, D. H.; Chang, R. P. H.; Kanatzidis, M. G. Lead-Free Solid-State Organic−Inorganic Halide Perovskite Solar Cells. *Nat. Photonics* **2014**, *8*, 489−494.
(492) Liao, Y.; Liu, H.; Zhou, W.; Yang, D.; Shang, Y.; Shi, Z.; Li, B.; Jiang, X.; Zhang, L.; Quan, L. N.; et al. Highly Oriented Low-Dimensional Tin Halide Perovskites with Enhanced Stability and Photovoltaic Performance. *J. Am. Chem. Soc.* **2017**, *139*, 6693−6699.
(493) Liao, W.; Zhao, D.; Yu, Y.; Grice, C. R.; Wang, C.; Cimaroli, A. J.; Schulz, P.; Meng, W.; Zhu, K.; Xiong, R. G.; et al. Lead-Free Inverted Planar Formamidinium Tin Triiodide Perovskite Solar Cells Achieving Power Conversion Efficiencies up to 6.22%. *Adv. Mater.* **2016**, *28*, 9333−9340.
(494) Zhao, Z.; Gu, F.; Li, Y.; Sun, W.; Ye, S.; Rao, H.; Liu, Z.; Bian, Z.; Huang, C. Mixed-Organic-Cation Tin Iodide for Lead-Free Perovskite Solar Cells with an Efficiency of 8.12%. *Adv. Sci.* **2017**, *4*, 1700204.
(495) Shao, S.; Liu, J.; Portale, G.; Fang, H.-H.; Blake, G. R.; ten Brink, G. H.; Koster, L. J. A.; Loi, M. A. Highly Reproducible Sn-Based Hybrid Perovskite Solar Cells with 9% Efficiency. *Adv. Energy Mater.* **2018**, *8*, 1702019.
(496) Kumar, M. H.; Dharani, S.; Leong, W. L.; Boix, P. P.; Prabhakar, R. R.; Baikie, T.; Shi, C.; Ding, H.; Ramesh, R.; Asta, M.; et al. Lead-Free Halide Perovskite Solar Cells with High Photocurrents Realized through Vacancy Modulation. *Adv. Mater.* **2014**, *26*, 7122−7127.
(497) Lee, S. J.; Shin, S. S.; Kim, Y. C.; Kim, D.; Ahn, T. K.; Noh, J. H.; Seo, J.; Seok, S. I. Fabrication of Efficient Formamidinium Tin Iodide Perovskite Solar Cells through SnF_2-Pyrazine Complex. *J. Am. Chem. Soc.* **2016**, *138*, 3974−3977.
(498) Hao, F.; Stoumpos, C. C.; Guo, P.; Zhou, N.; Marks, T. J.; Chang, R. P.; Kanatzidis, M. G. Solvent-Mediated Crystallization of $CH_3NH_3SnI_3$ Films for Heterojunction Depleted Perovskite Solar Cells. *J. Am. Chem. Soc.* **2015**, *137*, 11445−11452.
(499) Cao, D. H.; Stoumpos, C. C.; Yokoyama, T.; Logsdon, J. L.; Song, T.-B.; Farha, O. K.; Wasielewski, M. R.; Hupp, J. T.; Kanatzidis, M. G. Thin Films and Solar Cells Based on Semiconducting Two-Dimensional Ruddlesden−Popper $(CH_3(CH_2)_3NH_3)_2(CH_3NH_3)_{n-1}Sn_nI_{3n+1}$ Perovskites. *ACS Energy Lett.* **2017**, *2*, 982−990.
(500) Song, T.-B.; Yokoyama, T.; Aramaki, S.; Kanatzidis, M. G. Performance Enhancement of Lead-Free Tin-Based Perovskite Solar Cells with Reducing Atmosphere-Assisted Dispersible Additive. *ACS Energy Lett.* **2017**, *2*, 897−903.
(501) Wang, N.; Zhou, Y.; Ju, M.-G.; Garces, H. F.; Ding, T.; Pang, S.; Zeng, X. C.; Padture, N. P.; Sun, X. W. Heterojunction-Depleted Lead-Free Perovskite Solar Cells with Coarse-Grained B-γ-$CsSnI_3$ Thin Films. *Adv. Energy Mater.* **2016**, *6*, 1601130.
(502) Song, T.-B.; Yokoyama, T.; Stoumpos, C. C.; Logsdon, J.; Cao, D. H.; Wasielewski, M. R.; Aramaki, S.; Kanatzidis, M. G. Importance of Reducing Vapor Atmosphere in the Fabrication of Tin-Based Perovskite Solar Cells. *J. Am. Chem. Soc.* **2017**, *139*, 836−842.
(503) Yokoyama, T.; Song, T.-B.; Cao, D. H.; Stoumpos, C. C.; Aramaki, S.; Kanatzidis, M. G. The Origin of Lower Hole Carrier Concentration in Methylammonium Tin Halide Films Grown by a Vapor-Assisted Solution Process. *ACS Energy Lett.* **2017**, *2*, 22−28.
(504) Yang, Z.; Rajagopal, A.; Jen, A. K.-Y. Ideal Bandgap Organic-Inorganic Hybrid Perovskite Solar Cells. *Adv. Mater.* **2017**, *29*, 1704418.
(505) Leijtens, T.; Prasanna, R.; Gold-Parker, A.; Toney, M. F.; McGehee, M. D. Mechanism of Tin Oxidation and Stabilization by Lead Substitution in Tin Halide Perovskites. *ACS Energy Lett.* **2017**, *2*, 2159−2165.
(506) Kapil, G.; Ripolles, T. S.; Hamada, K.; Ogomi, Y.; Bessho, T.; Kinoshita, T.; Chantana, J.; Yoshino, K.; Shen, Q.; Toyoda, T.; et al. Highly Efficient 17.6% Tin-Lead Mixed Perovskite Solar Cells Realized through Spike Structure. *Nano Lett.* **2018**, *18*, 3600−3607.
(507) Xu, X.; Chueh, C.-C.; Yang, Z.; Rajagopal, A.; Xu, J.; Jo, S. B.; Jen, A. K.-Y. Ascorbic Acid as an Effective Antioxidant Additive to Enhance the Efficiency and Stability of Pb/Sn-Based Binary Perovskite Solar Cells. *Nano Energy* **2017**, *34*, 392−398.
(508) Shai, X.; Zuo, L.; Sun, P.; Liao, P.; Huang, W.; Yao, E.-P.; Li, H.; Liu, S.; Shen, Y.; Yang, Y.; et al. Efficient Planar Perovskite Solar Cells Using Halide Sr-Substituted Pb Perovskite. *Nano Energy* **2017**, *36*, 213−222.
(509) Chan, S.-H.; Wu, M.-C.; Lee, K.-M.; Chen, W.-C.; Lin, T.-H.; Su, W.-F. Enhancing Perovskite Solar Cell Performance and Stability by Doping Barium in Methylammonium Lead Halide. *J. Mater. Chem. A* **2017**, *5*, 18044−18052.
(510) Lau, C. F. J.; Zhang, M.; Deng, X.; Zheng, J.; Bing, J.; Ma, Q.; Kim, J.; Hu, L.; Green, M. A.; Huang, S.; et al. Strontium-Doped Low-Temperature-Processed $CsPbI_2Br$ Perovskite Solar Cells. *ACS Energy Lett.* **2017**, *2*, 2319−2325.
(511) Zhang, H.; Wang, H.; Williams, S. T.; Xiong, D.; Zhang, W.; Chueh, C.-C.; Chen, W.; Jen, A. K.-Y. $SrCl_2$ Derived Perovskite Facilitating a High Efficiency of 16% in Hole-Conductor-Free Fully Printable Mesoscopic Perovskite Solar Cells. *Adv. Mater.* **2017**, *29*, 1606608.
(512) Shannon, R. D. Revised Effective Ionic Radii and Systematic Studies of Interatomic Distances in Halides and Chalcogenides. *Acta Crystallogr., Sect. A: Cryst. Phys., Diffr., Theor. Gen. Crystallogr.* **1976**, *32*, 751−767.
(513) Navas, J.; Sánchez-Coronilla, A.; Gallardo, J. J.; Martín, E. I.; Hernández, N. C.; Alcántara, R.; Fernández-Lorenzo, C.; Martín-Calleja, J. Revealing the Role of Pb^{2+} in the Stability of Organic-

DOI: 10.1021/acs.chemrev.8b00318
Chem. Rev. 2019, 119, 3193−3295

Inorganic Hybrid Perovskite $CH_3NH_3Pb_{1-x}Cd_xI_3$: an Experimental and Theoretical Study. *Phys. Chem. Chem. Phys.* **2015**, *17*, 23886−23896.
(514) Dunlap-Shohl, W. A.; Younts, R.; Gautam, B.; Gundogdu, K.; Mitzi, D. B. Effects of Cd Diffusion and Doping in High-Performance Perovskite Solar Cells Using CdS as Electron Transport Layer. *J. Phys. Chem. C* **2016**, *120*, 16437−16445.
(515) Watthage, S. C.; Song, Z.; Shrestha, N.; Phillips, A. B.; Liyanage, G. K.; Roland, P. J.; Ellingson, R. J.; Heben, M. J. Enhanced Grain Size, Photoluminescence, and Photoconversion Efficiency with Cadmium Addition during the Two-Step Growth of $CH_3NH_3PbI_3$. *ACS Appl. Mater. Interfaces* **2017**, *9*, 2334−2341.
(516) Tong, G.; Song, Z.; Li, C.; Zhao, Y.; Yu, L.; Xu, J.; Jiang, Y.; Sheng, Y.; Shi, Y.; Chen, K. Cadmium-Doped Flexible Perovskite Solar Cells with a Low-Cost and Low-Temperature-Processed CdS Electron Transport Layer. *RSC Adv.* **2017**, *7*, 19457−19463.
(517) Frolova, L. A.; Anokhin, D. V.; Gerasimov, K. L.; Dremova, N. N.; Troshin, P. A. Exploring the Effects of the Pb^{2+} Substitution in $MAPbI_3$ on the Photovoltaic Performance of the Hybrid Perovskite Solar Cells. *J. Phys. Chem. Lett.* **2016**, *7*, 4353−4357.
(518) Náfrádi, B.; Szirmai, P.; Spina, M.; Lee, H.; Yazyev, O. V.; Arakcheeva, A.; Chernyshov, D.; Gibert, M.; Forró, L.; Horváth, E. Optically Switched Magnetism in Photovoltaic Perovskite $CH_3NH_3(Mn:Pb)I_3$. *Nat. Commun.* **2016**, *7*, 13406.
(519) Jahandar, M.; Heo, J. H.; Song, C. E.; Kong, K.-J.; Shin, W. S.; Lee, J.-C.; Im, S. H.; Moon, S.-J. Highly Efficient Metal Halide Substituted $CH_3NH_3I(PbI_2)_{1-x}(CuBr_2)_x$ Planar Perovskite Solar Cells. *Nano Energy* **2016**, *27*, 330−339.
(520) Slavney, A. H.; Hu, T.; Lindenberg, A. M.; Karunadasa, H. I. A Bismuth-Halide Double Perovskite with Long Carrier Recombination Lifetime for Photovoltaic Applications. *J. Am. Chem. Soc.* **2016**, *138*, 2138−2141.
(521) McClure, E. T.; Ball, M. R.; Windl, W.; Woodward, P. M. Cs_2AgBiX_6 (X = Br, Cl): New Visible Light Absorbing, Lead-Free Halide Perovskite Semiconductors. *Chem. Mater.* **2016**, *28*, 1348−1354.
(522) Volonakis, G.; Filip, M. R.; Haghighirad, A. A.; Sakai, N.; Wenger, B.; Snaith, H. J.; Giustino, F. Lead-Free Halide Double Perovskites via Heterovalent Substitution of Noble Metals. *J. Phys. Chem. Lett.* **2016**, *7*, 1254−1259.
(523) Slavney, A. H.; Leppert, L.; Bartesaghi, D.; Gold-Parker, A.; Toney, M. F.; Savenije, T. J.; Neaton, J. B.; Karunadasa, H. I. Defect-Induced Band-Edge Reconstruction of a Bismuth-Halide Double Perovskite for Visible-Light Absorption. *J. Am. Chem. Soc.* **2017**, *139*, 5015−5018.
(524) Volonakis, G.; Haghighirad, A. A.; Milot, R. L.; Sio, W. H.; Filip, M. R.; Wenger, B.; Johnston, M. B.; Herz, L. M.; Snaith, H. J.; Giustino, F. $Cs_2InAgCl_6$: A New Lead-Free Halide Double Perovskite with Direct Band Gap. *J. Phys. Chem. Lett.* **2017**, *8*, 772−778.
(525) Wei, F.; Deng, Z.; Sun, S.; Zhang, F.; Evans, D. M.; Kieslich, G.; Tominaka, S.; Carpenter, M. A.; Zhang, J.; Bristowe, P. D.; et al. Synthesis and Properties of a Lead-Free Hybrid Double Perovskite: $(CH_3NH_3)_2AgBiBr_6$. *Chem. Mater.* **2017**, *29*, 1089−1094.
(526) Deng, Z.; Wei, F.; Sun, S.; Kieslich, G.; Cheetham, A. K.; Bristowe, P. D. Exploring the Properties of Lead-Free Hybrid Double Perovskites Using a Combined Computational-Experimental Approach. *J. Mater. Chem. A* **2016**, *4*, 12025−12029.
(527) Deng, Z.; Wei, F.; Brivio, F.; Wu, Y.; Sun, S.; Bristowe, P. D.; Cheetham, A. K. Synthesis and Characterization of the Rare-Earth Hybrid Double Perovskites: $(CH_3NH_3)_2KGdCl_6$ and $(CH_3NH_3)_2KYCl_6$. *J. Phys. Chem. Lett.* **2017**, *8*, 5015−5020.
(528) Connor, B. A.; Leppert, L.; Smith, M. D.; Neaton, J. B.; Karunadasa, H. I. Layered Halide Double Perovskites: Dimensional Reduction of $Cs_2AgBiBr_6$. *J. Am. Chem. Soc.* **2018**, *140*, 5235−5240.
(529) Hoye, R. L. Z.; Eyre, L.; Wei, F.; Brivio, F.; Sadhanala, A.; Sun, S.; Li, W.; Zhang, K. H. L.; MacManus-Driscoll, J. L.; Bristowe, P. D.; et al. Fundamental Carrier Lifetime Exceeding 1 μs in $Cs_2AgBiBr_6$ Double Perovskite. *Adv. Mater. Interfaces* **2018**, *5*, 1800464.
(530) Savory, C. N.; Walsh, A.; Scanlon, D. O. Can Pb-Free Halide Double Perovskites Support High-Efficiency Solar Cells? *ACS Energy Lett.* **2016**, *1*, 949−955.
(531) Greul, E.; Petrus, M. L.; Binek, A.; Docampo, P.; Bein, T. Highly Stable, Phase Pure $Cs_2AgBiBr_6$ Double Perovskite Thin Films for Optoelectronic Applications. *J. Mater. Chem. A* **2017**, *5*, 19972−19981.
(532) Gao, W.; Ran, C.; Xi, J.; Jiao, B.; Zhang, W.; Wu, M.; Hou, X.; Wu, Z. High-Quality $Cs_2AgBiBr_6$ Double Perovskite Film for Lead-Free Inverted Planar Heterojunction Solar Cells with 2.2% Efficiency. *ChemPhysChem* **2018**, *19*, 1696.
(533) Lei, L.-Z.; Shi, Z.-F.; Li, Y.; Ma, Z.-Z.; Zhang, F.; Xu, T.-T.; Tian, Y.-T.; Wu, D.; Li, X.-J.; Du, G.-T. High-Efficiency and Air-Stable Photodetectors based on Lead-Free Double Perovskite $Cs_2AgBiBr_6$ Thin Films. *J. Mater. Chem. C* **2018**, *6*, 7982−7988.
(534) Pantaler, M.; Cho, K. T.; Queloz, V. I. E.; García Benito, I.; Fettkenhauer, C.; Anusca, I.; Nazeeruddin, M. K.; Lupascu, D. C.; Grancini, G. Hysteresis-Free Lead-Free Double-Perovskite Solar Cells by Interface Engineering. *ACS Energy Lett.* **2018**, *3*, 1781−1786.
(535) Ning, W.; Wang, F.; Wu, B.; Lu, J.; Yan, Z.; Liu, X.; Tao, Y.; Liu, J. M.; Huang, W.; Fahlman, M.; et al. Long Electron-Hole Diffusion Length in High-Quality Lead-Free Double Perovskite Films. *Adv. Mater.* **2018**, *30*, No. e1706246.
(536) Pantaler, M.; Fettkenhauer, C.; Nguyen, H. L.; Anusca, I.; Lupascu, D. C. Deposition Routes of $Cs_2AgBiBr_6$ Double Perovskites for Photovoltaic Applications. *MRS Adv.* **2018**, *3*, 1819−1823.
(537) Ju, M.-G.; Chen, M.; Zhou, Y.; Garces, H. F.; Dai, J.; Ma, L.; Padture, N. P.; Zeng, X. C. Earth-Abundant Nontoxic Titanium(IV)-based Vacancy-Ordered Double Perovskite Halides with Tunable 1.0 to 1.8 eV Bandgaps for Photovoltaic Applications. *ACS Energy Lett.* **2018**, *3*, 297−304.
(538) Chen, M.; Ju, M.-G.; Carl, A. D.; Zong, Y.; Grimm, R. L.; Gu, J.; Zeng, X. C.; Zhou, Y.; Padture, N. P. Cesium Titanium(IV) Bromide Thin Films Based Stable Lead-free Perovskite Solar Cells. *Joule* **2018**, *2*, 558−570.
(539) Noh, J. H.; Im, S. H.; Heo, J. H.; Mandal, T. N.; Seok, S. I. Chemical Management for Colorful, Efficient, and Stable Inorganic-Organic Hybrid Nanostructured Solar Cells. *Nano Lett.* **2013**, *13*, 1764−1769.
(540) Sabba, D.; Mulmudi, H. K.; Prabhakar, R. R.; Krishnamoorthy, T.; Baikie, T.; Boix, P. P.; Mhaisalkar, S.; Mathews, N. Impact of Anionic Br−Substitution on Open Circuit Voltage in Lead Free Perovskite $CsSnI_{3-x}Br_x$ Solar Cells. *J. Phys. Chem. C* **2015**, *119*, 1763−1767.
(541) Slotcavage, D. J.; Karunadasa, H. I.; McGehee, M. D. Light-Induced Phase Segregation in Halide-Perovskite Absorbers. *ACS Energy Lett.* **2016**, *1*, 1199−1205.
(542) Xiao, Z.; Zhao, L.; Tran, N. L.; Lin, Y. L.; Silver, S. H.; Kerner, R. A.; Yao, N.; Kahn, A.; Scholes, G. D.; Rand, B. P. Mixed-Halide Perovskites with Stabilized Bandgaps. *Nano Lett.* **2017**, *17*, 6863−6869.
(543) Niezgoda, J. S.; Foley, B. J.; Chen, A. Z.; Choi, J. J. Improved Charge Collection in Highly Efficient $CsPbBrI_2$ Solar Cells with Light-Induced Dealloying. *ACS Energy Lett.* **2017**, *2*, 1043−1049.
(544) Yoon, S. J.; Kuno, M.; Kamat, P. V. Shift Happens. How Halide Ion Defects Influence Photoinduced Segregation in Mixed Halide Perovskites. *ACS Energy Lett.* **2017**, *2*, 1507−1514.
(545) Yu, J. C.; Kim, D. B.; Jung, E. D.; Lee, B. R.; Song, M. H. High-Performance Perovskite Light-Emitting Diodes via Morphological Control of Perovskite Films. *Nanoscale* **2016**, *8*, 7036−7042.
(546) Kulkarni, S. A.; Baikie, T.; Boix, P. P.; Yantara, N.; Mathews, N.; Mhaisalkar, S. Band-Gap Tuning of Lead Halide Perovskites Using a Sequential Deposition Process. *J. Mater. Chem. A* **2014**, *2*, 9221−9225.
(547) Chen, Y.; Li, B.; Huang, W.; Gao, D.; Liang, Z. Efficient and Reproducible $CH_3NH_3PbI_{3-x}(SCN)_x$ Perovskite Based Planar Solar Cells. *Chem. Commun.* **2015**, *51*, 11997−11999.
(548) Jiang, Q.; Rebollar, D.; Gong, J.; Piacentino, E. L.; Zheng, C.; Xu, T. Pseudohalide-Induced Moisture Tolerance in Perovskite

DOI: 10.1021/acs.chemrev.8b00318
Chem. Rev. 2019, 119, 3193−3295

$CH_3NH_3Pb(SCN)_2I$ Thin Films. *Angew. Chem., Int. Ed.* **2015**, *54*, 7617−7620.
(549) Daub, M.; Hillebrecht, H. Synthesis, Single-Crystal Structure and Characterization of $(CH_3NH_3)_2Pb(SCN)_2I_2$. *Angew. Chem., Int. Ed.* **2015**, *54*, 11016−11017.
(550) Ganose, A. M.; Savory, C. N.; Scanlon, D. O. $(CH_3NH_3)_2Pb(SCN)_2I_2$: A More Stable Structural Motif for Hybrid Halide Photovoltaics? *J. Phys. Chem. Lett.* **2015**, *6*, 4594−4598.
(551) Xiao, Z.; Meng, W.; Saparov, B.; Duan, H.-S.; Wang, C.; Feng, C.; Liao, W.; Ke, W.; Zhao, D.; Wang, J.; et al. Photovoltaic Properties of Two-Dimensional $(CH_3NH_3)_2Pb(SCN)_2I_2$ Perovskite: A Combined Experimental and Density Functional Theory Study. *J. Phys. Chem. Lett.* **2016**, *7*, 1213−1218.
(552) Younts, R.; Duan, H. S.; Gautam, B.; Saparov, B.; Liu, J.; Mongin, C.; Castellano, F. N.; Mitzi, D. B.; Gundogdu, K. Efficient Generation of Long-Lived Triplet Excitons in 2D Hybrid Perovskite. *Adv. Mater.* **2017**, *29*, 1604278.
(553) Chiang, Y.-H.; Li, M.-H.; Cheng, H.-M.; Shen, P.-S.; Chen, P. Mixed Cation Thiocyanate-Based Pseudohalide Perovskite Solar Cells with High Efficiency and Stability. *ACS Appl. Mater. Interfaces* **2017**, *9*, 2403−2409.
(554) Cronin, H. M.; Jayawardena, K. D. G. I.; Stoeva, Z.; Shkunov, M.; Silva, S. R. P. Effects of Ambient Humidity on the Optimum Annealing Time of Mixed-Halide Perovskite Solar Cells. *Nanotechnology* **2017**, *28*, 114004.
(555) Gangishetty, M. K.; Scott, R. W. J.; Kelly, T. L. Effect of Relative Humidity on Crystal Growth, Device Performance and Hysteresis in Planar Heterojunction Perovskite Solar Cells. *Nanoscale* **2016**, *8*, 6300−6307.
(556) Xu, Y.; Zhu, L.; Shi, J.; Xu, X.; Xiao, J.; Dong, J.; Wu, H.; Luo, Y.; Li, D.; Meng, Q. The Effect of Humidity upon the Crystallization Process of Two-Step Spin-Coated Organic−Inorganic Perovskites. *ChemPhysChem* **2016**, *17*, 112−118.
(557) Jeong, B.; Cho, S. M.; Cho, S. H.; Lee, J. H.; Hwang, I.; Hwang, S. K.; Cho, J.; Lee, T.-W.; Park, C. Humidity Controlled Crystallization of Thin $CH_3NH_3PbI_3$ films for High Performance Perovskite Solar Cell. *Phys. Status Solidi RRL* **2016**, *10*, 381−387.
(558) Aguiar, J. A.; Wozny, S.; Alkurd, N. R.; Yang, M.; Kovarik, L.; Holesinger, T. G.; Al-Jassim, M.; Zhu, K.; Zhou, W.; Berry, J. J. Effect of Water Vapor, Temperature, and Rapid Annealing on Formamidinium Lead Triiodide Perovskite Crystallization. *ACS Energy Lett.* **2016**, *1*, 155−161.
(559) Gong, X.; Li, M.; Shi, X.-B.; Ma, H.; Wang, Z.-K.; Liao, L.-S. Controllable Perovskite Crystallization by Water Additive for High-Performance Solar Cells. *Adv. Funct. Mater.* **2015**, *25*, 6671−6678.
(560) Wu, C.-G.; Chiang, C.-H.; Tseng, Z.-L.; Nazeeruddin, M. K.; Hagfeldt, A.; Grätzel, M. High Efficiency Stable Inverted Perovskite Solar Cells without Current Hysteresis. *Energy Environ. Sci.* **2015**, *8*, 2725−2733.
(561) Chiang, C.-H.; Nazeeruddin, M. K.; Grätzel, M.; Wu, C.-G. The Synergistic Effect of H_2O and DMF towards Stable and 20% Efficiency Inverted Perovskite Solar Cells. *Energy Environ. Sci.* **2017**, *10*, 808−817.
(562) Yang, J.; Siempelkamp, B. D.; Liu, D.; Kelly, T. L. Investigation of $CH_3NH_3PbI_3$ Degradation Rates and Mechanisms in Controlled Humidity Environments Using in Situ Techniques. *ACS Nano* **2015**, *9*, 1955−1963.
(563) Heo, J. H.; Song, D. H.; Han, H. J.; Kim, S. Y.; Kim, J. H.; Kim, D.; Shin, H. W.; Ahn, T. K.; Wolf, C.; Lee, T.-W.; et al. Planar $CH_3NH_3PbI_3$ Perovskite Solar Cells with Constant 17.2% Average Power Conversion Efficiency Irrespective of the Scan Rate. *Adv. Mater.* **2015**, *27*, 3424−3430.
(564) Xiao, Z.; Wang, D.; Dong, Q.; Wang, Q.; Wei, W.; Dai, J.; Zeng, X.; Huang, J. Unraveling the Hidden Function of a Stabilizer in a Precursor in Improving Hybrid Perovskite Film Morphology for High Efficiency Solar Cells. *Energy Environ. Sci.* **2016**, *9*, 867−872.
(565) Zhang, W.; Pathak, S.; Sakai, N.; Stergiopoulos, T.; Nayak, P. K.; Noel, N. K.; Haghighirad, A. A.; Burlakov, V. M.; deQuilettes, D. W.; Sadhanala, A.; et al. Enhanced Optoelectronic Quality of Perovskite Thin Films with Hypophosphorous Acid for Planar Heterojunction Solar Cells. *Nat. Commun.* **2015**, *6*, 10030.
(566) Noel, N. K.; Congiu, M.; Ramadan, A. J.; Fearn, S.; McMeekin, D. P.; Patel, J. B.; Johnston, M. B.; Wenger, B.; Snaith, H. J. Unveiling the Influence of pH on the Crystallization of Hybrid Perovskites, Delivering Low Voltage Loss Photovoltaics. *Joule* **2017**, *1*, 328−343.
(567) Liang, P.-W.; Liao, C.-Y.; Chueh, C.-C.; Zuo, F.; Williams, S. T.; Xin, X.-K.; Lin, J.; Jen, A. K.-Y. Additive Enhanced Crystallization of Solution-Processed Perovskite for Highly Efficient Planar-Heterojunction Solar Cells. *Adv. Mater.* **2014**, *26*, 3748−3754.
(568) Chueh, C.-C.; Liao, C.-Y.; Zuo, F.; Williams, S. T.; Liang, P.-W.; Jen, A. K.-Y. The Roles of Alkyl Halide Additives in Enhancing Perovskite Solar Cell Performance. *J. Mater. Chem. A* **2015**, *3*, 9058−9062.
(569) Fei, C.; Li, B.; Zhang, R.; Fu, H.; Tian, J.; Cao, G. Highly Efficient and Stable Perovskite Solar Cells Based on Monolithically Grained $CH_3NH_3PbI_3$ Film. *Adv. Energy Mater.* **2017**, *7*, 1602017.
(570) Lee, J.-W.; Kim, H.-S.; Park, N.-G. Lewis Acid-Base Adduct Approach for High Efficiency Perovskite Solar Cells. *Acc. Chem. Res.* **2016**, *49*, 311−319.
(571) Ye, S.; Rao, H.; Zhao, Z.; Zhang, L.; Bao, H.; Sun, W.; Li, Y.; Gu, F.; Wang, J.; Liu, Z.; et al. A Breakthrough Efficiency of 19.9% Obtained in Inverted Perovskite Solar Cells by Using an Efficient Trap State Passivator Cu(thiourea)I. *J. Am. Chem. Soc.* **2017**, *139*, 7504−7512.
(572) Wang, Q.; Zheng, X.; Deng, Y.; Zhao, J.; Chen, Z.; Huang, J. Stabilizing the α-Phase of $CsPbI_3$ Perovskite by Sulfobetaine Zwitterions in One-Step Spin-Coating Films. *Joule* **2017**, *1*, 371−382.
(573) Smith, I. C.; Hoke, E. T.; Solis-Ibarra, D.; McGehee, M. D.; Karunadasa, H. I. A Layered Hybrid Perovskite Solar-Cell Absorber with Enhanced Moisture Stability. *Angew. Chem., Int. Ed.* **2014**, *53*, 11232−11235.
(574) Stoumpos, C. C.; Soe, C. M. M.; Tsai, H.; Nie, W.; Blancon, J.-C.; Cao, D. H.; Liu, F.; Traoré, B.; Katan, C.; Even, J.; et al. High Members of the 2D Ruddlesden-Popper Halide Perovskites: Synthesis, Optical Properties, and Solar Cells of $(CH_3(CH_2)_3NH_3)_2(CH_3NH_3)_4Pb_5I_{16}$. *Chem.* **2017**, *2*, 427−440.
(575) Chen, Y.; Sun, Y.; Peng, J.; Zhang, W.; Su, X.; Zheng, K.; Pullerits, T.; Liang, Z. Tailoring Organic Cation of 2D Air-Stable Organometal Halide Perovskites for Highly Efficient Planar Solar Cells. *Adv. Energy Mater.* **2017**, *7*, 1700162.
(576) Zhou, N.; Shen, Y.; Li, L.; Tan, S.; Liu, N.; Zheng, G.; Chen, Q.; Zhou, H. The Exploration of Crystallization Kinetics in Quasi Two-Dimensional Perovskite and High Performance Solar Cells. *J. Am. Chem. Soc.* **2018**, *140*, 459−465.
(577) Tsai, H.; Nie, W.; Blancon, J.-C.; Stoumpos, C. C.; Soe, C. M. M.; Yoo, J.; Crochet, J.; Tretiak, S.; Even, J.; Sadhanala, A.; et al. Stable Light-Emitting Diodes Using Phase-Pure Ruddlesden-Popper Layered Perovskites. *Adv. Mater.* **2018**, *30*, 1704217.
(578) Stoumpos, C. C.; Cao, D. H.; Clark, D. J.; Young, J.; Rondinelli, J. M.; Jang, J. I.; Hupp, J. T.; Kanatzidis, M. G. Ruddlesden−Popper Hybrid Lead Iodide Perovskite 2D Homologous Semiconductors. *Chem. Mater.* **2016**, *28*, 2852−2867.
(579) Hu, Y.; Schlipf, J.; Wussler, M.; Petrus, M. L.; Jaegermann, W.; Bein, T.; Müller-Buschbaum, P.; Docampo, P. Hybrid Perovskite/Perovskite Heterojunction Solar Cells. *ACS Nano* **2016**, *10*, 5999−6007.
(580) Li, N.; Zhu, Z.; Chueh, C.-C.; Liu, H.; Peng, B.; Petrone, A.; Li, X.; Wang, L.; Jen, A. K.-Y. Mixed Cation $FA_xPEA_{1-x}PbI_3$ with Enhanced Phase and Ambient Stability toward High-Performance Perovskite Solar Cells. *Adv. Energy Mater.* **2017**, *7*, 1601307.
(581) Peng, W.; Miao, X.; Adinolfi, V.; Alarousu, E.; El Tall, O.; Emwas, A. H.; Zhao, C.; Walters, G.; Liu, J.; Ouellette, O.; et al. Engineering of $CH_3NH_3PbI_3$ Perovskite Crystals by Alloying Large Organic Cations for Enhanced Thermal Stability and Transport Properties. *Angew. Chem., Int. Ed.* **2016**, *55*, 10686−10690.

DOI: 10.1021/acs.chemrev.8b00318
Chem. Rev. 2019, 119, 3193−3295

(582) Wang, Y.; Zhang, T.; Li, G.; Xu, F.; Wang, T.; Li, Y.; Yang, Y.; Zhao, Y. A Mixed-Cation Lead Iodide $MA_{1-x}EA_xPbI_3$ Absorber for Perovskite Solar Cells. *J. Energy Chem.* **2018**, *27*, 215−218.
(583) Chen, J.; Lee, D.; Park, N.-G. Stabilizing the Ag Electrode and Reducing J-V Hysteresis through Suppression of Iodide Migration in Perovskite Solar Cells. *ACS Appl. Mater. Interfaces* **2017**, *9*, 36338−36349.
(584) Grancini, G.; Roldán-Carmona, C.; Zimmermann, I.; Mosconi, E.; Lee, X.; Martineau, D.; Narbey, S.; Oswald, F.; De Angelis, F.; Graetzel, M.; et al. One-Year Stable Perovskite Solar Cells by 2D/3D Interface Engineering. *Nat. Commun.* **2017**, *8*, 15684.
(585) Fu, Y.; Rea, M. T.; Chen, J.; Morrow, D. J.; Hautzinger, M. P.; Zhao, Y.; Pan, D.; Manger, L. H.; Wright, J. C.; Goldsmith, R. H.; et al. Selective Stabilization and Photophysical Properties of Metastable Perovskite Polymorphs of $CsPbI_3$ in Thin Films. *Chem. Mater.* **2017**, *29*, 8385−8394.
(586) Zhang, T.; Dar, M. I.; Li, G.; Xu, F.; Guo, N.; Grätzel, M.; Zhao, Y. Bication Lead Iodide 2D Perovskite Component to Stabilize Inorganic α-$CsPbI_3$ Perovskite Phase for High-Efficiency Solar Cells. *Sci. Adv.* **2017**, *3*, No. e1700841.
(587) Park, B.-W.; Philippe, B.; Zhang, X.; Rensmo, H.; Boschloo, G.; Johansson, E. M. Bismuth Based Hybrid Perovskites $A_3Bi_2I_9$ (A: Methylammonium or Cesium) for Solar Cell Application. *Adv. Mater.* **2015**, *27*, 6806−6813.
(588) Harikesh, P. C.; Mulmudi, H. K.; Ghosh, B.; Goh, T. W.; Teng, Y. T.; Thirumal, K.; Lockrey, M.; Weber, K.; Koh, T. M.; Li, S.; et al. Rb as an Alternative Cation for Templating Inorganic Lead-Free Perovskites for Solution Processed Photovoltaics. *Chem. Mater.* **2016**, *28*, 7496−7504.
(589) Saparov, B.; Hong, F.; Sun, J.-P.; Duan, H.-S.; Meng, W.; Cameron, S.; Hill, I. G.; Yan, Y.; Mitzi, D. B. Thin-Film Preparation and Characterization of $Cs_3Sb_2I_9$: A Lead-Free Layered Perovskite Semiconductor. *Chem. Mater.* **2015**, *27*, 5622−5632.
(590) Khazaee, M.; Sardashti, K.; Sun, J.-P.; Zhou, H.; Clegg, C.; Hill, I. G.; Jones, J. L.; Lupascu, D. C.; Mitzi, D. B. A Versatile Thin-Film Deposition Method for Multidimensional Semiconducting Bismuth Halides. *Chem. Mater.* **2018**, *30*, 3538−3544.
(591) Saparov, B.; Sun, J.-P.; Meng, W.; Xiao, Z.; Duan, H.-S.; Gunawan, O.; Shin, D.; Hill, I. G.; Yan, Y.; Mitzi, D. B. Thin-Film Deposition and Characterization of a Sn-Deficient Perovskite Derivative Cs_2SnI_6. *Chem. Mater.* **2016**, *28*, 2315−2322.
(592) Choi, J. J.; Yang, X.; Norman, Z. M.; Billinge, S. J.; Owen, J. S. Structure of Methylammonium Lead Iodide within Mesoporous Titanium Dioxide: Active Material in High-Performance Perovskite Solar Cells. *Nano Lett.* **2014**, *14*, 127−133.
(593) Park, B.-W.; Philippe, B.; Gustafsson, T.; Sveinbjörnsson, K.; Hagfeldt, A.; Johansson, E. M. J.; Boschloo, G. Enhanced Crystallinity in Organic−Inorganic Lead Halide Perovskites on Mesoporous TiO_2 via Disorder−Order Phase Transition. *Chem. Mater.* **2014**, *26*, 4466−4471.
(594) De Bastiani, M.; D'Innocenzo, V.; Stranks, S. D.; Snaith, H. J.; Petrozza, A. Role of the Crystallization Substrate on the Photoluminescence Properties of Organo-Lead Mixed Halides Perovskites. *APL Mater.* **2014**, *2*, 081509.
(595) Huang, F.; Pascoe, A. R.; Wu, W.-Q.; Ku, Z.; Peng, Y.; Zhong, J.; Caruso, R. A.; Cheng, Y.-B. Effect of the Microstructure of the Functional Layers on the Efficiency of Perovskite Solar Cells. *Adv. Mater.* **2017**, *29*, 1601715.
(596) Wu, W.-Q.; Huang, F.; Chen, D.; Cheng, Y.-B.; Caruso, R. A. Solvent-Mediated Dimension Tuning of Semiconducting Oxide Nanostructures as Efficient Charge Extraction Thin Films for Perovskite Solar Cells with Efficiency Exceeding 16%. *Adv. Energy Mater.* **2016**, *6*, 1502027.
(597) Wu, W.-Q.; Huang, F.; Chen, D.; Cheng, Y.-B.; Caruso, R. A. Thin Films of Dendritic Anatase Titania Nanowires Enable Effective Hole-Blocking and Efficient Light-Harvesting for High-Performance Mesoscopic Perovskite Solar Cells. *Adv. Funct. Mater.* **2015**, *25*, 3264−3272.
(598) Pascoe, A. R.; Meyer, S.; Huang, W.; Li, W.; Benesperi, I.; Duffy, N. W.; Spiccia, L.; Bach, U.; Cheng, Y.-B. Enhancing the Optoelectronic Performance of Perovskite Solar Cells via a Textured $CH_3NH_3PbI_3$ Morphology. *Adv. Funct. Mater.* **2016**, *26*, 1278−1285.
(599) Safdari, M.; Svensson, P. H.; Hoang, M. T.; Oh, I.; Kloo, L.; Gardner, J. M. Layered 2D Alkyldiammonium Lead Iodide Perovskites: Synthesis, Characterization, and Use in Solar Cells. *J. Mater. Chem. A* **2016**, *4*, 15638−15646.
(600) Sanehira, Y.; Numata, Y.; Ikegami, M.; Miyasaka, T. Photovoltaic Properties of Two-dimensional $(CH_3(CH_2)_3NH_3)_2PbI_4$ Perovskite Crystals Oriented with TiO_2 Nanowire Array. *Chem. Lett.* **2017**, *46*, 1204−1206.
(601) Hörantner, M. T.; Zhang, W.; Saliba, M.; Wojciechowski, K.; Snaith, H. J. Templated Microstructural Growth of Perovskite Thin Films via Colloidal Monolayer Lithography. *Energy Environ. Sci.* **2015**, *8*, 2041−2047.
(602) Chen, B.-X.; Rao, H.-S.; Chen, H.-Y.; Li, W.-G.; Kuang, D.-B.; Su, C.-Y. Ordered Macroporous $CH_3NH_3PbI_3$ Perovskite Semitransparent Film for High-Performance Solar Cells. *J. Mater. Chem. A* **2016**, *4*, 15662−15669.
(603) Kwon, H.-C.; Kim, A.; Lee, H.; Lee, D.; Jeong, S.; Moon, J. Parallelized Nanopillar Perovskites for Semitransparent Solar Cells Using an Anodized Aluminum Oxide Scaffold. *Adv. Energy Mater.* **2016**, *6*, 1601055.
(604) Zheng, X.; Wei, Z.; Chen, H.; Zhang, Q.; He, H.; Xiao, S.; Fan, Z.; Wong, K. S.; Yang, S. Designing Nanobowl Arrays of Mesoporous TiO_2 as an Alternative Electron Transporting Layer for Carbon Cathode-Based Perovskite Solar Cells. *Nanoscale* **2016**, *8*, 6393−6402.
(605) Zhang, F.; Song, J.; Chen, M.; Liu, J.; Hao, Y.; Wang, Y.; Qu, J.; Zeng, P. Enhanced Perovskite Morphology and Crystallinity for High Performance Perovskite Solar Cells Using a Porous Hole Transport Layer from Polystyrene Nanospheres. *Phys. Chem. Chem. Phys.* **2016**, *18*, 32903−32909.
(606) Hu, X.; Huang, Z.; Zhou, X.; Li, P.; Wang, Y.; Huang, Z.; Su, M.; Ren, W.; Li, F.; Li, M.; et al. Wearable Large-Scale Perovskite Solar-Power Source via Nanocellular Scaffold. *Adv. Mater.* **2017**, *29*, 1703236.
(607) Yang, G.; Wang, C.; Lei, H.; Zheng, X.; Qin, P.; Xiong, L.; Zhao, X.; Yan, Y.; Fang, G. Interface Engineering in Planar Perovskite Solar Cells: Energy Level Alignment, Perovskite Morphology Control and High Performance Achievement. *J. Mater. Chem. A* **2017**, *5*, 1658−1666.
(608) Singh, T.; Öz, S.; Sasinska, A.; Frohnhoven, R.; Mathur, S.; Miyasaka, T. Sulfate-Assisted Interfacial Engineering for High Yield and Efficiency of Triple Cation Perovskite Solar Cells with Alkali-Doped TiO_2 Electron-Transporting Layers. *Adv. Funct. Mater.* **2018**, *28*, 1706287.
(609) Lee, J.; Kang, H.; Kim, G.; Back, H.; Kim, J.; Hong, S.; Park, B.; Lee, E.; Lee, K. Achieving Large-Area Planar Perovskite Solar Cells by Introducing an Interfacial Compatibilizer. *Adv. Mater.* **2017**, *29*, 1606363.
(610) Kagan, C. R.; Breen, T. L.; Kosbar, L. L. Patterning Organic−Inorganic Thin-Film Transistors Using Microcontact Printed Templates. *Appl. Phys. Lett.* **2001**, *79*, 3536−3538.
(611) Wu, J.; Chen, J.; Zhang, Y.; Xu, Z.; Zhao, L.; Liu, T.; Luo, D.; Yang, W.; Chen, K.; Hu, Q.; et al. Pinhole-Free Hybrid Perovskite Film with Arbitrarily-Shaped Micro-Patterns for Functional Optoelectronic Devices. *Nano Lett.* **2017**, *17*, 3563−3569.
(612) Feng, J.; Yan, X.; Zhang, Y.; Wang, X.; Wu, Y.; Su, B.; Fu, H.; Jiang, L. "Liquid Knife" to Fabricate Patterning Single-Crystalline Perovskite Microplates toward High-Performance Laser Arrays. *Adv. Mater.* **2016**, *28*, 3732−3741.
(613) Geske, T.; Li, J.; Worden, M.; Shan, X.; Chen, M.; Bade, S. G. R.; Yu, Z. Deterministic Nucleation for Halide Perovskite Thin Films with Large and Uniform Grains. *Adv. Funct. Mater.* **2017**, *27*, 1702180.
(614) Wang, L.; Chen, P.; Thongprong, N.; Young, M.; Kuttipillai, P. S.; Jiang, C.; Zhang, P.; Sun, K.; Duxbury, P. M.; Lunt, R. R.

DOI: 10.1021/acs.chemrev.8b00318
Chem. Rev. 2019, 119, 3193−3295

Unlocking the Single-Domain Epitaxy of Halide Perovskites. *Adv. Mater. Interfaces* **2017**, *4*, 1701003.
(615) Wang, Y.; Sun, X.; Chen, Z.; Sun, Y.-Y.; Zhang, S.; Lu, T.-M.; Wertz, E.; Shi, J. High-Temperature Ionic Epitaxy of Halide Perovskite Thin Film and the Hidden Carrier Dynamics. *Adv. Mater.* **2017**, *29*, 1702643.
(616) Chen, J.; Morrow, D. J.; Fu, Y.; Zheng, W.; Zhao, Y.; Dang, L.; Stolt, M. J.; Kohler, D. D.; Wang, X.; Czech, K. J.; et al. Single-Crystal Thin Films of Cesium Lead Bromide Perovskite Epitaxially Grown on Metal Oxide Perovskite $SrTiO_3$. *J. Am. Chem. Soc.* **2017**, *139*, 13525−13532.
(617) Dember, H. Über eine Photoelektronische Kraft in Kupferoxydul-Kristallen. *Phys. Z.* **1931**, *32*, 554.
(618) Chen, J.; Fu, Y.; Samad, L.; Dang, L.; Zhao, Y.; Shen, S.; Guo, L.; Jin, S. Vapor-Phase Epitaxial Growth of Aligned Nanowire Networks of Cesium Lead Halide Perovskites ($CsPbX_3$, X = Cl, Br, I). *Nano Lett.* **2017**, *17*, 460−466.
(619) Qin, P.; He, Q.; Yang, G.; Yu, X.; Xiong, L.; Fang, G. Metal Ions Diffusion at Heterojunction Chromium Oxide/$CH_3NH_3PbI_3$ Interface on the Stability of Perovskite Solar Cells. *Surf. Interfaces* **2018**, *10*, 93−99.
(620) Shao, Y.; Xiao, Z.; Bi, C.; Yuan, Y.; Huang, J. Origin and Elimination of Photocurrent Hysteresis by Fullerene Passivation in $CH_3NH_3PbI_3$ Planar Heterojunction Solar Cells. *Nat. Commun.* **2014**, *5*, 5784.
(621) Yang, J.; Siempelkamp, B. D.; Mosconi, E.; De Angelis, F.; Kelly, T. L. Origin of the Thermal Instability in $CH_3NH_3PbI_3$ Thin Films Deposited on ZnO. *Chem. Mater.* **2015**, *27*, 4229−4236.
(622) Liu, D.; Kelly, T. L. Perovskite Solar Cells with a Planar Heterojunction Structure Prepared Using Room-Temperature Solution Processing Techniques. *Nat. Photonics* **2014**, *8*, 133−138.
(623) Liu, P.; Liu, X.; Lyu, L.; Xie, H.; Zhang, H.; Niu, D.; Huang, H.; Bi, C.; Xiao, Z.; Huang, J.; et al. Interfacial Electronic Structure at the $CH_3NH_3PbI_3/MoO_x$ Interface. *Appl. Phys. Lett.* **2015**, *106*, 193903.
(624) Liu, J.; Pathak, S. K.; Sakai, N.; Sheng, R.; Bai, S.; Wang, Z.; Snaith, H. J. Identification and Mitigation of a Critical Interfacial Instability in Perovskite Solar Cells Employing Copper Thiocyanate Hole-Transporter. *Adv. Mater. Interfaces* **2016**, *3*, 1600571.
(625) Kirchartz, T.; Markvart, T.; Rau, U.; Egger, D. A. Impact of Small Phonon Energies on the Charge-Carrier Lifetimes in Metal-Halide Perovskites. *J. Phys. Chem. Lett.* **2018**, *9*, 939−946.
(626) Saliba, M.; Correa-Baena, J.-P.; Wolff, C. M.; Stolterfoht, M.; Phung, N.; Albrecht, S.; Neher, D.; Abate, A. How to Make over 20% Efficient Perovskite Solar Cells in Regular (n−i−p) and Inverted (p−i−n) Architectures. *Chem. Mater.* **2018**, *30*, 4193−4201.
(627) Tsai, H.; Nie, W.; Lin, Y.-H.; Blancon, J. C.; Tretiak, S.; Even, J.; Gupta, G.; Ajayan, P. M.; Mohite, A. D. Effect of Precursor Solution Aging on the Crystallinity and Photovoltaic Performance of Perovskite Solar Cells. *Adv. Energy Mater.* **2017**, *7*, 1602159.
(628) Zhao, J.; Deng, Y.; Wei, H.; Zheng, X.; Yu, Z.; Shao, Y.; Shield, J. E.; Huang, J. Strained Hybrid Perovskite Thin Films and their Impact on the Intrinsic Stability of Perovskite Solar Cells. *Sci. Adv.* **2017**, *3*, No. eaao5616.
(629) Bush, K. A.; Rolston, N.; Gold-Parker, A.; Manzoor, S.; Hausele, J.; Yu, Z. J.; Raiford, J. A.; Cheacharoen, R.; Holman, Z. C.; Toney, M. F.; et al. Controlling Thin-Film Stress and Wrinkling during Perovskite Film Formation. *ACS Energy Lett.* **2018**, *3*, 1225−1232.
(630) Jacobsson, T. J.; Schwan, L. J.; Ottosson, M.; Hagfeldt, A.; Edvinsson, T. Determination of Thermal Expansion Coefficients and Locating the Temperature-Induced Phase Transition in Methylammonium Lead Perovskites Using X-ray Diffraction. *Inorg. Chem.* **2015**, *54*, 10678−10685.
(631) Fabini, D. H.; Stoumpos, C. C.; Laurita, G.; Kaltzoglou, A.; Kontos, A. G.; Falaras, P.; Kanatzidis, M. G.; Seshadri, R. Reentrant Structural and Optical Properties and Large Positive Thermal Expansion in Perovskite Formamidinium Lead Iodide. *Angew. Chem., Int. Ed.* **2016**, *55*, 15392−15396.
(632) Schueller, E. C.; Laurita, G.; Fabini, D. H.; Stoumpos, C. C.; Kanatzidis, M. G.; Seshadri, R. Crystal Structure Evolution and Notable Thermal Expansion in Hybrid Perovskites Formamidinium Tin Iodide and Formamidinium Lead Bromide. *Inorg. Chem.* **2018**, *57*, 695−701.

DOI: 10.1021/acs.chemrev.8b00318
Chem. Rev. 2019, 119, 3193−3295